

GEOMECHANICAL CHARACTERIZATION OF
GEOTHERMAL RELEVANT FAULT PATTERNS IN
SOUTHWEST GERMANY

Zur Erlangung des akademischen Grades eines

DOKTORS DER NATURWISSENSCHAFTEN

von der Fakultät

Bauingenieur-, Geo- und Umweltwissenschaften

des Karlsruher Instituts für Technologie (KIT)

genehmigte

DISSERTATION

von

Dipl.-Geol. Jörg Meixner

aus Potsdam

Tag der mündlichen

Prüfung: 22. Juli 2016

Referent: Prof. Dr. Thomas Kohl

Korreferent: Prof. Dr. Christoph Hilgers

Karlsruhe 2016

ABSTRACT

This thesis addresses to the analysis and evaluation of structural patterns in the Upper Rhine Graben and adjacent Schwarzwald within the regional stress field in order to identify relevant faults for hydrothermal reservoirs and enhanced geothermal systems (EGS). Critically stressed faults, favorably oriented for shear and dilational reactivation in the ambient state of stress, are the most promising targets for geothermal exploitation. They are assumed to exhibit zones of high permeability, thus probably controlling fluid flow in hydrothermal reservoirs, and outlining the best stimulation potential in EGS reservoirs. Estimates on the reactivation potential of faults require both definition of the fault or fracture geometry and the in-situ state of stress. Both sub-topics will be addressed to in this thesis.

The **first study** shows, exemplary for the geothermal site of Bruchsal, how stress measurements in deep-seated sedimentary reservoirs can be evaluated to infer the local stress condition in the crystalline basement. Therefore the quality and uncertainty range of earlier stress field models are evaluated and an alternative stress regime on the basis of the critically stressed crust concept is proposed. The derived stress field model at Bruchsal shows good accordance with the robust stress characterization for the Soultz-sous-Forêts reservoir.

The **second study** aims at identification of structural controls in the hydrothermal reservoirs of the Bruchsal and Riehen geothermal sites. Slip- and dilation tendency analyses reveal a distinct geometrical anisotropy in the complex fault pattern geometry at both sites. The results show that (W)NW-(E)SE trending faults, which dissect the dominant graben-parallel faults, are characterized by large slip and dilation tendencies. This is of crucial importance since such transfer faults represent a controlling factor for permeability variations within fault-hosted geothermal reservoirs and can be found in the entire Upper Rhine Graben.

The **third study** addresses the fault pattern in the crystalline basement of the southern Schwarzwald. The area is assumed to be a fairly good analogue for the EGS relevant, petrothermal reservoir rocks in the Upper Rhine Graben. It is shown, how remote sensing techniques can be applied to high-resolution digital elevation models in order to determine the structural inventory of the crystalline basement. A statistical assessment of the obtained lineament sets will investigate the impact of the resolution of different elevation data sets on the lineament extraction and furthermore allow the determination of representative statistics of the orientation, average length, and the total length of the mapped lineaments. The results show that the predomi-

nant WNW-ENE and NNE-SSW fault trends in the Schwarzwald are prone for shear reactivation in the ambient regional stress field indicating neotectonic activities.

The **fourth study** aims to test the applicability of several geomorphometric analyses to assess whether these critically stressed faults account for possible neotectonic activities. It is shown how geomorphometric methods in combination with precise leveling data can be used to quantitatively designate the interplay of active deformation processes in the upper crust and consequent geomorphological changes of landforms and landscapes. The results show that structural compartmentalization may apply for a large part of the crystalline basement and probably are expressed by uneven uplift motions in the basement.

Verification of the assumed presence of critically stressed faults in the Upper Rhine Graben is challenging since only few information on fault distributions in the basement are available. The former Basel geothermal site provides an unique access to an enhanced EGS reservoir in a distance to the outcropping analogue rocks of only 10 km and allows to compare the occurrence of critically stressed fractures/-faults in a natural and engineered environment. A structural geological interpretation of the 2006 stimulation of the Basel EGS reveals that W(NW)-E(SE) and N-S striking structures are critically stressed for shear reactivation during pressurization of the reservoir. The combination of primarily dilatant opening, secondarily shear reactivation, and aseismic fault creep of NNW striking fractures partly explains the occurrence of small magnitude earthquake events subparallel to the maximum horizontal stress and thus explains the observed NNW alignment of determined multiplets. The overall shape of the NNE oriented lens-shaped seismic cloud seems to be controlled by dilatant failure of pre-existing and non-critically stressed fracture zones in the direction of the maximum dilation tendency.

ZUSAMMENFASSUNG

Das Thema dieser Arbeit ist die Bewertung von Störungsmustern und tektonischen Spannungsfeldern im Oberrheingraben und im südlichen Schwarzwald. Das Ziel der Arbeit ist die Identifikation von Störungen, die für hydrothermale und petrothermale Energiegewinnung von großer Bedeutung sind. Für die Identifikation von günstigen geologischen Strukturmustern im Oberrheingraben sind belastbare Informationen über das Reaktivierungspotenzial einzelner Störungen von großer Bedeutung. Es wird gezeigt, dass kritisch gespannte Störungen Hauptziele für die geothermische Exploration darstellen. Diese Strukturen sind im regionalen Spannungsfeld optimal für eine Dehnungs- bzw. Scherreaktivierung orientiert. Für diese Strukturen werden erhöhte Permeabilitäten und deshalb wichtige kontrollierende Funktionen für den Fluidfluss im Reservoir angenommen. Diese Strukturen weisen deshalb wahrscheinlich auch die höchsten Stimulationspotenziale auf. Abschätzungen für das Reaktivierungspotenzial hängen wesentlich von der Orientierung und der Geometrie einer Bruchstruktur im umgebenden regionalen Spannungsfeld ab.

Die **erste Studie** zeigt beispielhaft am Geothermiestandort Bruchsal, wie Spannungsmessungen in tiefgelegenen sedimentären Reservoiren genutzt werden können, um auf lokale Spannungsverhältnisse im kristallinen Sockel zu schließen. Dafür werden frühere Spannungsabschätzungen diskutiert und neu bewertet. Auf der Grundlage des Konzeptes einer kritisch gespannten Kruste wird ein neues Spannungsfeldmodell vorgeschlagen, das mit der Charakterisierung des Spannungsfeldes am Geothermiestandort Soultz-sous-Forêts sehr gut übereinstimmt.

Die **zweite Studie** hat zum Ziel, die strukturellen Kontrollen der hydrothermalen Reservoire an den Geothermiestandorten Bruchsal und Riehen im Oberrheingraben zu charakterisieren. Slip- und Dilation Tendency Analysen weisen deutliche geomechanische Anisotropien in den strukturell komplexen Reservoiren beider Standorte aus. (W)NW-(E)SE-streichende Störungen, die die Graben-parallelen Störungen schneiden, zeigen eine hohe Tendenz, reaktiviert zu werden. Dies könnte von entscheidender Bedeutung für störungskontrollierte Reservoire sein, da kritisch gespannte Transferstörungen als hochleitfähige Strukturen deutliche Variationen in der Permeabilitätsverteilung im Reservoir verursachen können. Diese Transferstörungen treten möglicherweise im gesamten Oberrheingraben auf.

Die **dritte Studie** beschäftigt sich mit Störungsmustern im kristallinen Sockel des südlichen Schwarzwaldes. Dieses Gebiet stellt ein geeignetes Reservoiranalog für petrothermale Reservoire des Ober-

rheingrabens dar. Die Anwendung von Fernerkundungsmethoden auf unterschiedlich auflösende digitale Höhenmodelle und die statistische Auswertung der daraus resultierenden Lineamentdatensätze zeigt bevorzugte WNW-ESE und NNE-SSW-Streichrichtungen an. Diese Strukturen sind im regionalen Spannungsfeld günstig orientiert, um auf Scherung reaktiviert zu werden.

In der **vierten Studie** wird die Anwendbarkeit geomorphometrischer Analysen getestet, um zu untersuchen, ob kritisch gespannte Störungen im Südschwarzwald für mögliche neotektonische Aktivitäten in Frage kommen. Die Ergebnisse der geomorphometrischen Analyse zeigen eine gute Übereinstimmung mit Feinnivellement-Daten in der Region. Beide deuten auf neotektonische Bewegungen (störungegebundene Blocktektonik) im Südschwarzwald, dessen Einfluss sich durch deutlich Morphologieänderungen äußert. Eine strukturelle Zerblockung des kristallinen Sockels ist wahrscheinlich repräsentativ für große Bereiche des Südschwarzwaldes, was möglicherweise durch unregelmäßige Hebungsbewegungen zum Ausdruck kommt. Der Wissenstransfer aus einem Reservoiranalog ins Reservoir ist oft kritisch und bedarf immer einer Plausibilitätsprüfung. Beobachtungen während der hydraulischen Stimulation des EGS Reservoirs am nahegelegenen Geothermiestandort Basel ermöglichen dies. Herdflächenlösungen für die 28 stärksten Beben zeigen, dass N-S- und W(NW)-E(SE)-streichende Strukturen ebenfalls kritisch gespannt sind und während der Stimulation im Jahr 2006 reaktiviert wurden. Die Kombination aus primär sich öffnenden Dehnungsstrukturen, sekundären Scherbrüchen und aseismischem Kriechen entlang NNW-streichender Bruchstrukturen erklärt zudem die NNW-Ausrichtung der seismischen Wolke und ermittelter Multiplets. Die NNW-Ausrichtung der seismischen Wolke in Basel scheint von Dehnungsbrüchen prä-existierender und unkritisch gespannten Klüftzonen kontrolliert zu werden.

*Dedicated to my lovely children
Valerie & Erik*

CONTENTS

1	Introduction	1
2	Fundamentals of geomechanics and faulting	7
2.1	Stress in the Earth's crust	7
2.1.1	Definition of stress	7
2.1.2	Stress in two dimensions	10
2.1.3	Stress in three dimensions	12
2.1.4	Effective stress concept	14
2.2	Failure of rock	15
2.2.1	Rock failure criteria	15
2.2.2	Stress regimes and faulting mechanisms	19
2.3	The critical stressed crust	20
2.3.1	Critical stress theory	20
2.3.2	The stress polygon	23
2.3.3	Theory of slip and dilation tendency	24
3	Tectonic framework of Southwest Germany	27
3.1	Geological setting of the Upper Rhine Graben	27
3.1.1	Pre-rift setting of the URG area	28
3.1.2	Syn-rift Cenozoic evolution of the URG	32
3.2	Geological setting of the Schwarzwald	34
3.3	Present day stress state in SW Germany	37
4	Inferring the in-situ stress regime in deep sediments: an example from the Bruchsal geothermal site	41
4.1	Introduction	41
4.2	Geological Setting	42
4.3	Methods	45
4.3.1	S_{Hmax} orientation	45
4.3.2	S_v and P_p calculation	46
4.3.3	Stress field profiles for Bruchsal and adjacent areas	48
4.3.4	Critical stress concept	49
4.4	Results	50
4.4.1	Leak-off tests and S_{hmin} magnitude	50
4.4.2	Critical stresses of S_{hmin}	51
4.4.3	Critical stresses of S_{Hmax}	53
4.5	Discussion	54
4.5.1	Stress field variations	54
4.5.2	Stress profile	55
4.6	Conclusions	58

5	Structural control of geothermal reservoirs in extensional tectonic settings: an example from the Upper Rhine Graben	61
5.1	Introduction	62
5.2	Geological Setting	63
5.2.1	General overview	63
5.2.2	Structural setting of Bruchsal and Riehen	66
5.2.3	Stress states	73
5.3	Fault Modeling	74
5.3.1	Slip- and dilation tendency	74
5.3.2	Model geometry	74
5.4	Results	76
5.4.1	Normal faulting and normal faulting/strike-slip regimes in Bruchsal	76
5.4.2	Strike-slip regime in Riehen	77
5.5	Sensitivity of T_S and T_D calculation	81
5.6	Geomechanical interpretation	84
5.6.1	Absence of critically stressed faults	84
5.6.2	Anisotropy of the Slip- and Dilation Tendency	85
5.7	Conclusion	87
6	Lineament analysis for identification of fault zones in crystalline basement of the southern Schwarzwald (Germany)	89
6.1	Introduction	90
6.2	Regional setting	91
6.2.1	Geological overview	91
6.2.2	Regional stress state	94
6.3	Methods	96
6.3.1	Data	96
6.3.2	Lineament mapping	97
6.3.3	Slip- and Dilation Tendency Analysis	98
6.4	Results	99
6.4.1	The ASTER-DEM and LIDAR-DEM ₅ lineament maps	99
6.4.2	Statistical evaluation of the lineament sets	101
6.4.3	Slip- and dilation tendency analysis	103
6.5	Discussion	105
6.5.1	Lineament statistic and elevation models	105
6.5.2	Fault geometry and reactivation potential	108
6.6	Conclusion	112
7	Estimating fault activities by remote sensing at a geothermal reservoir analogue of crystalline rocks	115
7.1	Introduction	115
7.2	Neogene evolution of the southern Schwarzwald	116
7.2.1	Uplift of the southern Schwarzwald block	116
7.2.2	Evolution of the drainage pattern	117

7.3	Input data and Methods	119
7.3.1	Geomorphological indices	119
7.3.2	Precise leveling data	119
7.4	ZR-ratio analysis	122
7.4.1	Introduction	122
7.4.2	Methodology	123
7.4.3	Results & Discussion	123
8	Concluding discussion	133
8.1	Implications for EGS reservoirs in the Upper Rhine Graben	133
8.1.1	The 2006 stimulation of the Basel EGS	133
8.2	Implications for hydrothermal reservoirs in the Upper Rhine Graben	138
8.3	Implications for stress field characterizations	139
	Bibliography	159
	Declaration of authorship	161
	Acknowledgments	163

INTRODUCTION

There is a pressing need to accelerate the development of advanced energy technologies in order to address the global challenges of providing clean energy, mitigating climate change and sustainable development.¹

This statement by the International Energy Agency highlights one of the major challenges our society has to tackle in the next decades. To achieve this ambitious goal, successive transition from fossil and nuclear energy sources toward renewable energy technologies needs to be encouraged and realized by joint collaboration of all incorporated participants and stakeholders: technology-specific research, development, demonstration and deployment. Because of the huge technical potential of the resource for electricity and heat production, geothermal power has to supply a substantial part of future energy production. Global technical potentials for geothermal electricity and heat have been estimated in 2011 at 45 EJ/yr - 12'500 TWh_e (~62% of 2008 global electricity generation) and 1'040 EJ/yr - 289'000 TWh_t (~650% of 2008 global energy use for heat, [IEA \[2011\]](#)). In Germany, the technical potential for electricity generation is estimated at 1'200 EJ - 300'000 TWh that corresponds approximately to 600 times the annual electricity production of about 2 EJ [[Paschen et al., 2003](#)].

The advantages of geothermal power and heat production are undeniable. Since it is generally immune from weather effects and does not show seasonal variation, geothermal power typically provides base-load generation. With capacity factors of power plants up to 95%, the base-load characteristic distinguishes geothermal energy production from several other renewable technologies. Geothermal energy is an attractive energy option but is not (yet) competitive with wind and solar, i.e. in low enthalpy regions. Its exploitation is hampered by larger investment costs for the realization of projects, often large distances from energy demand centers, and the level of uncertainty in the exploratory phase. However, geothermal energy is still an attractive energy option since power plants can combine

¹ source: [[IEA, 2011](#)]

heat and power production, generate high rates of CO₂-neutral base-load electricity, and have a low space demand and environmental impact. Today, geothermal resources can be exploited reliably and economically from high enthalpy reservoirs, which are related to favorable geological settings with a 'shallow' seated volcanic heat source that provides temperatures up to 350°C. The vast majority of geothermal energy within drilling reach, such as in Germany, is in relatively dry and low-permeability rock. Here, application of the enhanced geothermal systems (EGS) technology seems to be the most promising way to still access the huge resource of heat. The estimated increase in worldwide geothermal production from today 12 GW_e up to 140-160 GW_e in 2050 [IEA, 2011] includes a fraction of 60% that should be achieved solely by EGS. In Germany, 95% of the technical potential account for heat resources that are associated with crystalline rocks, 4% with fault zones, and 1% with deep seated hydrothermal aquifers [Paschen et al., 2003]. These considerations highlight the important role of the EGS concept, as a way to increase the magnitude of economically recoverable geothermal resources.

During the past century several strategies and concepts for exploiting certain types of geothermal resources have been developed always with the basic premise to create commercial-grade geothermal system that mimics a natural geothermal reservoir. The EGS technology is one of them and has its roots in the 1970s and 1980s with development of the hot dry rock (HDR) concept. Generally, geothermal energy production is limited by the necessity of a high formation temperature, sufficient fluid to carry heat from the reservoir, and high formation permeability to transport the fluid through the subsurface at a high flow rate. In depth ranges of appropriate temperatures, down to 5-6 km in low enthalpy reservoirs, permeability adequate to achieve economic production is mostly not present and needs to be developed. Whereas HDR aimed at creation of an artificial heat exchanger in the deep crystalline basement, EGS focus on enhancing existing permeable structures. Figure 1.1 shows a schematic view of the EGS concept. The cold water enters the fracture network through the injection well, where it is heated up and brought back to the surface through the production well.

EGS today is best developed in the Upper Rhine Graben (URG). Cenozoic rifting activity caused subsidence of granitic and gneissic reservoir rocks in the Graben center of up to 5 km into appropriate temperature ranges for geothermal exploitation. Uplift along the Graben shoulders (e.g. Schwarzwald) successively exhumed the Paleozoic units providing access to the petrothermal reservoir rocks. Extensional tectonic settings favored development of hydrothermal convective cells circulating along cataclastic fault zones in the Paleozoic basement and in the Mesozoic cover rocks. The thermal regime

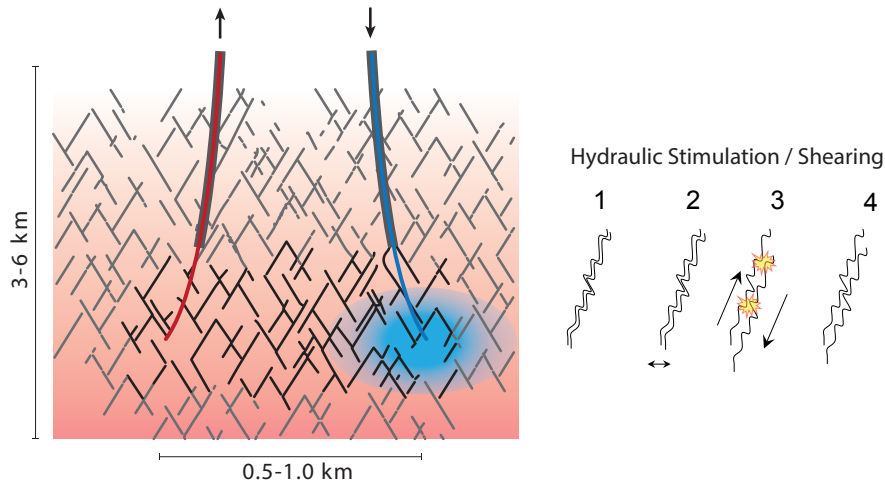


Figure 1.1: Principle of an enhanced geothermal system (left). Cool water is injected into an enhanced fracture network penetrating the geothermal reservoir. The heated water is extracted by a production well and used in a binary power plant for electricity generation. Enhancement of the fracture network aims at the creation of artificial flow paths between both wells by hydraulic stimulation (hydro-shearing) of existing fractures (right). 1: initial fracture, 2: normal opening of the fracture by pressurizing, 3: coseismic and/or aseismic shearing of the fracture, 4: permeability enhancement by larger fracture aperture

of the URG is characterized by a series of geothermal anomalies, e.g. near Soultz-sous-Forêts, Rittershoffen, and Landau, with local thermal gradients up to $100\text{ }^{\circ}\text{C}/\text{km}$ and heat flow densities up to $140\text{ mW}/\text{m}^2$ [Pribnow and Schellschmidt, 2000; Clauser and Villinger, 1990]. Almost 30 years of intense exploration and testing at the pilot EGS in Soultz-sous-Forêts (Alsace, France) has produced a huge quantity of geoscientific data. The more recently developed EGS Project of Landau, Insheim, and Rittershoffen prove applicability of the technology in the URG and promote the continuation of the existing learning curve.

Foundation of the concept of EGS is the use of hydraulic and chemical stimulation to generate permeability, and then circulate fluid in a closed loop between injector and production wells. Success of stimulation techniques becomes apparent e.g. for the Soultz-sous-Forêts and Landau reservoirs where injectivity and productivity of the wells could be increased by several orders in magnitude [e.g. Schindler et al., 2010; Schill et al., 2015]. Whereas HDR was focused on hydraulic fracturing techniques, EGS primarily aims at hydraulic shearing (pure shear stimulation) albeit the fact that occurrence of both mechanisms during stimulation is inevitable [e.g. McClure and Horne, 2014]. The advantage of hydraulic shearing is seen in the per-

manent permeability increase due to self-propping of fractures and the lower injection pressure required [Gischig and Preisig, 2015].

Problems associated with induced and triggered seismicity limit the extensiveness of a hydraulic stimulation. During stimulation of the 5 km deep reservoir in Soultz-sous-Forêts and the 2.5 km deep reservoir in Landau, induced seismicity was generated up to $M_L = 2.9$ and $M_L = 2.7$, respectively [Cuenot et al., 2006; Bönnemann et al., 2010]. In the Basel Deep Heat Mining project a $M_L = 3.4$ event was induced as reaction to a massive high pressure fluid injection [Häring et al., 2008]. The occurrence of felt earthquakes have led to public aversion against geothermal projects and resulted in a project suspension (Basel) and a limited power plant operation with distinct restrictions by local authorities (Landau). However, the phenomena associated to induced seismicity are two-fold, on the one hand deliberately induced seismicity indicates fluid pathways and is a key information for the planning of borehole trajectories of further wells, on the other hand it can create sensible seismicity that can harm project development due to public concerns. In order to manage concerns about induced seismicity, existing methods need to be improved to mitigate the seismic hazard. This affects not only the geothermal projects but also hydrocarbon or CO₂ sequestration projects and requires scientific investigations for the understanding of the associated processes. This thesis aims to improve the understanding of the hydro-mechanical interaction under stimulation conditions and covers especially the geological and mechanical constraints that lead to reactivation of crustal discontinuities and that are responsible for induced seismicity.

During a hydraulic stimulation reservoir over-pressure may induces slip along pre-existing fractures that are favorably oriented in the stress field for reactivation in shear. Whether a fracture or fault is optimally oriented for shear failure depends on:

- the frictional properties of the rupture plane,
- the in-situ state of stress,
- the orientation of the pressurized discontinuities in the reservoir.

Time- and slip-dependent frictional properties of fault or fractures surfaces are controlled by various parameters such as the existence of interlocking asperities, local changes in lithology, or the occurrence of a weak clay-bearing fault gouge. In-situ determination of these parameters at reservoir scale seems impossible because of their heterogeneous distribution and spatial variation. Hence, focus in this thesis is on the evaluation of structural patterns and tectonic stress fields in the Rhine Graben and the adjacent Schwarzwald.

Failure criteria can be used to describe frictional failure of rock (Section 2.2.1) but they require definition of the stress state and the fault or fracture geometry. In the URG, however, both parameters are still poorly constrained. Only few measurements of the in-situ state of stress have been conducted in crystalline basement rocks (Section 3.3). Extrapolation of measurements from sedimentary cover rocks to greater depths is still a challenging task since both magnitude and orientation of the principal stresses are often biased by topography, geological unconformities such as stratifications and lithology, or discontinuities such as faults or fractures [e.g. Heidbach et al., 2010; Zang and Stephansson, 2010; Sahara et al., 2014]. I will show in section 4, exemplary for the geothermal site of Bruchsal, how stress measurements in deep seated sediments can be evaluated to still infer indirectly the local stress condition. Therefore we evaluate the quality and uncertainty range of earlier stress field models and propose an alternative stress regime on the basis of the critical stressed crust concept (Section 2.3) and new available logging and well test data. The derived state of stress at Bruchsal shows good accordance with the well constrained stress models at Soultz, which is located in the same segment of the URG.

Hydrothermal, non-stimulated systems (economically viable over many years) occur generally in deep sediments along the main boundary faults. Identification of the structural controls at reservoir scale is of crucial importance since they represent a controlling factor for permeability variations within fault-hosted geothermal reservoirs [e.g. Curewitz and Karson, 1997; Faulds et al., 2011a; Moeck, 2014]. A number of fault zones of different orientations are observed at the Bruchsal and Riehen geothermal site, indicating a distinct fault-bounded compartmentalization of both hydrothermal reservoirs. Section 5 addresses the potential impact of geomechanical anisotropies in such orthogonal fault patterns on the hydraulic communication of geothermal wells. Slip and dilation tendency analysis are used to infer the criticality of the structures for reactivation in the local state of stress.

Structural models for hydrothermal reservoirs commonly base on seismic surveys. They built up a comprehensive database of the structural inventory in the uppermost 2-5 km of the URG but almost solely show good resolutions within the Mesozoic sediments and Cenozoic syn-rift deposits (Section 3). In the Paleozoic crystalline basement of the URG, however, reconnaissance of structures is a much more challenging task. General overview of the basement lithology and the Variscan structural grain has been inferred from gravity and magnetics (Section 3.1.1). Fault traces often need to be extrapolated to greater depths. A detailed structural map of the URG basement is lacking. The fact that Soultz has achieved perhaps the highest per-

meability EGS reservoir to date, probably because it involves flow in highly fractured fault zones, highlights the urgent need for further research on these geothermal relevant structures in the basement.

I approach the general distribution of fault zones from lineament mapping in the southern Schwarzwald, where EGS relevant basement rocks are cropping out. The area is assumed to be a fairly good analogue for the EGS relevant, petrothermal reservoir rocks in the URG. Unfortunately, only few structural geological information are available for the entire study area. Large areas of the exhumed crystalline basement appears to be devoid of faults, when believing the the existing geological maps. This is in marked contrast to the abundantly mapped faults in the Triassic cover rocks in the vicinity. I will show in section 6, how remote sensing techniques can be applied to high-resolution elevation data in order to determine the structural inventory of the basement. A statistical assessment of the obtained lineament sets will investigate the impact of the resolution of different elevation data sets on the lineament extraction and furthermore allow the determination of representative statistics of the orientation, average length, and the total length of the mapped lineaments.

Section 7 aims to test the applicability several morphotectonic and hydrographic analyses to further assess (neo)tectonic activity of these critically stressed faults. I will show how tectonic geomorphology techniques in combination with precise leveling data can be used to quantitatively designate the interplay of active deformation processes in the upper crust and consequent morphological changes of landforms and landscapes. The results show that tectonic compartmentalization and block tectonics may apply for large part of the crystalline basement and probably are expressed by uneven uplift motions in the basement. A detailed study along the Vorwald Fault Zone highlights that (neo)tectonic activity of (N)NW to (W)NW striking structures can be inferred from distinct geomorphological imprints along their fault traces.

The existence of critically stressed faults in the basement of the URG is of high interest for geothermal exploitation. Improvement of geomechanical models as basis for stimulation campaigns may help to mitigate induced seismicity, i.e. the occurrence of show-stopping events of large magnitudes. Knowledge of preferential structures would furthermore facilitate development of undeveloped and expansion in producing fields and improve the identification of possible blind (or hidden) geothermal resources.

2

FUNDAMENTALS OF GEOMECHANICS AND FAULTING

The following chapter aims to give a brief introduction to the physical concepts of stress and strain that are commonly applied in solid Earth science. The first part is dedicated to fundamental concepts of continuum mechanics and focuses on the definition and the description of rock stress in the Earth's crust. It also introduces principles about the tectonic stress field which generally is associated to all kind of brittle deformation processes in the crust. I give a brief overview about potential sources of tectonic stresses and summarize causes that can lead to significant perturbations of tectonic stresses on local or regional scales.

The second part aims to describe basic concepts of geomechanics and faulting which is the focus of this thesis. This includes the Mohr-Coulomb's theory of sliding deformation in rocks and introduces fundamental principles of fracture mechanics and fault reactivation such as the slip- and dilation tendency analysis. The introduction of the fundamentals of geomechanics and faulting mainly follows the existing literature of [Scholz \[2010\]](#); [Zoback \[2010\]](#); [Cornet \[2015\]](#); [Zang and Stephansson \[2010\]](#); [Jaeger et al. \[2007\]](#); [Fjaer et al. \[2008\]](#).

2.1 STRESS IN THE EARTH'S CRUST

2.1.1 *Definition of stress*

A key component of a comprehensive geomechanical model is knowledge of the current state of stress. It is of high importance in solid Earth science and need to be understood for a broad range of applications such as in civil, mining, and energy (petroleum, geothermal) engineering, as well as in geology, and geophysics. Stresses in the Earth's crust originate from and are also the driving mechanism of geological processes at a variety of different spatial and temporal scales.

The stress state in the lithosphere is the result of forces acting upon and within it. In simplest terms, the stress vector, \vec{T} , at an arbitrary point P is defined as the force \vec{F} acting on a plane of the area A:

$$\vec{T} = \lim_{\Delta A \rightarrow 0} \frac{\Delta \vec{F}}{\Delta A}. \quad (2.1)$$

To be more precise, in an elementary volume the stress vector \vec{T} can comprise any possible angle which corresponds to any possible intersection plane passing through the point P (infinite number). Stress acting on a homogeneous, isotropic body at depth is thus describable as a tensor, σ . It consists of nine components σ_{ij} with $i, j = 1, 2, 3$:

$$\sigma = \begin{pmatrix} \sigma_{xx} & \tau_{xy} & \tau_{xz} \\ \tau_{yx} & \sigma_{yy} & \tau_{yz} \\ \tau_{zx} & \tau_{zy} & \sigma_{zz} \end{pmatrix} \quad (2.2)$$

The subscripts of the individual stress components refer to the direction the force \vec{F} is acting and the direction of the plane normal (face of the unit cube upon which the stress components acts - normally referred to as the x,y, and z direction). Normal stresses, acting in direction of the plane normal, are denoted with σ_{ii} , these are the diagonal elements of the stress tensor. All other components are called shear stresses and are denoted by τ_{ij} (Fig. 2.1a).

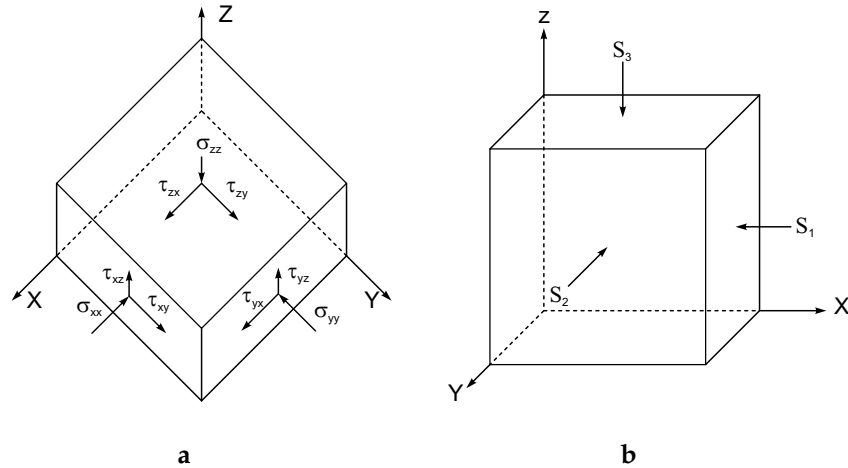


Figure 2.1: Definition of stress tensor in an arbitrary Cartesian coordinate system (a), [after Engelder and Leftwich, 1997] and with principal stresses as defined in a reference coordinate system where shear stresses vanish (b), [after Zoback, 2010].

Following the algebraic sign convention in geosciences a positive value of σ_{xx} , σ_{yy} , and σ_{zz} indicate a compressional state of stress. For simplification notation of the normal stress components is changed to σ_x , σ_y , and σ_z in the following. Because of equilibrium conditions

$$\tau_{xy} = \tau_{yx}, \quad \tau_{xz} = \tau_{zx}, \quad \tau_{yz} = \tau_{zy}.$$

Although each of these equivalent pairs are numerically equal, it is rather noteworthy that they are in fact physically distinct stress components which act on different faces of a volumetric element. The number of independent stress components in the symmetric stress tensor reduces, consequently, from nine to the following six:

$$\sigma = \begin{pmatrix} \sigma_x & \tau_{xy} & \tau_{xz} \\ \tau_{xy} & \sigma_y & \tau_{yz} \\ \tau_{xz} & \tau_{yz} & \sigma_z \end{pmatrix} \quad (2.3)$$

To determine the state of stress at one point one must define magnitudes for these six components or three stress magnitudes and the three angles that define the orientation of the arbitrary Cartesian coordinate system with respect to the reference coordinate system. The rotation of an arbitrary Cartesian coordinate system into any other reference coordinate system is called tensor transformation and is of fundamental importance:

1. It can be applied to derive the stress field surrounding a well-bore, a tunnel, or a fault zone of arbitrary orientation when the in-situ stress state in a geographic coordinate system is known.
2. It opens up the possibility to describe the state of stress at depth in terms of principal stresses (acting in the principal coordinate system).

The principal coordinate system which is the one in which the stress vectors of the tensor are purely normal and shear stresses vanish. The three remaining stress vectors fully describe the stress field and are called principal stresses (Fig. 2.1b). Here, magnitude and direction of the principal stresses correspond to the eigenvalues of the stress tensor and its eigenvectors, respectively. The stress matrix has now the following (diagonal) form:

$$\sigma = \begin{pmatrix} \sigma_1 & 0 & 0 \\ 0 & \sigma_2 & 0 \\ 0 & 0 & \sigma_3 \end{pmatrix} \quad (2.4)$$

with $\sigma_1 \geq \sigma_2 \geq \sigma_3$, where σ_1 is the maximum, σ_2 is the intermediate, and σ_3 is the least (minimum) principal stress component. The difference between the maximum and the least principal stress is called differential stress. The differential stress defines the magnitude of the shear stresses and is widely used to assess rock failure conditions, e.g. in structural geology.

2.1.2 Stress in two dimensions

For geoscientific purposes discussion on stress distribution is often idealized to two-dimensional simplifications of three-dimensional problems. Common examples of such problems are e.g. boreholes, tunnels, or fault zones. Such idealizations are based on the basic assumption that stresses do not vary along one Cartesian coordinate. Hence, it is worthwhile to discuss properties of a two-dimensional stress tensor as well as its graphical representation.

Following [Mohr, 1914], the following simple graphical construction can be used to access the state of stress at an arbitrary surface point. One consider the normal (σ) and shear stress (τ) acting on the slanted face of small triangular element of rock. The unit normal direction of this surface is rotated by a counterclockwise angle θ in the xy -plane (Fig. 2.2).

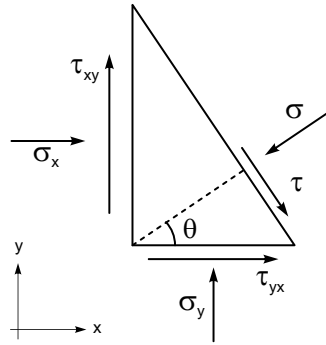


Figure 2.2: Two-dimensional representation of a failure plane that is inclined by an angle θ with respect to the σ_x -plane normal. Arrows indicate directions of the normal (σ) and shear (τ) stress components of the inherent force equilibrium [after Fjaer et al., 2008].

The normal stress (σ) and the shear stress (τ) which act on the failure plane can now be expressed as:

$$\sigma = \sigma_x \cos^2 \theta + \sigma_y \sin^2 \theta + 2\tau_{xy} \sin \theta \cos \theta \quad (2.5)$$

$$= \frac{\sigma_x + \sigma_y}{2} + \frac{\sigma_x - \sigma_y}{2} \cos 2\theta + \tau_{xy} \sin 2\theta \quad (2.6)$$

$$\tau = \sigma_y \sin \theta \cos \theta - \sigma_x \cos \theta \sin \theta + \tau_{xy} \cos^2 \theta - \tau_{yx} \sin^2 \theta \quad (2.7)$$

$$= \frac{\sigma_y - \sigma_x}{2} \sin 2\theta + \tau_{xy} \cos 2\theta \quad (2.8)$$

It is obvious from equation 2.8 that with the following choice of θ the shear stress becomes zero:

$$\tan 2\theta = \frac{2\tau_{xy}}{\sigma_x - \sigma_y} \quad (2.9)$$

Solving of Eq. 2.9 leads to the two solutions θ_1 and θ_2 which correspond to two directions for which the shear stress vanishes. As mentioned above, stress vectors which are aligned in these directions are denoted as the principal stress components; in this two-dimensional case σ_1 and σ_2 . They can be derived by introducing Eq. 2.9 into Eq. 2.6:

$$\sigma_1 = \frac{\sigma_x + \sigma_y}{2} + \sqrt{\tau_{xy}^2 + \frac{1}{4}(\sigma_x - \sigma_y)^2}, \quad (2.10)$$

$$\sigma_2 = \frac{\sigma_x + \sigma_y}{2} - \sqrt{\tau_{xy}^2 + \frac{1}{4}(\sigma_x - \sigma_y)^2} \quad (2.11)$$

with the principal stress axes in an orthogonal alignment and with the definition that $\sigma_1 \geq \sigma_2$. Due to a reorientation of the coordinate system in such a way that the σ_1 - and τ -principal axes are oriented parallel to the x- and y-axes the stresses σ and τ can be expressed as:

$$\sigma = \frac{\sigma_1 + \sigma_2}{2} + \frac{\sigma_1 - \sigma_2}{2} \cos 2\theta, \quad (2.12)$$

$$\tau = -\frac{\sigma_1 - \sigma_2}{2} \sin 2\theta. \quad (2.13)$$

These are equations of a circle in the (σ, τ) plane, with its center at the point $[\sigma = (\sigma_1 + \sigma_2)/2, \tau = 0]$ and the radius $(\sigma_1 - \sigma_2)/2$. This graphic representation is called the Mohr circle of stress [Mohr, 1914]. For a point P it illustrates the relation of the principal stresses to the normal and shear stresses applied on an arbitrarily tilted failure plane (Fig. 2.3).

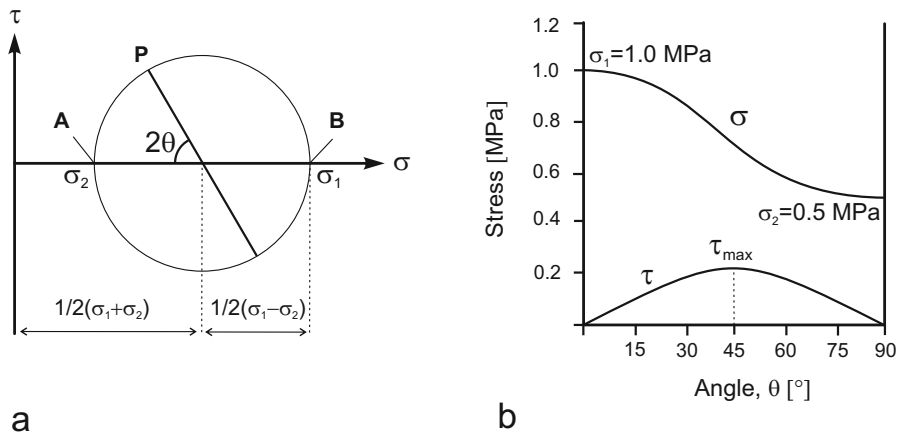


Figure 2.3: a) Mohr circle construction for the graphical representation of the relation of principal (σ_1, σ_2) to normal and shear stresses on an arbitrarily tilted failure plane. b) Variation of the normal and shear stress values with respect to the shear angle [after Zang and Stephansson, 2010].

The point B in figure 2.3a indicates that $\sigma = \sigma_1$ and $\tau = 0$. This stress state is observable for a failure plane which is oriented parallel

to the σ_1 direction ($\theta = 0$). The point A in figure 2.3a is characterized by $\sigma = \sigma_2$ and $\tau = 0$ and thus represent a failure plane which is rotated from the σ_1 direction by 90° (angle $2\theta = 180^\circ$ in the Mohr circle). The Mohr circle also clearly shows that the magnitude of the shear stress is equal to the radius of the circle and that maximum shear stress occurs on planes for which $2\theta = \pm 90^\circ$. These two failure planes are aligned in 45° angles from the σ_1 and σ_2 directions (Fig. 2.3b).

2.1.3 Stress in three dimensions

Mohr's circle representation of stress can also be used for three dimensions when directions in the 3D space are defined. Considering an arbitrarily tilted plane in a 3D space, the components of the unit normal vector \mathbf{n} relative to the principal coordinate system (x,y,z) can be expressed by l, m, n (Fig. 2.4).

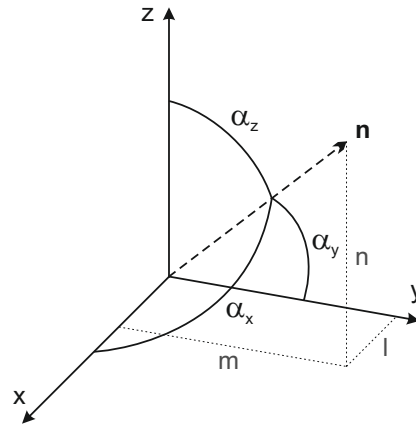


Figure 2.4: Stress components (l,m,n) and direction cosines ($\alpha_x, \alpha_y, \alpha_z$) of a failure plane in a 3D space and with the unit normal vector \mathbf{n} [after Fjaer et al., 2008].

According to figure 2.4, one can clearly see that for a transformation of the stresses into the principal coordinate system specification of the rotation for each component of the unit normal vector is needed. This can be done by the direction cosines:

$$\begin{aligned} l &= \cos(\mathbf{n}, x) = \cos \alpha_x \\ m &= \cos(\mathbf{n}, y) = \cos \alpha_y \\ n &= \cos(\mathbf{n}, z) = \cos \alpha_z \end{aligned}$$

The normal and shear stresses acting on the failure plane can now be expressed by

$$\sigma = l^2 \sigma_1 + m^2 \sigma_2 + n^2 \sigma_3 \quad (2.14)$$

$$\tau^2 = l^2 \sigma_1 + m^2 \sigma_2 + n^2 \sigma_3 - \sigma^2, \quad (2.15)$$

where

$$l^2 + m^2 + n^2 = 1. \quad (2.16)$$

Solving these equations for the direction cosines yields

$$l^2 = \frac{(\sigma_2 - \sigma)(\sigma_3 - \sigma) + \tau^2}{(\sigma_2 - \sigma_1)(\sigma_3 - \sigma_1)}, \quad (2.17)$$

$$m^2 = \frac{(\sigma_3 - \sigma)(\sigma_1 - \sigma) + \tau^2}{(\sigma_3 - \sigma_2)(\sigma_1 - \sigma_2)}, \quad (2.18)$$

$$n^2 = \frac{(\sigma_1 - \sigma)(\sigma_2 - \sigma) + \tau^2}{(\sigma_1 - \sigma_3)(\sigma_2 - \sigma_3)}. \quad (2.19)$$

Now one can consider three cases. In each case one of the direction cosines l , m , and n is suppose to be fixed. As a result, in each case possible orientations of the normal vector are represented by a cone around the corresponding axis and equation 2.17 to 2.19 can be rearrange to

$$\tau^2 = \left[\sigma - \frac{1}{2}(\sigma_2 + \sigma_3) \right]^2 = \frac{1}{4}(\sigma_2 - \sigma_3) + l^2(\sigma_2 - \sigma_1)(\sigma_3 - \sigma_1), \quad (2.20)$$

$$\tau^2 = \left[\sigma - \frac{1}{2}(\sigma_1 + \sigma_3) \right]^2 = \frac{1}{4}(\sigma_1 - \sigma_3) + m^2(\sigma_3 - \sigma_2)(\sigma_1 - \sigma_2), \quad (2.21)$$

$$\tau^2 = \left[\sigma - \frac{1}{2}(\sigma_1 + \sigma_2) \right]^2 = \frac{1}{4}(\sigma_1 - \sigma_2) + n^2(\sigma_1 - \sigma_3)(\sigma_2 - \sigma_3). \quad (2.22)$$

These are equations for circles in the (σ, τ) plane. This graphic representation is called the Mohr circle of stress in three dimensions (Fig. 2.5). The three circles represent the normal and shearing stresses acting on a point on an arbitrarily oriented plane.

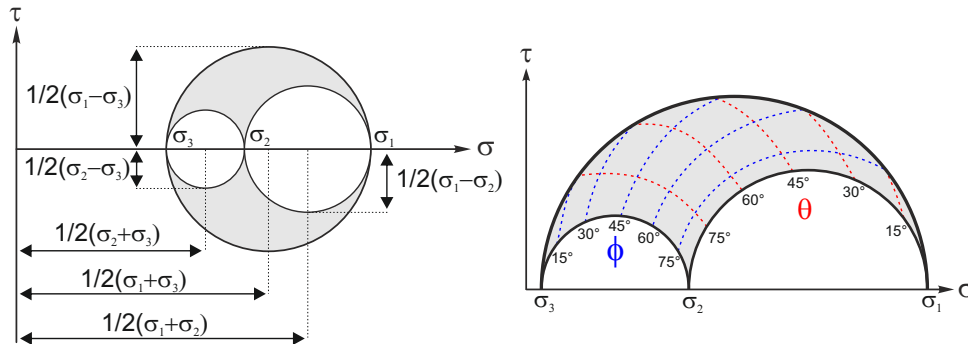


Figure 2.5: Mohr's circle construction in three dimensions [after Jaeger et al., 2007] (see text for description).

The midpoints of the circles, described by equation 2.20 to 2.22, are located at

$$\sigma = (\sigma_2 + \sigma_3)/2, \tau = 0, \quad (2.23)$$

$$\sigma = (\sigma_1 + \sigma_3)/2, \tau = 0, \quad (2.24)$$

$$\sigma = (\sigma_1 + \sigma_2)/2, \tau = 0. \quad (2.25)$$

Since cosines l , m , and n vary from 1 to 0 the radii of the circles as described by the equation 2.20 to 2.22 range between

$$(\sigma_2 - \sigma_3)/2 \text{ and } \sigma_1 - [(\sigma_2 + \sigma_3)/2] \text{ (for } 0 \leq l \leq 1) \quad (2.26)$$

$$(\sigma_1 - \sigma_3)/2 \text{ and } [(\sigma_1 + \sigma_3)/2] - \sigma_2 \text{ (for } 0 \leq m \leq 1) \quad (2.27)$$

$$(\sigma_1 - \sigma_2)/2 \text{ and } [(\sigma_1 + \sigma_2)/2] - \sigma_3 \text{ (for } 0 \leq n \leq 1) \quad (2.28)$$

A graphic representation of both the midpoints and the radii are shown in (Fig. 2.5a). Similar to the visualization of stress in two dimensions, the radius of the largest circle depends on the differential stress ($\sigma_1 - \sigma_3$) and yields the maximum shearing stress. It is obvious that Mohr's circle of stress displays every stress state possible in a 3D space. If $l = 0$ (yz-plane in Fig 2.4), the stresses σ and τ are located on the small circle spanning from σ_3 to σ_2 . If $n = 0$ (xy-plane in Fig 2.4), σ and τ are located on the circle spanning from σ_2 to σ_1 and, finally, if $m = 0$ (xz-plane in Fig 2.4), σ and τ are located on the large circle spanning from σ_3 to σ_1 . For a generic point of an arbitrary position in a 3D space, σ and τ can now be found by locating the intersections of the proper circles. This location can be expressed by the two angles $\theta = \arccos(n)$ and $\phi = \arccos(l)$ which completely describe the deviation of the normal vector from the the principal stress axes (shown as shaded area in figure 2.5b).

2.1.4 Effective stress concept

In the previous sections on stresses in the Earth's crust rock has always been assumed to be a solid and homogeneous body. Of course, this a simplification and hence does not reflect the real world. Rocks in the upper crust are porous and the presence of fluids (water, oil, gas) can not be neglected. Observations from deep boreholes such as the KTB project indicate hydraulic permeabilities of fractured rock masses in depths down to approximately 10 km [e. g. Huenges and Zimmermann, 1999; Brudy et al., 1997; Emmermann and Lauterjung, 1997]. Saturation of rocks with fluids leads to a pore pressure, P_p , that may affect the in-situ state of stress and the failure of the rock. The geomechanical behavior of rock from the last sections thus has to be modified.

The value of the pore pressure at depth is usually described in relation to hydrostatic pressure, a pressure associated to a column of water from the surface to the depth of interest, z . This implies an open and fully interconnected pore volume in the overburden. The pore pressure is obtained from integrating fluid density, ρ_w , in the column above the point of interest:

$$P_P = \int_0^z \rho_w(z)g \, dz \approx \rho_w g z \quad (2.29)$$

where g is the gravitational acceleration. The pore pressure acts "outward" from the pore space, in some sense in a negative direction like a tensile stress. This effect should be the same in any three mutually orthogonal directions and implies that the principal stresses, reckoned positive if compressive, need to be reduced by the pore pressure. These "reduced" stresses are referred to as the effective stresses [Terzaghi, 1936]:

$$\sigma_{1\text{eff}} = \sigma_1 - P_P, \quad \sigma_{2\text{eff}} = \sigma_2 - P_P, \quad \sigma_{3\text{eff}} = \sigma_3 - P_P. \quad (2.30)$$

2.2 FAILURE OF ROCK

2.2.1 Rock failure criteria

Stresses in the Earth cannot exceed the strength of rocks. The maximum rock strength limits magnitudes of principal stresses, i. e. the differential stress that can be applied on it. This geomechanical constraint is referred to as the critical state of stress [Zoback et al., 2003]. Once the critical stress is reached, rock failure occurs. In the brittle crust this become apparent either by reactivation of pre-existing faults or by creation of new ones. Geomechanical descriptions of the transition between stable and unstable conditions are called failure criteria. They define the relationship between material properties and the effective stresses acting at the point of failure.

A very simple failure criterion is that of Coulomb [1773]. It postulated that a shear fracture occurs in isotropic material, if the maximum shear stress is reached. According to figure 2.3 the failure criterion reads

$$\tau_{\text{max}} \geq \frac{\sigma_1 + \sigma_3}{2} \quad (2.31)$$

In the Mohr circle representation this equation defines a straight line in the σ - τ -plane that intersects the τ -axis at τ_{max} . If principal stress are such that the Mohr circle touches the failure line, shear failure occurs along $\pm 45^\circ$ dipping conjugated shear angles.

An other widely used failure criterion is that of Mohr-Coulomb. It postulated that failure in a rock takes place along a plane due to the shear stress τ acting along that plane. The shear strength of the rock and hence the resistance to failure is assumed to be made up of two parts: (1) a stresses-dependent frictional force created by the normal stresses multiplied by a coefficient of friction ($\sigma\mu$) and (2) a constant term c referred to as the cohesion coefficient. Failure occurs if the shear stresses are larger than the cohesion plus the frictional strength:

$$\tau \geq \mu\sigma + c. \quad (2.32)$$

The coefficient of internal friction μ is a rock material property. Values range approximately between 0.2 and 1.2 and they are, remarkably, only little dependent on lithology. [Byerlee \[1978\]](#) deduced from shear experiments on crustal rocks with low-displacement rates (<10 mm) that the frictional resistance is dependent on the applied normal stress. At low confining pressures with normal stresses below 200MPa a mean value of 0.85 is found for μ . With normal stresses exceeding 200MPa μ typically takes values in the order of 0.6. Due to the fact that all rock samples were treated as homogeneous bodies, this relation, known as Byerlee's law, provides only a rough estimate on μ . The experimentally derived values for μ may not account for fracture and fault planes at field scale since mineralogical variations along and across such failure planes (as caused e.g. by alteration or by grain size reduction due to brittle deformation) were neglected. There are various observations that indicate that frictional resistance can deviate significantly from that predicted by Byerlee's law. Especially with existence of high pore pressures or clayey fault gauges friction coefficients of much smaller values of 0.2 and even below were inferred [e.g. [Plenefisch and Bonjer, 1997](#); [Lockner et al., 2011](#); [Collettini et al., 2009](#); [Brown et al., 2003](#)]. These observations indicate existence of very weak fault zones that probably deform by aseismic creep rather than coseismic stick-slip processes. In contrast, e.g. [Zoback and Healy \[1992\]](#) or [Brudy et al. \[1997\]](#) could show for a number of borehole measurements that the strength of the crust is limited by critically stressed faults with hydrostatic pore fluid pressures and coefficients of friction in the range 0.6-1.0.

In the Mohr circle representation equation 2.32 defines a straight line in the σ - τ -plane that intersects the τ -axis at c . The slope of the line is μ and the angle φ to the σ -axis is called the angle of internal friction and is given by $\varphi = \tan^{-1}\mu$ (Fig. 2.6).

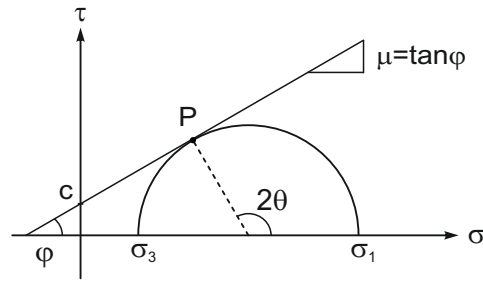


Figure 2.6: Graphical representation of the Mohr-Coulomb failure criterion [after Jaeger et al., 2007].

The Mohr circle touches the failure line for a plane at point P and at an angle 2θ from the σ_1 direction where θ is the angle between the fault normal and σ_1 . According to equation 2.12 and 2.13 the angle θ of a fault plane which is optimally oriented for failure and the friction angle φ are related by:

$$\theta = \pm \left(\frac{\pi}{4} \mp \frac{\varphi}{2} \right). \quad (2.33)$$

For mathematical consistency it should be mentioned here that this equation actually covers four angles in total. In a compressive state of stress conjugate shear planes may occur in $\theta=45^\circ-(\varphi/2)$ and $\theta=-45^\circ+(\varphi/2)$ direction. When failure envelope crosses the transition to from a compressive to a tensile stress state, a second pair of fracture angles exists at conjugate angles in $\theta=45^\circ+(\varphi/2)$ and $\theta=-45^\circ-(\varphi/2)$ direction. This relation of the rupture plane orientation is used in structural geology and tectonics to distinguish between different types of faulting and is discussed in section 2.2.2. According to equation 2.33 the failure angle θ is given solely by the friction angle φ which is a constant in the Mohr-Coulomb failure criterion. Orientation of the failure plane is thus independent of the confining stress. This is in contradiction to observations where the failure angle decreases with increasing confining pressure.

Mohr [1914] suggested the following non-linear failure relation, often referred to as the *generalized Mohr fracture criterion*:

$$|\tau| = f(\sigma). \quad (2.34)$$

Failure occurs if a certain threshold $f(\sigma)$ of shear stress is exceeded. Graphically, the failure criterion can be described as the envelope of all Mohr circles with critical stress states that cause failure. The failure curve is usually concave downward with decreasing failure angles for increasing confining pressures. In frictional faulting

equilibrium shear stresses τ parallel to the fracture are balanced by frictional forces acting through stresses normal to fractures σ and stabilizing the rock.

It is well known that the frictional strength of the crust depends not only on the intrinsic frictional strength of faulted rock, but also on the pore pressure at depth [King Hubbert and Rubey, 1959]. Considering the Mohr-Coulomb criterion with the effective stress concept (section 2.1.4), one can see that pore fluid pressure reduces the absolute stresses by the same amount. Considering a pore pressure the Mohr circle gets shifted to the left and towards the failure envelope until a critical state of stress is reached. At this point the Mohr circle touches the failure curve and failure should occur (Fig. 2.7).

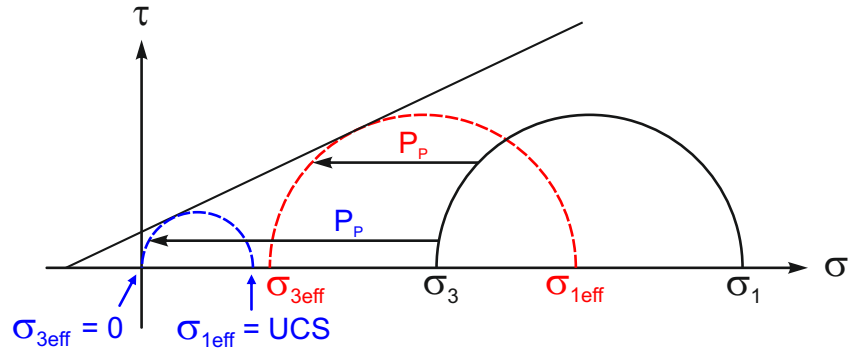


Figure 2.7: Mohr-Coulomb criterion for a two-dimensional stress tensor showing the effect of pore pressure, p , on total stresses σ_1 and σ_3 . The red Mohr circle indicates how an increase in pore pressure changes the stress state towards failure condition without variations of the differential stress. The blue Mohr circle shows how failure conditions due to a pore pressure increase can be compensated by reduction of the differential stress (radius of the Mohr circle decreases).

It is obvious that an additional increase of the pore fluid pressure may result in unstable overcritical conditions. To prevent failure and to remain stable conditions an additional pore pressure increase can be only compensated by a decrease of the Mohr circle radius. At the point where the confining pressure is zero ($\sigma_{3\text{eff}} = 0$), the $\sigma_{1\text{eff}}$ magnitude corresponds to the unconfined compressive strength (UCS) of the rock (Fig. 2.7). According to equation 2.32 one could also describe the linear Mohr-Coulomb failure curve in terms of its intercept when $\sigma_{3\text{eff}} = 0$ which is referred to as the cohesive strength or cohesion c . Following Zoback [2010], the relation between c and UCS can be expressed as:

$$\text{UCS} = 2c \left[(\mu^2 + 1)^{1/2} + \mu \right] \quad (2.35)$$

2.2.2 Stress regimes and faulting mechanisms

Anderson [1951] argued that the spatial orientation of the principal stresses is a function of the Earth's free surface, which can carry no shear stresses. The vertical stress is thus suggested to be a principal stress component. This assumption is no longer valid when the surface of the Earth shows significant topography. Topography causes inclined principal stress trajectories due to the fact that they cut free surfaces always at right angles. However, if this approximation can be made, the vertical stress σ_v at depth z is given by the weight of the overburden and the gravitational acceleration:

$$\sigma_v = \int_0^z \rho(z)g \, dz, \quad (2.36)$$

with the depth-dependent density of the rock formation $\rho(z)$. The other principal stresses are the maximum and minimum horizontal stresses, S_{Hmax} and S_{hmin} . They are, again, assumed to be aligned parallel to principal stress axes and are commonly referred to as *tectonic stresses*. Their magnitudes are primarily determined by plate tectonics and a result of broad-scale tectonic forces that act on lithospheric plates. Based on these assumptions, Anderson [1951] established the traditional classification of stresses by their orientation relative to the Earth's free surface. Based on observable deformation patterns they can be grouped in three principal stress regimes and related styles of faulting (Fig. 2.8):

$$\begin{aligned} \text{Normal faulting} & S_v \geq S_{Hmax} \geq S_{hmin}, \\ \text{Strike slip faulting} & S_{Hmax} \geq S_v \geq S_{hmin}, \\ \text{Reverse faulting} & S_{Hmax} \geq S_{hmin} \geq S_v. \end{aligned}$$

According to equation 2.33 fracture takes place in one or both of a pair of conjugate failure planes that pass through the direction of the intermediate principal stress at an angle less than 45° from the direction of the maximum principal stress. The actual failure angle θ is solely dependent on the angle of internal friction φ . Since measured values of φ commonly range from 30° and 55° , values of θ between 17° and 30° might be expected in the field.

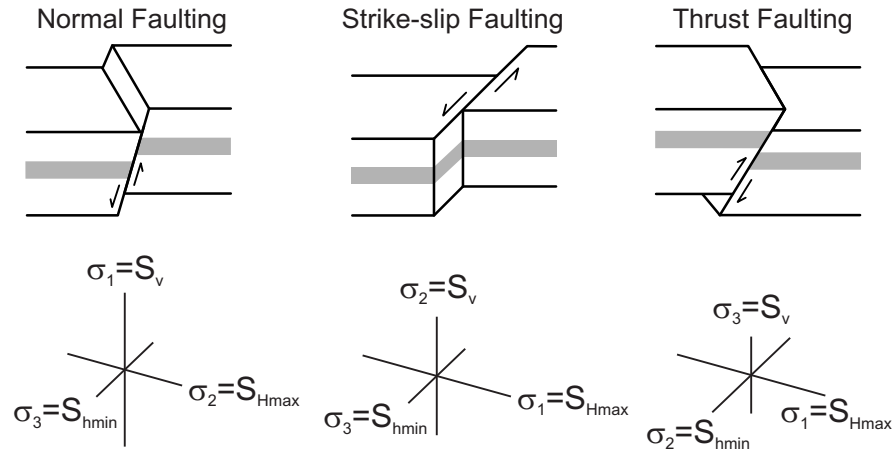


Figure 2.8: Andersonian stress regimes and corresponding alignment of the principal stresses of the 3D stress tensor [after Fjaer et al., 2008].

Anderson's theory predicts only the orientation of faults with respect to the ambient state of stress in which they are formed. But one should consider that the frictional strength of faults is less than the stress necessary to form them. Once faults are formed they constitute as plane of weakness and may be reactivated even if they are not optimally oriented in the ambient stress field. With other words, it is more likely to reactivate a pre-existing fault which is favorably oriented than to form a new one in the most optimal orientation. This may lead to ambiguity in both:

- inferring the in-situ stress field orientation from earthquake focal mechanisms
- inferring paleo stress states on basis of fault orientations or analysis of slickenlines.

This can be illustrated in the Mohr circle representation with two parallel failure envelopes: one failure curve represents the frictional strength of a fault and intersects the ordinate at the point of origin (no cohesion); one failure curve represents the strength of the surrounding rock and intersects the ordinate at a point with a given cohesion.

2.3 THE CRITICAL STRESSED CRUST

2.3.1 Critical stress theory

Various observations indicate that intraplate crust can generally be considered to be in a state of frictional failure equilibrium. Following Townend [2003] and Townend and Zoback [2000], most of these observations can be related to one of three independent lines of evidences:

1. occurrence of seismicity induced by either reservoir impoundment or fluid injection [e. g. Roeloffs, 1988; Simpson et al., 1988],
2. earthquakes that are triggered by other earthquakes [e. g. Stein et al., 1992, 1997; Scholz, 2010],
3. in-situ observations in deep wells such as the KTB [e. g. Zoback and Healy, 1992; Brudy et al., 1997].

The hypothesis of a critical stressed crust implies that the possible range of stress magnitudes are limited regardless of the pore pressure and the depth. Deep well stress measurements in different tectonic regimes clearly support this hypothesis (Fig. 2.9). Here, applied stress ratios follow predictions according to the Mohr-Coulomb frictional-failure theory incorporating frictional coefficients in the range of 0.6–1.0. The measured effective stress ratios of maximum and the least principal stresses appear to be limited leading to two important implications for geomechanics. First, the experimentally derived Beyerlee’s law also appears to correspond to faults *in situ*, regardless the difference in scale of the samples. Second, measured stress ratios indicate that they are controlled by the frictional strength of pre-existing faults in the crust and can thus be described by the simple law of the Mohr-Coulomb failure theory. This observation not only applies for active plate boundaries but also for relatively stable intraplate areas and is likewise observed for normal, strike-slip, and reverse faulting environments.

According to equation 2.32 failure initiation of a pre-existing and critically stressed fault plane is given by $\tau \geq \mu\sigma$. By transforming of equation 2.12 and 2.13 into the 3D space, the Mohr-Coulomb failure criterion can be expressed by the effective principal stresses

$$\frac{\sigma_1 - \sigma_3}{2} \sin 2\theta = \mu \left[\frac{\sigma_1 + \sigma_3}{2} + \frac{\sigma_1 - \sigma_3}{2} \cos 2\theta \right], \quad (2.37)$$

which can be rearranged to

$$\begin{aligned} \frac{\sigma_1}{\sigma_3} &= \frac{\sin 2\theta + \mu(1 - \cos 2\theta)}{\sin 2\theta - \mu(1 + \cos 2\theta)} \\ &= \frac{\cos \varphi + \mu(1 + \sin \varphi)}{\cos \varphi - \mu(1 - \sin \varphi)}. \end{aligned} \quad (2.38)$$

Since $\mu = \tan \varphi$ and thus $\sin \varphi = \mu/\sqrt{\mu^2 + 1}$ and $\cos \varphi = 1/\sqrt{\mu^2 + 1}$, equation 2.38 simplifies to:

$$\frac{\sigma_1}{\sigma_3} = \frac{S_1 - p}{S_3 - p} = \left[(\mu^2 + 1)^{1/2} + \mu \right]^2 \quad (2.39)$$

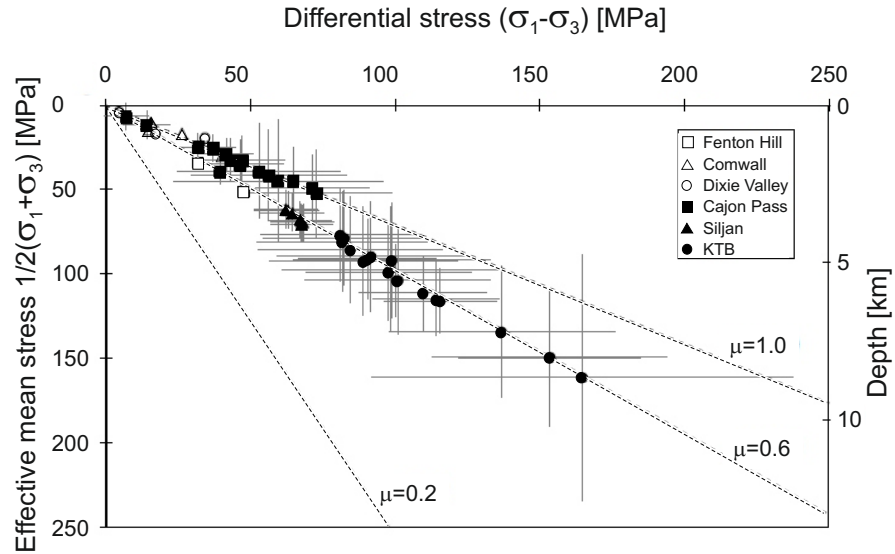


Figure 2.9: Indications for a critical stressed crust based on deep well stress measurements [after Townend, 2003]. Dashed lines illustrate limitation of effective stresses in the upper crust according to the predictions made by the Coulomb frictional failure theory for various coefficients of μ . With respect to the Mohr circle representation, the effective mean stress defines the midpoint and the differential stress defines the size of the circle (see Fig. 2.5)

Equation 2.39 illustrates that the possible range of differential stresses in the crust is limited. Their magnitude solely depends on μ . Following Byerlee's law, maximum stress ratios for σ_1 and σ_3 of 3.1 and 4.7 are calculated for friction coefficients of 0.6 and 0.85, respectively. The pore fluid pressure has no effect on these predicted stress ratios but can change significantly the magnitude of the differential stress ($\sigma_1 - \sigma_3$). Under hydrostatic pore pressure conditions the differential stress constantly increases due to a constant increase of the vertical stress. In some areas of sedimentary basins pore fluid overpressures can be observed which are close to lithostatic conditions. Under these $\sigma_3 \approx p$ conditions the limiting stress magnitude is not significantly different from the vertical stress magnitudes regardless of the considered faulting regime. With other words, the σ_1 and σ_3 magnitudes differ only slightly but the maximum σ_1/σ_3 ratio remain unaffected. This implies that when pore pressure is very high failure on the most favorably oriented fault might occurs even when the differential stress is small. Relatively small stress perturbations are furthermore sufficient to change the style of faulting from one stress regime to another.

Next to the reactivation potential, faults and fractures that are favorably oriented and critically stressed for frictional failure seem also to control subsurface fluid flow [Barton et al., 1995; Sibson, 1996; Ito and Zoback, 2000]. The existence of a critical stress crust implies

that near-hydrostatic pore pressures may exist to great depth and that pre-existing faults that are critically stressed probably maintain the crust's high permeability [Townend and Zoback, 2000; Townend, 2003].

2.3.2 The stress polygon

By combining the concept of limited crustal stresses with Anderson's faulting theory (section 2.2.2), equation 2.39 can be used to estimate an upper bound for the maximum and least principal stresses for each faulting regime:

$$\text{Normal faulting} \quad \frac{S_v - p}{S_{hmin} - p} = [(\mu^2 + 1)^{1/2} + \mu]^2 \quad (2.40)$$

$$\text{Strike - slip faulting} \quad \frac{S_{Hmax} - p}{S_{hmin} - p} = [(\mu^2 + 1)^{1/2} + \mu]^2 \quad (2.41)$$

$$\text{Reverse faulting} \quad \frac{S_{Hmax} - p}{S_v - p} = [(\mu^2 + 1)^{1/2} + \mu]^2 \quad (2.42)$$

Geomechanically stable stress conditions for the different stress regimes can be illustrated by the so-called stress polygon [Moos and Zoback, 1990; Zoback et al., 2003]. For a given friction coefficient, the area inside the polygon illustrates the range of allowable states of stress (point of mechanical equilibrium), whereas values lying outside the borders are unstable and yield failure (Fig. 2.10).

The trivial fact that $S_{Hmax} \geq S_{hmin}$ requires all possible stress states to be above a diagonal line of unit slope. Points at the periphery of the polygon correspond to a state of stress at the frictional limit and correspond to the Anderson's faulting and stress regimes: I - radial extension, II - normal faulting, III - transitional normal/strike-slip faulting, IV - strike-slip faulting, V - transitional strike-slip/reverse faulting, VI - reverse faulting, VII - radial compression.

Construction of the fault polygon is straight forward when one principal stress magnitude is known. In practice, minimum horizontal stresses often are obtained from extended leak-off tests or hydraulic fracturing. By assuming linear stress-depth trends, gradient for the vertical stress and the pore pressure can be reasonably estimated. By doing this, critical stress theory can be applied and magnitude of the maximum principal stress can be easily constrained.

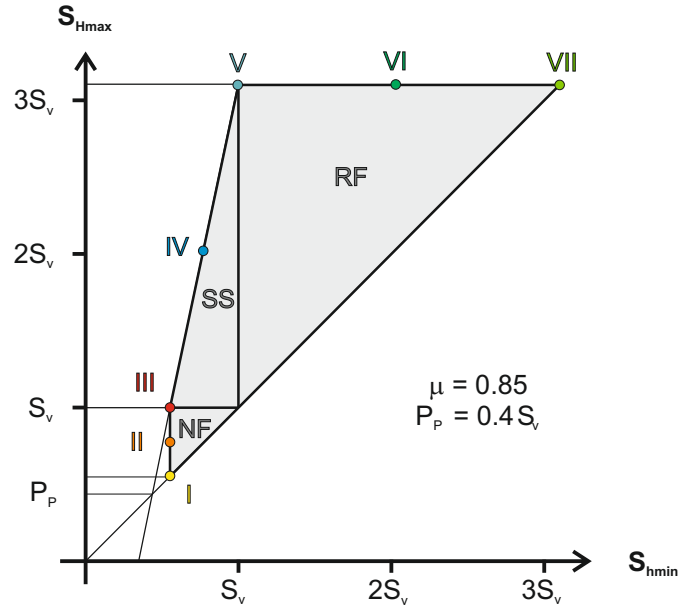


Figure 2.10: Stress polygon of allowed stress states (gray shaded area) following Mohr-Coulomb faulting theory with $\mu = 0.85$, after Zoback [2010]. Anderson's faulting regimes are bound by triangles in σ_H - σ_h -space. NF is normal faulting, SS is strike-slip faulting, RF is reverse faulting.

2.3.3 Theory of slip and dilation tendency

As discussed in section 2.2 the magnitude of fault plane friction, in relation to available shear stress, is the controlling factor for reactivation of faults. Fault slip is likely to occur when effective shear stress equals or exceeds this frictional resistance to sliding. For pre-existing faults the cohesive strength of the rock might be negligible. As consequence, frictional failure is solely governed by the magnitude of the coefficient of static friction. In this case the Mohr-Coulomb failure criterion (Eq. 2.32) simplifies to $\tau \geq \mu\sigma$. This implies that the ratio of resolved shear stress to resolved normal stress equals μ . This ratio has been referred to as the slip tendency, T_s . Analysis of the slip tendency was first suggested by Morris et al. [1996] as parameter for determining fault instabilities and reactivation potentials. Similar studies have been proven to be appropriate in different tectonic environments and for different scopes of application, e.g. for seismological studies of aftershock sequences [Collettini and Trippetta, 2007], for characterization of neotectonic fault activity at basin scale [Worum et al., 2004, 2005], or for investigation of induced seismicity during hydraulic reservoir stimulation [Moeck et al., 2009].

The slip tendency analysis does not incorporate any variations in frictional properties on a fault surface and assumes the fault zone to consist of two planar and cohesion-less planes. This may not al-

ways the case. When fault cores are cemented and show an apparent cohesive strength slip tendency analysis probably tends to overestimates the reactivation potential of the fault [Streit and Hillis, 2004]. However, several studies have demonstrated that neglecting cohesion along pre-existing fault surfaces is a reasonable simplification due to the fact that cohesion along fault surfaces significantly decreases as subsequent slip occurs [e.g. Brace and Kohlstedt, 1980; Twiss and Moore, 2007; Zoback and Healy, 1992].

There is ample evidence that a rupture plane is characterized by a considerably smaller resistance for frictional failure when the fracture and fault core contains clay minerals. Contrary to the predictions based on Beyerlee's law, for clayey formations frictional coefficient can take much smaller values of 0.2 and even below [e.g. Tembe et al., 2006, 2010], leading to very weak fault zones that deform by creep rather than seismically. This is crucial when a fault gouge consists of swelling clays and significant intracrystalline pore pressures evolve. Morrow et al. [1992] and Moore and Lockner [2007] could show that, next to pore pressure and clay mineralogy, frictional strength is dependent on the resolved stress state. Their tests reveal, that clays have a low frictional strength at low effective pressures but have higher frictional strength at higher effective pressures. However, both observations of increasing or decreasing resistances for frictional failure illustrate that estimates on fault reactivation potential is very complex, i.e. in shaley or evaporitic rocks and when clay bearing fault gauges exist.

Dilation tendency, T_D , is the relative probability for a fracture or a fault plane to dilate under the local stress field [Ferrill et al., 1999]. T_D is defined as the difference between the maximum principal compressive stress (σ_1) and the normal stress (σ_n), normalized by the differential stress ($\sigma_1 - \sigma_3$). T_D is a relative value ranging between 0 ($\sigma_1 = \sigma_n$) and 1 ($\sigma_3 = \sigma_n$). The calculation is straight forward if fault plane geometry and in-situ stress state is known. A Mohr's circle representation of both parameters is shown in Fig. 2.11.

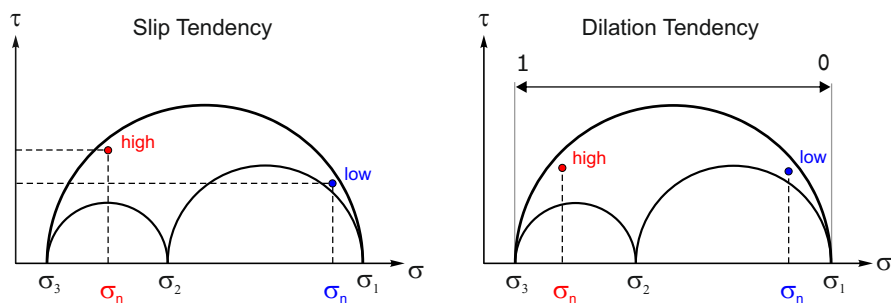


Figure 2.11: Mohr's circle representation of slip- and dilation tendency as parameters for quantification of fault and fracture reactivation potentials.

TECTONIC FRAMEWORK OF SOUTHWEST GERMANY

3.1 GEOLOGICAL SETTING OF THE UPPER RHINE GRABEN

The 300-km-long and about 40 km wide Upper Rhine Graben (URG) represents the central part of the European Cenozoic rift system (ECRIS; Ziegler, 1990a, 1992), extending over a distance of more than 1000 km across central Europe (Fig. 3.1). The URG is subdivided into a NNE-striking southern, a NE-striking central, and a NNW to N-striking northern segment. A triple junction connects the northern end of the URG with the NNE trending Hessian grabens and the northwest striking Lower Rhine (Roer Valley) Graben, representing the northern branch of ECRIS. To the south ECRIS includes the grabens of the Massif Central, the Bresse Graben, the Limagne Graben, and minor graben systems along the Rhône Valley. The sinistral NE-striking Burgundy transfer zone represents the structural link to the southern URG [Ustaszewski, 2004].

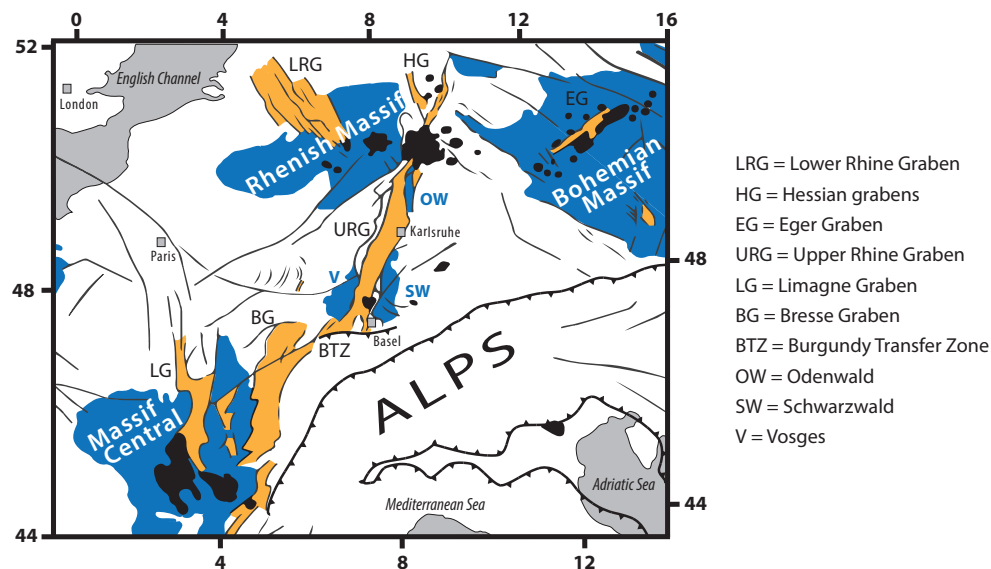


Figure 3.1: A) Structural overview map of Europe including the ECRIS rift system (orange), the Alpin deformation front (thrust fault signature), major Cenozoic fault zones (black lines), Variscan massifs (blue), and volcanic massifs (black); after Dezes et al. [2004].

Continental rifting and graben formation started in Early Cenozoic (40-35 Ma) and was synchronous to large scale reorientation of plate boundaries in central Europe such as the Alpine orogen and the opening of the northern Atlantic Ocean. Evolution of the Cenozoic URG was controlled by polyphase reactivations of a complex set of crustal discontinuities of Late Paleozoic structures. The following summary mainly follows the comprehensive discussions about the influence of pre-rift settings on the Cenozoic graben formation that are given by [Schumacher \[2002\]](#), [Dezes et al. \[2004\]](#), and [Ziegler et al. \[2006\]](#).

3.1.1 *Pre-rift setting of the URG area*

Along its strike, the URG crosses different tectonostratigraphic units of the Variscan orogenic belt in central Europe (Fig. 3.3A). The URG area is characterized by a complex pre-Tertiary crustal architecture comprising NE to ENE trending terranes and terrane boundaries consolidated and aligned during the main phases of the Variscan orogeny between about 345-325 Ma [[Kalt et al., 2000](#); [Schaltegger, 2000](#)]. Information of the basement lithology and the Variscan structural grain has been almost entirely inferred from gravity and magnetics (Fig. 3.2). In the north the URG is bound by the South Hunsrück-Taunus border fault (SHTBF), a major ENE trending structure (suture) which is supposed to separate the external Rhenohercynian and Saxothuringian zones of the Variscides. The ENE striking Lalaye-Lubine-Baden-Baden-Shear Zone (LBZ) in the north represents the southernmost parts of the Saxothuringian Zone of the Variscan orogen.

Carboniferous convergence was followed by a phase of Late Carboniferous to Early Permian extension between about 325 and 280 Ma. Re-equilibration of the lithosphere with the asthenosphere accounted for the long-term thermal subsidence and thinning of the crust. This phase was accompanied by extrusive and intrusive magmatism and caused formation of a system of Permo-Carboniferous troughs and highs, which followed the ENE structural trend of the Variscides (e. g. [Henk, 1993](#); [Boigk and Schoeneich, 1970](#); [Korsch and Schäfer, 1995](#); Fig. 3.3B). Uplift and erosional and tectonic unroofing of the Variscan orogen significantly reduced crustal thickness. Foreland basins and Permo-Carboniferous troughs were successively filled with continental red beds deposits and volcanic units.

Early Permian evolution of the Central European crust, i.e. regarding the tectonic processes that controlled the crustal extension and thinning, is controversially discussed. A wrench-induced collapse of the Variscides is proposed e.g. by [Ziegler et al. \[2006\]](#); [Ziegler and Dezes \[2005\]](#); [Edel and Weber \[1995\]](#). They proposed that continental-scale wrench tectonics caused reactivation of the Variscan structural grain,

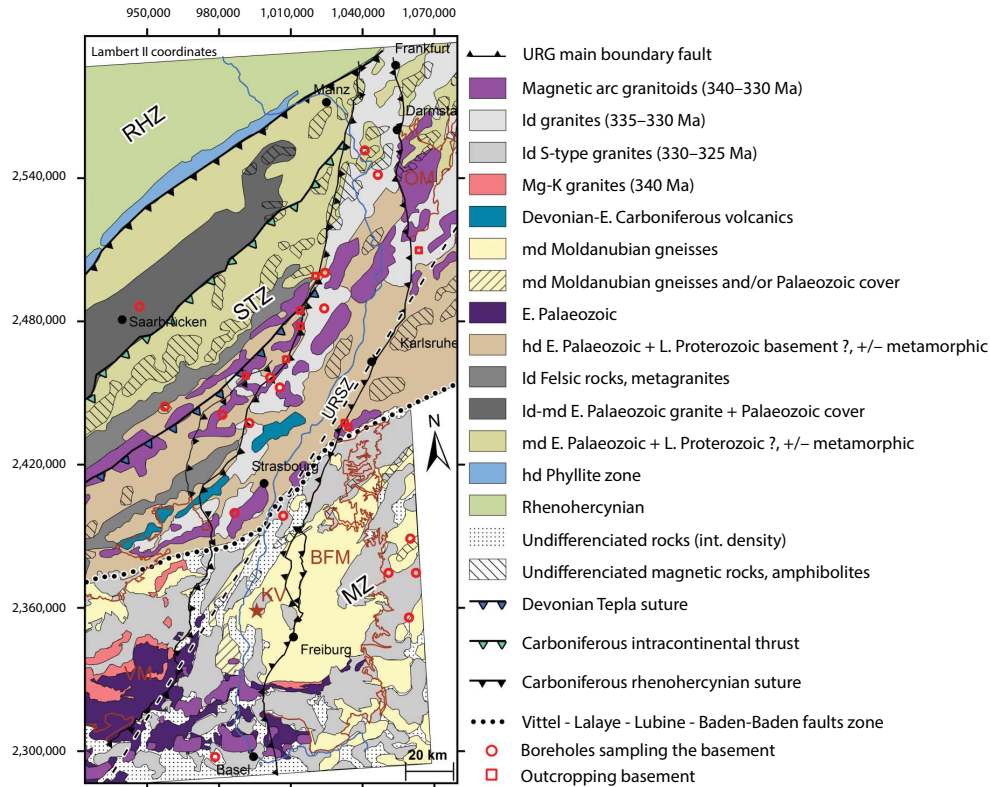


Figure 3.2: Major units and tectonic features of the Variscan basement in the URG and adjacent areas (after Baillieux et al. [2013]). Id, low density; md, medium density; hd, high density; RHZ, Rhenohercynian Zone; STZ, Saxo-Thuringian Zone; MZ, Moldanubian Zone; URSZ, Upper Rhine Shear Zone; VM, Vosges Mountains; BFM, Black Forest Mountains; OM, Odenwald Mountains; KV, Kaiserstuhl volcanic massif.

predominantly by (W)NW trending dextral shear, but also caused development of (N)NE trending sinistral shears in the URG area. This trend is furthermore associated with Lower Carboniferous to Permian intrusive bodies and dyke swarms, which outcrop along the rift axis in the exposed basement of the graben shoulders [Flöttmann and Oncken, 1992; Schumacher, 2002]. Elongated gravity and magnetic anomalies within the URG area are interpreted to confirm NNE trending sinistral shear zones [Edel and Fluck, 1989; Edel and Weber, 1995; Edel et al., 2007] but slip rates along these basement structures are still poorly constrained. Outcrop studies in the Vosges mountains indicate slip rates of 4-6 km, only, for individual faults [Edel et al., 2007]. A distinct lateral NNE-SSW displacement along this structural trend is described for basement discontinuities within the URG. Here, an apparent offset of about 40-45 km, visible for the NE-SW striking LBZ, is interpreted to reflect Late Variscan activity of major sinistral strike-slip zones [e.g. Edel et al., 2007]. However, since displacement rates do not reflect continental-scale

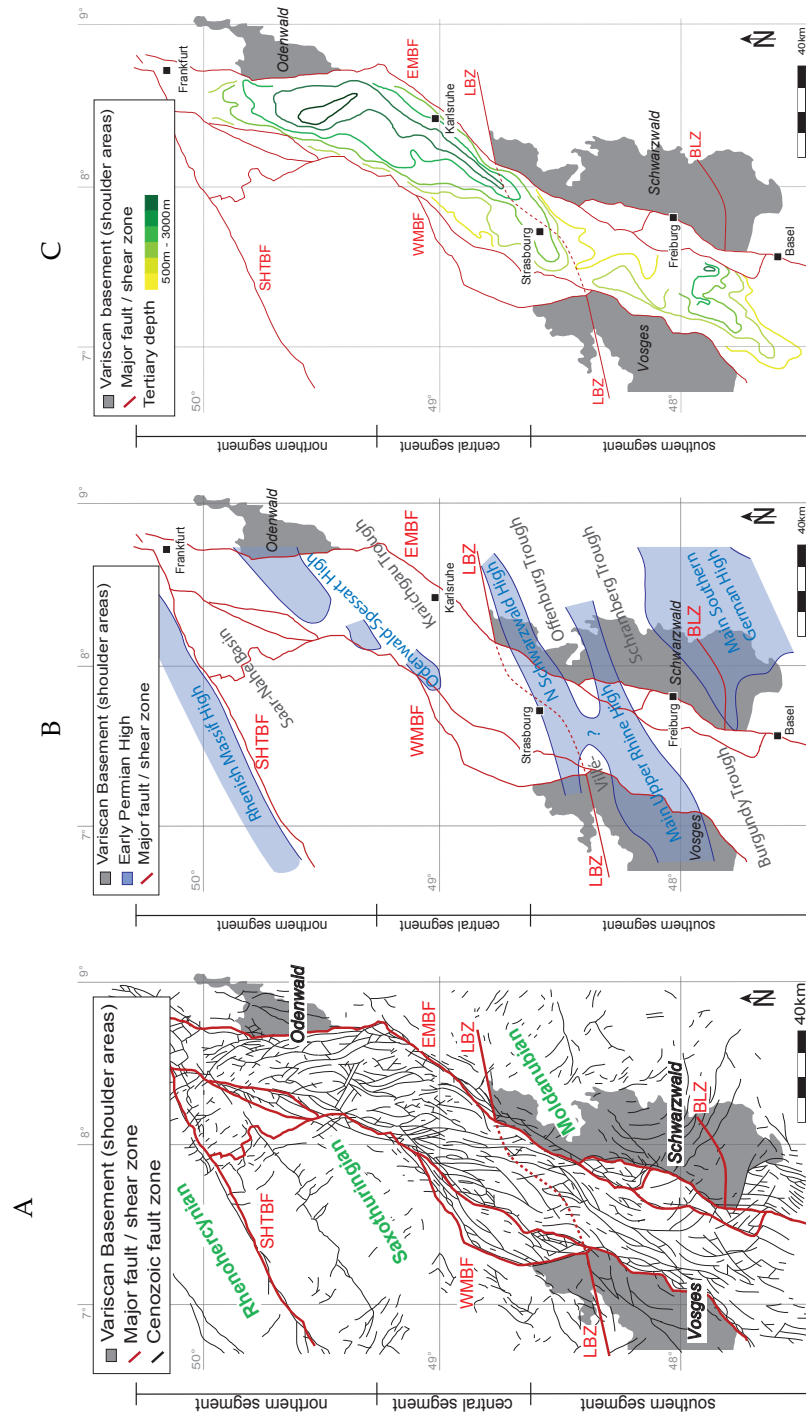


Figure 3.3: A) Variscan terrains and terrain boundaries in the URG area with superimposed fault pattern within the URG developed during Cenozoic rifting (after Illies and Greiner [1979]). B) Permo-Carboniferous troughs and highs representing major pre-rift structural features and zones of weakness in the URG area (after Boigk and Schoeneich [1970]). C) Depth of the base of the Cenozoic graben fill indicating significant thickness variation of Tertiary sediments along the rift axis (after Pflug [1982] and Doebel et al. [1974]).

wrench tectonics and lateral displacements of Permo-Carboniferous troughs and highs are not described, these observations may be related to local fault activities rather than basin-scale tectonics. The NNE structural trends are often considered to have controlled the Cenozoic graben formation, due to the fact that they partly outline the shape of the URG [Boigk and Schoeneich, 1970]. Since wrench tectonics are commonly associated with subvertical strike-slip fault zones, reactivation of these weakness zones in an extensional normal faulting regime during the URG rifting seems questionable.

Large scale extensional reordering of the crust by W to WNW dipping detachments is proposed by Eisbacher and Fielitz [2008]. They state, that crustal thinning by E-W extension is indicated by westwards dipping stretching lineations along ductile, mylonitic shear zones that are exposed along the eastern graben shoulder in the Schwarzwald and Odenwald. W to WNW dipping detachments induced emplacement of major post-tectonic batholiths and may also explain asymmetries that are observed between the eastern and western graben shoulder, such as for the exposed basement rocks, which represent different crustal levels and uneven uplift rates.

However, post-orogenic reactivation of Variscan structural features arranged a large-scale fragmentation pattern which partly predetermined structural evolution of the Central European crust in the Mesozoic and Cenozoic [Edel and Weber, 1995; Ziegler et al., 2006]. Stages of thermal relaxation and subsidence within the tectonically thinned and reordered Variscan lithosphere between about 260 Ma and 150 Ma caused formation of transgressive Mesozoic deposits that discordantly overly the peneplaned Variscan basement and Permo-Carboniferous strata [Pflug, 1982; Eisbacher et al., 1989b]. Large-scale Triassic and Jurassic intraplate tectonics are not documented for the URG area. However, diffuse Triassic extension, controlling subsidence of the Permo-Carboniferous troughs, appears to indicate reactivation of Variscan zones of weakness [Ziegler, 1990b]. A distinct erosional hiatus from Late Cretaceous to Early Cenozoic that is observed in the URG area may indicate a large-scale change of the intra-plate deformation to a phase of compression accompanied with local uplift and erosion as observed for the Rhenish Shield in Late Mesozoic [Ziegler, 1990b; Geyer and Gwinner, 2011]. At present, Triassic to Late Jurassic sediments are exposed along the graben shoulders, lifted up during Cenozoic rifting of the URG. Within the URG, the Mesozoic formations describe gentle synclinal and anticlinal structures that were superimposed on Permo-Carboniferous troughs and highs, respectively [Sittler, 1969; Pflug, 1982]. This subcrop pattern reflects reactivation of crustal Variscan weakness zones, presumably under a transpressional stress regime and may indicate very initial phases of a new rifting cycle [Schumacher, 2002].

3.1.2 *Syn-rift Cenozoic evolution of the URG*

Rifting history and kinematic evolution of the URG is still under debate and several models have been proposed in the last decades. A comprehensive discussion on the existing kinematic models for the graben formation is given by Schwarz [2005]. The existing models, as e.g. proposed by Illies [1975]; Michon et al. [2003]; Behrmann et al. [2003]; Schumacher [2002]; Dezes et al. [2004], differ mainly in the number of involved rifting phases and the stress field orientations and kinematics during individual phases. However, common to all models is description of a polyphase rift evolution caused by repeatedly changes of the ambient stress field and related faulting conditions. Changes in subsidence patterns, as indicated by isopach maps of the synrift sedimentary succession [Pflug, 1982], reflects this uneven Cenozoic rifting activity along the graben axis. Variations of the rift polarity caused formation of repeatedly shifted depocenters and sub-basins within the URG. The total thickness of Tertiary to Quaternary sediments within the URG exceeds 3 km in an elongated depocenter situated along the EMBF in the northern URG [Doebel et al., 1974; Pflug, 1982; Bartz, 1974]. In the southern URG, a smaller depocenter south of Freiburg exists, filled by a sequence of 2.5 km thick sediments. The crustal extension perpendicular to the rift axis is estimated to be in the order of approximately 5 to 7 km [Ziegler and Dezes, 2005; Hinsken et al., 2007; Villemin et al., 1986].

The main extensional rifting and crustal NW-SE extension started in Late Eocene [Sissingh, 1998] during which Late Variscan and Permo-Carboniferous crustal discontinuities were transtensionally reactivated [Schumacher, 2002]. The opening of the graben was controlled by a paleostress field with a S_{Hmax} orientation of NNE-SSW [Ahorner, 1975; Illies, 1975] resulting in the development of the NE-SW to NNE-SSW striking rift segments. Initial subsidence starts in the southern and middle parts of the URG in Late Eocene and is deduced from deposition of lacustrine sediments, which rest unconformably on the subcropping Mesozoic strata. Sedimentation in the southern and middle segment of the URG was restricted to two depocenters that are superimposed on the ENE trending late Paleozoic Burgundy and Kraichgau troughs, respectively. They are linked by a narrow NNE striking subbasin that crosses the less rapidly subsided crust in the area of the Northern Black Forest and the Main Upper Rhine Highs (Fig. 3.3B). Alternating and gradual sedimentation of marine and evaporitic deposits is interpreted to be caused by temporary transgression from the south [Sissingh, 1998]. Continuous uplift and erosion of the graben shoulders is indicated by clastic and conglomeratic deposits close to the rift flanks.

In Lower Oligocene crustal extension and subsidence successively shifted further north but synrift sedimentation also reflects local changes in basin geometry. In the southern URG, the main depocenter shifted to the W along to the active western main boundary fault (WMBF). In the middle URG, NE trending elongation of the depocenter close to the eastern rift flank reflects development of the eastern main boundary fault (EMBF). By this time, the area along the Northern Black Forest high is assumed acting as sinistral transfer zone that connected both asymmetric graben segments. Structural control of this transfer zone by the LBZ during Oligocene seems questionable since opposite dips are inferred for the transfer zone (NW vergent - based on isopach maps Schwarz and Henk [2005]; Schwarz [2005]) and LBZ (SW vergent - based on refraction seismic data Eisbacher et al. [1989b]). During Oligocene transgression and regression sporadically formed a marine channel from the Alpine Foreland Basin to the North German Basin and marine clay and marl series and evaporitic sediments were deposited throughout the entire graben system. Uplift in the southern URG interrupted the marine connection and may reflect beginning of large-scale tectonic changes in the URG area.

A major reorientation of the regional stress field in the early Miocene established a NE-SW-extensional to transtensional stress field. Border fault segments were reactivated showing sinistral and dextral oblique displacements, but also local inversion and contraction [e.g. Illies et al., 1979; Rotstein et al., 2005; Rotstein and Schaming, 2011]. The change of the regional stress field initiated a new tectono-sedimentary regime. Subsidence and sedimentation were restricted to the northern graben segment [Bartz, 1974; Pflug, 1982] whereas synrift deposits and older strata in the central and southern segments of the URG were partly eroded [e.g. Villemin et al., 1986; Sissingh, 1998]. Uplift and erosion also affected the Vosges and Black Forest and is indicated by fluvial deposits of erosion products in the graben center. The phase of uplift in the southern URG was accompanied by local volcanic activity such as in the Freiburg area where the Kaiserstuhl volcano built up. Thermal doming of the Rhenish shield during the Miocene was also accompanied by major volcanic activity and finally interrupted marine sedimentation in the northern URG. The configuration of the Miocene depocenter in the northern graben segment is already similar to that reflected by the Quaternary isopachs (Bartz [1974], 3.3C). Here, Quaternary alluvial deposits reach a maximum thickness of more than 380 m near Heidelberg. During the early Quaternary, subsidence resumed in the southern URG. Here, sedimentation was restricted to a N-S to NNE trending subbasin SW of Freiburg [Schumacher, 2002].

3.2 GEOLOGICAL SETTING OF THE SCHWARZWALD

The Schwarzwald is part of the central polymetamorphic crystalline belt of the Variscan orogen developed between about 420 and 280 Ma. Exhumation of the Variscan basement rocks was caused by the Cenozoic rifting of the URG. Tertiary updoming along the flanks of the southern URG has caused erosion of about 2 km of Mesozoic sedimentary platform cover rocks and has exposed the crystalline basement in the Schwarzwald and Vosges Mountains. Uplift along the graben shoulders of the southern URG was accommodated along broad boundary fault zones with maximum displacement rates of about 5 km. Tectonic evolution and major structural setting of the exposed Variscan units coincide with that described for the URG as pre-rift settings in section 3.1.1.

From north to south the Schwarzwald comprises four NE-trending lithotectonic units accreted by oblique convergence during early Carboniferous time (Fig. 3.4, Eisbacher et al. [1989b]).

The low to medium grade metasedimentary and metavolcanic rocks of the Baden-Baden Zone (BBZ) in the north represent the southernmost parts of the Saxothuringian Zone of the Variscan orogen. The rocks of the BBZ mainly comprise schists, meta-greywackes, and marbles but also isolated lenses of basic metavolcanics and altered ultramafic rocks. The BBZ is bounded to the southeast by the ENE striking Lalaye-Lubine-Baden-Baden-Shear Zone (LBZ, see Fig. 3.3) that represents the diffuse structural boundary to the medium and high-grade metamorphic rocks of the Central Schwarzwald Gneiss Complex (CSGC). The tectonic contact between the BBZ and the CSGC represents a dextral-transpressive ductile shear zone, indicating high temperature metamorphism around 330-335 Ma [Eisbacher et al., 1989b; Kalt et al., 2000]. It can be traced towards SW along strike to the northern Vosges and is widely veiled by a postkinematic biotite-muscovite granite, which intruded between 325-330 Ma and which was cataclastically deformed during sinistral brittle reactivation [Krohe and Eisbacher, 1988; Kalt et al., 2000; Wickert et al., 1990; Hess et al., 1995].

The CSGC represents the Moldanubian Zone of the Variscan orogen and mainly consists of migmatic and, locally, mylonitic paragneisses, orthogneisses, and minor metabasites, hosting isolated lenses of relic eclogites and serpentized peridotites [Kalt et al., 1995; Marschall et al., 2003]. The CSGC was intruded at about 330-325 Ma by two major batholiths in the north and in the east and two minor bodies accompanied by numerous, commonly NE-SW striking, granitic to porphyritic dykes (Fig. 3.4). The contact between the metamorphic CSGC and the sedimentary Badenweiler-Lenzkirch Zone (BLZ) is a major crustal thrust. It is represented by

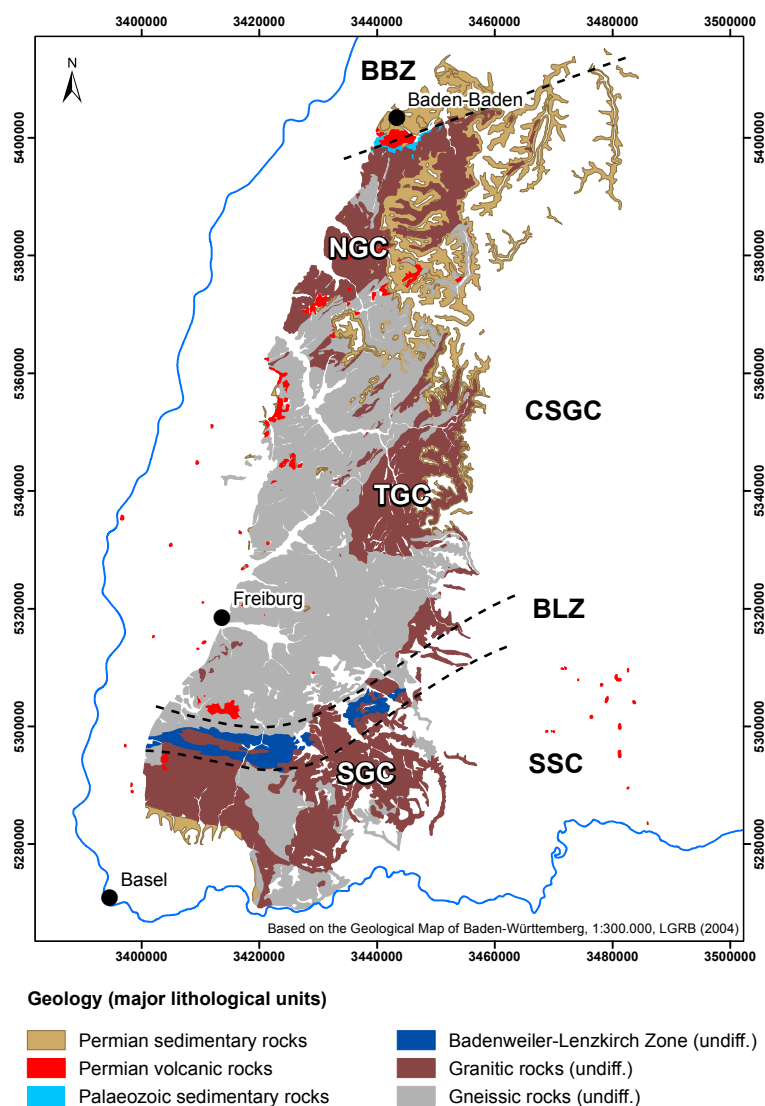


Figure 3.4: Simplified geological map of the Schwarzwald area showing the four NE-trending major lithotectonic units of the Variscan belt and the Carboniferous granite batholiths (blue - NGC: Northern Schwarzwald granite complex; SGC: Southern Schwarzwald granite complex; TGC - Triberg granite complex).

the mylonitic-cataclastic Todtnau shear zone that indicates dextral-transpressive, SSE-directed convergence at about 330 Ma [Krohe and Eisbacher, 1988; Eisbacher et al., 1989b]. The CSGC in the hangingwall overthrust the Palaeozoic sedimentary-volcanic infold of the BLZ. The about 5-10 km wide BLZ is a tectonic melange of metasedimentary and metavolcanic series that includes low-grade to non-metamorphic Ordovician to late Carboniferous sedimentary and volcanic rocks [e.g. Sawatzki et al., 2003]. The southern boundary of the BBZ is a WNW-trending sinistral transtensive shear zone and appears to be partly sealed by granitic intrusions [e.g. Krecher and

Behrmann, 2007].

The migmatitic gneisses of the SSC form W- to NW-dipping panels that were intruded by N- to NW-trending granitic plutons (Fig. 3.5). Emplacement of the massive granitic intrusions from middle to high crustal levels between about 332-334 Ma [Schaltegger, 2000] are related to a transitional regime of crustal reordering in late Early Carboniferous, characterized by an extensional phase that followed the phase of Early Carboniferous convergence [Eisbacher et al., 1989b; Henk, 1997; Krohe and Eisbacher, 1988]. Due to the transitional tectonic regime, the SSC batholiths can be subdivided into a pre- and a post-tectonic granite series [Schaltegger, 2000]. The first series comprise pre- to syn-tectonic, ductilely deformed batholiths such as the Klemmbach- and the Schlächtenhaus granites that are considered to be deformed during the compressive deformation of the CSGC and BLZ assigned to a period between 340 and 330 Ma [Krohe and Eisbacher, 1988]. The second series comprise the post-tectonic little to non-deformed Albtal-, St.-Blasien-, Marlsburg, and Bärhalde-Schluchsee granites that were emplaced during a period of post-convergence crustal thinning and extension [Schaltegger, 2000; Ehtler and Chauvet, 1991].

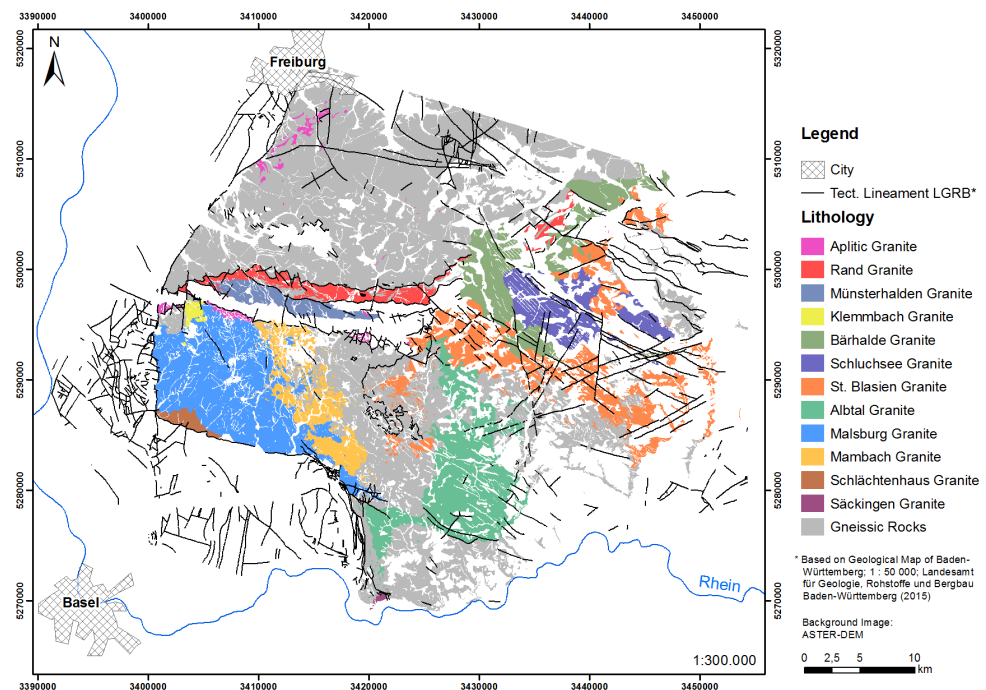


Figure 3.5: Overview map of the Southern Schwarzwald Complex between Freiburg and Basel showing the distribution of the gneissic rocks and location of the Carboniferous pre- and post-tectonic batholiths.

At present, major fault zones between and within the four litho-tectonic units of the Schwarzwald are commonly documented as

cataclastic and mineralized fault zones [e.g. Krohe and Eisbacher, 1988]. During late Variscan times, between about 330 to 325 Ma, high-level crystalline basement rocks cooled down due to the uplift of the CSGC and SSC in upper crustal brittle levels. As a result, retrograde mylonitic shear zones evolved into cataclastic fault zones [e.g. Eisbacher et al., 1989b] that repeatedly provided preferential pathways for highly mineralized fluids [e.g. Bons et al., 2014].

3.3 PRESENT DAY STRESS STATE IN SW GERMANY

Determination of the present day stress state in the URG has been the subject of numerous studies in the last decades. Regional models of the recent state of stress mostly base on stress inversions from URG earthquake data [e.g. Bonjer et al., 1984; Larroque and Laurent, 1988; Delouis et al., 1993; Plenefisch and Bonjer, 1997; Kastrup et al., 2004] or have been deduced from neotectonic studies [e.g. Larroque and Laurent, 1988; Bertrand et al., 2006; Peters and van Balen, 2007]. Additional, very local, information on the in-situ stress state were determined from overcoring and hydraulic fracturing campaigns [e.g. Greiner, 1975; Baumann, 1981; Klee and Rummel, 1999] or rely on interpretations of borehole breakouts and drilling-induced tensile fractures [e.g. Valley and Evans, 2007, 2009]. An overview of reliable data is provided by the World Stress Map [Heidbach et al., 2008] and is shown in Fig. 3.6.

Although local stress field variations are documented, rather stable stress and deformation conditions are observed for the URG area. An autonomous stress regime within the Central European crust is hence not inferred for the graben system [Müller et al., 1992]. The URG is characterized by a generally uniform NW-SE orientation of the largest horizontal stress component ($S_{H_{max}}$). This stress state is interpreted to be driven by plate boundary processes and reflects a combination of forces related to continued convergence of the Adriatic Block and the central European Plate and North Atlantic ridge push [Regenauer-Lieb and Petit, 1997; Dezes et al., 2004].

Along strike of the URG slight variations of the $S_{H_{max}}$ orientation are observed. Stress indicators reveal a gradual counterclockwise rotation of the σ_1 and σ_2 plane as well as of the σ_3 direction of about 30° from S to N [Plenefisch and Bonjer, 1997]. Values range from $N130^\circ E$ to $N135^\circ E$ in the northern URG and from $N145^\circ E$ to $N160^\circ E$ in the southern URG and northern Switzerland [e.g. Carey-Gailhardis and Mercier, 1992; Delouis et al., 1993]. Interpretations of fault-plane solutions also reveal a change in faulting regime along the graben axis [e.g. Plenefisch and Bonjer, 1997]. The northern part of the URG is characterized by an extensional stress state and active

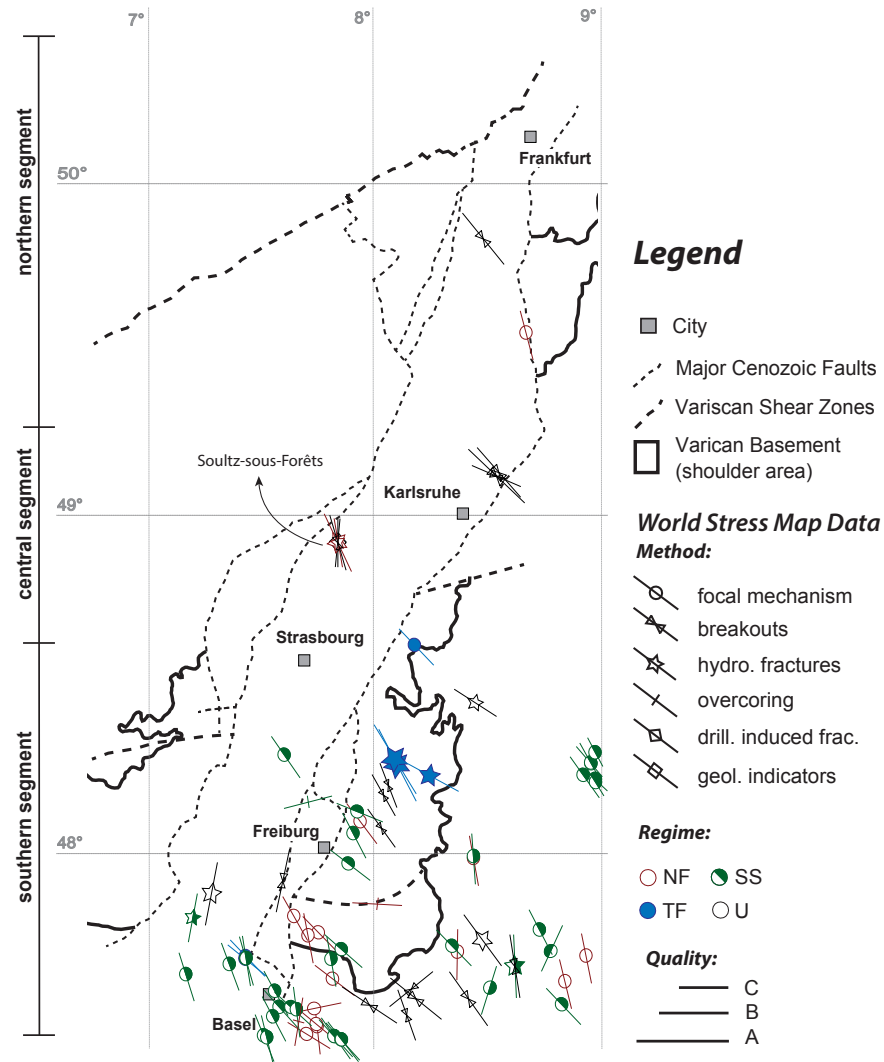


Figure 3.6: In-situ stress indicators for the URG area, compiled in the World Stress Map [Heidbach et al., 2008], indicate a relatively homogeneous NW–SE to NNW–SSE orientation of the maximum horizontal stress component (S_{Hmax}). Few local perturbations of the S_{Hmax} orientation are observed in northern Switzerland, the Sultz area, and along the EMBF.

normal faulting ($\sigma_1 = S_v$, $\sigma_2 = S_{Hmax}$) whereas in the seismically more active southern part strike-slip faulting ($\sigma_1 = S_{Hmax}$, $\sigma_2 = S_v$) with secondary normal faulting prevails. Transition of the stress orientation and change of the faulting regime, by permutation of σ_1 and σ_2 [Larroque et al., 1987], occurs in the central segment of the URG and was documented for the Sultz area at the western rift flank [Cuenot et al., 2006]. Here, stress indicators indicate a transitional stress state with a change from normal to strike-slip faulting at a depth of about 3.4 km [Cuenot et al., 2006].

Next to these stress variations at basin scale also local perturbations of the S_{Hmax} orientation are documented, e.g. at the western flank of the central URG in the Soultz-sous-Forêts area. Here, an extensive set of in-situ stress data has been gathered for depths down to 5 km. Determined S_{Hmax} orientations range from N125°E to N185°E with mean values between N175°E \pm 10° [Cornet et al., 2007] or N169°E \pm 14° [Valley and Evans, 2007]. A slight deviation from the regional NW-SE to a N-S trend is evident and probably reflects stress heterogeneities in the crystalline basement that are caused by local structural geological settings such as horst and graben structures, transfer and accommodation zones, or complex fault patterns.

Deep well investigations on the in-situ state of stress have been conducted almost exclusively within the graben center. For the crystalline basement of the Schwarzwald only few in-situ stress measurements are available. Existing studies are based almost always on near-surface overcoring measurements [Greiner, 1978; Wolter, 1987], analyses of hydrofracs [Rummel and Baumgärtner, 1987], and the use of triaxial strain cells in shallow wellbores [Wolter, 1987; Hauser-Fuhlberg et al., 2012]. However, among inherent uncertainties related to the measurement techniques, significant stress perturbations due to the topography hamper an unambiguous interpretation of these near-surface data. More reliable data base on interpretations of earthquake data. For the seismically active region of the southern Schwarzwald stress inversions performed on earthquake focal plane solutions provide additional information about the S_{Hmax} orientation and the tectonic regime. Here, comprehensive studies confirm the generally uniform NW-SE orientation of S_{Hmax} and indicate that strike-slip faulting with secondary normal faulting are the dominant faulting regimes (Plenefisch and Bonjer [1997]; Bonjer [1997]; Kastrup et al. [2004]; Fig. 3.7).

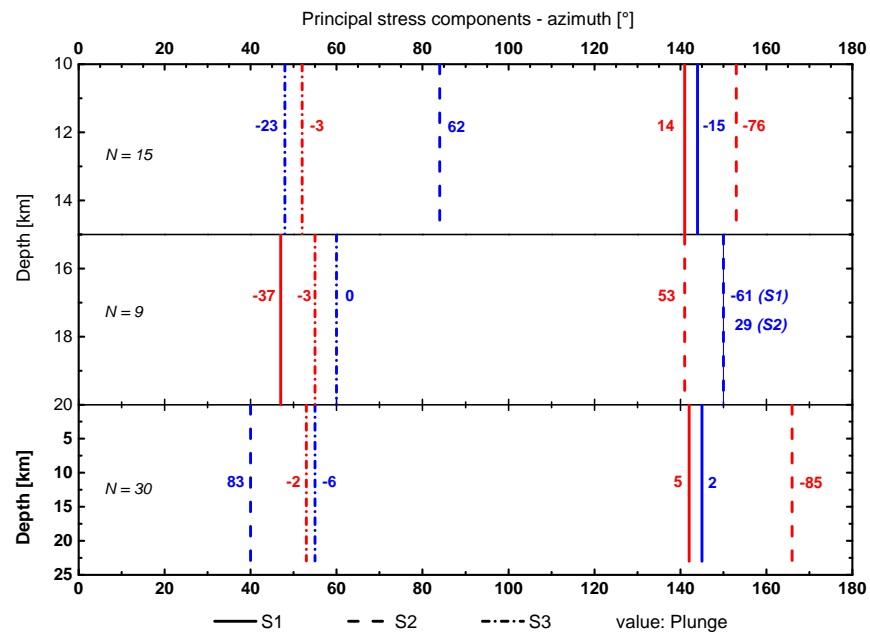


Figure 3.7: Results of stress inversions performed by [Kastrup et al. \[2004\]](#) for 30 earthquakes in the southern Schwarzwald area, presented for different depth ranges and for the whole data set. Shape of the stress tensor was determined by two different inversion techniques ([Gephart and Forsyth \[1984\]](#): blue; [Michael \[1984\]](#): red), indicating a strike-slip faulting regime with a S_{Hmax} orientation of about N140-145°E.

4

INFERRING THE IN-SITU STRESS REGIME IN DEEP SEDIMENTS: AN EXAMPLE FROM THE BRUCHSAL GEOTHERMAL SITE

This section is published in *Geothermal Energy*, **2**, **7**, doi:10.1186/s40517-014-0007-z with minor changes in the designation of the sections.

ABSTRACT

Knowledge of the ambient state of stress is of crucial importance for understanding tectonic processes and an important parameter in reservoir engineering. In the framework of the 2500 m deep geothermal project of Bruchsal in the central part of the Upper Rhine Graben new evidence is presented for the stress field in deep-seated sedimentary rocks. With a sophisticated data analysis based on the concept of critical stress ratios, we evaluate the quality and uncertainty range of earlier stress field models in the Bruchsal area. New data from borehole logging and leak-off tests in deep sediments are used to propose an alternative stress profile for this part of the Upper Rhine Graben. The revised stress field model for the Bruchsal area predicts a normal with transition to strike-slip faulting regime. Stress field perturbations and potential decoupling processes within specific clay-, salt-, and anhydrite-bearing units of the Keuper can be observed. By comparison with other models, we can show a regional consistency of our stress field model that is reliable throughout the central Upper Rhine Graben extending from Bruchsal in the East to the Soultz-sous-Forêts EGS site in the West.

4.1 INTRODUCTION

In a regional context, the stress field is typically used for investigation of neo-tectonic and recent geodynamic processes. The world stress map [Heidbach et al., 2008] provides a sound database with respect to determination of fault reactivation, tectonic deformation and related earthquake hazard [e.g. Hergert and Heidbach, 2011].

Moreover, stress is a key parameter in unconventional reservoir engineering. Faults and fractures that are favorably oriented and critically stressed for frictional failure often dominate fluid flow [Barton et al., 1995; Townend and Zoback, 2000]. In this respect, a higher resolution of the stress field is required and linear stress-depth profiles should be used with caution, as principal stress magnitudes can vary locally by topography, geological unconformities, stratifications, lithology or geological structures like faults or fractures [Heidbach et al., 2010; Zang and Stephansson, 2010]. In sedimentary rocks, stress field orientation and principal stress magnitudes show significant variations depending on their rheological characteristics [Anderson et al., 1973; Cornet and Burlet, 1992]. Interstratification of stiff clastic sediments and clay-, salt-, and anhydrite-bearing formations causes significant deviations from linear stress-depth profile in deep sedimentary basins such as the North German basin, the Paris Basin, and in continental rift systems such as the Upper Rhine Graben (URG) [Cornet and Röckel, 2012; Wileveau et al., 2007]. Thus, stress measurements in sediments (orientation and magnitude) need to be evaluated with respect to the lithological characteristics of the corresponding formation, and extrapolation of measured stress values to depth should be conducted with care, especially when only few measurements are available. With this in mind and although the world stress map provides a large amount of data, determination of local stress appears often to be insufficient.

In this study, we present a methodology for stress field estimation in areas where a detailed knowledge of the local stress conditions is unavailable. The approach is applied on the example of the Bruchsal geothermal site, where a number of earlier studies have been carried out with a similar aim. We will present a comparative review of the existing data and add new unpublished data from two leak-off tests (LOT) and our resulting approach applied to the Bruchsal area.

4.2 GEOLOGICAL SETTING

Bruchsal is located in the central segment of the URG close to its Eastern boundary fault (Figure 4.1). The Bruchsal geothermal doublet system operates through a 1932-meter-deep injection (GB1) and a 2542-meter-deep production well (GB2). The highly fractured geothermal reservoir, located at a depth ranging between 1.8 and 2.5 km, mainly consists of fine to coarse-grained sandstones of the Lower Triassic (Buntsandstein) and gravelly sandstones and breccia conglomerates of the Upper Permian (Rotliegend and Zechstein). The overlying Triassic units are characterized by

clay-rich formations with carbonate and dolomitic layers (Muschelkalk) and gypsum- and anhydrite-bearing layers of the Keuper.

The 300-km-long URG represents the central part of the European Cenozoic rift system [Schumacher, 2002], extending over a distance of more than 1000 km across central Europe. It is subdivided into a NNE-striking southern, a NE-striking central, and a NNW to N-striking northern segment (Figure 4.1). The evolution of the Cenozoic URG was controlled by polyphase reactivations of a complex set of crustal discontinuities of Late Paleozoic structures [Ziegler, 1990a]. The main extensional rifting and crustal NW-SE extension started in Late Eocene [Sissingh, 1998] during which Late Variscan and Permo-Carboniferous crustal discontinuities were transtensionally reactivated [Schumacher, 2002]. The opening of the graben was controlled by a paleostress field with a S_{Hmax} orientation of NNE-SSW [Ahorner, 1975; Illies, 1975] resulting in the development of a NE-SW to NNE-SSW striking graben. A major reorientation of the regional stress field during early Miocene times established a NE-SW-extensional to transtensional stress field with reactivated fault segments showing sinistral and dextral oblique displacements, but also local inversion and contraction [e.g. Illies et al., 1979]. The change of the regional stress field initiated a new tectono-sedimentary regime. The synrift deposits and older strata in the central and southern segments were uplifted and partly eroded due to transpressional reactivation of these graben segments [e.g. Rotstein et al., 2005; Rotstein and Schaming, 2011]. A number of thermal anomalies in the western part of the central and northern part of the URG are linked to different structural features such as zones of uplift [Baillieux et al., 2013]. Subsidence and sedimentation were restricted to the northern graben segment with a maximum Cenozoic graben fill of up to 3.0 km [Bartz, 1974; Pflug, 1982].

Numerous local studies have been carried out to determine the tectonic stress field in the URG. Most of them are based on the analysis and interpretation of earthquakes, tectonic studies, overcoring data, hydraulic fracturing data, and borehole breakouts [Greiner, 1975; Baumann, 1981; Larroque and Laurent, 1988; Plenefisch and Bonjer, 1997; Valley, 2007]. Figure 4.1 presents an extensive data compilation for the present-day stress field in the URG and shows the above mentioned major structural units of the rift system. The seismological data are derived from fault plane solutions of earthquakes from 1971 to 1980 and incorporate 33 fault plane solutions selected by Larroque et al. (1987), based mostly on data from Bonjer et al. [1984]. The fault traces from Illies et al. [1979] are based on the interpretation of 2D seismic sections. The information on the stress field orientation and the faulting regime are taken from the world stress map [Heidbach et al., 2008].

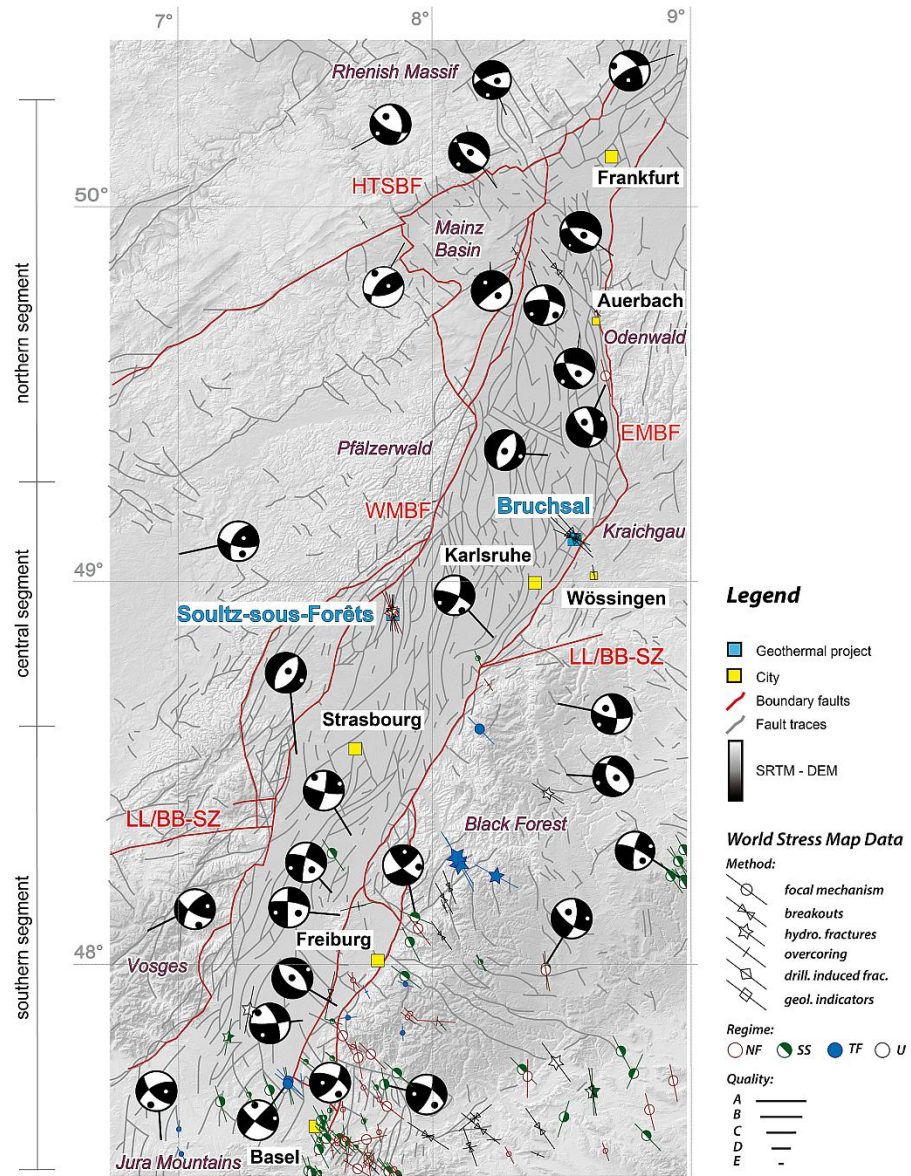


Figure 4.1: Compilation of data relevant to the stress field in the URG. Shown are stress field indicators derived from seismological and well test data compiled in the world stress map [Heidbach et al., 2008]. The underlying map shows a digital elevation model based on SRTM data and the major tectonic fault systems (grey lines; [Illies et al., 1979]). Position of the boundary faults and major shear zones are displayed as red lines. Abbreviations: WMBF – western main boundary fault, EMBF – eastern main boundary fault, LL/BB-SZ – Lalaye-Lubine/Baden-Baden shear zone, HTSBF – Hunsrück-Taunus southern boundary fault. For further information on the data, see text.

The compilation of stress field indicators in Figure 4.1 highlights the generally uniform NW-SE orientation of $S_{H_{max}}$ demonstrated earlier by Müller et al. [1992]. This general trend is confirmed by stress inversion of earthquake fault plane solutions [Delouis et al., 1993; Plenefisch and Bonjer, 1997]. The general trend of the stress field shows a local variation with $S_{H_{max}}$ orientation in the northern URG ranging N130°E - N135°E and in the southern URG / northern Switzerland ranging N145°E - N160°E. Interpretations of fault plane solutions also reveal a change in faulting regime in the URG [e.g. Plenefisch and Bonjer, 1997]. The northern part of the URG is characterized by an extensional stress state and active normal faulting ($\sigma_1 = S_v$, $\sigma_2 = S_{H_{max}}$). In the seismically more active southern part, strike-slip faulting ($\sigma_1 = S_{H_{max}}$, $\sigma_2 = S_v$) with secondary normal faulting is the predominant mechanism. The transition of the stress orientation and the change of the faulting regime by permutation of σ_1 and σ_2 [Larroque et al., 1987] occurs in the central segment of the URG, in the area of the site of investigation, probably causing a transitional stress state between normal and strike-slip faulting.

At the western central margin of the URG, an extensive set of in-situ stress data is available for the geothermal site of Soultz-sous-Forêts (France). Measured and derived orientations of $S_{H_{max}}$ determined down to 5 km varies between N125°E and N185°E with a mean value of N175°E \pm 10° [Cornet et al., 2007] and indicate a transitional stress state down to 5 km with a change from normal to strike-slip faulting at depths below 3 km [Cuenot et al., 2006].

4.3 METHODS

4.3.1 $S_{H_{max}}$ orientation

For the Bruchsal geothermal wells Eisbacher et al. [1989a] have derived the $S_{H_{max}}$ orientation from borehole breakouts in GB1 and GB2 using oriented caliper logging. The logs were acquired in the depth range of 1632-1900 m (GB1) and 2023-2525 m (GB2) in the Keuper, Muschelkalk and Buntsandstein formations and have been azimuth-corrected for the deviated wells. The values were subdivided into zones of fairly homogeneous orientation (Table 4.1) ranging between 50 and 100 m in depth. $S_{H_{max}}$ orientation was determined by stacking caliper data in each zone, with uncertainties of up to 20°. In addition to the stress-relevant data, the classification of reservoir rocks is indicated in Table 4.1. The grey rows indicate $S_{H_{max}}$ orientations determined in the clay-, gypsum-, and anhydrite-bearing formations of the Muschelkalk and Keuper. These

low-permeable units seal the reservoir which mainly consists of sandstones and conglomerates.

Table 4.1: Depth intervals (MD) of the analyzed borehole breakouts and determined S_{Hmax} orientations in the wells GB1 and GB2 (Reservoir rocks are marked in white).

Depth interval	$\angle S_{Hmax}$	stratigraphic formation
<i>GB1</i>		
1650 – 1700 m	N104°E	M. Muschelkalk & U. Buntsandstein
1700 – 1775 m	N137°E	M. Buntsandstein
1775 – 1850 m	N142°E	M. Buntsandstein
1850 – 1900 m	N145°E	L. Buntsandstein & U. Permian
<i>GB2</i>		
2026 – 2070 m	N090°E	M. Keuper
2070 – 2130 m	N163°E	L. Keuper
2130 – 2230 m	N125°E	U. Muschelkalk & U. Buntsandstein
2250 – 2328 m	N125°E	M. Buntsandstein
2330 – 2385 m	N145°E	M. Buntsandstein & U. Permian
2385 – 2475 m	N131°E	U. Permian
2475 – 2535 m	N128°E	U. Permian

U. = Upper; *M.* = Middle; *L.* = Lower

4.3.2 S_v and P_p calculation

The magnitude of the vertical stress, S_v , is generally equal to the weight of the overburden and can be calculated by integration of the rock densities from the surface to the depth of interest. Consequently, the stratigraphic units of the overburden were subdivided in two major groups. The first group includes the Quaternary and Tertiary formations of the graben fill, while the second one includes the occurring Mesozoic formations. We assume an average density of 2400 kg m^{-3} for the Cenozoic sedimentary succession based on Rotstein et al. [2006]. For the Triassic Muschelkalk and Buntsandstein, densities were determined from a litho-density log (LDL) acquired in GB1 between 1650 and 1900 m (Figure 4.2). A weighted mean rock density of about 2500 kg m^{-3} is indicated in the reservoir formations. This value is close to the literature data [Müller et al., 1988; Plaumann et al., 1967]. With an average thickness of the Tertiary graben sediments in Bruchsal of about 1350 m, a mean density of 2430 kg m^{-3} for the overburden is calculated for a reservoir depth of 2000 m. This leads to a vertical

stress magnitude of $S_v = 47.7$ MPa and a gradient of 23.8 MPa km^{-1} .

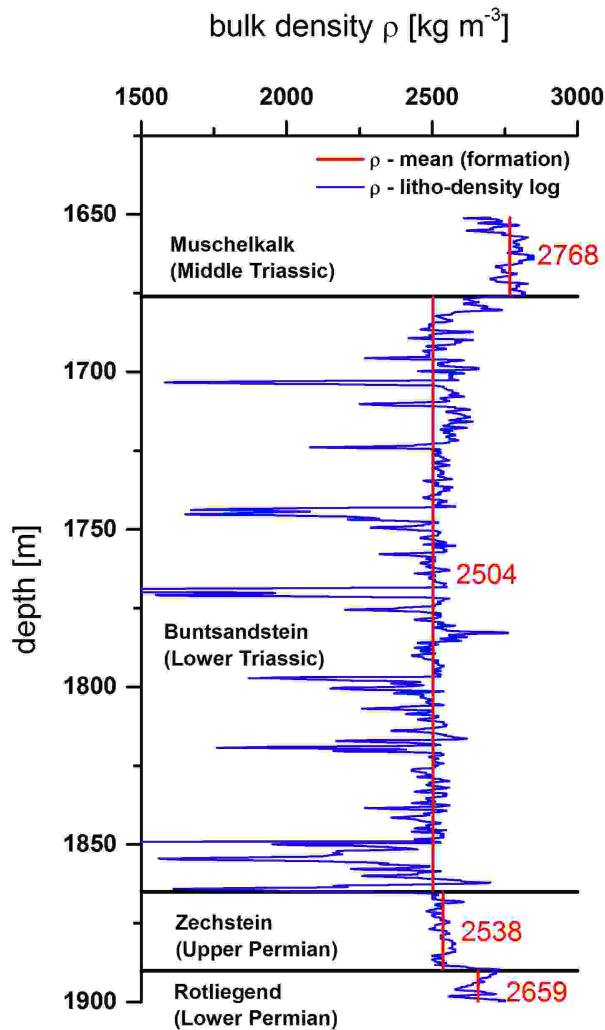


Figure 4.2: Measured rock densities obtained from a litho-density log in GB1 between 1650 and 1900 m. Red lines show mean density values for the drilled stratigraphic units. Zones of very small rock densities (< 2000 kg m^{-3}) and increased porosities in the Buntsandstein are associated with major fracture and fault zones in the geothermal reservoir.

The pore pressure, P_p , was calculated similarly, assuming that it is close to hydrostatic. With an average depth of the free water table 60 m below ground level, the reservoir reveals tendency to slight under-pressure condition. The fluid density of the geothermal brine is 1070 kg m^{-3} (T. Kölbl, 2013, pers. comm.). At mean reservoir depth of 2000 m, a pore pressure of $P_p = 20.4$ MPa and a gradient of 10.2 MPa km^{-1} was calculated. This leads to a ratio of pore pressure to vertical stress magnitude of $P_p = 0.43 S_v$.

4.3.3 Stress field profiles for Bruchsal and adjacent areas

Eisbacher et al. [1989a] prepared two different stress profiles including the minimum (S_{hmin}) and maximum (S_{Hmax}) horizontal stress components. The first stress field profile is based on the linear extrapolation of overcoring data from outcrops and shallow wells measured by Greiner [1978] hereafter referred to as the Greiner profile. In detail, the model is based on S_{Hmax} and S_{hmin} magnitudes of 4.9 MPa and 3.7 MPa, respectively, from the 140-meter-deep Auerbach tunnel, about 60 km north of Bruchsal (Figure 4.1). These data were interpolated with measurements from the Wössingen outcrop, 10 km SE of Bruchsal (Figure 4.1), with magnitudes of $S_{Hmax} = 2.2$ MPa and $S_{hmin} = 1.0$ MPa. The obtained stress profile results in a normal faulting regime for the Bruchsal area of:

$$\begin{aligned} S_{Hmax} &= 2.2 + 0.019z \text{ (MPa)} \\ S_{hmin} &= 1.0 + 0.019z \text{ (MPa)} \end{aligned}$$

The second profile is based on the stress field compilation of Rummel and Baumgärtner (1982, unpublished) for central Europe with data originating from 120 hydraulic fracturing measurements. In SW Germany this compilation is based on wells at depths down to 500 m. The linear extrapolation (hereafter referred to as the Rummel & Baumgärtner profile) predicts a strike-slip regime with:

$$\begin{aligned} S_{Hmax} &= 0.8 + 0.034z \text{ (MPa)} \\ S_{hmin} &= 0.9 + 0.021z \text{ (MPa)} \end{aligned}$$

At a reservoir depth of 2000 m, the Rummel & Baumgärtner and Greiner profiles differ in S_{hmin} by 3.9 MPa, only, but in S_{Hmax} by 28.6 MPa. In the following, we compare these profiles to the well-defined stress field models prepared for the Soultz geothermal site. In Soultz, two profiles have been prepared recently: Cornet et al. [2007] show that the S_{Hmax} magnitude is close to S_v (mean S_v gradient of 24.5 MPa km^{-1}) resulting in a range of $0.95 S_v < S_{Hmax} < 1.1 S_v$ between 2800 and 3600 m (Figure 4.3 A) and Valley [2007] characterized the stress at Soultz between 1500 and 5000 m to be in the range of $0.90 S_v < S_{Hmax} < 1.05 S_v$ (with the same S_v gradient, see Figure 4.3 B). Both describe the transitional stress field between a normal faulting (NF) and strike-slip (SS) regime.

With exception of S_{Hmax} of the Greiner profile, the two Bruchsal stress profiles differ significantly from the Soultz profiles (Figure 4.3). With a rather similar S_v gradient of 23.8 MPa km^{-1} , the

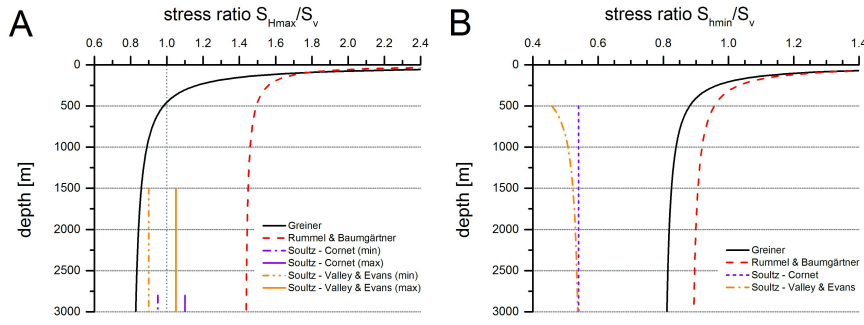


Figure 4.3: Comparison of existing stress-depth relationships and stress ratios for the geothermal sites of Bruchsal and Soultz. Stress magnitudes of S_{Hmax} and S_{hmin} are normalized by S_v . The stress profiles of Greiner and Rummel & Baumgärtner are based on the combination and linear extrapolation of stress magnitudes obtained from near surface hydro frac and overcoring measurements. The Soultz stress profiles from Cornet et al. [2007] and Valley [2007] are based on evaluations of large-scale injection experiments and interpretations of borehole breakouts in the deep crystalline reservoir of Soultz.

Rummel & Baumgärtner and the Greiner stress profiles would yield S_{Hmax}/S_v ratios at depths over 500 m of 1.4-1.5 and 0.8-1.0, respectively (Figure 4.3A). Hence, the Rummel & Baumgärtner profile predicts a strike-slip regime, while the Greiner profile indicates normal faulting at depths below 500 m. In contrast, the ratios of S_{hmin}/S_v in both Bruchsal profiles are similar (0.8-0.9, Figure 4.3B), but differ from the Soultz profiles with ratios of approx. 0.5. Finally, it must be stated that the two Bruchsal profiles are debatable since they are derived from measurements at shallow depth only.

4.3.4 Critical stress concept

In-situ measurements and detailed analyses to determine the magnitude of S_{Hmax} are rare in the URG. In such conditions, the critical stress concept may constrain the S_{Hmax} magnitude [Zoback et al., 2003]. According to frictional equilibrium, one can assume that the ratio between maximum and minimum effective stresses cannot exceed the one required to cause slip on pre-existing faults that are optimally oriented to the principal stress field [Jaeger et al., 2007; Moos and Zoback, 1990]. Hence, effective differential stresses are bounded by a critical ratio. Assuming that one of the principal stresses is vertical and that there is no cohesion, the critical stress ratio can be written after Jaeger et al. [2007] as:

$$\sigma_1/\sigma_3 = (S_1 - P_P)/(S_3 - P_P) \leq \left(\sqrt{\mu^2 + 1} + \mu \right)^2 \quad (4.1)$$

where P_p is the in-situ pore pressure and μ the coefficient of frictional sliding. To predict limiting stress differences at depth, Anderson's faulting theory has to be applied to determine which of the principal stresses S_{Hmax} , S_{hmin} , and S_v correspond to S_1 , S_2 , and S_3 . This will depend on whether it is a normal (Eq. 4.2), strike-slip (Eq. 4.3) or reverse faulting regime (Eq. 4.4):

$$\sigma_1/\sigma_3 = (S_v - P_p)/(S_{hmin} - P_p) \leq (\sqrt{\mu^2 + 1} + \mu)^2 \quad (4.2)$$

$$\sigma_1/\sigma_3 = (S_{Hmax} - P_p)/(S_{hmin} - P_p) \leq (\sqrt{\mu^2 + 1} + \mu)^2 \quad (4.3)$$

$$\sigma_1/\sigma_3 = (S_{Hmax} - P_p)/(S_v - P_p) \leq (\sqrt{\mu^2 + 1} + \mu)^2 \quad (4.4)$$

Based on these equations, the critical ratio of the principal stress magnitudes depends on depth, pore pressure, and the coefficient of frictional sliding. A coefficient of friction of 0.85 has been shown to be applicable under shallow crustal conditions for normal stresses up to 200 MPa, i.e. depths of approx. 6 km [Byerlee, 1978]. However, it is generally accepted that hydrothermal alteration and clay content in shear planes contribute to a significant reduction of the friction angle during fault reactivation [Krantz, 1991]. But, since no data on the mineralogical composition of the faults and fractures in Bruchsal were acquired, we assume $\mu = 0.85$, which results in an effective stress ratio of $\sigma_1/\sigma_3 \leq 4.68$. The possible mechanically stable stress conditions in different stress regimes have been comprised by Zoback et al. [2003] to the so-called stress polygon. For a given friction coefficient, the area inside the polygon represents the allowed stress, whereas values lying outside the borders are unstable and yield failure.

4.4 RESULTS

In the following, we will present the results of the determination of S_{hmin} by two leak-off tests from the well GB2 as well as the application of the critical stress concept to further constrain S_{hmin} and S_{Hmax} .

4.4.1 Leak-off tests and S_{hmin} magnitude

For the determination of the least principal stress magnitude, S_{hmin} , we interpreted new available data sets of two leak-off tests (LOT) that were carried out in 1984 (Table 4.2).

The leak-off pressure (LOP) at the depth of the test is the sum of the well head pressure and the pressure in the wellbore due to the wellbore fluid. According to Zoback et al. [2003], we consider the clear LOP of each test (corresponding to a distinct break-in-slope

Table 4.2: Key parameters of the two leak-off tests conducted in the geothermal well Bruchsal GB2 in 1984.

	LOT-2023	LOT-2245
Depth	2023 m	2245 m
Formation	M. Keuper	M. Buntsandstein
Drilling mud density	1.11 g cm ⁻³	1.05 g cm ⁻³
Well-head pressure	9 MPa	4.5 MPa
LOP = S_{hmin} magnitude	31.0 MPa	27.6 MPa
S_{hmin} gradient	15.3 MPa km ⁻¹	12.3 MPa km ⁻¹
S_{hmin}/S_v - ratio	0.64	0.52

M: Middle

of the linear pressure build-up) to be approximately equal to the S_{hmin} magnitude. While LOT-2023 is conducted in the weak Keuper, LOT-2245 is located in stiff units of the Middle Buntsandstein. We would like to emphasize that LOT-2023 results in a higher LOP of 31.0 MPa compared to LOT-2245 with a LOP of 27.6 MPa. This finding is consistent with S_{hmin} magnitudes obtained in comparable environments [Cornet and Röckel, 2012]. The determined S_{hmin}/S_v ratios show contradictory results to those from Soultz.

4.4.2 Critical stresses of S_{hmin}

Based on the statements in section 4.2, a normal faulting regime (NF) close to strike-slip transition is assumed for the Bruchsal area. In a first step, the S_v gradient of 23.8 MPa km⁻¹ is calculated for a mean rock density of 2430 kg m⁻³. The application of the critical stress concept is illustrated in Figure 4.4 A. Applying eq. 4.2, the S_{hmin} magnitude of LOT-2023 (15.3 MPa km⁻¹) results in a σ_1/σ_3 ratio that is smaller than the critical value of $\sigma_1/\sigma_3 < 4.68$, whereas the σ_1/σ_3 ratio of LOT-2245 (12.3 MPa km⁻¹) is larger in depths over 500 m. The latter ratio violates the critical stress concept. This may be due to errors in the determination of the S_v (in the following called upper bound) or S_{hmin} (in the following called lower bound) gradient. It should be mentioned here that a higher magnitude of μ also reveals higher critical stress ratios. The interpretation of LOT-2245 ($S_{hmin}/S_v = 0.52$) leads to stress ratios between 6 and 7 at 3000 m depth. In order to be consistent with the critical stress concept, a μ of 1.1 is needed. We consider this rather unlikely and discuss potential uncertainties in S_v and S_{hmin} determination only.

Therefore, a sensitivity study on the rock density (or vertical stress gradient) was conducted to fit the critical stress concept. In this case, the lower bound of the stress ratio is modified. For the

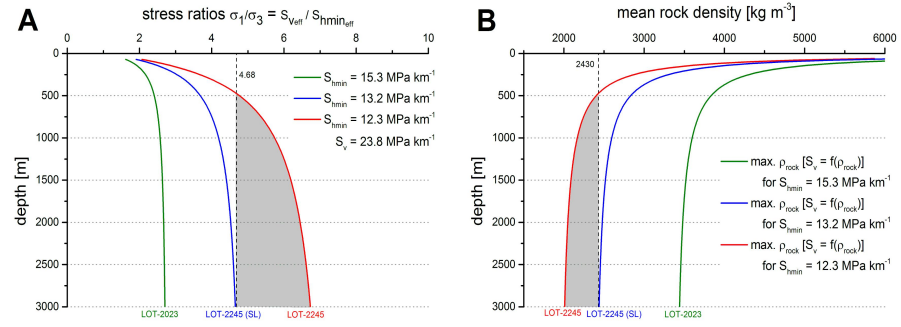


Figure 4.4: Application of the critical stress concept and uncertainty analysis of the determined S_v gradient. A) Comparison of the effective stress ratios σ_1/σ_3 for Bruchsal calculated for the S_{hmin} magnitudes of the leak-off tests LOT-2023 (green line) and LOT-2245 (red line) in GB2. The vertical dashed line represents the critical σ_1/σ_3 ratio of 4.68, i.e. the maximum stress ratio for which the critical stress concept is valid. The blue line shows corrected stress ratios for LOT-2245 to be consistent with the critical stress concept (see text). B) Overview of maximum possible rock density for derived S_{hmin} magnitudes with respect to fulfilling the criteria for the critical stress concept.

S_{hmin} of LOT-2245, the assumed density of the overburden has to be decreased at least from 2430 to 2000 kg m^{-3} (Figure 4.4 B), yielding a decrease of the S_v gradient by 18%, from 23.8 to 19.6 MPa km^{-1} . After comparing this value with the LDL measurements in GB2 (section 4.3.2), we can conclude that it is unrealistically low. On the other hand, the lower bound of the ratio can be investigated keeping the density distribution fixed. To comply with the critical stress concept, S_{hmin} of LOT-2245 needs to be increased by 7%, from 12.3 MPa km^{-1} to 13.2 MPa km^{-1} . Figure 4.5 shows the corresponding stress profiles including the measured LOT data.

There are no error estimates given on the Bruchsal LOT measurements. Based on the example from Soultz, we can assume a reasonable uncertainty range for S_{hmin} magnitudes of $\pm 0.45z$ [km] + 1.82, as derived from several large and small volume injection tests [Valley and Evans, 2007]. If we assume similar error margins for Bruchsal, a bandwidth of the S_{hmin} profile can be determined. An increase of the S_{hmin}/S_v ratio from 0.52 to 0.55 is consistent with the critical stress concept and remains consistent with the error margins determined for the deep geothermal wells in Soultz. This represents a minimum S_{hmin} gradient of LOT-2245, referred to as LOT-2245 (SL) in the following (Figure 4.4 - blue lines).

The hypothesis on the NF tectonic regime also influences the consistency with the critical stress concept. Following the same procedure,

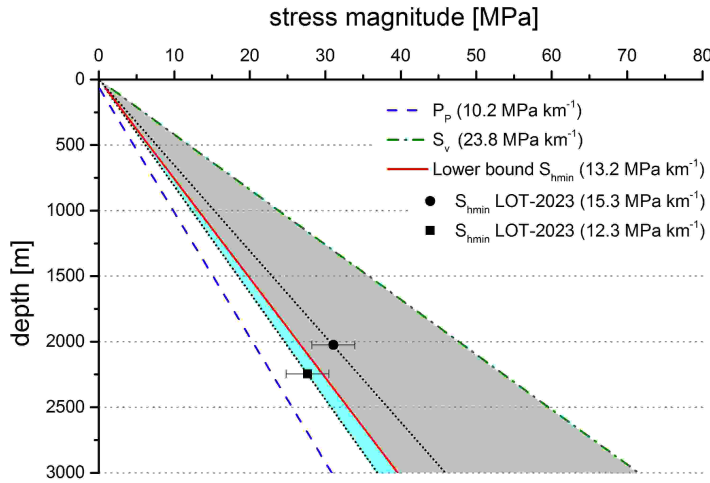


Figure 4.5: Uncertainty analysis of the determined S_{hmin} gradients derived from LOT-2023 and LOT-2245. According to the critical stress concept, the effective stress ratio σ_1/σ_3 should not exceed a factor of 4.68 (grey shaded area). Assuming a S_v gradient of 23.8 MPa km^{-1} and a NF regime, the σ_1/σ_3 ratio for LOT-2023 is within this range whereas LOT-2245 shows inconsistent ratios between 6 and 7. The slight increase of S_{hmin} from 12.3 to 13.2 MPa km^{-1} (blue shaded area) indicates the minimum necessary variation to keep the σ_1/σ_3 ratio of LOT-2245 within the predicted threshold of $\sigma_1/\sigma_3 \leq 4.68$. Uncertainty range of S_{hmin} magnitudes is estimated following observations of [Valley and Evans \[2007\]](#) for deep well injection tests in Soultz.

it is obvious that a strike-slip regime with $S_1 = S_{Hmax} > S_v$ would result in an effective stress ratio of $\sigma_1/\sigma_3 > 4.68$. This would rather lead to a larger increase of the S_{hmin} gradient for LOT-2245 to comply with the critical stress concept. Accordingly, this option is not further considered in this study.

4.4.3 Critical stresses of S_{Hmax}

As described by [Zoback et al. \[2003\]](#) the applied critical stress concept is illustrated in Figure 4.6 by the stress polygon. We assume a pore pressure of $P_p = 0.43 S_v$ and a frictional coefficient of $\mu = 0.85$. Points at the periphery of the polygon correspond to a state of stress at the frictional limit (I - radial extension, II - normal faulting, III - transitional normal/strike-slip faulting, IV - strike-slip faulting, V - transitional strike-slip/reverse faulting, VI - reverse faulting, VII - radial compression). According to eq. 4.2 and eq. 4.4, the lower bound on S_{Hmax} is given by $S_{Hmax} = 0.55 S_v$ (see previous discussion, Point I in Figure 4.6 A) and the upper bound

by $S_{H_{max}} = 3.10 S_v$ (line between points V and VII in Figure 4.6 A).

The range of possible values from $S_{h_{min}}$ (i.e. measured LOT-2023 and corrected LOT-2245 (SL)) is constrained in Figure 4.6 B. The lower bound of $S_{H_{max}}$ as defined from LOT-2245 (SL) would correspond to a radial extensional faulting regime. According to our assumptions on a NF regime, $S_{H_{max}}$ may take any value between $S_{h_{min}}$ and S_v (segment I-III in Figure 4.6 B) and reaches the limit to a strike-slip regime. For LOT-2023 a stress ratio of $S_{H_{max}} = S_{h_{min}} = 0.64 S_v$ marks the lower bound for $S_{H_{max}}$. With a relation of $S_{H_{max}} = 1.42 S_v$, a strike-slip regime seems possible, too.

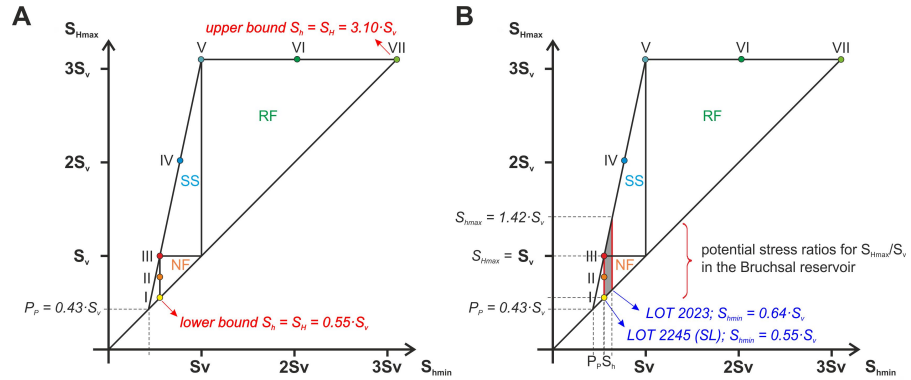


Figure 4.6: Stress polygon concept in Bruchsal to constrain allowable stress ratios and related faulting regimes. A) Possible range for horizontal stress components $S_{H_{max}}$ and $S_{h_{min}}$ (each normalized by S_v) B) $S_{H_{max}}$ magnitudes accounting for $S_{h_{min}}$ from the leak-off tests LOT-2023 and LOT-2245 (SL). Grey shaded area indicates the range of possible stress states between a strike-slip and a radial extensional faulting regime.

4.5 DISCUSSION

The following discussion includes an assessment of the obtained stress profile in a regional context and with respect to the well-defined Soultz stress field. It should be mentioned that the sedimentary cover at Soultz reaches a maximum depth of about 1400 m. Consequently, at the depth of the Bruchsal reservoir at Soultz, we are already in the upper granitic reservoir [Genter et al., 2010].

4.5.1 Stress field variations

The orientation of $S_{H_{max}}$ in Bruchsal between 125° and 145° agrees with the general NW-SE trend of the regional stress field in SW Ger-

many [Heidbach et al., 2008; Müller et al., 1992] and thus, differs from the values in Soultz by about 30-40°. This variation may be attributed to decoupling at the interface between the crystalline basement and the overlying sedimentary rock. Such a behavior is also observed in the Otterbach-2 well in Basel. Breakouts and drilling induced fractures identified above and below the sediment-basement interface suggest a clockwise ~30° rotation of S_{Hmax} [Valley and Evans, 2009]. In Bruchsal, internal variation of orientation seems to be linked to lithological changes. A comparison of the S_{Hmax} orientations for different depth sections including their variation with the litho-log of the two wells GB1 and GB2 is presented in Figure 4.7.

Generally, S_{Hmax} orientation exhibits a high variability in the upper part of the investigated section of the Mesozoic sediments. Orientations stabilize at about 140° below the Muschelkalk in GB1. With the exception of the Middle Buntsandstein to Upper Permian in GB2, the orientations stabilize below the Keuper at about 130°. Thus, highest variation is observed for the sections with a high clay, gypsum, or anhydrite content. LOT-2023 is located in such lithology. Measured S_{Hmax} orientation is by about 30-40° off the general GB2 trend in this depth range. The determined S_{hmin} magnitude of LOT-2023 is 3.4 MPa higher than that of LOT-2245. This observation is consistent with results summarized by Cornet and Röckel [2012] and the increase in S_{hmin} by about 4 MPa in the Callovo-Oxfordian argillite of the Paris basin [Wileveau et al., 2007]. It suggests that the leak-off tests in rocks with a low friction coefficient behave generally in this manner, which is also indicated by laboratory experiments [e.g. Krantz, 1991]. The stronger rocks of the Middle Buntsandstein can support higher differential stresses without failing than the weaker rocks of the Middle Keuper. It is rather noteworthy that for the same stratigraphic unit internal deformation processes have also been described [Wirth, 1962]. Litho-log interpretations of numerous oil wells of the former oil field Forst, 3 km north of Bruchsal, suggest massive internal shearing and sub-horizontal deformation within the Keuper and especially in the evaporitic layers of the Lower Keuper. With regard to our results, both orientation and magnitude of LOT-2023 show similar deviations and, thus, are not considered to be representative for the reservoir zone of Bruchsal. In contrast, LOT-2245 is located within the section of stable S_{Hmax} orientation.

4.5.2 Stress profile

The discussion on the suitability of earlier stress field concepts as well as the new leak-off test data, lead us to propose an alternative stress profile for the Bruchsal area that is presented in Figure 4.8. Our resulting stress field model is based on the LOT-2245 (SL) applying

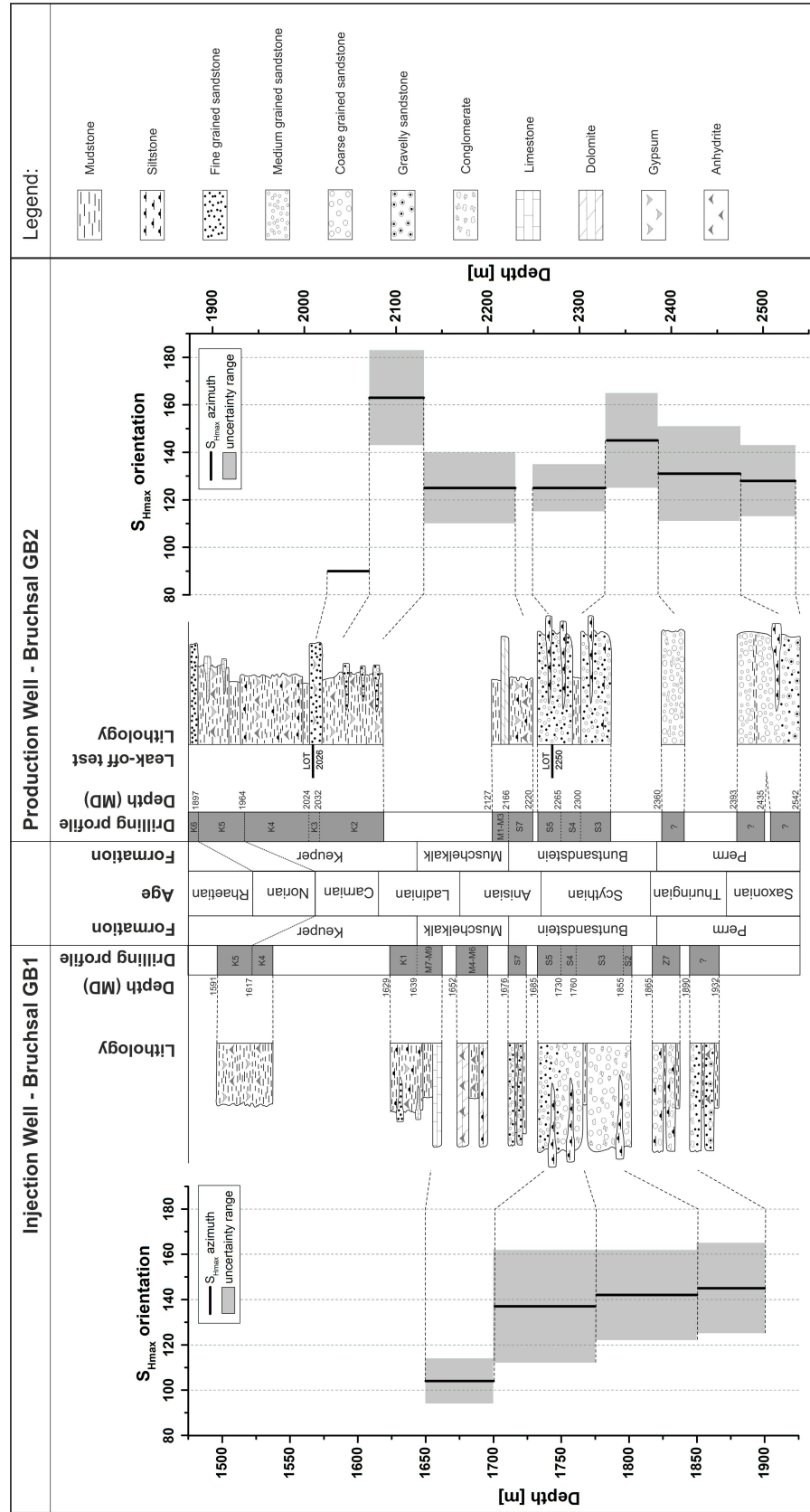


Figure 4.7: Comparison of the stratigraphic and lithological well profiles of the Bruchsal geothermal wells. Stress field orientations based on breakout analysis of oriented caliper logging data [Eisbacher et al., 1989a]. Mean S_{Hmax} azimuths were determined by stacking breakout data in zones of fairly homogeneous orientations to take lithological characteristics into account.

the critical stress concept. It should be mentioned that the critical stress concept restricts the ratio σ_1/σ_3 depending on the coefficient of frictional sliding. An increase of this ratio leads to shear failure on the most favorable oriented fault or fracture plane. We are aware that, if this fracture trend does not exist in the subsurface, larger stress ratios may be applicable. However, with no detailed information on the orientation of the fracture network, such as in Bruchsal, the application of the critical stress concept is a rather conservative approach.

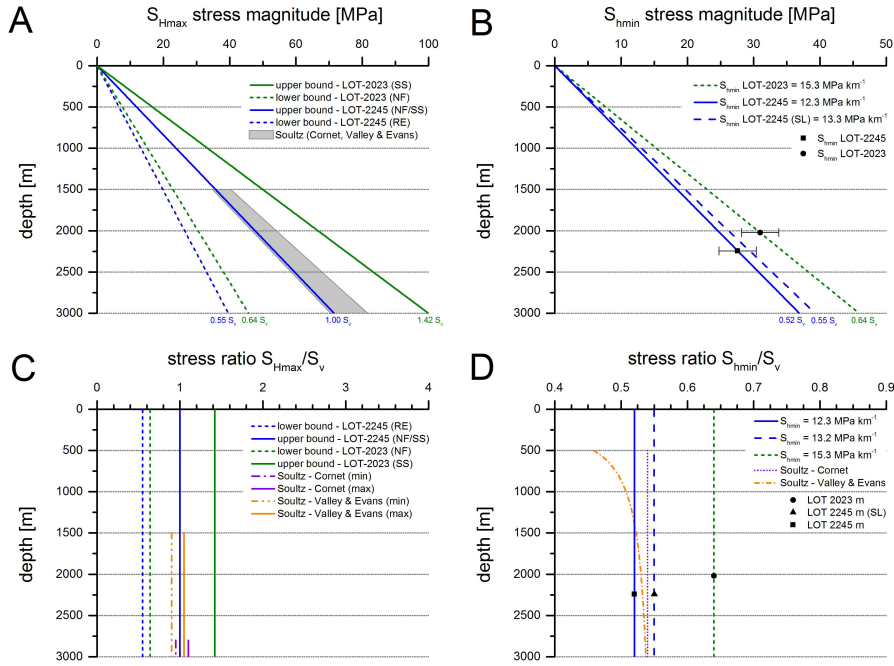


Figure 4.8: Comparison of the estimated stress-depth relations and stress ratios for the Bruchsal geothermal site. A) Predicted magnitudes for S_{Hmax} based on the stated Greiner and Rummel & Baumgärtner profiles and the newly derived Bruchsal profile, respectively. The range between the assumed upper and lower bound of S_{Hmax} covers a potential normal (NF), a radial extensional (RE), and a transitional (NF/SS) faulting regime for the Bruchsal model (see Figure 4.4 B) Overview of the minimum horizontal stress component S_{hmin} . C&D) Comparison of the potential stress magnitudes of S_{Hmax} and S_{hmin} normalized by S_v .

Theoretically, our stress model has a S_{Hmax} -depth relation constrained by LOT-2245 (SL) with radial extension as a lower bound faulting regime and NF/SS transition as an upper bound (Figure 4.8 A). Geologically, the validity of the radial extension under the tectonic settings of Bruchsal is, however, questionable. As discussed in section 4.2, a transitional to normal faulting stress regime in the central part of the URG in general and in Bruchsal in particular is rather likely. This is consistent with the Soutz stress profiles or determined

earthquake fault plane solutions [e.g. Ritter et al., 2009]. Thus, we suggest our model to be valid for NF and NF/SS faulting regimes. It should be mentioned that the Greiner profile is within our range of S_{Hmax} for depths larger than 500 m. The proposed S_{Hmin} -depth relation (Figure 4.8 B) presents the steepest gradient (except the results for the uncorrected LOT-2245) and clearly deviates from the earlier Greiner and Rummel & Baumgärtner profiles.

4.6 CONCLUSIONS

World-wide, geothermal projects are often located in active tectonic terrains with highly fractured subsurface reservoir rocks. The evaluation of the stress field in these projects is of main importance. It improves the understanding of the structural setting of the reservoir and supports the definition of an optimum exploration strategy by targeting zones of high transmissivity. The geothermal sites in the URG in central Europe are typically characterized in this context. The Rhine Graben tectonics yields large differential stress levels and favors therefore the existence of large fault and fracture systems. Due to a rather complex history, local evidence of the stress field needs to be evaluated. However, this importance of the stress field has only been pointed out gradually and many earlier projects provide only little relevant data. In this perspective, new concepts and methodologies need to be considered. Our application of the critical stress concept to measured data may lead to better constrained results and this within their uncertainty of the measurements. The critical stress concept provides a number of solutions for the stress field model depending on possible stress regimes. Using indications such as the local geology and structural setting, the number of solutions has been reduced to normal faulting and transition of normal faulting to strike-slip regimes. Finally, based on new leak-off test data, we have constrained a new stress field model for the Bruchsal area.

Our results show that in accordance with earlier studies, sedimentary layers may have a large influence on both the orientation of the mean principal stress direction and the magnitudes. This applies in particular to clay- and anhydrite-rich layers that occur in this case in the Keuper Formations and partly in the Muschelkalk. Stress decoupling and aseismic deformation within this formation cannot be excluded as also indicated by the results from the nearby Forst oil reservoir. We could show that stress magnitudes obtained in sedimentary formations vary significantly due to different rheological characteristics, and a linear stress-depth relation has to be treated only as a first approach. The result from a leak-off test in the Middle Buntsandstein

in Bruchsal is, however, consistent with the S_{hmin}/S_v ratio of Soultz. We may attribute this consistency across the entire E-W extension of the URG and different lithologies to small differences in the mechanical properties of the Soultz granitic basement and the sedimentary rocks of the Middle Buntsandstein in Bruchsal.

ACKNOWLEDGMENTS

We would like to thank EnBW Energie Baden-Württemberg AG for providing the well logs and leak-off test data. Financial support has been kindly granted by the Federal Ministry for the Environment, Nature Conservation, Building and Nuclear Safety (BMU) and EnBW Energie Baden-Württemberg AG within the framework of the Logro project (FKZ 0325111 A). Further supports from the Helmholtz Portfolio GEOENERGIE and the geothermal research center of Baden Württemberg (LFZG). We would like to thank I. Moeck, F. Cornet, B. Müller and T. Röckel for fruitful discussions.

STRUCTURAL CONTROL OF GEOTHERMAL
RESERVOIRS IN EXTENSIONAL TECTONIC
SETTINGS: AN EXAMPLE FROM THE UPPER RHINE
GRABEN

A large part of this section is published in *Journal of Structural Geology*,
82, p. 1-15, doi: 82, 10.1016/j.jsg.2015.11.003.

ABSTRACT

In extensional tectonic settings major structural elements such as graben boundary faults are typically oriented subparallel to the maximum horizontal stress component S_{Hmax} . They are often structurally accompanied by transfer zones that trend subparallel to the extension direction. In the Upper Rhine Graben, such transfer faults are typically characterized by strike-slip or oblique-slip kinematics. A major re-orientation of the regional stress field by up to 90° of the Upper Rhine Graben in the Early Miocene led to the present-day normal and strike-slip faulting regimes in the North and South of the Upper Rhine Graben, respectively, and a transition zone in-between. Consequently, conditions for fault frictional failure changed significantly. Moreover, it has been observed during tracer and stimulation experiments that such transfer faults may be of major importance for the hydraulic field of geothermal reservoirs under the present stress condition, especially, when located between production and injection well.

In this context we have investigated slip and dilation tendencies (T_S and T_D) of major structural elements at reservoir scale for two representative geothermal sites, Bruchsal (Germany) and Riehen (Switzerland), located close to the Eastern Main Boundary Fault of the Upper Rhine Graben. We have evaluated the quality and uncertainty range of both tendencies with respect to potential variation in S_{Hmax} orientation. Despite significant differences in orientation of the structures and the stress regimes, the resulting variation of T_S and T_D reveal major similarities concerning the reactivation potential of both, the graben-parallel structures and the transfer faults. The conditions of criticality for tensile failure and non-criticality for

shear failure suggest that transfer faults are most likely naturally permeable structures with low stimulation potential. This is in agreement with the absence of both immediate tracer recovery and seismicity in the studied geothermal sites.

5.1 INTRODUCTION

Most of the geothermal systems world-wide are controlled by their tectonic setting and related structural features. Extensional tectonic settings and related structures comprising normal and transtensional faults and fractures dominate in intra- and back-arc basins, extending zones of orogenic belts, spreading ridges, and continental rifts [Angelier et al., 1997; Curewitz and Karson, 1997; Bellani et al., 2004]. Faults and fractures that are favorably oriented and critically stressed for frictional failure commonly control both fluid flow and reactivation potential [Barton et al., 1995; Sibson, 1996; Ito and Zoback, 2000].

Extensional terrains and, in particular, continental rifts are commonly characterized by closely spaced and complex en-echelon normal faults that represent main structural boundaries as described for the West Anatolian or Basin and Range provinces [Faulds et al., 2010, 2011b]. These normal faults can be linked either by accommodation zones or transfer faults. Complex interplay of such extensional faults, including stress concentrations at and along fault tips and fault intersections, favors localization of geothermal anomalies [e.g. Curewitz and Karson, 1997; Baillieux et al., 2013]. Intersections of graben-parallel normal faults with transversely oriented oblique-slip faults are common structural features of some of the most productive geothermal fields world-wide, e. g.. the Taupo Volcanic Zone in New Zealand [Rowland and Sibson, 2004].

In this study, we highlight the interplay of graben-parallel normal faults with high-angle transfer- or strike-slip faults and its implication for the localization of geothermal reservoirs in continental rifts by slip and dilation tendency (T_S and T_D) analyses. The distribution of geothermal projects in the Upper Rhine Graben (URG) allows the investigation and comparison of different geothermal projects along its Eastern Main Boundary Fault (EMBF). With Bruchsal and Riehen, we investigate two cases that are sufficiently well-documented, geologically and structurally comparable, but differ in their ambient stress field. We developed structural models and determined the in-situ stress state for both fields. T_S and T_D analyses on local fault patterns were then

interpreted in terms of structural control of the geothermal reservoirs.

To underline the complexity of structural control on geothermal reservoirs, we note the well-documented anisotropy of flow and geomechanical behavior of faults in the Soultz-sous-Forêts EGS reservoir. Here, fracture propagation during stimulation develops mainly in N-S direction that is parallel to a secondary fault system [Dorbath et al., 2009; Baillieux et al., 2011]. However, it is most likely that an E-W striking fault impedes the connection of the southernmost well GPK₄ to the main reservoir as indicated from tracer tests [Sanjuan et al., 2010]. This anisotropy in hydraulic conductivity among fault zones is attributed to S_{Hmax} trending approximately N-S [Cornet et al., 2007; Valley, 2007]. It may account for the occurrence of large scale convection cells and temperature anomalies along N-S striking fault zones in the western part of the URG [Bächler et al., 2003].

At the eastern margin of the URG, comparable stress based observations were not acquired. The orientation of the EMBF zone in Bruchsal and Riehen indicates a predominant trend of graben-parallel NE-SW to NNE-SSW striking fault systems [Illies et al., 1979]. NW-trending structures are observed in Riehen, but numerical simulation of pressure data indicates reservoir extension in graben-parallel direction [e. g. Mégel and Rybach, 2000].

In Bruchsal and Riehen, tracer tests were conducted through the geothermal doublets that are aligned parallel to the EMBF zone in order to investigate possible connection between the producer and injector. As conservative tracer for such geothermal environment, 10 kg of uranine were injected into the RB-2 injection well in Riehen in Nov/2009 [Schill and Klingler, 2011]. After 12 months of production, the tracer could not be recovered. These results are somehow contradictory to a graben-parallel alignment of the hydrothermal reservoir. In the following, we will investigate and discuss the influence of fault zones striking at a high angle to the graben axis on subsurface fluid flow in deep systems.

5.2 GEOLOGICAL SETTING

5.2.1 *General overview*

The approximately 300 km long URG is part of the European Cenozoic rift system [Ziegler, 1992], which extends over more than 1000 km in Central Europe (Fig. 5.1 A). The URG can be subdivided into a NNE-striking southern, a NE-SW-striking central, and a NNW-SSE-

to N-S-striking northern segment (Fig. 5.1 B). The evolution of the Cenozoic URG was controlled by polyphase reactivations of a complex pattern of Late Variscan and Permo-Carboniferous crustal discontinuities [Schumacher, 2002; Ziegler et al., 2006]. NW-SE extension started in Late Eocene [Sissingh, 1998] resulting in the development of a SW-NE to SSW-NNE striking URG. A major reorientation of the regional stress field during Early Miocene established a NE-SW-extensional to transtensional stress field with reactivated fault segments. They are characterized by sinistral and dextral oblique displacement, local inversion and contraction [e.g. Illies et al., 1979], and erosion occurring predominantly in the central and southern segments of the URG [Rotstein et al., 2005; Rotstein and Schaming, 2011]. Subsidence and sedimentation shifted northward during Miocene time with a maximum Cenozoic graben-fill of up to 3.0 km in the northern graben segment [Bartz, 1974; Pflug, 1982].

Determination of the recent tectonic stress field orientation has been the subject of numerous studies in the URG. As shown in the World Stress Map [Heidbach et al., 2008], the URG is characterized by a generally uniform NW-SE orientation of the largest horizontal stress component (S_{Hmax} , Fig. 5.1 C). This general trend shows local variations along strike: S_{Hmax} orientations in the northern URG range from N130°E to N135°E and in the southern URG / northern Switzerland from N145°E to N160°E [Delouis et al., 1993; Plenefisch and Bonjer, 1997]. Interpretations of fault-plane solutions also reveal a change in faulting regime in the URG [e.g. Plenefisch and Bonjer, 1997]: the northern part of the URG is characterized by an extensional stress state and active normal faulting ($\sigma_1 = S_v$, $\sigma_2 = S_{Hmax}$), but in the seismically more active southern part, strike-slip faulting ($\sigma_1 = S_{Hmax}$, $\sigma_2 = S_v$) with secondary normal faulting prevails (Fig. 5.1 D). The transition of the stress orientation and the change of the faulting regime by permutation of σ_1 and σ_2 [Larroque et al., 1987] occurs in the central segment of the URG and was documented for the Soultz area (western margin; [Cuenot et al., 2006]) and the Bruchsal area (eastern margin, [Meixner et al., 2014]).

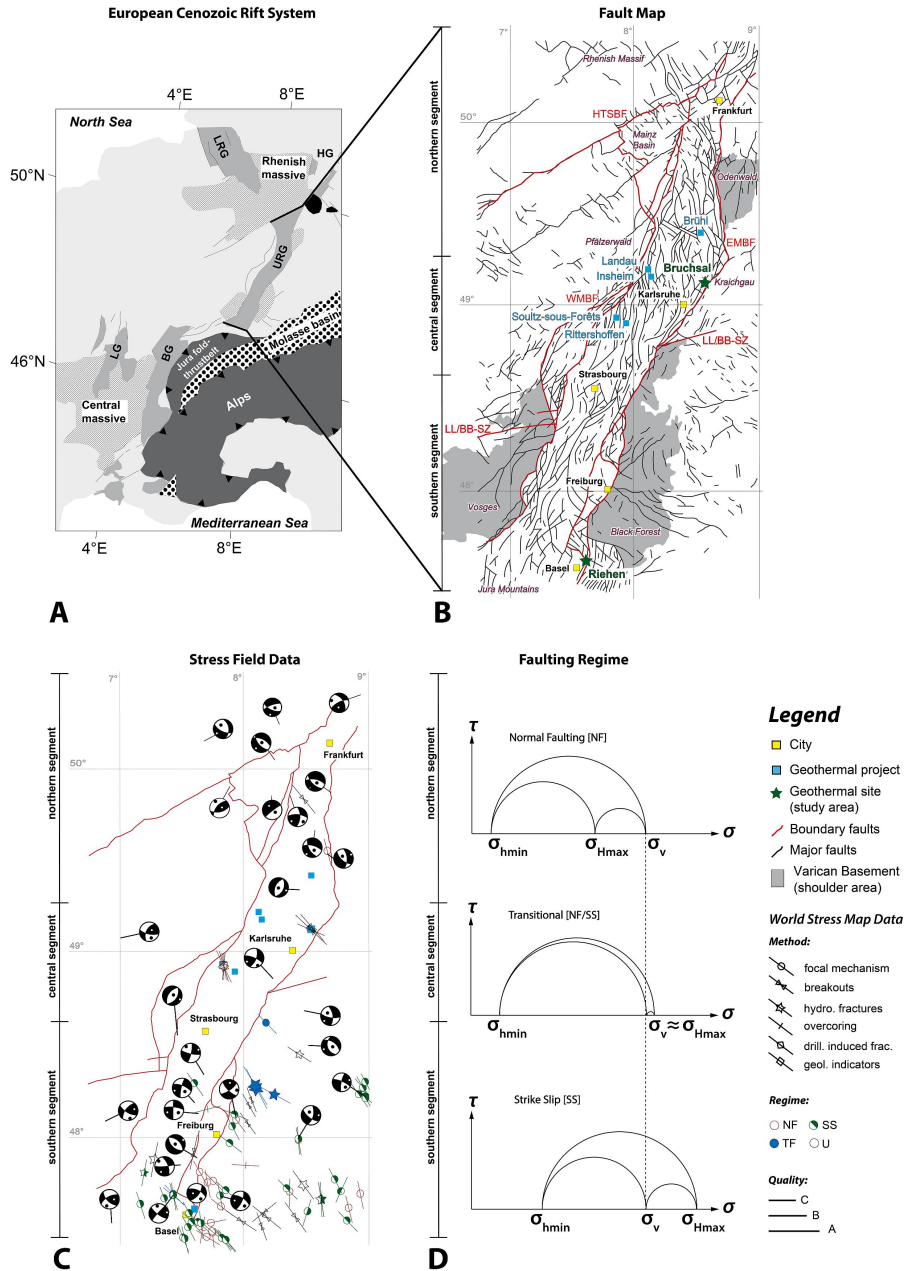


Figure 5.1: Overview maps of the URG incorporating structural and stress relevant data. A) Sketch map of Central European Cenozoic Rift System (modified from Schumacher [2002]). BG: Burgundy Graben, HG: Hessian Graben system, LG: Limagne Graben, LRG: Lower Rhine Graben, URG: Upper Rhine Graben. B) Fault map compilation based on Illies et al. [1979] and Peters and van Balen, R T [2007] showing major fault zones in the URG and the adjacent shoulder areas. The main boundary faults and major shear zones are displayed in red. WMBF: western main boundary fault, EMBF: eastern main boundary fault, LL/BB-SZ: Lalaye-Lubine/Baden-Baden shear zone, HTSBF: Hunsrück-Taunus southern boundary fault. C) Stress field indicators derived from seismological and well test data compiled in the World Stress Map showing a regional NW-SE oriented compressional stress [Heidbach et al., 2008]. D) Variation of the magnitude of the horizontal stress components along the URG axis leading to the different faulting regimes from strike-slip faulting in the southern segment to pure normal faulting in the northern segment.

5.2.2 Structural setting of Bruchsal and Riehen

The Bruchsal and Riehen geothermal doublets are both located close to the EMBF zone in the central and southern segment of the URG (Fig. 5.1), respectively. The doublets consist of graben-parallel arrangements of 1932 m and 1247 m deep injectors (GB1 and RB-2) and 2542 m and 1547 m deep producers (GB2 and RB-1) at Bruchsal and Riehen, respectively. At both sites, production occurs in naturally fractured and non-stimulated reservoirs at a length of 1100 m and 960 m, respectively. The reservoirs are located at depths between 1.1-1.5 km in the Upper Muschelkalk Group [Hauber, 1993] and 1.7-2.5 km in the Buntsandstein Group and the possibly underlying Permian Zechstein Group [Bertleff et al., 1987]. Typical flow rates are about 25 l s⁻¹ in both projects. Reservoir temperature differs between 130°C at Bruchsal [Bertleff et al., 1987] and 66°C at Riehen [Mégel and Rybach, 2000].

Available data in Bruchsal include six analogue, migrated post-stack seismic sections from the early 1980s (processed by Wintershall AG, courtesy of EnBW AG). Five lines (Br8301, Br8302, Br8401, Br8402, KBr8304) were acquired perpendicular to the EMBF zone (Fig. 5.2 A). The graben-parallel seismic line Br8303 was not processed due to a very low signal-noise ratio. Reinterpretation in this study resulted in seven dominant reflectors that were attributed to lithological changes in the Cenozoic graben fill and the Mesozoic successions. Due to limited quality of the processed seismic lines, their vertical resolution is restricted to about 2000 m depth. Additionally, it is significantly impaired in the vicinity of the EMBF zone due to lateral refraction.

Four of the ten boreholes with available stratigraphic information are deeper than 1000 m in the study area. Lithological and stratigraphic logs of all ten boreholes were correlated and unified. Due to completeness, the uppermost five reflectors in the Cenozoic Graben fill, only, can be used to identify and correlate fault traces and formation boundaries. The stratigraphic columns of the wells GB1 and GB2 (modified after Bertleff et al. [1987], Fig. 5.3) were used to verify the fault traces as suggested by the seismic lines.

The geological setting of the Riehen area has been previously described by Schill and Klingler [2011]. It is based on 2D seismic reflection surveys, geological cross-sections, and structural maps [Fischer et al., 1971; Gürlér et al., 1987; Hauber, 1993]. Structural information was also obtained from stratigraphic logs of 14 deep boreholes; including eight boreholes shallower than 1000 m (ALL-1, ALL-2, SLM, STJ, HAL, GRE, BET, and WYL) and six boreholes deeper than 1000 m (RB-1, RB-2, BS-1, OT-2, REI, NEU; Fig. 5.2 B).

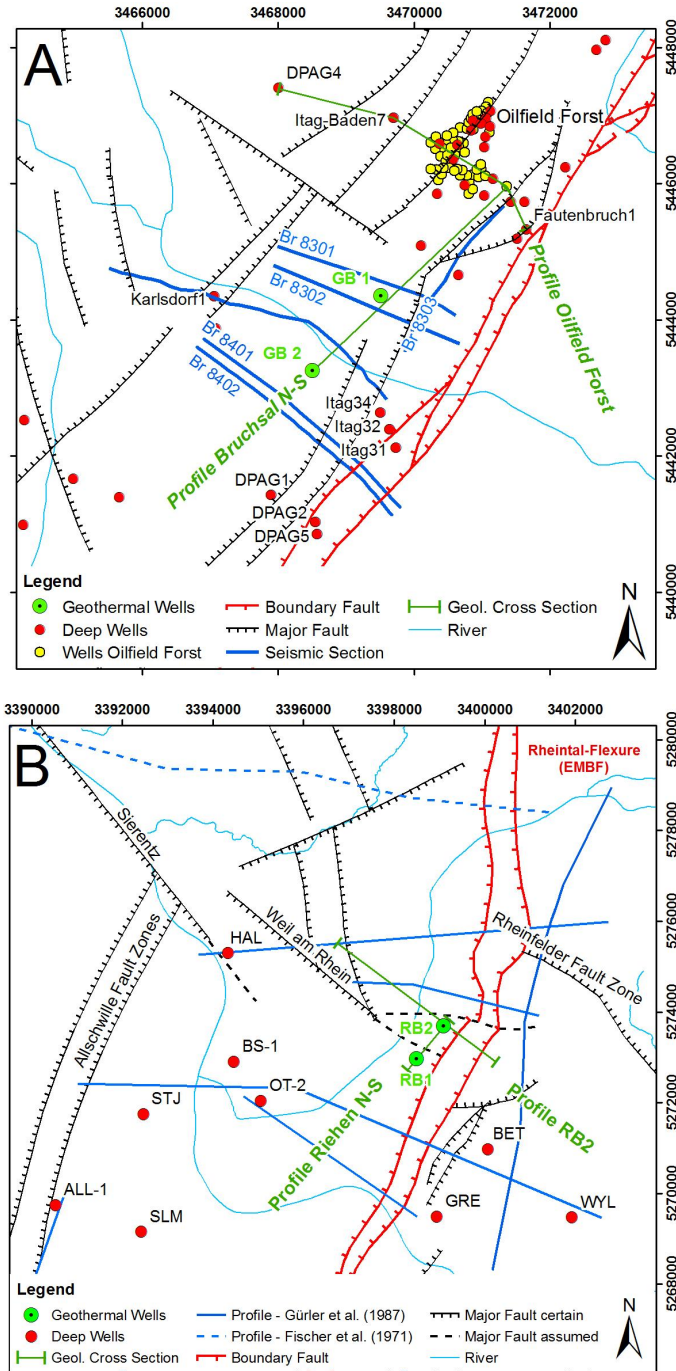


Figure 5.2: Structural overview of the two geothermal sites under study A) Bruchsal and B) Riehen (coordinates: Germany Gauß-Krüger Zone 3), including available data used for 3D structural modeling. The blue lines show the location of 2D seismic-reflection surveys (Bruchsal) and interpreted geological cross-sections (Riehen). EMBF (red lines) and major fault zones (black lines) are obtained from Sauer et al. [1981] for Bruchsal and from Schill and Klingler [2011] for Riehen. Indicated deep wells reach a depth of > 300 m. The green lines show the location of the newly constructed geological cross-sections which are shown in Fig. 5.4-5.5.

Fault structures in the Bruchsal area

At Bruchsal the subsurface is characterized by a complex fault pattern that resulted from the deformation during URG tectonic development. Several fault zones dissect the Mesozoic and Cenozoic successions subdividing them into different fault-bound compartments. The fault pattern is characterized by three structural trends.

- A first EMBF-parallel set includes NNE-SSW striking faults with an average dip to W-NW. These faults show an en-echelon geometry along strike and are synthetic to the EMBF (Fig. 5.4). With an average dip of 60-80°, these faults accommodate the majority of the bulk displacement of about 2000 m during the main rifting phase. Termination of this main normal faulting phase is indicated by post-faulting coverage with Early to Middle Miocene sediments in this part of the URG (Fig. 5.3).
- A second set of faults comprises NE-SW to N-S striking antithetic normal faults. These antithetic normal faults can be divided in two sub-groups. In the southern part (Br8401, Br8402), they are confined to the Mesozoic sedimentary successions (Fig. 5.4 C). In the northern part (Br8301, Br8302, Oilfield Forst) several of them also cut the Cenozoic sequences (Fig. 5.4 A and Fig. 5.4 B). Latest fault activity is visible as a seismic reflector interpreted as the Lower Miocene Corbicula beds. The evolution of these antithetic fault zones seems to be kinematically linked to the EMBF -parallel fault set. In the area of GB1 and GB2, all antithetic normal faults join with the westernmost EMBF-parallel, synthetic normal fault at different depths.
- A third set of NW-SE striking faults is postulated to accommodate the observed and significant vertical offset of about 500 m between the Mesozoic sedimentary successions in the northern and the southern part of the study area. As documented in the seismic sections and the stratigraphic well logs, the top of the Buntsandstein Group is located at about 1685 m (GB1) in the north and 2220 m (GB2) in the south (Fig. 5.3). This discrepancy is only partly explained by the 200 m larger distance to the EMBF zone of GB2 compared GB1. Only a structural separation of both parts caused by extension-related transfer faults or preexisting and reactivated strike-slip faults can accommodate these discrepancies. Such a structure with similar offset has been described by Wirth [1962] and Bertleff et al. [1987] south of the Forst oil field (Fig. 5.2 A, Fig. 5.4 D). Furthermore, indication of a comparable NW-SE trending fault zone is also provided by analysis of slickenlines in a former Muschelkalk quarry on the graben shoulder NE of Bruchsal [Illies, 1962].

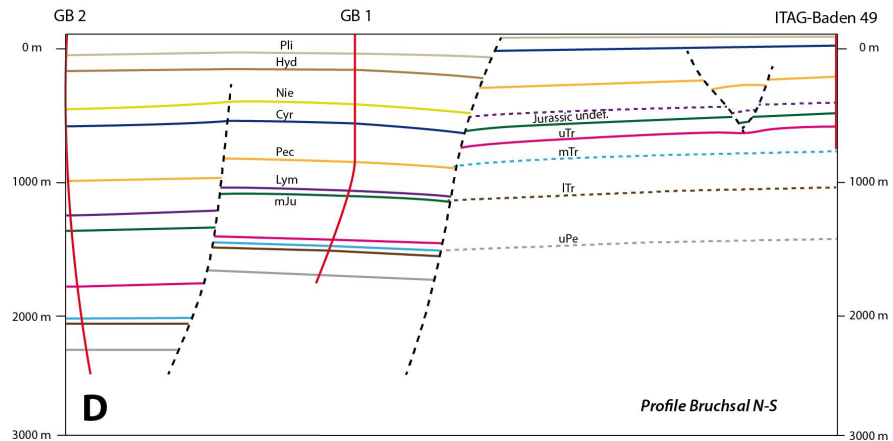
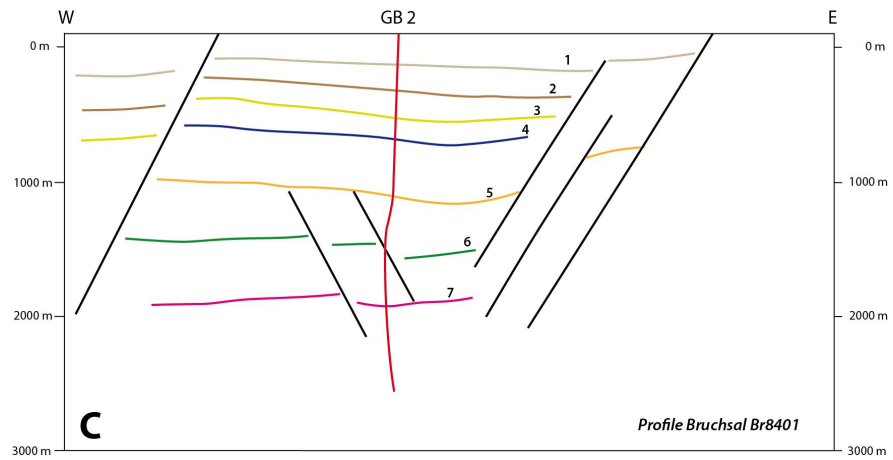


Figure 5.4: Structural setting in the Bruchsal area presented by geological cross-sections in E-W direction close to the Oilfield Forst (A), the injection well GB1 (B), the production well GB2 (C). Position and geometry of the faults has been inferred for GB1 and GB2 from 2D seismic data. The Oilfield Forst profile is based on stratigraphic well log data and is modified after Wirth [1962]. The geological cross-section in N-S direction show position of the assumed high angle transfer faults. Localization of the profiles are shown in Fig 5.2 A. Nomenclature of the identified seismic reflectors and the corresponding formations boundaries are summarized in Fig. 5.3.

Fault structures in the Riehen area

The structural setting of the Riehen area is characterized by a complex tectonic evolution from Late Eocene rift opening to Late Miocene - Early Pliocene Jura folding that originated in a zone of structural weakness of the Central European lithosphere [Ziegler, 1992]. Re-activations of the EMBF zone in the Miocene under a compressional stress state caused flexuring and associated back-folding of the graben fill and initiated the development of antithetic faults and overturned beds close to the EMBF zone ([Laubscher, 2001]; Fig. 5.5 A and 5.5 B). The mean strike of the EMBF zone north of Riehen is N-S; to the south it changes to NNE-SSW (Fig. 5.2 B). This structural change is related to an intersection of two major fault trends in this region. The geothermal wells RB-1 and RB-2 are aligned along this structural change of the EMBF zone and probably are separated by a NW striking fault (Fig. 5.5 C). Predominant fault trends constitute a distinctive fault pattern, which can be subdivided into three different fault sets.

- A first fault set is characterized by an average NW-SE strike (fault zones of *Sierentz*, *Weil am Rhein*, and *Rheinfelden* - Fig. 5.2 B). This structural trend was established in Palaeozoic times in the course of the Variscan orogeny [Schumacher, 2002].
- A second fault set contains Late Palaeozoic E-W to ENE-WSW striking, high-angle basement faults [Ustaszewski, 2004]. This trend is related to post-Variscan wrench tectonics that formed a system of E-W to ENE-WSW striking Permo-Carboniferous troughs and highs, which followed the general structural (E)NE-(W)SW trend of the Variscan orogen [Ziegler, 1990a].
- Late Eocene to Late Oligocene E-W to WSW-ENE extension [Lar-roque and Laurent, 1988; Ustaszewski, 2004] caused reactivation of the pre-existing crustal discontinuities and established a third fault set of graben-parallel N-S to NNE-SSE striking faults (fault zones of *Allschwil* and *Basel-Reinach* - Fig. 5.2 B). Most of these faults in the Riehen area are associated with the EMBF zone, which is called *Rheintal-flexure* in that area [Laubscher, 2001], outlining an average dip of about 65-70° to the west.

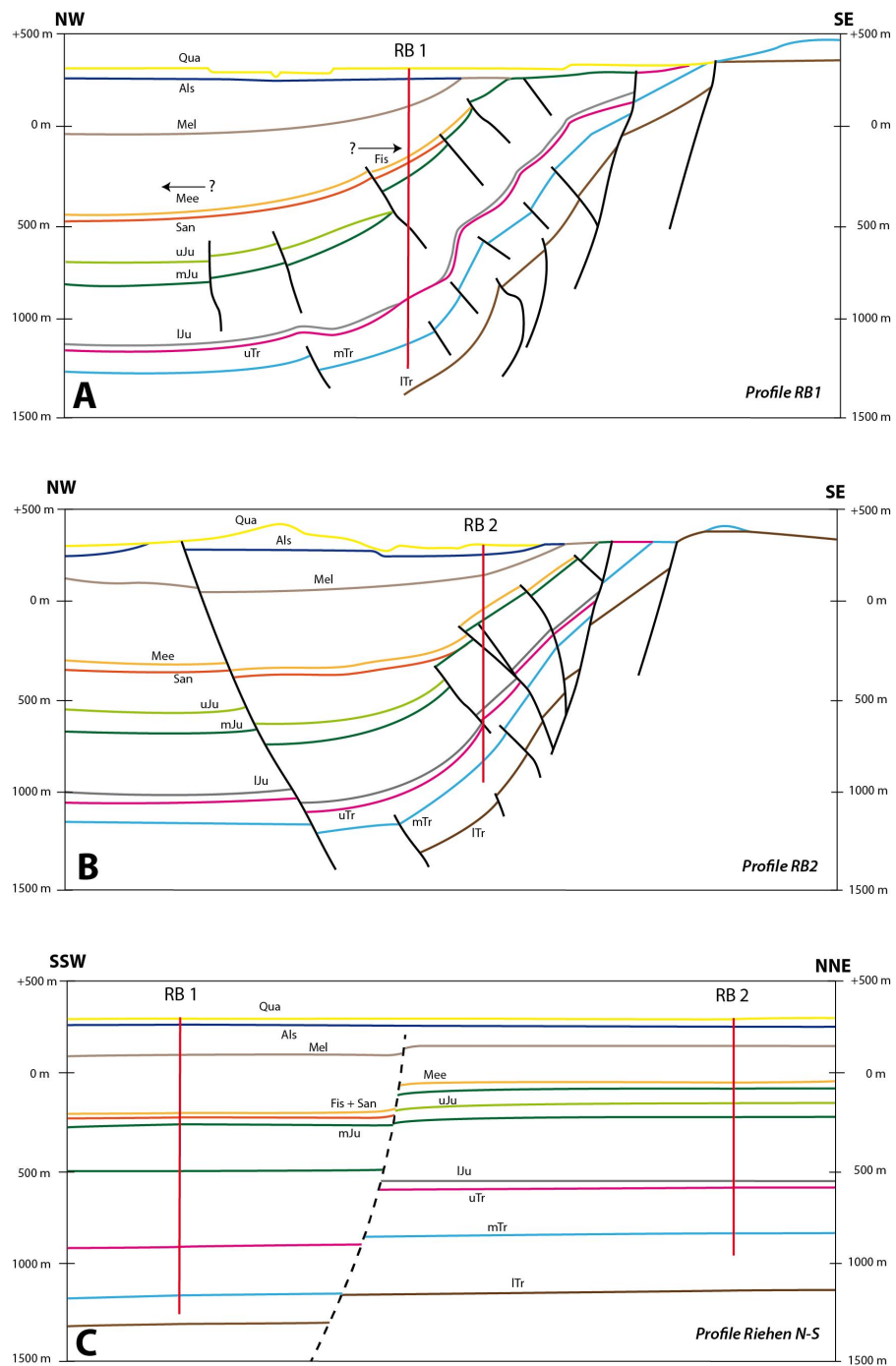


Figure 5.5: Structural setting in the Riehen area presented by geological cross-sections in E-W direction close to the production well RB1 (A) and the injection well RB2 (B, modified after Gürler et al. [1987]). The cross-section in N-S direction (C) show the position of the transfer fault which is assumed to be located between the geothermal wells and may explain the observed vertical displacements of the sedimentary succession as recorded in the stratigraphic well log. Localization of the profiles are shown in Fig 5.2 B. Nomenclature of the stratigraphic formations are summarized in Fig. 5.3.

5.2.3 Stress states

Mean $S_{H_{max}}$ orientation of $N142^{\circ}E \pm 20^{\circ}$ is based on borehole breakout analysis on oriented caliper logs [Eisbacher et al., 1989a], internal report of EnBW AG). A stress field model for the Bruchsal area at reservoir depth was suggested by Meixner et al. [2014] with the following stress gradients:

$$\begin{aligned} S_v &= 23.8 \text{ MPa km}^{-1} \\ S_{h_{min}} &= 13.2 \text{ MPa km}^{-1} \\ S_{h_{min}} &\leq S_{H_{max}} \geq S_v \\ P_p &= 10.2 \text{ MPa km}^{-1} \end{aligned}$$

The revised stress field model for the Bruchsal area predicts, due to the uncertainty of $S_{H_{max}}$, a potential faulting regime ranging from radial extension to the transition of normal faulting and strike-slip faulting. Geologically, a radial extensional stress state ($S_{h_{min}} = S_{H_{max}}$) seems to be questionable for the central URG. Hence, we calculate the slip- and dilation tendency only for a pure normal faulting ($S_{H_{max}} = 0.76 S_v$) and the most likely transitional faulting regime ($S_{H_{max}} = S_v$).

Although no in-situ stress measurements are available from the wells RB-1 and RB-2 in Riehen, constraints have been adopted from previous analysis of the 5000 m deep BS-1 and 2755 m deep OT-2 wells located about 3 km distance from the Riehen site (Fig. 5.2 B). The $S_{H_{max}}$ and $S_{h_{min}}$ orientation were determined by Häring et al. [2008], Valley and Evans [2009], and Sikaneta and Evans [2012] from analysis of borehole breakouts and drilling-induced tensile fractures (DITFs). The borehole breakouts and DITFs indicate a mean $S_{H_{max}}$ orientation of $N144^{\circ}E \pm 14^{\circ}$ and in a depth range between 2569 and 4992 m in BS-1. Similar values from OT-2 basement section indicate stable $S_{H_{max}}$ orientation in the granitic basement at depth > 2500 m. An estimate of the stress magnitudes of $S_{H_{max}}$, $S_{h_{min}}$, and S_v is given by Häring et al. [2008]:

$$\begin{aligned} S_v &= 24.9 \text{ MPa km}^{-1} \\ S_{h_{min}} &= 17.1 \text{ MPa km}^{-1} \\ S_{H_{max}} &= 32.6 \text{ MPa km}^{-1} \end{aligned}$$

Similar to Bruchsal, the lower bound estimate of $S_{H_{max}}$ magnitude was obtained by application of the critical stress concept. It should be noted that, here, a friction coefficient of $\mu = 0.6$ has been applied based on laboratory measurements of core samples [Häring et al., 2008]. Assuming a homogeneous stress state in the area, we infer

pure strike-slip faulting regime for Riehen. Pore pressure, P_p , was calculated using fluid density of 1010 kg m^{-3} [Hauber, 1993] resulting in pore pressure gradient of 9.91 MPa km^{-1} . The hydrothermal reservoir in Riehen is characterized by slight artesian conditions with $0.15\text{-}0.25 \text{ MPa}$ overpressure in RB-2 and RB-1, respectively. Thus, a mean hydrostatic overpressure of 0.2 MPa is taken into account.

5.3 FAULT MODELING

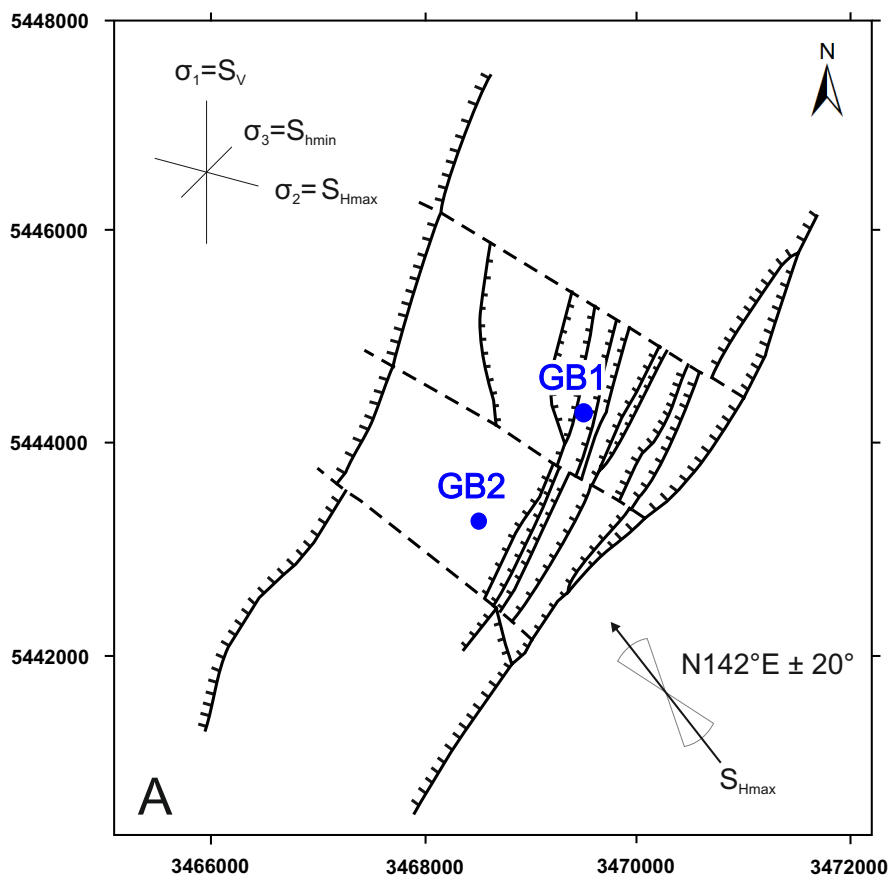
5.3.1 Slip- and dilation tendency

Slip tendency analysis is appropriate to determine reactivation potential of fractures and faults under given stress condition [Worum et al., 2004, 2005; Collettini and Trippetta, 2007]. At reservoir scale, it has been used in the past to link reactivation of faults with observed induced seismicity during hydraulic stimulation [Moeck et al., 2009]. Generally, slip is likely to occur on a surface for which effective shear stress (σ_τ) equals or exceeds the frictional resistance to sliding. The frictional resistance is proportional to the effective normal stress (σ_n), resolved across that shear plane. Slip tendency, T_S , is the ratio between the effective shear stress and the effective normal stress [Morris et al., 1996]. Whether a surface may slip depends on its cohesive strength (c) and the coefficient of static friction (μ). For a pre-existing surface cohesion may be neglected. In this case, T_S equals μ . Dilation tendency, T_D , is the relative probability for a fracture or a fault plane to dilate under the local stress field [Ferrill et al., 1999]. T_D is defined as the difference between the maximum principal compressive stress (σ_1) and the normal stress (σ_n), normalized by the differential stress ($\sigma_1 - \sigma_3$) and thus ranges between 0 ($\sigma_1 = \sigma_n$) and 1 ($\sigma_3 = \sigma_n$). Our calculations are based on 3D structural models of the two geothermal sites under study. For structural modelling, the *Corner Point Gridding* workflow implemented in Petrel® software (Schlumberger) has been used. The fault models were meshed into regular triangles (fault patches) using the *Structural Framework* tool. Finally, T_S and T_D are calculated with the software 3Dstress® for each fault patch. The results are plotted as stereonet projection in the lower hemisphere and additionally visualized on the 3D fault models.

5.3.2 Model geometry

A representative geometry of the faults in the two geothermal sites under study is shown in a horizontal cross-section at depth of 1000 m below sea level (Fig. 5.6). At Bruchsal, the 3D fault model covers an area of 18 km^2 and extends to a depth of 3 km below sea level. The

structural units incorporating the reservoir are bound by four major fault systems: the EMBF zone in the SE, a large regional normal fault zone in the NW, dipping to the W with a total vertical displacement of about 600 m, and two NW-SE striking faults in the NE and SW. The model includes a total of 29 faults that can be attributed to the different fault sets described in section 5.2.2: 18 faults within an overall fault area of about 104 km² are attributed to the EMBF-like set. The 2nd and 3rd fault set incorporates 7 and 4 faults with an overall area of about 9 km² and 30 km², respectively. The latter represents 20% of the total fault surface. The two wells are aligned parallel to the EMBF and separated by a NW-SE striking, most probably oblique normal fault with a vertical offset of about 500 m (fault set 3). The structural model of Riehen covers 10x10x6 km³. Comparable to the Bruchsal site, the tectonic units that incorporate the reservoir of Riehen are bound by the EMBF zone to the E and by a steep oblique normal fault to the SW. As observed in Bruchsal, the two wells are aligned parallel to the EMBF zone and are separated by a NW-SE striking, most probably oblique normal fault with an unknown offset.



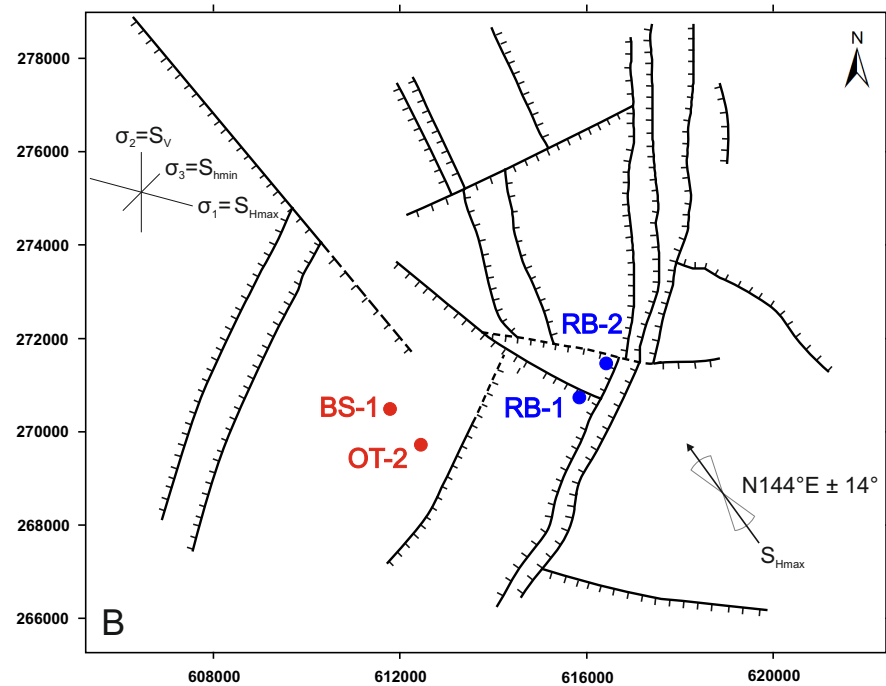


Figure 5.6: Fault pattern around the geothermal sites of Bruchsal (A) and Riehen (B) at a depth of 1000 m below sea level based on 3D fault models from 2D seismic sections, geological cross sections and deep well data (see Fig. 5.2). Dashed lines represent fault zones that are postulated by geological indications such as vertical displacements and stratigraphic and lithological well log variations.

5.4 RESULTS

In the following, we present T_S and T_D analyses of the two case geothermal projects, Riehen and Bruchsal. We performed the analysis in pure normal faulting and transitional normal faulting to strike-slip regimes for Bruchsal and in pure strike-slip regime for Riehen due to the range of valid magnitude ratios of the horizontal stress components according to the critical stress concept [Meixner et al., 2014].

5.4.1 Normal faulting and normal faulting/strike-slip regimes in Bruchsal

The results for the transitional model are shown in Fig. 5.7. Since S_{Hmax} ($N142^\circ E$) is orthogonal to the orientation of the URG, graben-parallel faults show generally low values and little variability of slip and dilation tendencies (Fig. 5.7 A and 5.7 B). Maximum slip tendency of $T_S = 0.85$ is obtained for faults dipping 60° to 70° to the NE or SW. Maximum dilation tendency of $T_D = 1.0$ is obtained for vertical faults striking parallel to S_{Hmax} . Although not observed, it should be mentioned that, for this stress state,

vertical fault segments with orientation parallel to S_{Hmax} may show minimum slip and maximum dilation tendencies. The NW-SE striking transfer faults inferred from geological constraints reveal both, high T_S and T_D values up to 0.85 and 0.97, respectively (Fig. 5.7 C and 5.7 D). The distribution of T_S and T_D is given in Fig. 5.7 E and 5.7 F. It reveals a bimodal distribution of both parameters. About 60% of the total fault surface have T_S between approximately 0 and 0.5, whereas about 20% have T_S around 0.8. A comparable pattern is observed for T_D , with about 50% of the total fault area showing values < 0.2 and 20% showing values between 0.8 and 1.0. Despite uncertainties in the fault geometry or the stress field characterization, anisotropy of both T_S and T_D is observed.

In a pure normal faulting regime (Fig. 5.8), T_S for different fault orientations is rather uniform. Almost 90% of the total fault surface in Bruchsal has T_S values between 0.2 and 0.5. In contrast to the bimodal distribution observed under transitional stress state, T_S values cluster around a single maximum between 0.3 and 0.4. Additionally, compared to the transitional stress state, transfer faults exhibit the highest dilation tendencies > 0.9 .

So, regardless of the faulting regime, T_D is highly anisotropic exhibiting large variation between transfer faults and the rest of the faults. In contrast, anisotropy of T_S , between transfer faults and the rest of the faults, increases when the stress state changes from the normal to the normal faulting/strike-slip regime. Since the stress ratio σ_1/σ_3 is constant in the considered stress field models, the large range of valid S_{Hmax} magnitudes is responsible for this observed increase. It is noteworthy that transfer faults are always favorably orientated for tensile failure, but shear reactivation would most likely happen under a normal faulting/strike-slip stress state, only.

5.4.2 Strike-slip regime in Riehen

The results for the pure strike-slip regime in Riehen are shown in Fig. 5.9. Here, highest T_S of 0.6 are calculated for conjugated fault segments that are aligned 30° from S_{Hmax} orientation of $N144^\circ E$ (Fig. 5.9 A). The majority of the modeled fault segments, striking E-W or N-S, have the largest slip tendencies, whereas segments striking NW-SE or NE-SW have the smallest slip tendencies (Fig. 5.9 C). About 70% of the total fault area has T_S values between 0.4 and the maximum of 0.6 (Fig. 5.9 E). Largest T_D values between 0.9 and 1.0 are observed for fault segments striking NW-SE with dip larger than 70° (Fig. 5.9 B and 5.9 D). For the entire set of modeled faults, however, rather homogeneously distributed T_D values from 0 to 1.0 occur (Fig. 5.9 F).

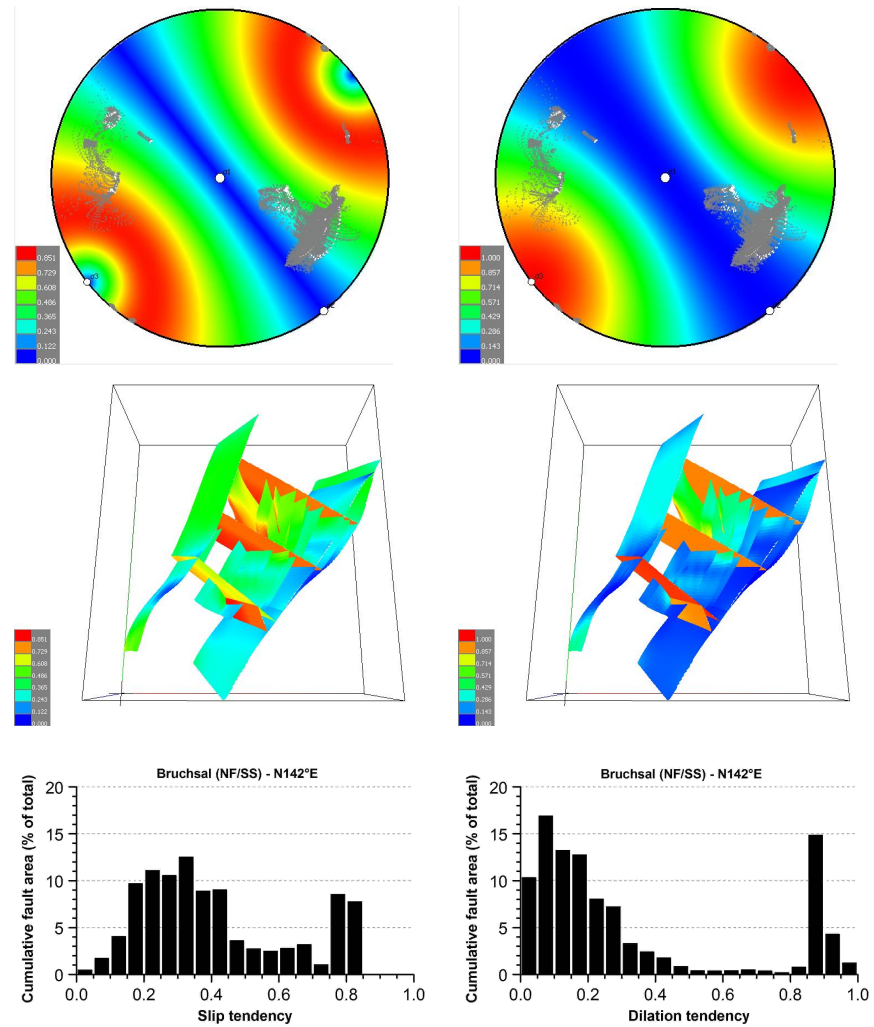


Figure 5.7: Slip tendency (left column) and dilation tendency (right column) for Bruchsal under transitional faulting regime (normal faulting/strike-slip). The first row shows stereonet projections of the tendency values (calculated at 2000 m) overlaid by the Bruchsal fault patch poles. The second row shows 3D views (oblique top view from south) of the tendency distributions over the Bruchsal fault pattern. The third row shows the percentage of the cumulative fault areas affected by the tendency value in 0.05 intervals.

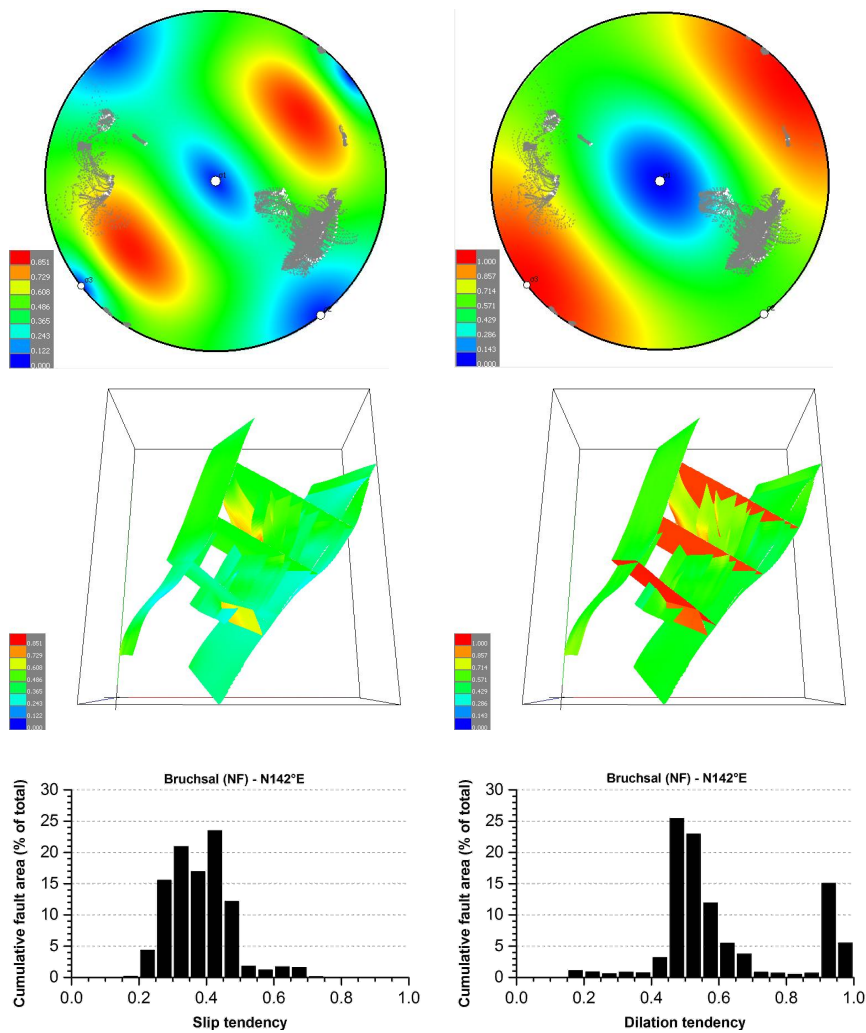


Figure 5.8: Slip tendency (left column) and dilation tendency (right column) for Bruchsal under normal faulting regime. The first row shows stereonet projections of the tendency values (calculated at 2000 m) overlaid by the Bruchsal fault patch poles. The second row shows 3D views (oblique top view from south) of the tendency distributions over the Bruchsal fault pattern. The third row shows the percentage of the cumulative fault areas affected by the tendency value in 0.05 intervals.

In contrast to a pure normal faulting regime, where maximum T_S depends on the dip of the fault, in the strike-slip regime, vertical faults that strike parallel to $S_{H_{max}}$ never reach the maximum T_S . Thus, they are comparably less prone for shear failure in a strike-slip regime. Similar to a normal faulting regime, vertical fault segments that are parallel to $S_{H_{max}}$ show $T_S = 0$ and $T_D = 1.0$ and show therefore no reactivation potential in shear failure. The group of NW-SE striking Sierentz, Weil am Rhein, and Rheinfeld fault zones as well as the assumed fault intersection between the two geothermal wells RB-1 and RB-2 approaches this optimal combination of T_S and T_D .

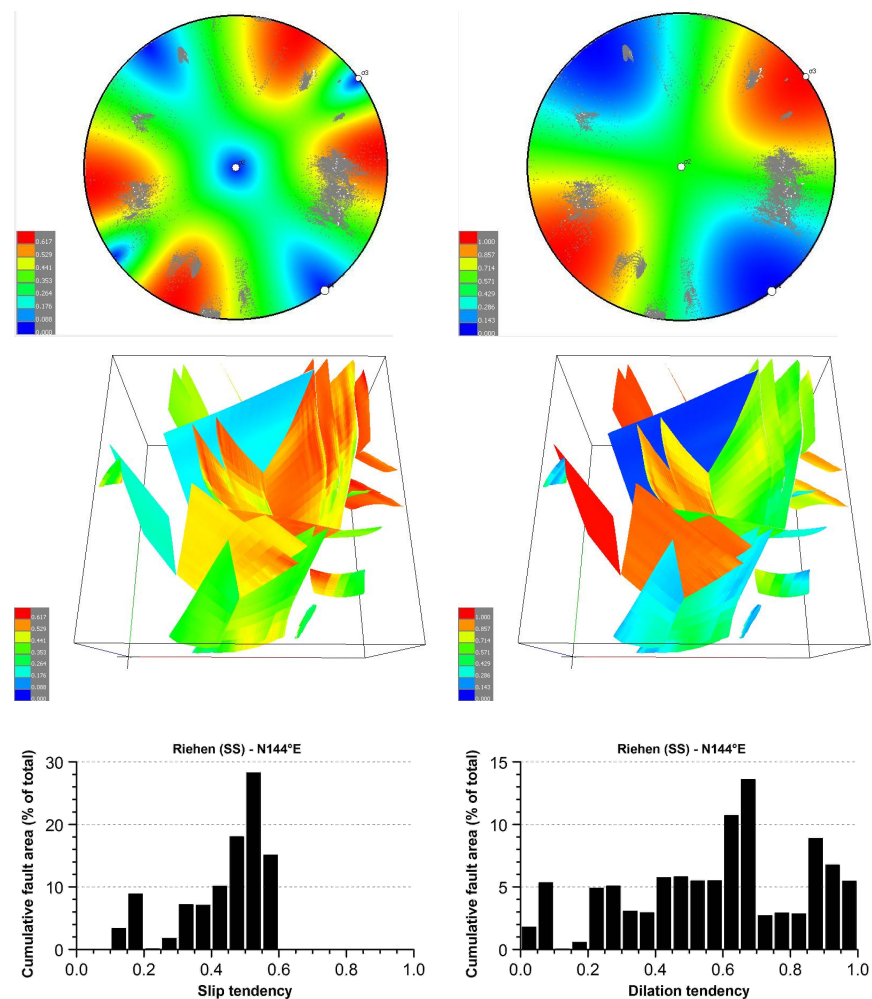


Figure 5.9: Slip tendency (left column) and dilation tendency (right column) for Riehen under strike-slip faulting regime. The first row shows stereonet projections of the tendency values (calculated at 2500 m) overlaid by the Riehen fault patch poles. The second row shows 3D views (oblique top view from south) of the tendency distributions over the Riehen fault pattern. The third row shows the percentage of the cumulative fault areas affected by tendency value intervals of 0.05.

5.5 SENSITIVITY OF T_S AND T_D WITH RESPECT TO THE S_{Hmax} ORIENTATION

The results of T_S and T_D analyses depend on the accuracy of the stress field orientation and the fault geometries. Absolute uncertainties introduced by input data are difficult to assess. However, relative uncertainties of geological models are often enhanced at crossing points of faults [Wellmann et al., 2010]. Against this background, we may assume that the orientation of the majority of the fault zone patches is characterized by low uncertainty.

Uncertainties in stress field orientation are well-quantified with $\pm 14^\circ$ and $\pm 20^\circ$ for the mean S_{Hmax} orientations in Riehen and Bruchsal, respectively. In the following, we will discuss the effect of uncertainty in the orientation S_{Hmax} on our analyses. It is noteworthy that variation of fault geometry may further increase the uncertainty of our results. However, such an analysis is beyond the scope of this paper.

For the Bruchsal fault model, we determined T_S and T_D for the given uncertainty range of S_{Hmax} from $N122^\circ E$ to $N162^\circ E$ in normal faulting and normal faulting/strike-slip regimes (Fig. 5.10). We present the percentage of the cumulative area of fault patches (over the whole 143 km^2 of fault surface) affected by different T_S and T_D intervals. For both, normal faulting and normal faulting/strike-slip faulting regimes, the rotation of the S_{Hmax} from $N122^\circ E$ to $N162^\circ E$ leads to a gradual increase of T_S on the majority of the fault patches (Fig. 5.10 A and 5.10 C). Hence, from unlikely shear reactivation, most of the fault surfaces can shift towards a range of possible shear reactivation. This is due to the fact that the associated fault patches become subparallel to S_{Hmax} for an orientation of $N162^\circ E$. In the range of the S_{Hmax} from $N122^\circ E$ to $N162^\circ E$, T_D distribution develops from bi-modal distribution to a single cluster for both stress regimes (Fig. 5.10 B and 5.10 D). The variation of S_{Hmax} in its uncertainty range has little influence on the T_D of potential transfer faults ($0.8 < T_D < 1.0$). The highest T_D of 1.0 is observed for transfer fault strikes close to S_{Hmax} . Additionally, increasing S_{Hmax} azimuth leads to an increase in T_D for the graben-parallel faults in the Bruchsal area.

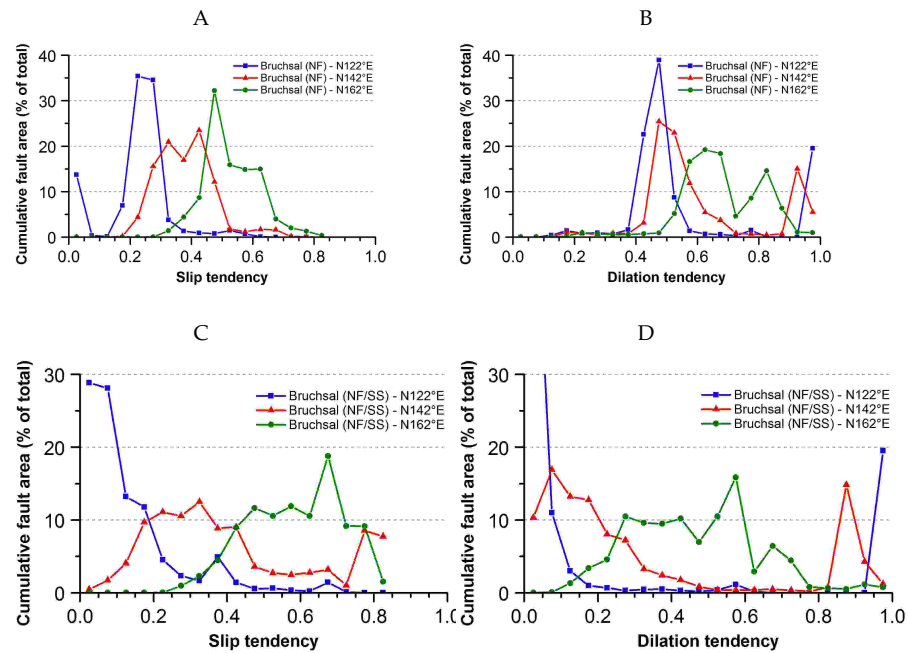


Figure 5.10: Uncertainty analysis of T_S and T_D with respect to variations of the stress field orientation in Bruchsal. Comparison of the cumulative fault areas exposed to slip tendency (A and C) and dilation tendency (B and D) intervals, each calculated for a normal faulting (A and B) and a transitional normal faulting to strike-slip regime (C and D).

Significant influence on both T_D and T_S with respect to the total fault surface of the Riehen model is not observed for clockwise rotation of mean S_{Hmax} ($N144^\circ E$) to $N158^\circ E$ (Fig. 5.11). The highest T_S values of 0.45-0.6 apply for about 70% of the total fault area in both cases. In contrast, anticlockwise rotation to $N130^\circ E$ substantially decreases the fault surfaces affected by the maximum T_S value of 0.45-0.6. In the latter case, the affected fault area is reduced to about 35% of the total amount. Variations of S_{Hmax} in the given uncertainty range cause only minor changes in the T_D distribution; about 10% of the total fault area show values between 0.9 and 1.0.

For the entire ranges of T_S and T_D , we observe different sensitivity to variation of S_{Hmax} azimuth for the entire fault models of Bruchsal and Riehen. Comparably smaller sensitivity is observed in T_S for the Riehen model. Different aspects may account for this fact: 1) the fault model of Riehen incorporates a much larger fault surface area (388 km^2) and a broader range of fault azimuths; 2) different faulting regimes lead to significantly different distribution of critical condition. Conjugated shear angles in pure strike-slip regime predict four favorable fault geometries (two optimal fault strikes with two dip directions each), whereas

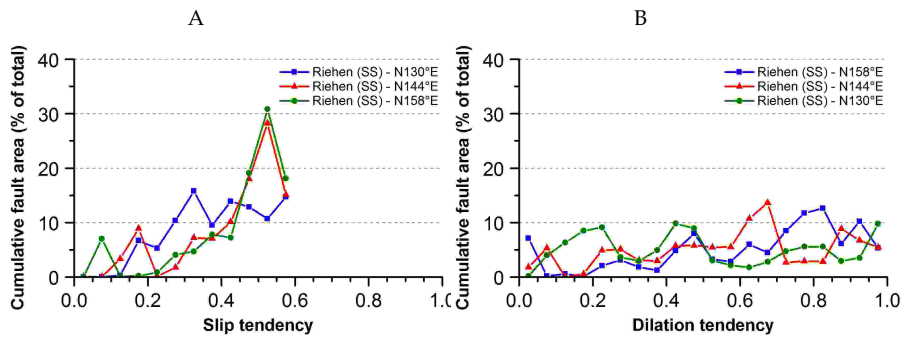


Figure 5.11: Uncertainty analysis of T_S and T_D with respect to variations of the stress field orientation in Riehen. Comparison of the cumulative fault area exposed to slip tendency (A) and dilation tendency (B) intervals in a pure strike-slip faulting regime.

in normal faulting regime two optimal fault geometries, only, exist (one favorable fault strike with two dip directions). Thus, the probability of hitting a fault with maximum T_S is higher in large structural models and for a pure strike-slip faulting regime.

In the following, we consider fault sensitivities to T_S and T_D ranges that are the closest to critical condition and reactivation (Table 5.1): $T_S = 0.65-0.85$ for Bruchsal, $T_S = 0.45-0.6$ for Riehen, and $T_D = 0.8-1.0$ for both models. As shown previously, T_S is most sensitive to changes in S_{Hmax} (within the given uncertainty range). Anticlockwise rotation of S_{Hmax} reduces the amount of fault patches within the nearly critical stress range to nearly zero in Bruchsal and from about 2/3 to 1/3 in Riehen. Since the majority of the fault patches in Bruchsal are subparallel to the strike of the URG, clockwise rotation of S_{Hmax} causes maximum alignment with these structures and therefore decreases criticality of the transfer faults. As mentioned above, in Riehen criticality is given for a large range of S_{Hmax} due to the conjugated shear angles causing four T_S maxima.

T_D of the NW-SE striking structures are relatively invariable for changes in S_{Hmax} within the given uncertainty ranges. Generally, about 20-30% of the fault patches are within the critical range of T_D . Structures striking subparallel to the URG, however, show an increase in T_D with increasing S_{Hmax} .

Table 5.1: Compilation of the cumulative fault areas exposed to maximum T_S values of 0.65-0.85 in Bruchsal and 0.45-0.6 in Riehen and maximum T_D values of 0.8-1.0 with respect to variations of S_{Hmax} orientation.

Site	Regime	Tendency	N122°E	N142°E	N162°E
<i>Bruchsal</i>					
	NF	T_S	1.5%	20.4%	38.6%
	NF	T_D	19.5%	21.1%	3.0%
	NF/SS	T_S	0%	1.7%	7.6%
	NF/SS	T_D	19.5%	21.7%	23.0%
<i>Riehen</i>					
	SS	T_S	38.3%	61.3%	68.0%
	SS	T_D	21.8%	23.9%	37.2%

NF: normal faulting, SS: strike-slip

5.6 GEOMECHANICAL INTERPRETATION

5.6.1 Absence of critically stressed faults

As described in section 5.2.2, the stress field models were determined using the critical stress concept [Zoback et al., 2003], which defines constant σ_1/σ_3 stress ratios based on friction coefficients of 0.85 for Bruchsal and 0.6 for Riehen. Since the critical stress concept and the slip tendency analysis are based on the same Mohr-Coulomb failure criterion, maximum T_S values always equal μ . Thus, regardless of the difference of the stress state between Bruchsal and Riehen, the maximum slip tendency values are 0.85 and 0.6, respectively. Variations of μ may change the magnitudes of T_S , but its relative distribution remains unaffected. Hence, only a comparison of the relative distribution of T_S and T_D between the two sites is meaningful.

Furthermore, since critically stressed fault or fracture zones are characterized by exceeding a defined Mohr-Coulomb failure criterion, they cannot be obtained in our slip tendency analysis. However, fluid flow in fractured reservoirs often occurs only on critically stressed zones [e.g. Barton et al., 1995; Ito and Zoback, 2000]. Since by definition critically stressed faults cannot be computed in our approach, we assume that those close to critical stress condition shift to critical if the σ_1/σ_3 stress ratio exceeds our assumptions.

5.6.2 Anisotropy of the Slip- and Dilation Tendency

As observed previously, T_S and T_D of fault segments strongly depend on their strike. We investigate here this dependency. In addition to the results of both geothermal fields, we performed this analysis for sets of generic normal and strike-slip faults modeled under Bruchsal and Riehen stress states. These modeled faults allow us to cover the full range of fault azimuth and can provide an overview of any potential fault behavior in the URG. Since for a given azimuth T_S and T_D depend on the dip and depth of the fault, 70° dipping normal faults and vertical strike-slip faults are considered and analyzed for the representative depths of 2000 m and 2500 m in Bruchsal and Riehen, respectively (Fig. 5.12).

We observe at both sites a similar behavior of T_S and T_D for fault azimuths between about 0° and 100° . For these structures, critical conditions are not observed and lowest values for both, T_D and T_S , occur at S_{Hmin} azimuth. Between 110° and 170° , normal faulting and normal faulting/strike-slip regime at Bruchsal exhibit parallel trends for T_D and T_S for normal faults with maximum values at S_{Hmax} azimuth. In contrast, for strike-slip faults, T_D has its maximum at S_{Hmax} , while T_S is equal to 0. In the strike-slip regime of Riehen, maximum T_S and T_D cannot coexist. Maximum T_D coincides always with minimum T_S . At S_{Hmax} azimuth, minima of $T_S = 0.35$ and $T_S = 0$ are observed for normal and strike-slip faults, respectively.

These results indicate that faults trending parallel to the URG are characterized by low reactivation potential for shear and tensile failure. In contrast, the geomechanical behavior of transfer faults depends strongly on their dip. Independent of the stress field, sub-vertical faults with this azimuth cannot be reactivated for shearing in any case. These structures, however, always show highest reactivation potential for tensile failure. Inclined transfer faults striking sub-parallel to S_{Hmax} azimuth exhibit highest potential for shear reactivation in normal faulting regimes.

We would like to point out that according to our results, the steeply dipping faults, which are assumed to be located between the injection and production wells, at Riehen and Bruchsal, have the largest tendency among all model faults to dilate in the related ambient stress fields.

Recalling that in both case studies no immediate connection between the production and the injection wells during tracer experiment was observed [Schill and Klingler, 2011], we may suppose that these steeply dipping faults act as hydraulic boundaries. Such bound-

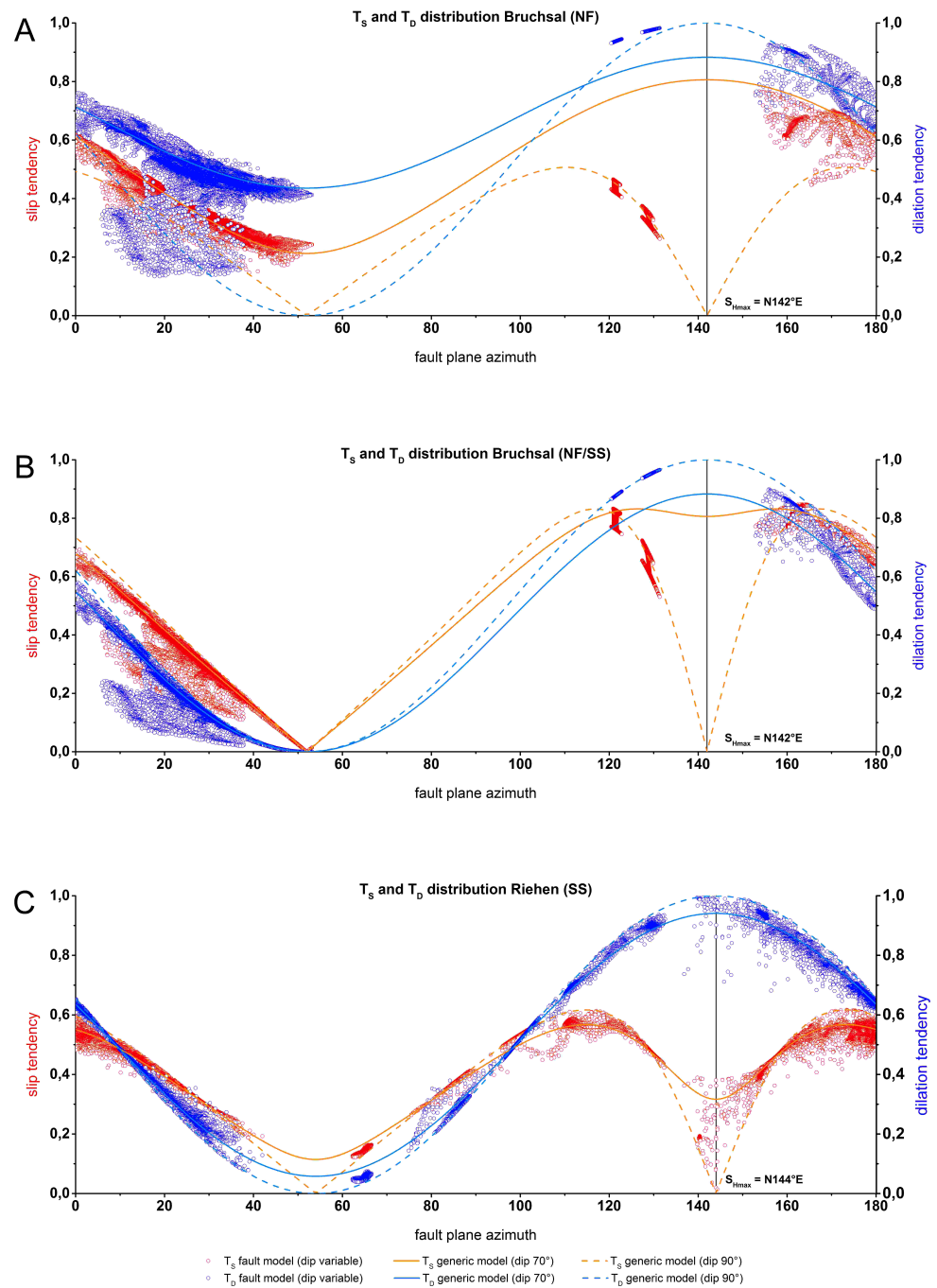


Figure 5.12: Distribution of the slip tendency (T_S , red) and dilation tendency (T_D , blue) as a function of the fault plane azimuth, for the Bruchsal fault model under normal faulting regime (A) and under transitional regime (normal faulting/strike-slip; B), and for the Riehen fault model under strike-slip regime (C). Dots correspond to single fault patches of the corresponding fault model. Lines represent T_S and T_D of generic normal and strike-slip faults dipping 70° and 90°, respectively. Generic T_S and T_D are calculated for depth of 2000 m and 2500 m in Bruchsal and in Riehen, respectively.

aries may be characterized either by low or by high permeability, but according to the observed high dilation tendencies, high fracture permeability is more likely. This is especially the case for comparably shallow reservoirs, since maximum T_D increases with decreasing depth. The fact that these structures are characterized by low shear reactivation potential may explain the absence of induced seismicity during reservoir operation [e. g. [Gaucher et al., 2015](#)].

5.7 CONCLUSION

Although located both at the EMBF zone of the URG, the overall tectonic setting, orientation and deformation type of the observed structures and the stress regimes differ at both geothermal sites in this study, Bruchsal and Riehen. However, our geomechanical study shows that a similar structural control of the geothermal reservoir may apply on both fields. The modeled ranges of T_S and T_D show major similarities regarding the reactivation potential of both the URG-parallel and the proposed transfer faults. Since transfer faults in Bruchsal and Riehen have been inferred from geological constraints, their geometry is not fully defined at these locations. They may be vertical strike-slip faults or about 70° -dipping oblique normal faults. Taking into account that the stress regime of the URG changes from normal faulting over normal faulting/strike-slip to a pure strike-slip regime, from the northern to the southern segments, the main observations are:

1. Apart from being a function of depth, T_S and T_D show strong dependency on both, fault strike and dip. While the influence of strike is rather uniform across the two areas, dip dependency varies significantly for the different stress regimes.
2. T_D behaves similar across the entire URG. Highest tendency for tensile failure is always observed for sub-vertical structures that are aligned parallel to S_{Hmax} . Along the EMBF zone, this accounts mainly for NW-SE striking transfer faults.
3. The azimuth of the most favorably oriented faults for shear reactivation changes within the URG. This is due to the change of the stress regime within the area. Sub-vertical transfer faults acting in strike-slip mode have no tendency to slip for orientations parallel to S_{Hmax} . Inclined transfer faults parallel to S_{Hmax} have slip tendency values ranging from a maximum critical T_S equal to μ , in normal faulting regime, to a small subcritical value, in strike-slip regime. In the latter case, maximum T_S is observed for faults striking approximately $\pm 30^\circ$ from S_{Hmax} .

The particular behavior of criticality for tensile failure and non-criticality for shear failure of the transfer faults leads to the assumption that such transfer faults are naturally permeable structures with low stimulation potential under the given stress condition. This is in agreement with both the observations of zero-tracer recovery and the lack of seismicity in both geothermal sites in this study.

Due to the major reorientation of the regional stress field in the URG during Late Miocene time with a S_{Hmax} rotation of about 90° , we suppose that NW-SE striking faults are of major interest for geothermal exploration since they are expected to have low stimulation potential and the highest permeability. This accounts for rifting-related transfer zones as well as for pre-existing and probably reactivated faults in general.

ACKNOWLEDGMENTS

We thank the EnBW Energie Baden-Württemberg AG for giving access to the Bruchsal data and financial support of the study. This study is part of the LOGRO project co-financed by the Bundesministerium für Umwelt, Naturschutz und Reaktorsicherheit. I. Moeck and J. Reinecker are acknowledged for fruitful discussions. The study benefited also from the HGF portfolio project "Geoenergy". The authors are also grateful to J. E. Faulds (University of Nevada, Reno, US) and A. Morris (Southwest Research Institute, San Antonio, US) for helpful reviews and improvements of the quality of the manuscript.

LINEAMENT ANALYSIS FOR IDENTIFICATION OF
FAULT ZONES IN CRYSTALLINE BASEMENT OF
THE SOUTHERN SCHWARZWALD (GERMANY)

This section is prepared for submission. The envisaged order of authorship is: Meixner, J.; Grimmer, J.C.; Schill, E.; Becker, A.; Kohl, T. (submission in 2016).

ABSTRACT

Remote sensing techniques, such as the mapping of lineaments, can provide additional information on the structural geological inventory of an area of interest, i.e. if the study area is very large or is characterized by bad outcrop conditions. However, evaluation of the accuracy of lineament mapping results is still a challenging task since relevant parameters, such as the inherent censoring and truncation bias, vary for different elevation models. In this study we show how statistical evaluations help to improve the reliability of lineament mappings. Therefore we present a lineament analysis in crystalline basement rocks based on two digital elevation models (ASTER, LIDAR) and satellite imagery data sets in order to identify fault traces and their possible neotectonic activity in the seismically active southern Schwarzwald. A statistical assessment of the orientation, average length, and the total length of mapped lineaments reveals an impact of the different resolutions of the data sets allowing to define maximum (censoring bias) and minimum (truncation bias) observable lineament length for each set. For an increase of the spatial resolution of the digital elevation model from 30 m x 30 m to 5 m x 5 m the total lineament lengths decrease by about 40 % and the average lineament lengths decrease by about 60 % with both still following a power law distribution as documented elsewhere for fault and fracture systems. Predominant NE-, N-, NNW-, and NW-directions of the lineaments are observed in all data sets and correlate well with known large-scale faults and associated minor faults and fractures in the southern Schwarzwald. Application of a slip- and dilation tendency analysis on the resulting fault pattern reveals the highest reactivation potentials for WNW-ESE and NNE-SSW striking faults as left- and right-lateral strike-slip faults whereas normal faulting may

occur along NW-striking faults within the ambient stress field. Remote sensing techniques in combination with highly resolved digital elevation models and a slip- and dilation tendency analysis thus can be used to quickly get first order results of the structural inventory of and critically stressed faults in crystalline basement terranes.

6.1 INTRODUCTION

Identification of brittle faults in crystalline basement rocks is still a challenging task because fault traces are commonly more difficult to recognize and to track along strike in crystalline basement than in sedimentary rocks. This is mainly because of missing markers - stratigraphic layers, sills, or dykes - that impedes quantification of displacements and finally hampers the reconstruction of the structural evolution of brittle fault patterns and the possible response of this fault pattern to the ambient stress field. The southern Schwarzwald in SW Germany is a seismically active crystalline basement area exposing Carboniferous granitic batholiths and high-grade metamorphic gneiss complexes. The crystalline basement appears to be devoid of faults in the geological maps, which is in marked contrast to the abundantly mapped faults in the Triassic cover rocks in the vicinity as for example in the Dinkelberg Block south of the Kandern-Hausen Fault Zone and the Bonndorf graben system in the east (Fig. 6.1). Digital elevation model and satellite imagery analyses provide complementary methods to geological mapping. Particularly, mapping of lineaments is proven suitable for a quick and reliable first-order estimate on the structural inventory in a study area [e.g. Castaing et al., 1996; Arlegui and Soriano, 1998; Jordan et al., 2005]. A lineament analysis of the southern Schwarzwald by Franzke et al. [2003] has been based on satellite imagery indicating almost identical lineament densities for the crystalline basement and the sedimentary cover rocks. In contrast to the geological maps, the results of Franzke et al. [2003] can be interpreted in such a way that major fault zones, although they are mapped almost exclusively in the sedimentary cover rocks, do not arrest at the basement-cover interface, but continue as brittle faults into the crystalline basement.

Information on the structural inventory of the crystalline basement in the southern Schwarzwald is of major interest for many ongoing research studies and crucial for sophisticated geomechanical and geophysical models that are needed for a better understanding of hydraulic and mechanical behavior of deep seated fault zones in the crystalline basement. Information about location and depth extension of brittle faults in the crystalline basement are needed

to improve understanding of origin and evolution of hydrothermal anomalies in mountain ranges, such as observed between the southern Schwarzwald area and northern Switzerland [Kohl et al., 2003; Rolker et al., 2015]. Here, coupling of tectonic and geothermal processes are not fully understood and most theories lack of information about subsurface fluid flow processes within the crystalline basement. Deep seated, cataclastic fault zones in mountain ranges can cause steep geothermal gradients probably driving hydrothermal circulation even in convergent environments [Derry et al., 2009; Guglielmetti et al., 2013]. Convective heat transfer can be an important process to trigger cooling of an orogen [Forster and Smith, 1989; Ingebritsen et al., 1989]. Especially faults and fractures that are favorably oriented and critically stressed for frictional failure dominate subsurface fluid flow [Barton et al., 1995; Ito and Zoback, 2000]. Stress concentrations along fault tips and fault intersections may favor localization of deep seated fault-bounded convection cells [Curewitz and Karson, 1997]. However, for the southern Schwarzwald such comprehensive investigations are missing due to the lack of information about brittle faulting patterns.

We present three lineament analyses applied on three different sources of remote sensing data: The first data set comprises satellite imagery data of Franzke et al. [2003], the other data sets comprise high-resolution ASTER-DEM and LIDAR-DEM data with spatial resolutions of approximately 30 m x 30 m and 5 m x 5 m, respectively.

To characterize the reactivation potential of the obtained (lineament-) fault pattern, we constrain both the ambient stress field and faulting regime in the southern Schwarzwald based on published data and apply a slip- and dilation tendency analysis as proposed by Morris et al. [1996] and Ferrill et al. [1999]. Identification of fault zones by lineament mapping and assessment of possible neotectonic activity of these zones (given that regional stress-field data are available) may be widely applicable since the coverage with high-resolution remote sensing data steadily increases worldwide.

6.2 REGIONAL SETTING

6.2.1 Geological overview

The Schwarzwald is part of the central polymetamorphic belt of the Variscan orogen that developed between about 420 Ma and 280 Ma. From north to south the Schwarzwald comprises four NE-trending lithotectonic units accreted by oblique convergence during early Carboniferous time (Fig. 6.1, Krohe and Eisbacher, 1988; Eisbacher et al., 1989b). The low to medium grade metasedi-

mentary and metavolcanic rocks of the Baden-Baden Zone (BBZ) in the north represent the southernmost parts of the Saxothuringian Zone of the Variscan orogen. The BBZ is separated to the southeast from the medium to high-grade metamorphic rocks of the Central Schwarzwald Gneiss Complex (CSGC) by a ductile shear zone.

The CSGC represents the Moldanubian Zone of the Variscan orogen and mainly consists of paragneisses, orthogneisses, minor metabasites, and isolated lenses of relic eclogites and serpentized peridotites [e.g. Kalt et al., 2000; Marschall et al., 2003]. Two large granitic batholiths accompanied by two minor bodies intruded into the CSGC in the north and east (Fig. 6.1A). Granitic dykes in the CSGC commonly trend NE-SW whereas in the granite dykes also trend NNE-SSW and NW-SE [e.g. Schleicher and Fritsche, 1978]. To the southeast, at the northern margin of the Badenweiler-Lenzkirch Zone (BLZ; Fig. 6.1A), the mylonitic-cataclastic Todtnau thrust indicates dextral-transpressive, SSE-directed convergence at about 330 Ma [Krohe and Eisbacher, 1988]. The CSGC in the hangingwall overthrust the low-grade to non-metamorphic Palaeozoic sedimentary-volcanic successions of the BLZ. Along the southern limb E-striking panels mark a transtensional fault boundary with the high-grade metamorphic Southern Schwarzwald Complex (SSC). The high-grade metamorphic gneisses of the SSC form W- to NW-dipping panels that were intruded by N- to NW-trending batholiths (Fig. 6.1B). These massive granitic plutons intruded into middle to high crustal levels and originated during late orogenic E-W-oriented extension-transtension that followed early Carboniferous NNW-SSE-convergence [Grimmer et al., 2016; Krohe and Eisbacher, 1988; Eisbacher et al., 1989a; Henk, 1997].

Our study area mainly covers the SSC, but extends also into the BLZ and CSGC. The study area is covered towards east by Permian and Triassic sedimentary rocks. To the west it is bound by the Cenozoic Upper Rhine Graben and to the south by a WSW-ENE-trending Permian basin largely covered by Mesozoic sedimentary rocks. The major structural units and fault zones in the SSC are shown in Fig. 6.1B. Structurally, they can be grouped into:

- (W)NW-(E)SE striking structures such as the Bonndorf Graben Zone (1), the Kandern-Hausen Fault Zone (4), and the Vorwald Fault Zone (6);
- NNE-SSW trending features associated with the main boundary fault zone of the Upper Rhine Graben (2);
- NNW-SSE striking fault zones such as the Schweighof Fault Zone (3) and the Wehratal Fault Zone (5).

Dextral displacement of the Albtal granite along the Vorwald Fault Zone (Fig. 6.1B) point to an origin of the NW to WNW trending

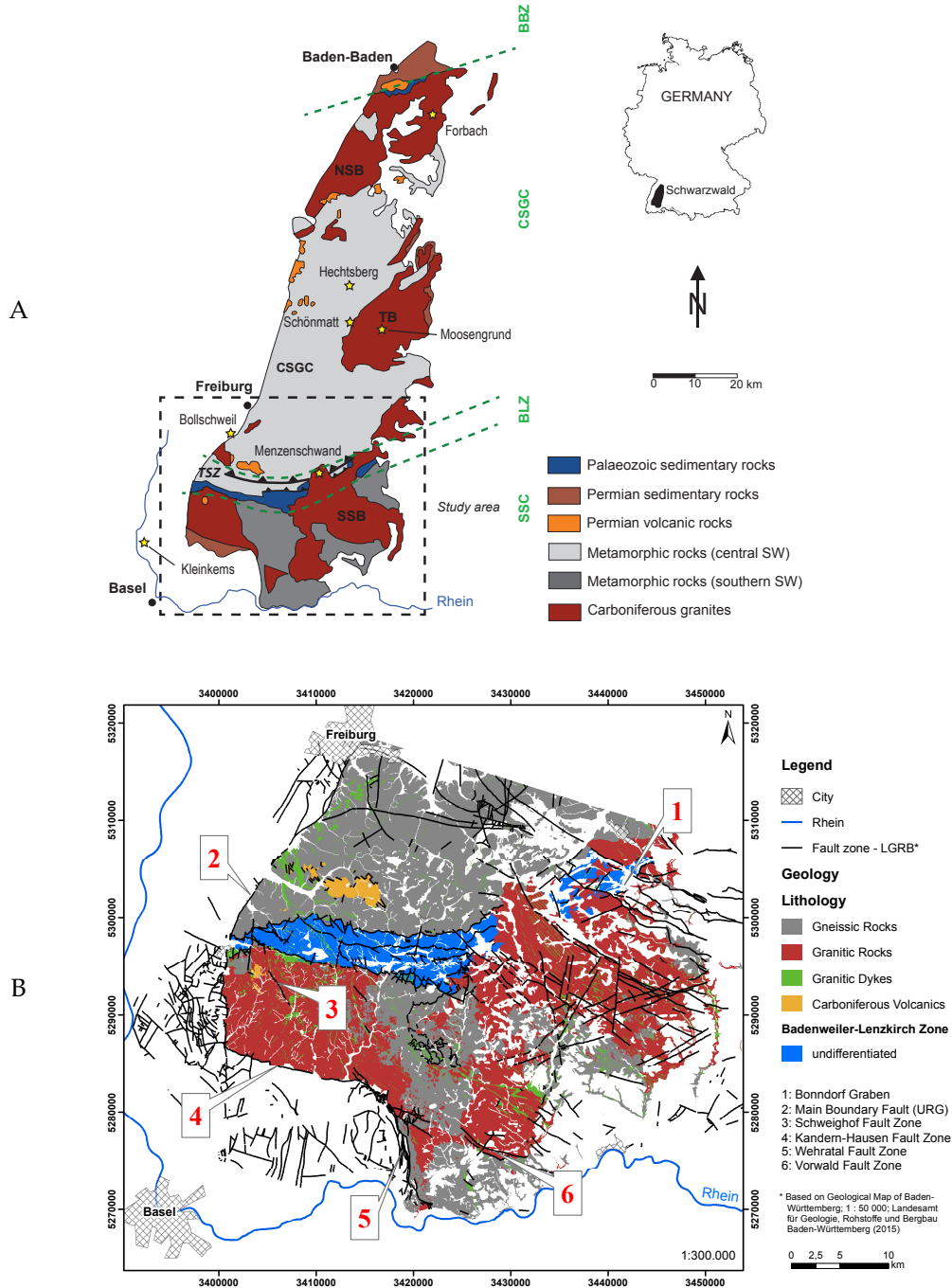


Figure 6.1: A) Simplified geological map of the Schwarzwald area showing the borders of the four NE-trending major lithotectonic units (dashed green lines) of the Variscan belt, the Carboniferous granitic batholiths (red), and the locations of in-situ stress measurements (stars). B) Overview map of the study area in the SSC between Freiburg and Basel showing the distribution of the gneissic and granitic rocks. The fault map clearly illustrates the lack of structural information in the Variscan basement. Abbreviations: NSB/SSB – northern/southern Schwarzwald batholith; TB – Triberg batholith; CSGC – central Schwarzwald gneiss complex; SSC – southern Schwarzwald Complex; BBZ – Baden-Baden Zone; BLZ – Badenweiler-Lenzkirch Zone; TSZ – Todtnau Shear Zone

faults during post-orogenic extensional-transtensional tectonics [Emmermann, 1967]. Polyphase Mesozoic and Cenozoic reactivations of these fault zones is documented in the crystalline basement (e.g. Vorwald Fault Zone: Huber and Huber-Aleffi, 1984) but can also be traced as structural gain in the cover rocks, such as the Bonndorf Graben Zone.

6.2.2 Regional stress state

The Alpine foreland is characterized by a systematic, fan-like orientation of the maximum (S_H) and minimum (S_h) horizontal stress directions [Müller et al., 1992; Heidbach et al., 2008]. For the crystalline basement in the southern Schwarzwald only few in-situ stress measurements are available (Fig. 6.1A, Table 6.1).

Table 6.1: Stress field orientation data of the southern Schwarzwald. For location see Fig. 6.1A.

Type	Location	Rock type	Depth Range [m]	Type	Q-WSM	mean S_H [N°E] (n)	Ref.
<i>Borehole</i>							
	Menzenschwand	Granite	95	TSC		164.0 (4)	1
	Menzenschwand	Granite	116 - 119	D	C	44.6 ± 23 (7) *	1
	Forbach	Granite	96 - 155	TSC	A	145.6 ± 5.7 (5)	2
	Hechtsberg	Gneiss	75 - 296	H	B	138.6 ± 17.7 (5)	3
	Schönmatt	Gneiss	78 - 264	H		165 (1)	3
	Moosengrund	Granite	83 - 258	H		123 (2)	3
<i>Quarry</i>							
	Bollschweil	Limestone	5	D	B	153.0 ± 19 (12)	4
	Kleinkems	Limestone	5	D	B	176 ± 13 (10)	4
	Menzenschwand	Granite	2 - 4	D	A	140.7 ± 5.9 (9)	1
<i>FPS</i>							
			10 - 15	SI (a)		144.0 (15)	5
	Southern Schwarzwald		10 - 15	SI (b)		141.0 (15)	5
			0 - 23	SI (a)		145.0 (30)	5
			0 - 23	SI (b)		142.0 (30)	5

*SI: stress inversion of focal plane solutions (FPS); In-situ measurement in wellbores - TSC: triaxial strain cell, D: doorstopper, H: hydrofrac analyses. Labels a and b indicate two different stress inversion methods [Kastrup et al., 2004]. QWSM: Quality assessment according to the world stress map classifies in-situ measurements as A, B, and C quality for a S_H azimuth uncertainty within 15°, 20°, and 25°, respectively. * test site very close to tectonic fault. References - 1: [Wolter, 1987]; 2: [Hauser-Fuhlberg et al., 2012]; 3: [Rummel and Baumgärtner, 1987]; 4: [Greiner, 1978]; 5: [Kastrup et al., 2004].*

Stress field measurements are based on near-surface in-situ measurements in quarries [Greiner, 1978; Wolter, 1987], analyses of hydrofracs [Rummel and Baumgärtner, 1987], and the use of triaxial strain cells [Wolter, 1987; Hauser-Fuhlberg et al., 2012]. Stress inversions performed on earthquake fault-plane solutions provide additional information about the σ_1 and σ_3 orientation in

deeper crustal levels. The data indicate a generally uniform NW-SE orientation of S_H within a predominant strike-slip faulting regime with secondary normal faulting [Plenefisch and Bonjer, 1997; Kastrup et al., 2004].

According to Table 6.1, we assume S_H azimuth trending $N140^\circ E \pm 10^\circ$. Wellbore measurements from greater depths are also used for the estimation of principal stress magnitudes (Fig. 6.2). The vertical stress magnitude (S_v) is assumed to follow a lithostatic pressure gradient with a mean rock density of 2650 kg m^{-3} . Almost all measured magnitudes of S_H are larger than S_v , excluding a pure normal faulting regime. All measurements with S_h magnitudes larger than S_v predict a thrust faulting regime which is at odds with natural seismicity showing no evidence for thrust faulting in the southern Schwarzwald [Kastrup et al., 2004]. Hence, we estimate the following stress-depth trends for S_H and S_h solely based on the in-situ measurements in the Forbach granite, describing the following strike-slip regime: $S_h = 0.017 \cdot z + 0.160$ and $S_H = 0.048 \cdot z + 0.189$ with z in m.

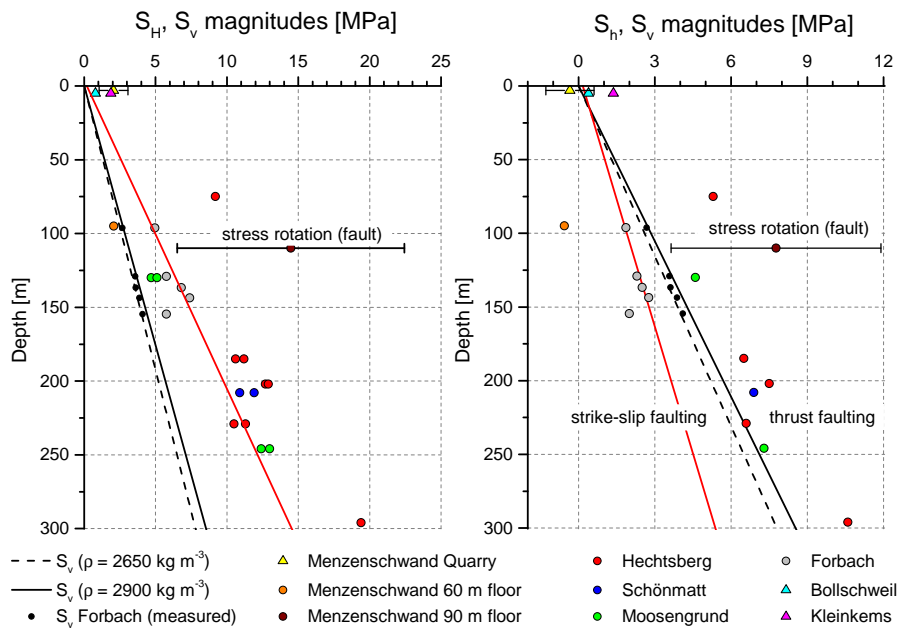


Figure 6.2: In-situ stress measurements in crystalline basement rocks of the Schwarzwald. The red lines follow the linear stress-depth relation that has been used in this study for the estimation of the S_H and S_h magnitudes. For references see Table 6.1.

6.3 METHODS

6.3.1 Data

We compare three lineament analyses using satellite imagery and different digital elevation models (DEM).

- The first lineament analysis (lineament set) in the Schwarzwald of Franzke et al. [2003] is based on processed Thematic Mapper (TM) and ERS-1 satellite imagery and is designated as the FRANZKE data set (Fig. 6.3). TM was an Earth scanning, multispectral sensor introduced in the NASA-Landsat 5 program with a spatial resolution of the three interpreted spectral bands of 30 m x 30 m. The analyzed ERS-1 raster data set originates from an ESA-European Remote Sensing satellite and provides a spatial resolution of 25 m x 25 m.

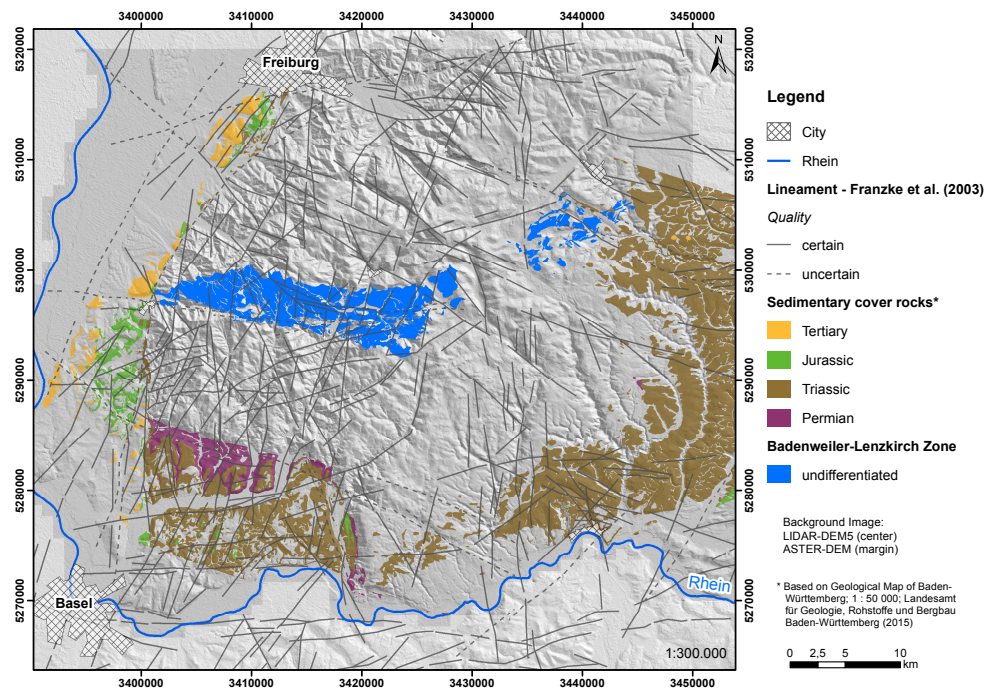


Figure 6.3: Lineament mapping in the southern Schwarzwald from Franzke et al. [2003] based on Thematic Mapper and ERS-1 satellite imagery with spatial resolutions of 30 m x 30 m and 25 m x 25 m, respectively. Lineaments outline predominant (S)SW, (W)NW, and N trending strike directions in the gneissic and granitic basement rocks.

- The second lineament set is based on spaceborn-derived elevation data that provides a spatial resolution of 1 arc-second which corresponds to a horizontal and vertical resolution of 27 m x 27 m and < 1 m, respectively. This lineament set is designated as the ASTER-DEM data set.

- The third lineament set, designated as the LIDAR-DEM₅ data set, is based on airborne laser scanning data with a horizontal resolution of 5 m x 5 m and a vertical resolution of < 0.5 m, respectively.

Both DEMs provide slightly different information about surface topography, since the ASTER-DEM represents a digital surface model, only, while the LIDAR-DEM₅ can be regarded as true digital terrain model.

6.3.2 *Lineament mapping*

Following O’leary et al. [1976], we define a lineament as a mappable, simple or composite linear feature on a surface, whose parts are aligned in a rectilinear or slightly curvilinear relationship and which differs distinctly from the patterns of adjacent features and presumably reflects a subsurface phenomenon. Especially in areas with a distinct topography (steep elevational gradients and hill slopes), inclination of faults has a significant impact on lineament identification. Fault traces of subvertical faults, as associated to strike-slip tectonics, are not influenced by the topography and should be clearly visible as linear features. In contrast, fault traces of inclined faults, as associated to dip-slip tectonics, follow topography. As curvilinear fault traces these features may not be clearly visible as lineaments. Hence, inclined faults in areas with a distinct topography probably are, a priori, statistically underestimated. Lineament length is furthermore relative to the scale of observation. This accounts for both the resolution of the DEM and the size of the study area.

For data processing and visualization we used the geoinformation system software suite Arc-GIS. For lineament mapping we choose a visual approach on the basis of slope gradient maps, aspect maps, and shaded relief maps. The latter were created for illumination azimuths of 45°, 90°, 135°, and 180° respectively. Depending on whether the lineaments were clearly detectable in all four illumination scenarios, we classified them into the categories ‘certain’ and ‘uncertain’. Each lineament was cross-checked with topographic maps for linear anthropogenic features such as roads or railroad tracks. Since the FRANZKE data set covers the entire Schwarzwald area, we clipped it to the same size of the ASTER-DEM and LIDAR-DEM₅ data sets.

For statistical consistency and comparability, e.g. for evaluation of the lineament orientation, we cut the lineaments of each set in nearly regular 250 m segments. The remaining end pieces of each lineament with lengths < 250 m are considered equivalent to the regular 250 m segments. As a result, each lineament data set describes a distinct left-skewed normal distribution.

6.3.3 Slip- and Dilation Tendency Analysis

Slip on faults is controlled by the balance between resolved shear stress and the magnitude of frictional resistance [Lisle and Srivastava, 2004]. Slip on faults thus may occur when effective shear stress (τ) equals or exceeds frictional resistance. Controlling mechanical parameter for slip on faults are the cohesive strength (c), the coefficient of static friction (μ), and the resolved normal stress (σ_n). For the reactivation of pre-existing faults cohesion may be neglected. In this case, the ratio of resolved shear stress to resolved normal stress equals the coefficient of static friction μ . This ratio is designated as the slip tendency (T_S ; Morris et al. [1996]). Slip tendency analysis of faults is appropriate to determine their reactivation potential in different tectonic settings as for example for seismological studies of aftershocks [Collettini and Trippetta, 2007] or for prediction of fault reactivation at the sedimentary basin scale [Worum et al., 2004, 2005]. At the reservoir scale slip tendency analysis has been used to link fault reactivation with induced seismicity during hydraulic stimulation [Moeck et al., 2009] or for prediction of geomechanical anisotropies in complex fault patterns [Meixner et al., 2016].

Dilation tendency, T_D , is the relative probability for a fracture or a fault to dilate within the ambient stress field [Ferrill et al., 1999]. T_D is defined as the difference between the maximum principal compressive stress (σ_1) and the normal stress (σ_n), normalized by the differential stress ($\sigma_1 - \sigma_3$). T_D is a relative value ranging between 0 ($\sigma_1 = \sigma_n$) and 1 ($\sigma_3 = \sigma_n$).

The calculation is straightforward if the geometry of the fault and the in-situ state of stress is known. For the calculation of T_S and T_D we assume that identified 1D lineaments are caused by brittle deformation processes and that they represent surface traces of fault zones. Since the geometry of fault zones cannot be inferred from lineament mapping, we created 500 m deep, vertical fault planes out of the LIDAR-DEM5 data set and meshed them into nearly equilateral triangles (fault patches). T_S and T_D are calculated with the software 3Dstress® for each fault patch. A schematic overview of our workflow is shown in Fig. 6.4.

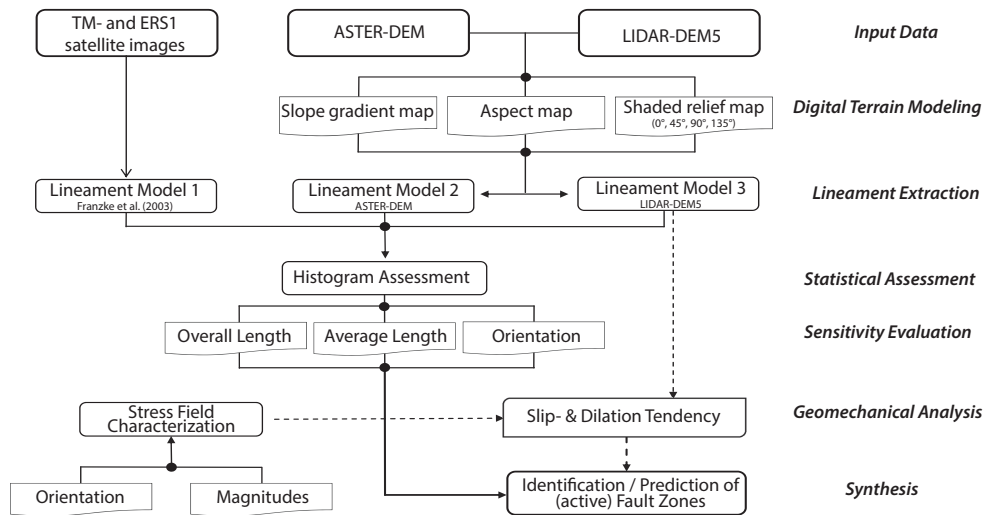


Figure 6.4: Generalized flowchart showing the steps for identification of fault zones in the crystalline basement rocks of the southern Schwarzwald. The three considered lineament data sets are based on remote sensing imagery and digital elevation models with horizontal resolutions ranging from 30 m x 30 m to 5 m x 5 m. Application of a slip- and dilation tendency analysis for the lineament model of the high-resolution LIDAR-DEM5 data set is used for a geomechanical characterization of potential fault zones in the ambient stress field.

6.4 RESULTS

6.4.1 The ASTER-DEM and LIDAR-DEM5 lineament maps

The lineaments extracted from ASTER-DEM and the LIDAR-DEM5 are shown in Fig. 6.5 and 6.6. The ASTER-DEM and LIDAR-DEM5 data sets consist of lineaments with a total length of about 1066.6 km and 887.1 km, respectively. In the ASTER-DEM data set the maximum lineament length is 13.4 km and in the LIDAR-DEM5 data set the maximum length is 10.4 km. Both data sets are characterized by a heterogeneous spatial distribution of the lineaments. In the northern part of the study area an apparent lower lineament density is observed in both data sets. The BLZ seems to separate a tectonic unit with few lineaments in the N from a tectonic unit with many lineaments in the S. Noteworthy, this separation also marks the structural boundary between the CSGC in the north and the SSC in the south. Next to this general N-S trend, local variations of the lineament density are observed. In the ASTER-DEM data set and the LIDAR-DEM5 data set the SW region of the study area, between the BLZ and the Triassic units NE of Basel, show the highest apparent lineament density. In the SSC, the apparent lineament density decreases to the E.

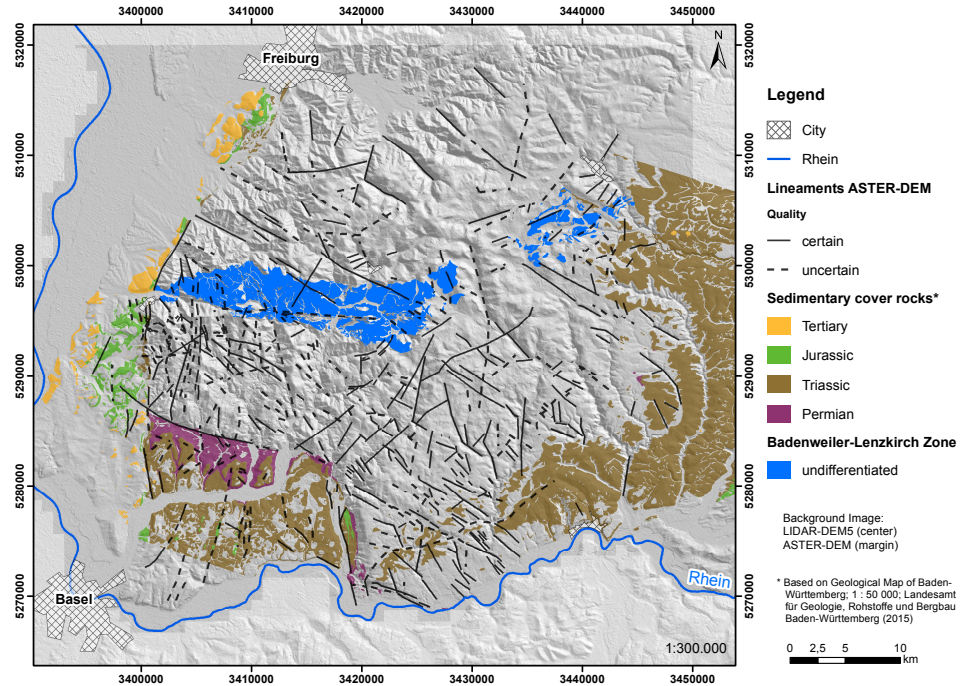


Figure 6.5: Lineament map of the southern Schwarzwald based on the ASTER-DEM with a spatial resolution of 27×27 m. Lineaments indicate predominant NE, NW, and N trending strike directions in the gneissic and granitic rocks.

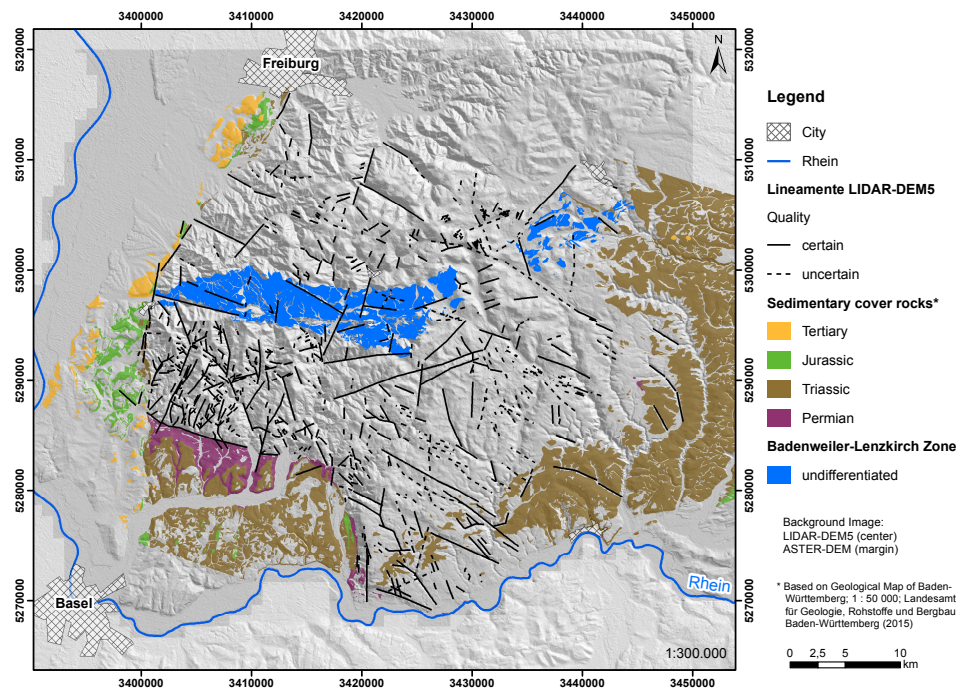


Figure 6.6: Lineament map of the southern Schwarzwald based on the LIDAR-DEM₅ with a spatial resolution of $5 \text{ m} \times 5 \text{ m}$. Similar to the ASTER-DEM data set (Fig. 6.5), lineaments show predominant NE, NW, and N trending strike directions in the crystalline basement.

Since both DEMs show rather comparable spatial distributions of the mapped lineaments the question arises whether the difference in spatial resolution of both input data sets has an impact on the mean lineament length or the lineament orientations, which will be discussed in the next section.

6.4.2 Statistical evaluation of the lineament sets

Lineament length

The total length of the identified lineaments significantly decreases with increasing resolution of the elevation data. Franzke et al. [2003] mapped lineaments with a total length of 1412.2 km based on TM and ERS-1 satellite imagery. We mapped lineaments with a total length of 1066.6 km for the ASTER-DEM data set and 887.1 km for the LIDAR-DEM₅ data set. This is a decrease of the overall lineament length of about 40% for an increase of the spatial resolution by a factor of 36. Histograms of the three data sets also indicate distinct variations in statistical distribution of the individual lineament lengths (Fig. 6.7).

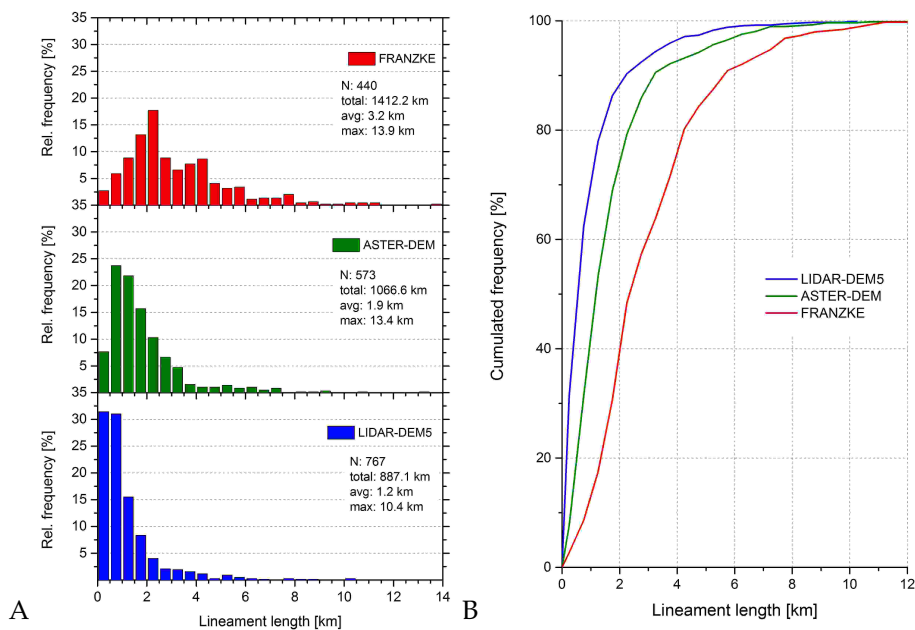


Figure 6.7: Statistical evaluation of the lineament data sets for the southern Schwarzwald mapped for satellite imagery (FRANZKE - red) and digital elevation models (ASTER-DEM - green; LIDAR-DEM₅ - blue) regarding the lineament lengths. Histogram assessment (A) and cumulative frequency distribution (B) show right-skewed normal distributions of the mapped lineaments for all input data sets but, remarkably, with an increase of the spatial resolution of the elevation models a significant decrease of the average lineament length is observed.

All three data sets are characterized by a similar, right-skewed normal distribution for lineament lengths of up to 14 km. The average lineament length is significantly decreasing for an increasing resolution of the elevation data (Fig. 6.7A). The average lineament length decreases by more than 60% from 3.2 km (FRANZKE data set) to 1.2 km (LIDAR-DEM₅ data set). The cumulative frequency distribution of the mapped lineament lengths illustrates this observation (Fig. 6.7B). The 80% interval of the mapped lineaments in the FRANZKE-, ASTER-, and LIDAR-DEM₅ data set is represented by a lineament length of about 4.2 km, 2.3 km, and 1.4 km, respectively.

Lineament orientation

In contrast to the lineament lengths, histogram assessments of the lineament orientations indicate rather comparable statistical distributions for the FRANZKE-, ASTER-, and LIDAR-DEM₅ data sets (Fig. 6.8A).

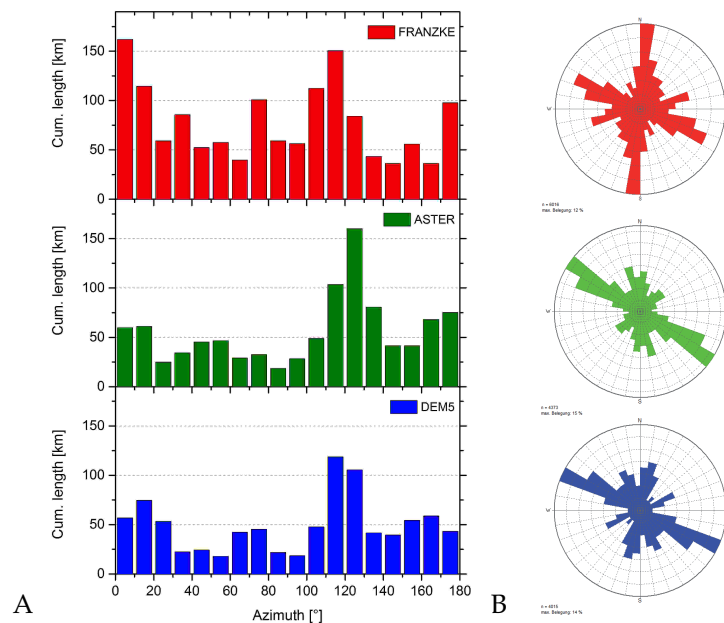


Figure 6.8: Statistical evaluation of the lineament data sets extracted from satellite imagery (FRANZKE - red) and digital elevation models (ASTER-DEM - green; LIDAR-DEM₅ - blue) regarding the orientation of the lineaments. The histograms (A) and the rose diagrams (B) indicate the existence of the similar predominant NW, NNW, NNE and NE strike directions in all lineament data sets but with a slightly different weighting of individual trends, especially for the NNE striking lineaments.

Four predominant trends of lineament orientations are observable in all data sets but weighting of individual trends shows variations: A well-defined maximum between 100° and 140° azimuth is visi-

ble in all data sets and contains all NW-SE trending lineament segments. Other trends are oriented in the NNW-SSE-, N-S-, and NE-SW-direction (Fig. 6.8B). Relative frequencies of these trends vary in the three data sets. In the FRANZKE data set the N-S trend seems to be statistically overrepresented and the NNW- and the N-trend seem to be clustered in a single maximum as with higher resolution of the elevation data the N-S-trend is less often observed and mapped.

6.4.3 Slip- and dilation tendency analysis

We performed a slip- and dilation tendency analysis on the base of the LIDAR-DEM5 data set for assessment of the reactivation potential of these faults. The results of these calculations are shown in Fig. 6.9. Generally, an anisotropic distribution of both parameters can be observed for the lineament set. Largest T_S values up to 0.875 are observed for NW-SE and for NNW-SSE striking lineaments (Fig. 6.9A). Faults with this orientation are preferably observable in the eastern part of the SSC. Here, the major regional fault zones such as the NW striking Kandern-Hausen- and the Vorwald fault zone (Fig. 6.1B) and all subparallel striking faults show large slip tendencies of $T_S > 0.75$. This NW fault trend is also observed in the CSGC, north of the BLZ. Here, this trend is visible from E to W throughout the study area. The longest identified lineaments follow this NW strike and are associated with major structural units like the NW-SE trending Bondorf Graben (Fig. 6.1B).

A secondary fault trend that is characterized by a high potential for shear reactivation comprises NNW striking faults such as the Schweighof- and the Wehratal fault zone (Fig. 6.1B) and is predominantly observed S of the BLZ, in the E of the SSC. In the strike-slip stress state of the southern Schwarzwald both fault trends are prone for reactivation as conjugated shear zones with the NW and NNW trending faults acting as sinistral and dextral strike-slip faults, respectively. Both the NNW and the NW trending fault zones also show largest dilation tendencies of $T_D > 0.8$ (Fig. 6.9B).

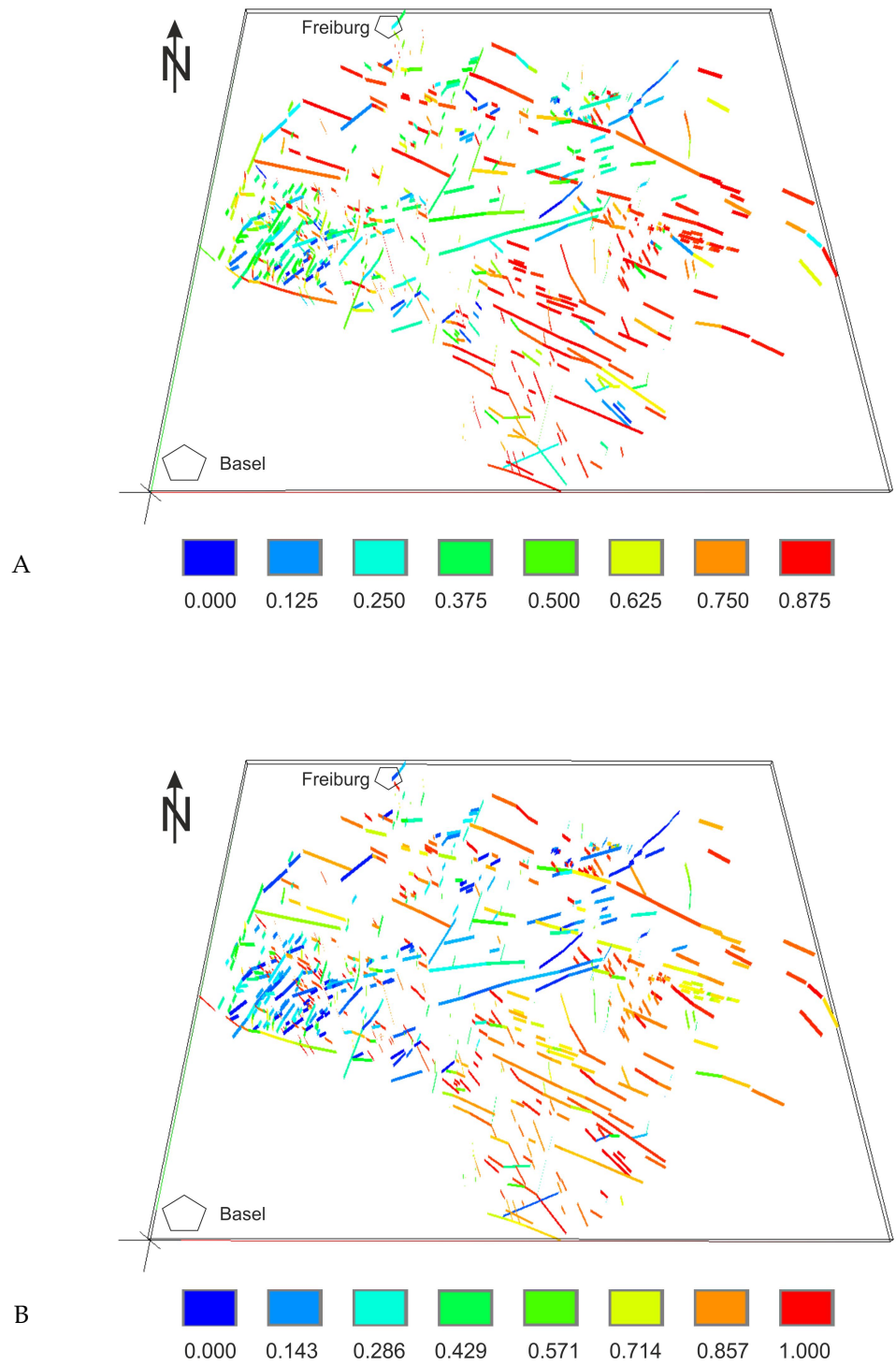


Figure 6.9: Slip tendency (A) and dilation tendency (B) calculations for the LIDAR-DEM5 lineament set in the southern Schwarzwald under strike-slip stress conditions and with an S_H orientation of N140°E. Both values are calculated for vertical fault planes and for a depth range of 500 m.

6.5 DISCUSSION

Generally, the obtained lineament sets clearly illustrate the apparent discrepancies between the mapped faults in the southern Schwarzwald and the results of remote sensing techniques. The FRANZKE, ASTER-DEM, and LIDAR-DEM₅ data sets all reveal a high lineament density in the SSC (Fig. 6.3) and show similar orientation distributions of lineament trends, but with variations of relative frequency of the different lineament trends. Especially the value of the maximum and minimum lineament length is significantly different in each data set. These differences seem to be related to the resolution of the remote sensing data. The question arises if the latter systematically predesignates the sampling bias for lineament extractions (see also Scheiber et al. [2015]). Completeness of mappable lineaments next to their upper and lower bound in each data set is difficult to assess, but may be compared to widely observed and better constrained length statistics of fault and fracture systems as discussed in the next section.

6.5.1 Lineament statistic and elevation models

The visibility of lineaments on the DEMs and especially on the satellite imagery is probably impaired by various causes such as geology, vegetation, anthropogenic influences (e.g. roads), and by bias that is typically related to the sampling and mapping process itself [e.g. Scheiber et al., 2015]. The latter one may lead to incompleteness of the identified lineaments and probably results in wrong spatial and statistical distributions. To quantify this sampling bias we performed a statistical evaluation of the lineament length distribution.

The frequency distribution of fault length and fracture length is generally approximated by one of the following functions Dershowitz and Einstein [1988]; Korvin [1989]: an exponential distribution, a lognormal distribution, a gamma law distribution, or a power law distribution. However, power law relationships associated with fractal fragmentation are widely used to describe distribution of fracture properties such as length and displacement [Bonnet et al., 2001] and can be expressed as: $n(w) = aw^{-\alpha}$; with a as a constant and α as the power law exponent. In order to characterize the lineament-length behavior for our three lineament sets, we have made a general log-log plot of the cumulative length distributions (Fig. 6.10A). A compilation of power law exponents is given by Bonnet et al. [2001] and is shown in Fig. 6.10B. The α -values determined for fracture and fault lengths at various scales range between 1.5 and 3.0 with a maximum between 2.0 and 2.5.

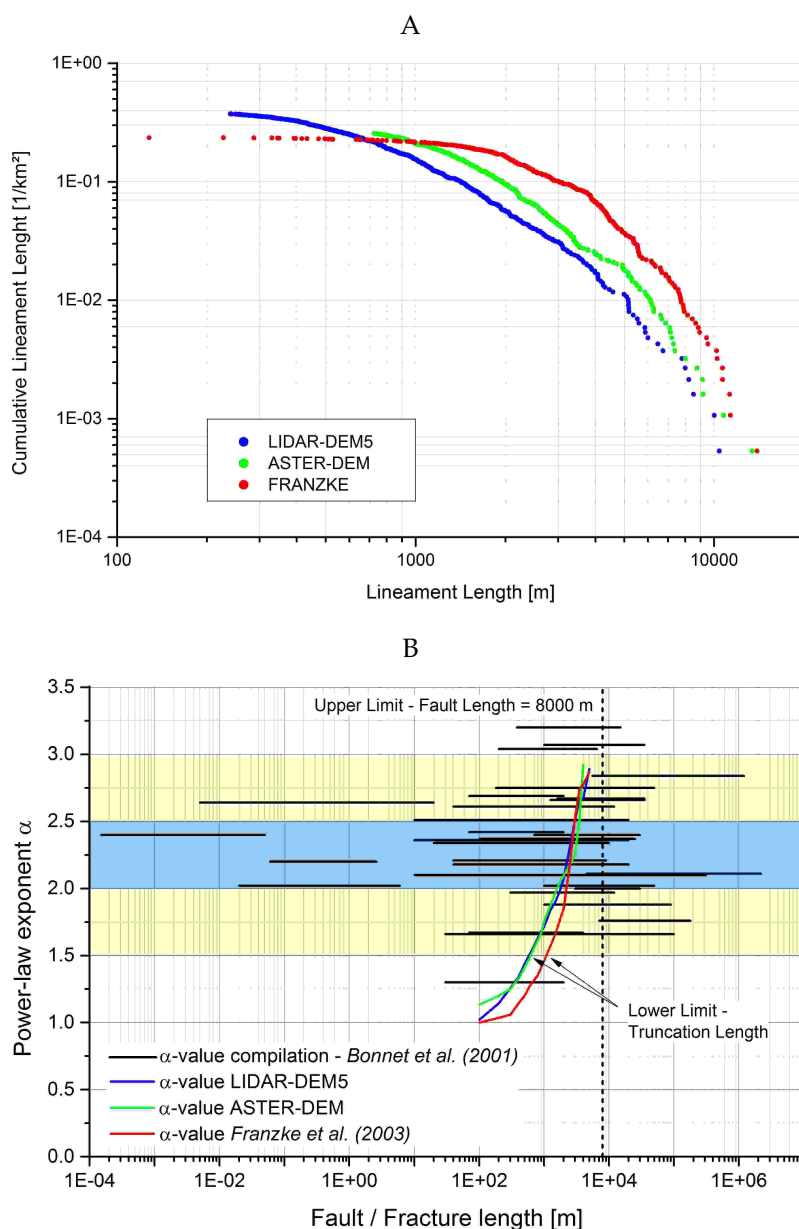


Figure 6.10: A) Cumulative frequency distribution of the fault length as observed in the LIDAR-DEM5, ASTER-DEM, and FRANZKE data sets. Cumulative lineament length is normalized to a map area of 1 km². Lineament length distributions can be described by either an exponential law or a power law function with distinct deviations for the shortest and longest lineaments indicating a sampling bias. B) Compilation of power law exponents, α , by Bonnet et al. [2001] show values mainly ranging between 1.5 and 3.0 (yellow area) with a maximum between 2.0 and 2.5 (blue area). The line elements indicate α -values that have been calculated in this study for different ranges of fault lengths between upper and lower length limits, representing the sampling bias for our lineament mapping.

In a log-log plot of the cumulative length-distribution a power law relationship will be expressed by a straight line with a constant slope. The length distributions in this study seem to follow an exponential relationship. On the one hand, exponential fits for fracture length distributions are also described in other studies [Dershowitz and Einstein, 1988] and are interpreted to reflect early stages of deformation as a result of fracture growth under a uniform state of stress [Bonnet et al., 2001]. On the other hand, resolution effects and finite-size effects imposed on a power law population can result in distributions that appear to be exponential or lognormal [e.g. Hudson and Priest, 1983; Odling et al., 1999]. In our study deviation from a power law function is obvious in the range of the maximum (censoring bias) and minimum (truncation bias) observable lineament lengths. These deviations from a power law relationship may be due to incomplete sampling of lineaments below a certain value (lower limit) and the limited size of the sampling area (upper limit).

Assuming a power law distribution in Fig. 6.10A we define a lineament length of 8 km as upper limit (censoring bias). There are very few representatives of these largest features and are only mapped sporadically. Whether this observation is the result of a geological threshold (e.g. limited fault lengths due to fault segmentations) or of a sampling bias (lineament cutoffs at the model boundary) remains unclear. However, regarding a power law fit the cumulative length distributions in all data sets a steepening of the distribution curve can be seen for lineaments longer than about 8 km. Here α -values larger than 3.0 are calculated (Fig. 6.10B).

An obvious lower limit (truncation bias) should be recognized as a distinct inflection point towards short lineament lengths, but is not observed. In order to get a rough estimate, we have calculated the α -values for increasing length ranges with a fixed maximum length of 8 km (line elements in Fig. 6.10B). For the LIDAR-DEM₅ and the ASTER-DEM data set a rather comparable truncation length of about 600 m and 1700 m is calculated for α -value limits of 1.5 and 2.0, respectively. The FRANZKE data set shows an about 50% larger truncation length of 1100 m and 2250 m for the same α -value limits. The differences between the FRANZKE and the ASTER data set (both with almost similar spatial resolution) clearly show the advantage of a DEM with shaded relief-, aspect-, and slope gradient maps compared to rather static satellite imagery. It clearly indicates the limited applicability of the latter one at small scales. In contrast, the resolution of our elevation data sets has no significant influence on visibility of the longest observed lineaments. Here power law exponents show rather comparable magnitudes.

Within these critical length ranges for the mappable lineaments α -values are calculated which are in good agreement with comparable studies [Castaing et al., 1996; Bonnet et al., 2001]. Linearity of the lineament length distribution between the upper and lower sampling bias may have the appearance of completeness of the detected lineaments but a systematic statistical underestimation for the considered scale range cannot be ruled out. We are also aware that the considerations about the length distribution in our lineament sets cannot be linked to the observed spatial lineament patterns. The apparent consistency to a power law fit would be still given if one lineament orientation was statistically underestimated and another one was statistically overestimated by the same amount. This effect of statistical uncertainty is hard to assess since fault trends are not distributed homogeneously but rather are aligned in predominant strike directions. This may be of great importance in areas with active tectonics. Completeness of our identified lineament sets is thus hard to evaluate and probably needs extensive field-work studies. However, our observations for the southern Schwarzwald confirm the generally accepted power law relationship for fracture and fault properties but conclusions about the statistical reliability can be done only within the scale range of the lineament/fault lengths we considered (about 1-8 km) and extrapolation of distribution patterns to other scales should be avoided. Since lineament lengths do not span more than an order of magnitude in scale range additional data, e.g. from field-work studies, are needed for determination of local and regional frequency distributions.

6.5.2 *Fault geometry and reactivation potential*

Reactivation potential of fault segments within an ambient stress field strongly depends on their strike and dip. For identified lineaments, where fault dip is not observable from remote sensing, slip- and dilation tendency analyses seem to be obsolete. As a first-order approach we thus calculated T_S and T_D for subvertical structures only (see section 6.3.3). To furthermore quantify the reactivation potential for varying performed fault dips we also calculate T_S and T_D for a set of generic faults covering the full range in fault strike in 0.25° steps. T_S and T_D were calculated for the maximum depth of 500 m and for fault dips of 60° , 70° , 80° , and 90° , respectively. The results of the T_S and T_D calculations are shown in Fig. 6.11.

Due to the fact that the underlying stress field model solely bases on in-situ measurements of the stress magnitudes, it is rather noteworthy that the maximum calculated slip tendency value is 0.875. This value is close to 0.85, a threshold value that is related to a coefficient of static friction of 0.85 as recommended for the considered

depth range [Byerlee, 1978]. The measured stress ratios in our study are in accordance with those which can be estimated by the critical stress concept of Zoback et al. [2003].

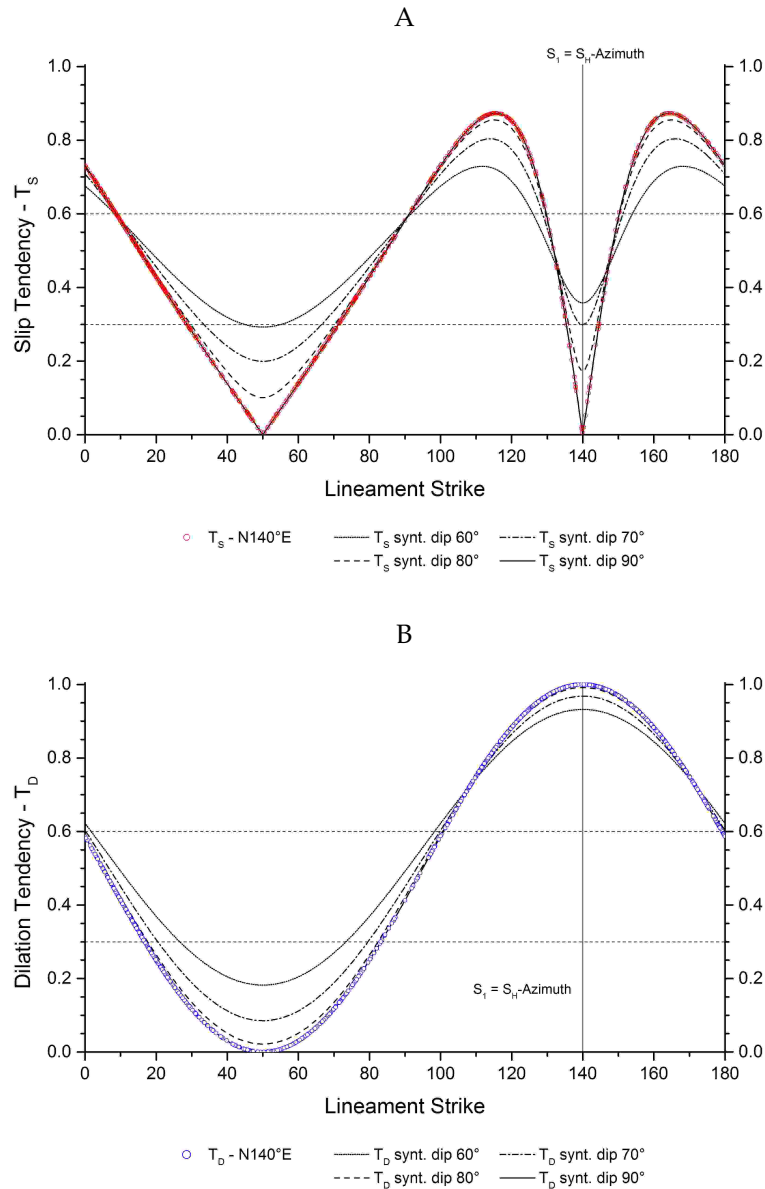


Figure 6.11: Distribution of the slip tendency (A) and dilation tendency (B) as a function of the fault plane azimuth. Considered is a strike-slip stress state for the southern Schwarzwald with a S_H azimuth of N140°E. Point elements represent T_S and T_D values calculated for 500 m deep, subvertical fault zones of the LIDAR-DEM5 data set. Line elements indicate T_S and T_D distributions for potential fault dip angles between 60 and 90°.

The slip tendency curve (Fig. 6.11A) clearly shows two local maxima and two local minima. This pattern for the shear reactivation potential of fault planes is typical for strike-slip faulting. A first minimum is calculated for faults striking $N50^{\circ}E$, parallel to S_H . Fault planes with this orientation show T_S values between 0.0 and 0.3 for dip angles varying from 90° to 60° , respectively. This fault trend, regardless of the fault dip, is not prone to shear reactivation in the ambient stress state. A second minimum is calculated for faults striking approx. $N140^{\circ}E$, i.e. almost parallel to S_H . Subvertical faults of this orientation cannot be reactivated for shearing in a strike-slip faulting regime, but in a normal faulting regime. Also inclined faults never show T_S values larger than 0.4. The largest T_S values of 0.85 are calculated for fault zones that are aligned about 30° from S_H orientation of $N140^{\circ}E$. Structures oriented parallel to these two trends show highest reactivation potential for dextral ($N110^{\circ}E$) and sinistral ($N170^{\circ}E$) shear reactivation. Maximum T_S values are solely calculated for vertical faults. Inclined structures, such as potential normal faults, always show values larger than 0.7. The distribution of the dilation tendency (Fig. 6.11B) is characterized by only one local maximum and minimum. Regardless of the dip, faults striking parallel to S_H always show minimum T_D values. Faults that strike parallel to S_H always show maximum T_D values and thus are prone for dilatant reactivation in the ambient stress state.

We would like to point out that faults striking $N110^{\circ}E$ and $N170^{\circ}E$ are characterized by both, large T_S and large T_D values. This incorporates the NNW-SSE striking Schweighof- and Wehratal fault zones and the NW-SE striking Kandern-Hausen- and Vorwald fault zone. Structures with this orientations show highest probability for shear and dilatant reactivation in the regional stress field, especially if they are subvertically oriented. Interestingly, both critical directions are clearly visible in all three data sets (Fig. 6.8). The $N110^{\circ}E$ fault strike is the most frequently mapped fault orientation. Consequently, a large amount of the total fault surface area of about 444 km^2 show largest T_S and T_D values. This observation is shown exemplarily in Fig. 6.12. for the LIDAR-DEM5 data set. Here, for the S_H orientation of $N140^{\circ}E$ almost 50% of the total fault surface is exposed to T_S values larger than 0.7 and T_D values 0.8. This unimodal distribution changes only slightly with respect to variations of the S_H orientation by $\pm 10^{\circ}$ which represents the uncertainty related to the measurement process.

However, predominant strike directions of all three data sets are oriented favorably for reactivation. The question arises whether this is coincidentally or whether favorably oriented faults are mapped more often. Since topography is affected by erosion, young active fault zones probably are easier to be recognized on elevation mod-

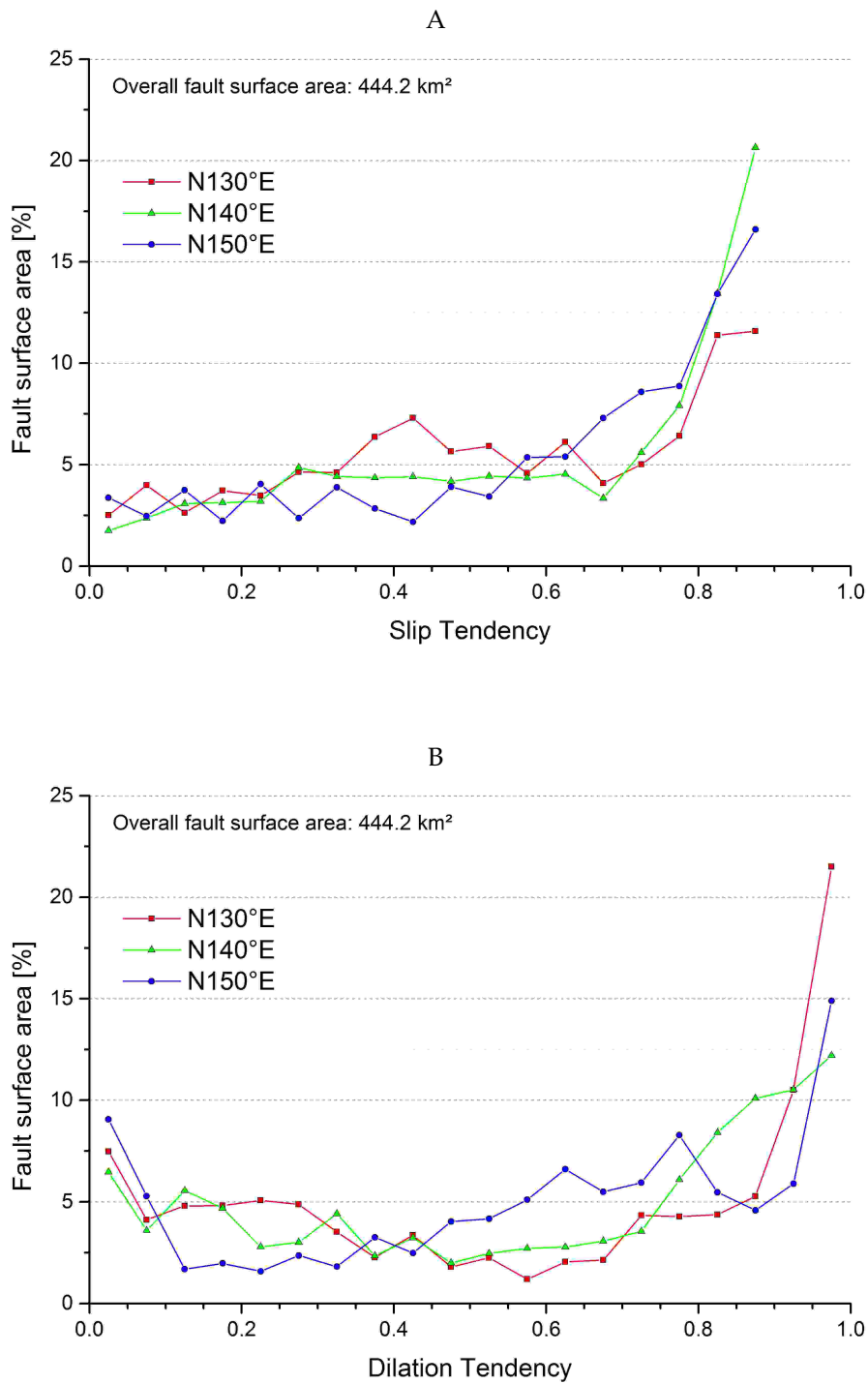


Figure 6.12: Uncertainty analysis of T_S and T_D of the LIDAR-DEM₅ data set with respect to a 10° variation of the mean S_H orientation in the southern Schwarzwald of N140°E. Visualized is the comparison of the cumulative fault area exposed to slip tendency (A) and dilation tendency (B) intervals.

els than inactive ones. Hence unfavorably oriented faults in the southern Schwarzwald, e.g. with NE-SW strike, may be less visible in the elevation data and are thus statistically underestimated. However, predominant NW to NNW strike directions and prediction of strike-slip reactivation of these faults correlate well with nodal planes determined for the southern Schwarzwald [Bonjer et al., 1984; Bonjer, 1997; Kastrup et al., 2004]. Correlation of natural seismicity to individual fault traces (identified as lineaments) seems futile because of uncertain fault geometries and hypocenters as deep as 30 km. Both ASTER- and LIDAR-based lineament maps outline heterogeneous spatial distributions of the lineaments with the predominant WNW-ESE-, N(NE)-S(SW)-, and NNW-SSE-trends that are also well displayed by well-documented faults (Fig. 6.1B). Heterogeneous distribution of lineaments is expressed by apparent lower lineament densities in the CSGC and higher lineament densities in the SSC. The origin for these heterogeneities is not yet understood, but may be related to the different lithologies since gneisses prevail in the CSGC whereas granites prevail in the western SSC. Cooling and associated embrittlement of the crystalline basement during exhumation occurred during late Variscan times within a predominant E-W-extensional to transtensional stress field [Grimmer et al., 2016]. Brittle faulting in the gneisses developed in cooling mylonitic shear zones that grade locally into cataclastic shear zones and hence from ductile to brittle faulting [e.g. Sibson, 1977; Krohe and Eisbacher, 1988; Eisbacher et al., 1989a]. These cataclastic fault zone may follow the structural grain of the inclined mylonitic shear zones and thus show smaller dip angles than faults and fractures in the granites. Here, orientation of the earliest faults and fractures is most likely expressed by dykes in the batholiths displaying the predominant NW-SE-, NE-SW-, and N-S-trends (Fig. 6.1B). With larger dip angles, and hence with more linear fault traces on the land surface, these faults may be easier to detect as lineaments in the crystalline basement rocks.

6.6 CONCLUSION

We presented three lineament analyses in crystalline basement rocks based on two digital elevation models (ASTER, LIDAR) and one satellite imagery data set in order to identify fault traces and their possible neotectonic activity in the seismically active southern Schwarzwald. In each analysis lineaments were identified in the Paleozoic basement. Our findings are in contrast to existing geological maps on which the crystalline basement appears to be devoid of faults but match well with fault patterns that have been documented for the Triassic cover rocks in the vicinity. Assuming

that the identified lineaments represent fault zones, our lineament analyses provide additional structural geological information for the southern Schwarzwald area.

A statistical assessment of the obtained lineament sets was performed to quantify the impact of the resolution of the elevation data on the lineament extraction. Evaluation of orientation, average length, and the total length of mapped lineaments reveals that for an increase of the spatial resolution of the elevation models from 30 m x 30 m to 5 m x 5 m the total lineament lengths decrease by about 40% and the average lineament lengths decrease by about 60%. Regarding the lineament orientations, similar predominant trends are observable in all data sets but with a slightly different weighting of individual trends. However, predominant NE-, N-, NNW-, and NW-directions of the lineaments that are observed in all data sets correlate well with known large-scale faults and associated minor faults and fractures in the southern Schwarzwald.

Comparison of the lineament sets furthermore allow to quantify maximum (censoring bias) and minimum (truncation bias) observable lineament length for each elevation model. Resolution of our elevation data sets has no significant influence on the censoring bias of approximately 8 - 10 km. In contrast, the truncation bias seems to be dependent on the elevation model with an about 50% larger truncation length for the satellite imagery (2250 m) compared to the LIDAR-DEM₅ and the ASTER-DEM data sets (1700 m). Within both limits, all lineament-length-distributions follow the well constrained power law distribution that is documented elsewhere for fault and fracture systems. Our approach shows how statistical assessments significantly improve the reliability of lineament mapping studies.

Application of a slip- and dilation tendency analysis on the resulting fault pattern in the southern Schwarzwald reveals the highest reactivation potentials for NW-SE and N-S striking faults as left- and right-lateral strike-slip faults within the ambient stress field. Normal faulting may occur along NW-striking dip-slip faults. Interestingly, the most frequently mapped lineament strike directions in all three data sets are oriented favorably for reactivation. Assuming that active fault zones are expressed by well-marked fault traces on the land surface, our observation may point to neotectonic activity along Paleozoic (N)NW to (W)NW trending fault zones.

Since worldwide coverage with high resolution digital elevation models is constantly increasing, lineament mapping in combination with slip- and dilation tendency analysis are suitable tools to quickly get first order results of the structural inventory and critically stressed

faults, particularly in very large areas lacking detailed structural information and with bad outcrop conditions.

ACKNOWLEDGMENTS

This study is part of the BWPLUS project “Kombinierte Voruntersuchungen für ein Tiefengeothermie-Labor” - L75 14001-14004. Thanks to the Landesamt für Geoinformation und Landentwicklung (LGL), Landesanstalt für Umwelt, Messungen und Naturschutz (LUBW), Ministerium für Umwelt, Klima und Energiewirtschaft Baden-Württemberg for providing the elevation data. Thanks to the EnBW Energie Baden-Wuerttemberg AG for providing in-situ stress measurements. Thanks to Prof. P. Blum for very fruitful discussions on fracture patterns and geostatistics. Finally, we would like to thank H.J. Franzke, W. Werner, and H.U. Wetzel for providing the original data of [Franzke et al. \[2003\]](#).

7

ESTIMATING FAULT ACTIVITIES BY REMOTE SENSING AT A GEOTHERMAL RESERVOIR ANALOGUE OF CRYSTALLINE ROCKS

7.1 INTRODUCTION

As described in Chapter 6, geological maps of the southern Schwarzwald area highlight the lack in structural geological information. Large areas of the seismically active crystalline basement appear to be devoid of faults. This is in marked contrast to the abundantly mapped faults in the Triassic cover rocks of the vicinity and does not reflect the complex tectonic evolution of this area. Conducted lineament analyses additionally indicate high densities of simple and composite linear features in this area, which presumably reflect tectonic processes. Geomechanical characterizations of these lineaments let us conclude that a group of lineaments is favorably oriented for frictional failure in the ambient state of stress. Neotectonic activity in the southern Schwarzwald, probably related to reactivation of Variscan fault trends, seems plausible and moderate seismic activity in this area [e.g. [Bonjer, 1997](#); [Kastrup et al., 2004](#)] clearly points at active, brittle deformation processes. However, extensive field work campaigns can fill the gap of missing information but the size of the study area of about 2000 km² quite obviously impedes the gain of detailed data in an appropriate time span. To still further evaluate (neo)tectonic activity in the southern Schwarzwald, a vast variety of geomorphological techniques can be applied. Especially morphotectonic approaches have been developed to quantitatively or qualitatively designate the interplay of active deformation processes in the upper crust and consequent morphological changes of landforms and landscapes.

Generally, shape of the Earth's surface is understood to reflect dynamic processes of exogenous and endogenous forces that interacted as result of an energetic disequilibrium. Landforms and landscapes change to attain equilibrium conditions in a nonsteady environment. This can be understood as continuous competition between tectonic forces that tend to build up topography and surface processes that tend to reduce topography. Numerous conceptual models and

techniques in tectonic geomorphology address to define this balance [e.g. Burbank and Anderson, 2012; Bull, 2007]. They always have to tackle the inherent complexity of landscape evolution because individual (tectonic and surface) processes occur at several spatial and temporal scales and because they are linked with multiple levels of feedback.

This chapter aims to test several morphotectonic approaches with respect to their applicability in crystalline basement rocks. Therefore we focus on two different scales: 1) the entire area of the southern Schwarzwald Crystalline to aim at a more regional characterization of active deformation processes, such as uplift motion or block rotation; 2) the Vorwald fault zone (see Fig. 6.1B) to investigate applicability of morphotectonic and hydrographic methods for identification of neotectonic fault activity along this major variscan fault trend. A number of research studies have been aimed at the similar focus to infer the tectono-sedimentary history of the area between the southern Schwarzwald and the Alpine foreland. A brief summary, which mainly bases on the comprehensive studies of Haldimann et al. [1984]; Naef et al. [1985]; Müller et al. [2002]; Ziegler and Dèzes [2007]; Ziegler and Fraefel [2009], is given in the following section.

7.2 NEOGENE EVOLUTION OF THE SOUTHERN SCHWARZWALD

7.2.1 *Uplift of the southern Schwarzwald block*

The Cenozoic tectonic history of the southern Schwarzwald and the northern foreland of the Alps was dominated by two main tectonic events: the main phase of the Alpine orogeny and the formation of the URG (see Chapter 3). During the Oligocene to early Miocene rifting phase, the entire URG subsided continuously. During Neogene, subsidence solely continued in the northern part of the URG. The southern parts of the URG and the adjacent graben shoulders were uplifted and subjected to erosion during late Burdigalian (early Miocene) to early Pliocene times [Dezes et al., 2004; Ziegler and Dezes, 2005]. Phases of uplift of the Schwarzwald basement can be inferred from the sedimentary record of erosional Molasse deposits such as the Jura-Nagelfluh. Onset in sedimentation of these conglomerates, that were shed from the Schwarzwald southeastwards, point at rapid bedrock uplift that started in the late Aquitanian and peaked between 17-21 Ma during the Burdigalian to Serravallian [Müller et al., 2002]. The overall uplift rate of the Schwarzwald Crystalline is purely constrained but can be deduced from the vertical uplift of Mesozoic cover rocks that outcrop E of the crystalline basement. Here, cumulative uplift of about 800 m (SW of Tuttlingen; about 50 km E of the Feldberg) and 500-600 m (NE of Ulm) can be inferred from

a 150 km long coastline that was formed within the Upper Jurassic units by a marine transgression during Burdigalian [Geyer and Gwinner, 2011]. Mean uplift rates of 0.04-0.05 mm a⁻¹ are calculated for the area of Tuttlingen if constant uplift motions are assumed but the observed E-W gradient in overall vertical uplift suggests that motion rates are even larger towards the W, in the central Schwarzwald area. Comparable uplift rates of 0.04-0.1 mm a⁻¹ (for the last 10 Ma) have been deduced from mass balance calculations of the Schwarzwald orogen, which indicate integrative bedrock uplift rates of 0.6-1.2 km between 40 and 10 Ma and 0.4-1.0 km within the last 10 Ma [Roll, 1979]. Thermo-chronological studies in the Schwarzwald Crystalline confirm this phase of tectonic activity since they indicate an accelerating cooling trend from early Miocene times onward that, probably, can be attributed to bedrock uplift and erosional unroofing [Link, 2009; Timar-Geng et al., 2006a,b; Dresmann et al., 2010]. Rapid uplift of the Schwarzwald basement during Burdigalian was accompanied by the volcanic activity in the Kaiserstuhl (15-19 Ma) and Hegau (16.2-6 Ma) area [Geyer and Gwinner, 2011]. After this early Miocene phase of rapid uplift, the crystalline basement continued to rise slowly in response to its isostatic adjustment to erosional unloading. Geodetic data confirm Quaternary activity in the Schwarzwald Crystalline and point at differential fault related uplift motions of large scale crustal blocks. Horst structures show uplift rates in the range of 0.1-0.25 mm a⁻¹ [Müller et al., 2002] and 0.2-0.3 mm a⁻¹ [Demoulin et al., 1998] whereas graben systems such as the Bonndorf graben show gradual subsidence since Miocene.

7.2.2 Evolution of the drainage pattern

Variation in the Schwarzwald drainage system generally was driven by topographic changes, which were induced by tectonic and climatic processes and which controlled deposition patterns of the adjacent sedimentary basins. The drainage pattern shows significant variations during the last 20 Ma as response to the Neogene uplift of the Schwarzwald basement and formation of the Jura fold-and-thrust belt (JFTB). Both tectonic activities exerted strong control on the location of the repeatedly shifting watersheds between the rivers Danube, Doubs, and Rhine that flow into the Black Sea, the Mediterranean, and the North Sea, respectively [e.g. Ziegler and Fraefel, 2009; Reiter et al., 2015].

During late Oligocene, the Schwarzwald area was characterized by low topographic reliefs. Rivers almost entirely drained to the SE, toward the Molasse basin. Burdigalian uplift of the Schwarzwald block caused development of a drainage system that was controlled by S- to SE-directed consequent rivers. At this time, the proto-Rhine drained the URG northwards, N of the watershed near the Kaiserstuhl.

The onset of the Late Miocene JFTB formation between ~8-5.3 Ma changed the general drainage direction in the Molasse basin from SW to NE that can be regarded as precursor of the Aare-Danube river system [Ziegler and Fraefel, 2009]. Progressive subsidence of the Bresse Graben at ~4.2 Ma caused the separation of the paleo-Aare from the Danube drainage system and the deflection of the paleo-Aare towards the W along the southern flank of the Schwarzwald [e.g. Ziegler and Dèzes, 2007; Ziegler and Fraefel, 2009]. This led to the amalgamation of the paleo-Aare with the proto-Doubs resulting in the Aare-Doubs river system.

In late Pliocene (~2.9 Ma), uplift of the Bresse Graben and coeval subsidence of the southern URG led to the deflection of the paleo-Aare to the north into the Rhine Graben and finally to the amalgamation with the proto-Rhine. The watershed between the North Sea and the Mediterranean Sea, thus, shifted towards the south at the southern end of the URG. Gradual subsidence of the graben basin with accompanying uplifting of the graben shoulders produced a new, deeper erosional base level with a short flow path to the North Sea. At this times, the Danube catchment area was reduced gradually but still included the Alpine Rhine. At ~1.7 Ma, ongoing subsidence of the Upper Rhine Graben caused eastwards directed incision of the Aare-Rhine tributaries towards the Danube system. [Ziegler and Fraefel, 2009; Villinger, 1998]. The Rhine river system was extended systematically eastwards capturing more of the Danube headwaters in response to headward erosion, assisted by the run-off of glacial melt waters during the Donau/Günz glacial stages [Villinger, 1998]. As a result, the Aare-Rhine tributaries captured the Alpine headwaters of the river Rhine in the area of Lake Constance.

During the Quaternary the Rhine river tributaries in the Schwarzwald area continued to incise in response to the gentle bedrock uplift of the basement and ongoing subsidence in the URG area [Haldimann et al., 1984]. The capture of the upper section of the Feldberg-Danube by continuing river incision of the river Wutach between 19-20 ka marks the youngest deflection of a river from the Danube to the Rhine drainage system. Adaption to the new erosional base level (Danube 678m asl in Donaueschingen; Rhine 345 m asl at the Aare confluence) caused formation of the up to 150 m deep Wutach gorge, which is interpreted to be incised in only 6 ka ($\sim 25 \text{ mm a}^{-1}$) during the late Würmian pleniglacial under periglacial conditions of the southern Schwarzwald [Einsele and Ricken, 1995].

7.3 INPUT DATA AND METHODS

7.3.1 *Geomorphological indices*

In this study, calculation of morphotectonic and hydrographic parameters focuses on the crystalline basement rocks of the southern Schwarzwald. Therefore, invariable climatic conditions throughout the study area and equivalent rock strength values for each rock type are assumed. These assumptions reflect a first order approach only but are basic requirements for comparison of landscape forms, i.e. for evaluation of exhumation and erosion processes. The study aims to characterize the topographic form of the landscape (surface roughness) in order to identify uplift and subsidence motion of crustal blocks. For the ZR-ratio calculation ASTER-DEM elevation data were used with a spatial and vertical resolution of 27×27 m and < 1 m, respectively. For the analyses of the river response high-resolution LIDAR-DEM₅ elevation data were used with a spatial and vertical resolution of 5×5 m and < 0.5 m, respectively.

Morphological forms of a landscape almost always reflect surface-shaping processes, operating on a variety of timescales. As a result, observed geomorphology may be representative of tectonics and climate that are not observable at the present time and probably do not point at recent crustal deformation processes and neotectonic fault activity. To still characterize the latter ones we used precise leveling data, which are described in the next section.

7.3.2 *Precise leveling data*

Generally, precise levelling campaigns provide very accurate data on relative vertical movements of the ground surface, i.e. when a) a dense network of benchmarks exists, and b) measurements have been repeated over a long period of time. Both basic requirements are fulfilled for an existing leveling network in SW Germany. These precise leveling data, which have been kindly provided by K. Zippelt from the Geodetic Institute (GIK) at KIT, were used to infer recent uplift or subsidence rates for the crystalline basement of the Schwarzwald area. Discussion on data acquisition and data treatment is far beyond the scope of this chapter but information are published by [Fuhrmann and Zippelt \[2013\]](#); [Fuhrmann et al. \[2013, 2014\]](#).

Precise leveling measurements base on the fundamental principle that observations of levelling are height differences between fixed benchmarks. Individual heights of these benchmarks can be estimated by consecutively adding the measured height differences to the height of a starting point, a benchmark with a well-known absolute height. In the southern Schwarzwald, the individual benchmarks are arranged in first and second-order leveling lines

that are grouped together in closed loops and build up a geodetic network (Fig. 7.1).

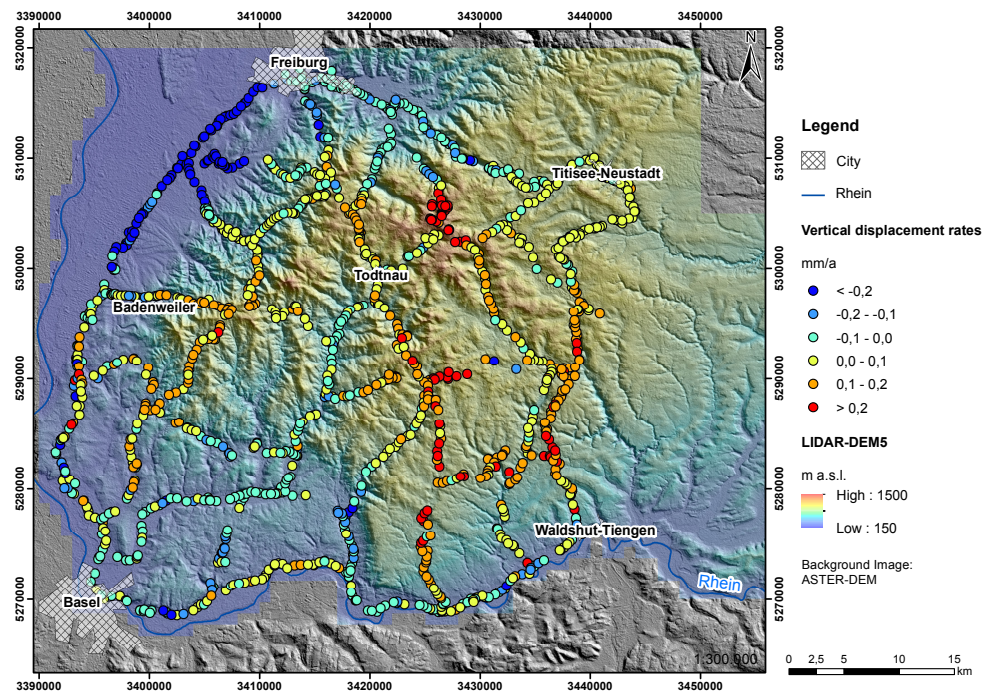


Figure 7.1: Leveling lines in the southern Schwarzwald. Shown are the relative motion rates with respect to the reference point in the city of Freudenstadt. Data Fuhrmann et al. [2014].

The marginal benchmarks of the network belong to a first-order loop whereas the internal benchmarks build up second-order loops. Due to a longer time period of repeated measurements, the first one yield a higher accuracy for vertical displacement rates [Fuhrmann et al., 2013, 2014]. Repeated levelling measurements along these loops finally allow calculation of vertical displacement rates (relative to a reference point in the city of Freudenstadt) for the entire network.

Measurements of vertical displacement rates have been conducted in SW Germany for more than half a century [Fuhrmann et al., 2014, and references therein]. Generally, they point to moderate height changes and tilt movements of crustal blocks in the southern Schwarzwald basement. Maximum vertical displacement rates between 0.3 and 0.4 mm a^{-1} are observed [Mälzer et al., 1988; Demoulin et al., 1998]. Since displacement rates and individual measurement errors (kinematic error, model-related error, loop error) are almost always of same order of magnitude (Fig. 7.2A), significance of the geodetic vertical motion rates may be questionable but probably indicate regional trends of uplift and subsidence.

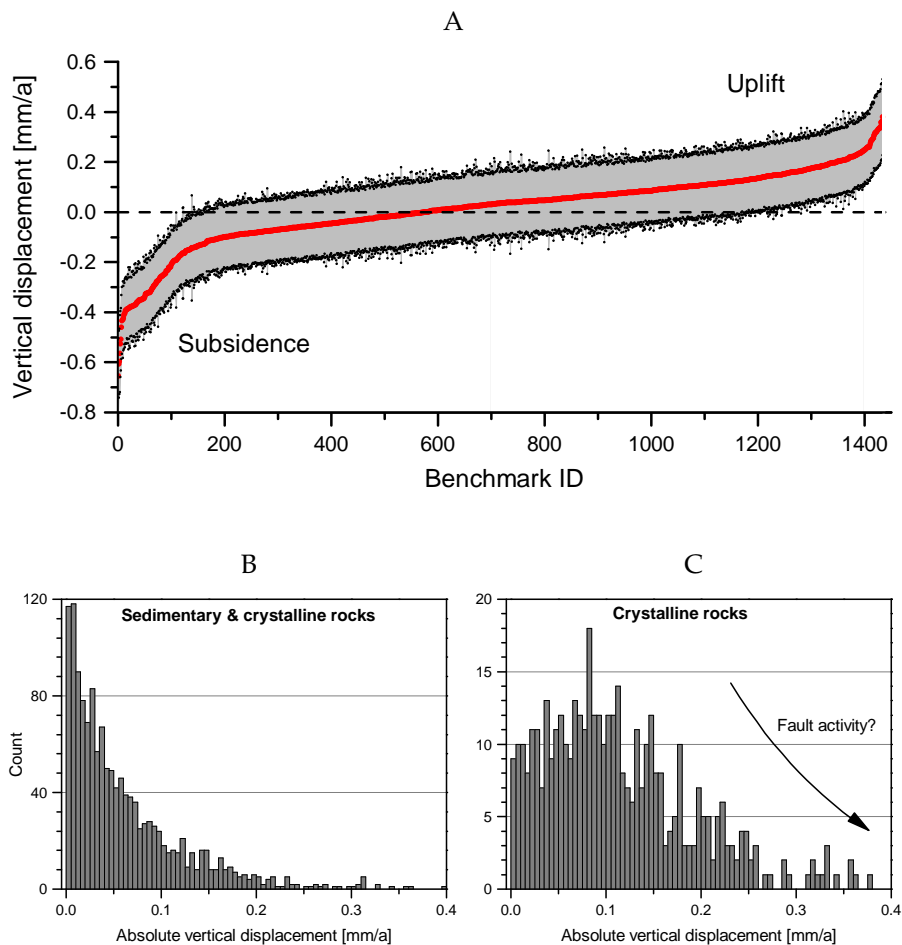


Figure 7.2: Precise leveling data of the southern Schwarzwald for first and second-order leveling lines. Shown are the displacement rates and error margins related to the data acquisition and data treatment procedures (A) and histograms of the absolute vertical motion rates between two neighboring benchmarks; undifferentiated for all benchmarks of the data set (B) and for benchmarks that are solely located in crystalline basement rocks (C). Motion rates larger than 0.3 mm a^{-1} exceed inherent error margin and may point at local fault activity.

It is noteworthy that interpretation of the leveling data depends on the rock type where the individual benchmark stands. Quality of the leveling data is significantly impaired when benchmarks are prone to non-tectonic natural phenomena or anthropogenic influences such as groundwater and oil extraction, consolidation of sediments, and mining activities. For example, rifting-related vertical motion may partly accounts for the large subsidence rates within the graben center SW of Freiburg (Fig. 7.1) but non-tectonic processes cannot be ruled out. In order to derive tectonic deformation processes from the data, we excluded all benchmarks with questionable stands such as

in sedimentary rocks. In this study, interpretations of precise leveling data solely depend on data from benchmarks, which are located in gneissic and granitic rocks. An statistical comparison of both data sets is shown in Fig. 7.2B, C.

7.4 ZR-RATIO ANALYSIS

7.4.1 Introduction

Following [England and Molnar, 1990] vertical change of a land surface is determined by a) the rate at which bedrock is being carried upward (bedrock uplift rate); b) the rate of deposition at the surface; c) the rate at which material in the subsurface is compacting; and d) the rate of denudation:

$$\text{surface uplift} = \text{bedrock uplift} + \text{deposition} - \text{compaction} - \text{denudation}$$

Because compaction and deposition both occur primarily in sedimentary basins, they are generally ignored. Denudation results from the steady removal of material from a region and comprises two different processes.

- Erosional denudation (erosion) results from mechanical, chemical, and organic weathering of rock and includes the mass-movement processes that transport eroded material from the point of degradation.
- Tectonic denudation reflects tectonic deformation processes in an extensional regime and thus is typically associated with normal or transtensional strike-slip faults. This process, e.g. as observed for low angle detachments, can result in rapid removal of very large volumes of rock and thereby promote isostatic rebound.

Both processes lower the surface altitude and enhance thinning of the upper crust. Analysis of tectonically active landscapes requires documentation of rates of bedrock uplift, tectonic and erosional denudation, and related geomorphic processes. Topographic characteristic of the landscape, such as slope angles, river incision rates, river valley asymmetries, forms of escarpments and mountain fronts are proven suitable to constrain uplift and subsidence rates [e.g. Burbank and Anderson, 2012; Bull, 2007].

Surface roughness is regarded as a key land-surface parameter to both identify individual landforms and determine the processes acting upon them. A variety of methods, mainly dependent on the investigated scale, have been proposed to calculate topographic roughness [Grohmann et al., 2011]. Common to all is the observation that surface roughness of a landform is dependent upon a) the material properties, b) processes acting upon it, and c) the time elapsed since landform formation. We calculate roughness by application of a ZR-ratio analysis to define the characteristic relief and geomorphic expression of the Schwarzwald mountain range. This analysis aims to investigate the surface morphology to infer uplift or subsidence of the crystalline basement, which may indicate crustal deformation processes and point at neotectonic fault activity.

7.4.2 Methodology

The ZR-ratio is a dimensionless, geomorphic parameter which characterizes the topographic form of a landscape [Formento-Trigilio and Pazzaglia, 1998; Nash and Johnson, 2003] and can be calculated by a moving window technique for a grid of elevation data. The ZR-ratio is defined as

$$ZR = (\bar{Z} - \bar{R}), \quad (7.1)$$

where \bar{Z} is the local mean elevation and \bar{R} is the local mean relief. The local mean elevation is calculated from:

$$\bar{Z} = \sum_n Z_r / n, \quad (7.2)$$

where $\sum_n Z_r$ is the sum of elevation values within a circle of radius r (measured in number of cells in the grid). A circular window of the radius $r = 1\text{km}$ was used in this study. The parameter n is the number of elevation values within the circle of radius r . As a result, a kind of a low-pass filter is produced. The local mean relief is calculated in a similar way:

$$\bar{R} = (\bar{Z}_{\max} - \bar{Z}_{\min})_r \quad (7.3)$$

where Z_{\max} and Z_{\min} are the maximum and minimum elevation, respectively, within a circular window of radius r . Local mean elevation values are compared to mean relief values for each map grid. The ZR-ratio thus defines the surface morphology and determines the local ruggedness of a landscape. It describes how a landscape expresses variable rates of rock uplift or subsidence. A schematic sketch of different landscapes with their corresponding ZR-ratios are shown in Fig. 7.3.

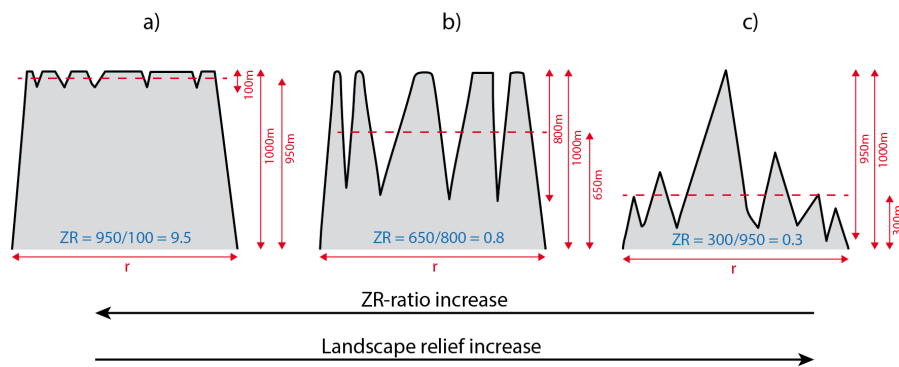


Figure 7.3: Exemplary calculation of the ZR-ratio for different topographic form of a landscape. (For further explanations see text.)

7.4.3 Results & Discussion

Southern Schwarzwald

The entire study area is characterized by a rather heterogeneous pattern for the ZR-ratio (Fig. 7.4 - 7.7). The URG area in the W, the Rhine river valley

in the S, and the eastern part of the crystalline Schwarzwald basement all show largest ZR-ratios of $ZR > 5$. These areas are characterized by flat landscape forms with a small surface roughness. The western part of the crystalline Schwarzwald basement, along the NNE-SSW striking main boundary fault of the URG, is characterized by a large surface roughness. Here, smallest ZR-ratios of $ZR < 1.5$ were calculated.

Despite a general NW-SE decrease in calculated ZR-ratios across the crystalline Schwarzwald basement, locally, large gradients of the surface roughness are observed. Sharp transitions in topographic roughness predominantly occur along river valleys (Fig. 7.4). From E to W, river valley reliefs successively increase in the study area. Topography along the upper reaches of the easternmost rivers (Wutach, Steina, Schlücht, Schwarza) shows almost no visible increase in relief by erosional processes whereas steep valleys were formed by the rivers at the W and SW flank of the southern Schwarzwald.

A general correlation between the ZR-ratios and the structural geological inventory seems questionable (Fig. 7.5, 7.6). Locally, e.g. along the river valleys of the Hauensteiner Alb and Schwarza or along the Wehratal shear zone (see Fig. 6.1B), the observed increase in topographic roughness seems to be related to structural zones of weakness. If these zones act as preferential rivers flow paths due to an increased bedrock erosion along them, it is likely that they have partially controlled formation and shape of the drainage pattern during uplift of the crystalline Schwarzwald basement. In this case the rivers partly follow preexisting fault zones which probably are hidden for lineament mappings due to their coverage by fluvial sediments. However, for large areas of the study area almost no significant correlation between the faults/lineaments and the topographic roughness is recognizable. Remarkably this also accounts for the NW-SE striking Bonndorf Graben system that shows gradual subsidence since the Miocene.

One should be aware of the fact that ZR-ratios do not allow unambiguous interpretations with respect to active tectonics. Distribution of ZR-ratios can be similar among contrasting regions and thus do not necessarily imply comparable tectono-sedimentary histories. Especially large ZR-ratios, which are calculated for plain topographies (see Fig. 7.3a), can be attributed to different tectonic settings. Such landscape forms are observed for areas that are characterized by subsidence, sedimentation, or intensive denudation. Large ZR-ratios thus can be calculated for both a sedimentary basin and a deeply-eroded, low-relief peneplain. It is obvious that the large ZR-ratios in the URG area and along the Rhine valley in the S (Fig. 7.4) are caused by sedimentation, which systematically decreases the topographic relief.

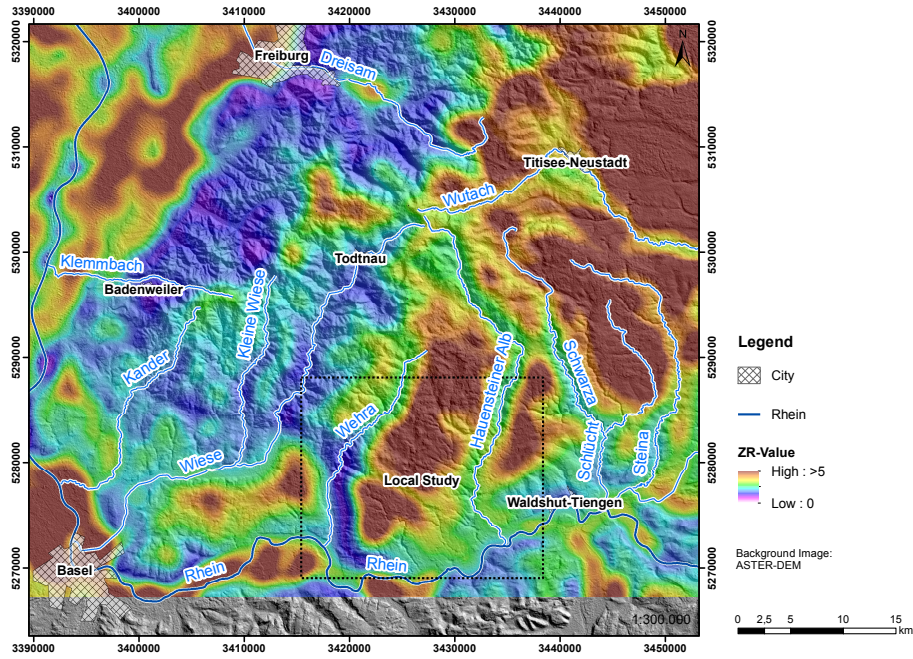


Figure 7.4: Surface roughness of the crystalline basement of the southern Schwarzwald as derived by the ZR-value calculation superposed by the major tributary stream network (line elements). Warm colors indicate a moderate, cold colors indicate a large surface roughness. For detailed explanation see text.

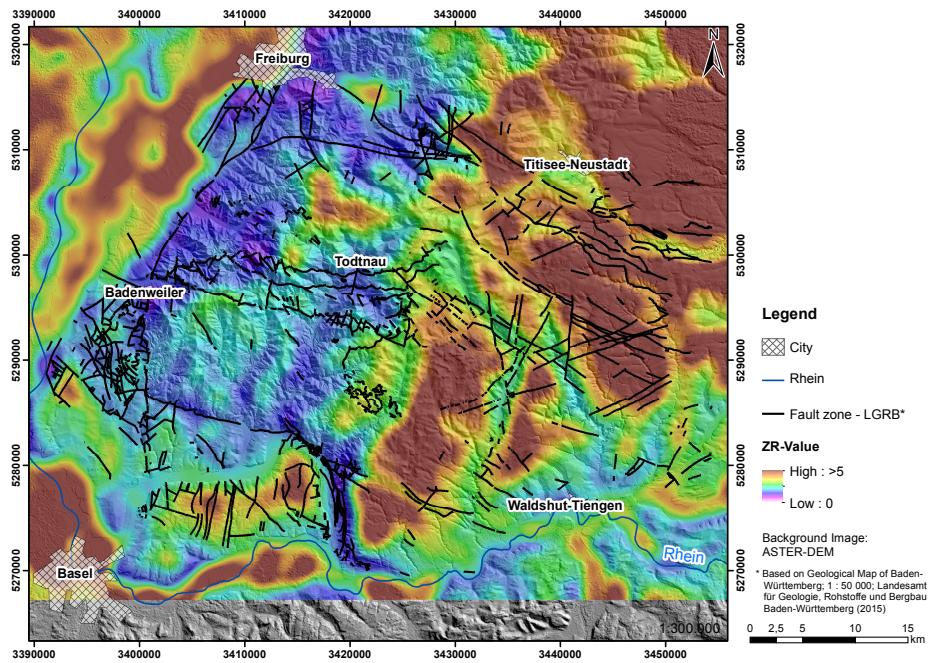


Figure 7.5: Surface roughness of the crystalline basement of the southern Schwarzwald as derived by the ZR-value calculation superposed by the mapped fault network (line elements). Warm colors indicate a moderate, cold colors indicate a large surface roughness. For detailed explanation see text.

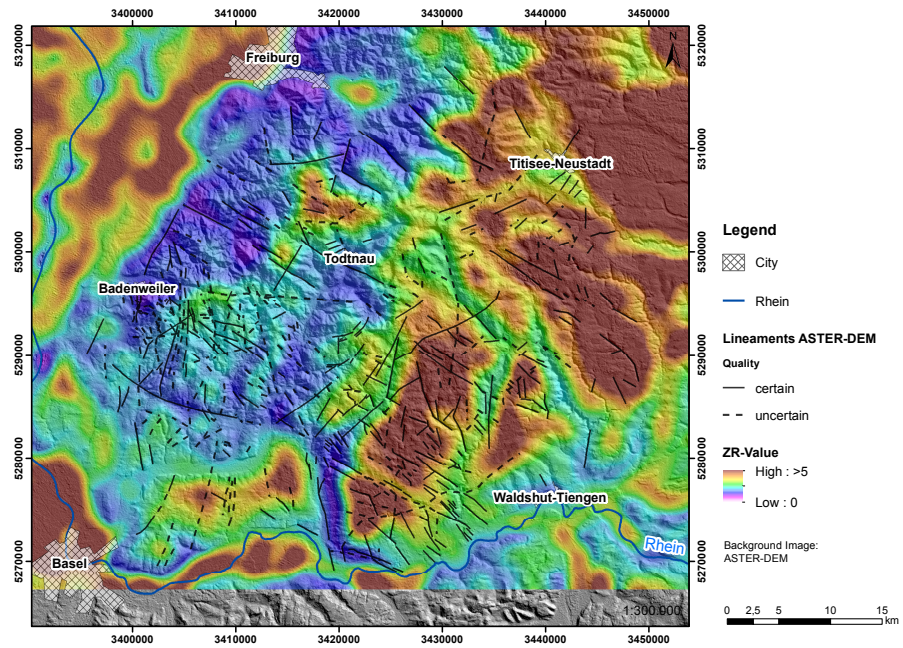


Figure 7.6: Surface roughness of the crystalline basement of the southern Schwarzwald as derived by the ZR-value calculation superposed by the identified lineaments of the ASTER-DEM data set (see Chapter 6, line elements). Warm colors indicate a moderate, cold colors indicate a large surface roughness. For detailed explanation see text.

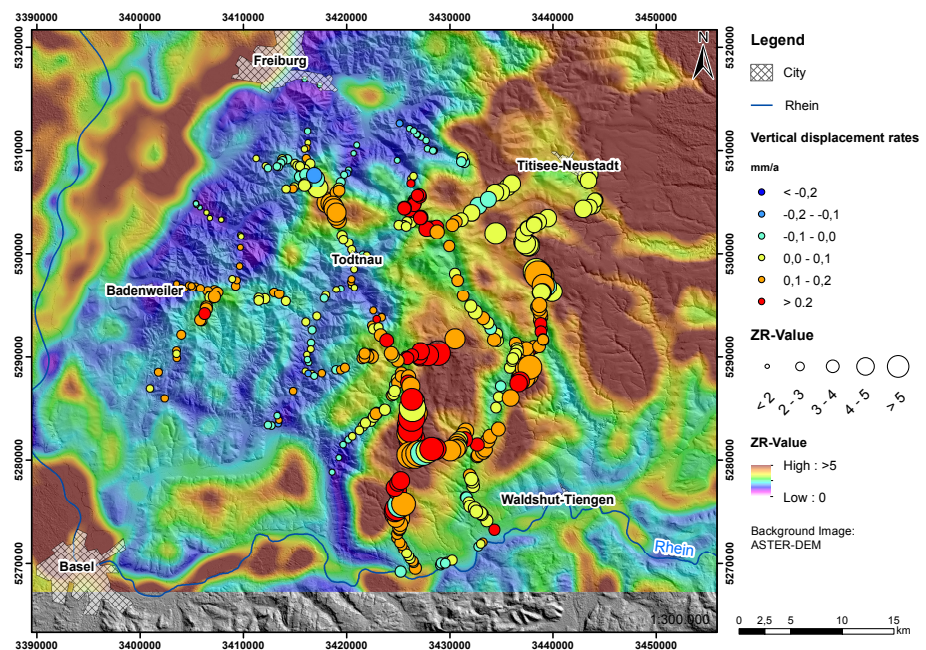


Figure 7.7: Surface roughness of the crystalline basement of the southern Schwarzwald as derived by the ZR-value calculation superposed by the vertical displacement rates, which are measured for benchmarks in crystalline rocks (circles). Warm colors indicate a moderate, cold colors indicate a large surface roughness. For detailed explanation see text.

The large ZR-ratios in the eastern part of the Schwarzwald basement are of similar magnitude but point at a different tectono-sedimentary regime. Rather flat landscape forms with a low surface roughness in the crystalline Schwarzwald can be interpreted in different ways and can lead to the following, partly contradictory, inferences with respect to past and recent deformation processes:

- Case 1) Large ZR-ratios can be interpreted to point at a deeply-eroded, low-relief peneplain. For the Schwarzwald basement such a structural setting can be ruled out since a heterogeneous topography and steep longitudinal river profiles are contradictory to a low-relief non-constructional plain, which is solely controlled by its close approach to its erosional base level.
- Case 2) Large ZR-ratios can also be interpreted to indicate crustal blocks that are characterized by young and rapid uplift motion. When uplift rates significantly exceed those of erosion, rapid exhumation of crustal blocks occurs and mountain ranges are formed. In this case, a low surface relief does not indicate subsidence and sedimentation but rather beginning of erosional denudation in an area with young and rapid bedrock uplift. Fast exhumation of plateau-like crustal blocks then seems conceivable. Assuming this case to be valid for the study area, the general NW-SE gradient of the ZR-ratios and partly sharp transitions between local roughness distributions may indicate differential uplift motions of crustal blocks rather than a uniform basement uplift of the Schwarzwald Crystalline. Small ZR-ratios in the western part of the Schwarzwald basement hence can be interpreted to be the result of an 'old', early Neogene phase of uplift motion. Here, intense erosive and tectonic denudation successively increased the relief and ruggedness of the topography (see Fig. 7.3b, c). The topographic relief of the eastern part of the Schwarzwald basement would indicate a slight contrary tectonic history. The rather small surface roughness can be interpreted to indicate separated crustal blocks, which are affected by 'younger', probably late Neogene to Quaternary uplift motions and which are at the beginning of a new cycle of erosive and tectonic denudation. Differential uplift and Neogene and Quaternary block tectonics were repeatedly discussed for the southern Schwarzwald and are mostly attributed to the reactivation of pre-existing Variscan discontinuities in the crystalline basement [e.g. Huber and Huber-Aleffi, 1984, 1990; Müller et al., 2002].
- Case 3) Both case 1 and case 2 base on the assumption that lateral variations of the surface roughness are the result of bedrock uplift and pure tectonics that control the erosional denudation for a static erosional base level. For the southern Schwarzwald one has to consider a second mechanism that has led to a significant increase in fluvial erosion: the distinct lowering of the hydraulic base level in the course of the Neogene changes of the Schwarzwald drainage network (see Chapter 7.2.2). The change of the drainage direction of the Schwarzwald rivers from the Aare-Danube over the Aare-Doubs to the Aare-Rhine river system in the last ~5 Ma repeatedly moved the Rhine/Danube watershed towards the SE. Driven by the gradual subsidence of the southern URG and Neogene uplift of the Schwarzwald basement, the headward erosion of the Rhine, first from the Kaiser-

stuhl area (Freiburg) to the S (Basel) and later to the E, caused stepwise deflection of the Schwarzwald rivers towards the drainage direction of the Rhine. Catchment of the Schwarzwald rivers by the Rhine are clearly visible along their upper reaches, i.e. for the rivers Hauensteiner Alb, Schwarza, Steina, and Wutach. Here, sharp deflections of the river courses up to 90° point at the change in drainage direction from ESE to S. Discharge rates of the receiving streams probably increased significantly during late Miocene (adaption to the Aare-Doubs system) and late Pliocene (adaption to the Aare Rhine system) times. Due to the different hydraulic base levels between the Danube and the Rhine river (difference ~300-400 m), the Schwarzwald rivers needed to adapt to new erosional base levels. As a result, increased river incision rates and successive headward erosion of the tributary streams may forced development of steep river gorges and larger topographic reliefs.

Multiple levels of feedback between tectono-sedimentary processes hamper unambiguous interpretations of the calculated ZR-values as geomorphic expression of the Schwarzwald mountain range, i.e. when aiming at identification of active tectonics. Low relief landforms, such as observed for the E Schwarzwald area, may reflect Late Neogene and Quaternary bedrock uplift but also can be explained by the repeated shifting of the Danube/Rhine watershed. As observed for the 150 m deep Wutach gorge, distinct increases of the erosional rates (Wutach ~25 mm a⁻¹) point at rapid adaptations of Schwarzwald rivers to the erosional base level of the Rhine. The observed E-W variations in surface roughness throughout the Schwarzwald basement probably reflects the stepwise catchment of the Schwarzwald rivers by the Rhine, along the western and the southern flank of the Schwarzwald block. In this case the calculated ZR-values can be interpreted such that the change in surface roughness divides 'old' low relief topographies of the Danube drainage area from 'young' large relief topographies from the Rhine drainage area. However, precise leveling data from the last decades give evidence for Quaternary uplift and subsidence motion in the Schwarzwald area (Fig. 7.7). A correlation of large ZR-values (low reliefs) and recent uplift motions and vice versa is indicated by the data for large parts of the study area. Subsidence mainly is observed SE of Freiburg and along the Wiese river valley, whereas uplift motion is observed in the area N of Todtnau and in the SE part of the Schwarzwald. Rapid bedrock uplift thus can not be ruled out as driving mechanism of the landscape evolution of the Schwarzwald Crystalline.

Case study - Vorwald block

Our analysis aims to investigate the surface morphology to infer crustal deformation processes that point at neotectonic fault activity in the southern Schwarzwald. Spatial patterns in the leveling data seem to be related to differential uplift motions and thus indicate active crustal deformation processes in the crystalline basement. Assuming that these uplift motions are the expression of fault-bounded block tectonics, fault activity should be observed in the southern Schwarzwald. A case study in the area of the Vorwald block in the SE Schwarzwald was carried out to identify recent

deformation processes in the basement (Fig. 7.8 - 7.9).

The Vorwald block mainly consists of granitic basement rocks and is structurally separated from the surrounding units by the NW-SE striking Vorwald fault and Eggberg fault zones and the N-S striking Wehratal shear zone (Fig. 7.8A). The crystalline basement of the Vorwald block and north of it is characterized by a moderate topographic relief. Small ZR-values suggest plain landscape forms and a small surface roughness. As indicated by precise leveling data, the ZR-value distribution correlates well with measured vertical motions of the basement (Fig. 7.8A & 7.7). Rapid uplift of the Vorwald block with uplift rates that exceed those of the starting erosional denudation may result in development of plain topographies across the exhumed crystalline basement.

Tectonic compartmentalization of the Vorwald block is clearly indicated by steep valley slopes that lead to rapid increases in the surface roughness, i.e. along the Wehratal shear zone and the Eggberg fault zone. The trace of the Vorwald fault zone can be clearly followed in NW-SE direction although its topographic expression is less clearly developed. A lineament analysis (see Chapter 6) hints at the existence of several unmapped NW to NNW striking faults across the Vorwald block. In contrast to the Vorwald or Eggberg fault they exhibit a less dominant topographic expression (e.g. label D in Fig. 7.8A). Whether this is the result of a different style of faulting (south-dipping normal faulting of the Vorwald fault zone vs. subvertical strike-slip faulting within the Vorwald block), or whether the difference is an indicator for the duration of fault activity is difficult to prove. However, precise leveling data suggest fault activity within the Vorwald block. When considering solely the motion rates between two neighboring benchmarks, differences in displacement rates that are larger than 1 mm a^{-1} probably point at fault activity between them. In the study area such a relation can be repeatedly observed (Fig. 7.8B). Interestingly no distinct variations in vertical motions are apparent across the first-order Vorwald fault zone. To the N and S local deviations in vertical motion seem to be related to individual NW to NNW striking lineaments, which is in good agreement with the results of our geomechanical analyses (see Chapter 6). Since individual structures show almost no topographic expression of activity, although leveling data point at recent slip movements, we conclude that a) recent fault activity in the crystalline basement exists, probably by sinistral and dextral strike-slip reactivation of Variscan trends, and b) fault activity may be young to increase the surface relief significantly.

Finally we can conclude that the morphotectonic analysis of the southern Schwarzwald basement and the precise leveling data clearly point at neotectonic activity of predominantly (W)NW-(E)SE striking faults. Fault traces of these structures at the surface, e.g. of the Vorwald Fault Zone, can be clearly followed along their fault traces on the surface by often clearly developed topographic expressions. Precise levelings across such faults indicate displacement rates of $>1 \text{ mm a}^{-1}$. Earthquake activity in the study area gives further evidence for neotectonic activity of these structures. Slip- and dilation tendency analysis on the obtained fault pattern reveals the highest reactivation potentials for WNW-ESE and NNE-SSW striking faults as left- and right-lateral strike-slip faults. These faults probably are critically stressed for shear reactivation in the ambient state of stress.

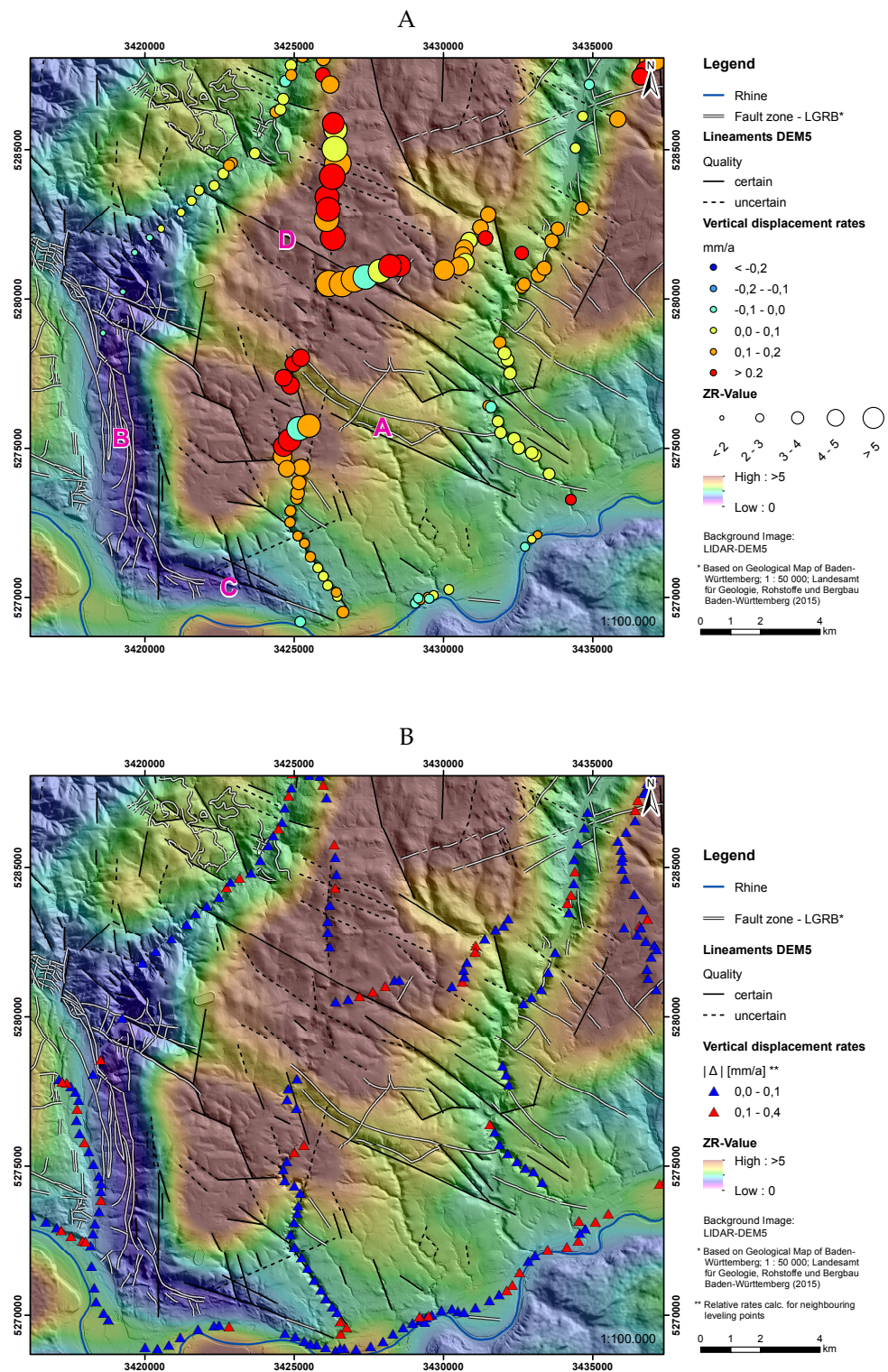


Figure 7.8: Morphotectonic analysis of the Vorwald block in the SE Schwarzwald. The ZR-value distribution (color code) reveal the topographic relief of the crystalline basement; warm colors indicate a moderate, cold colors indicate a large surface roughness. Neotectonic activity of the mapped faults and lineaments (line elements) is indicated by precise leveling data (circles). Shown are vertical displacement rates for benchmarks in crystalline rock, rel. to the reference point in Freudenstadt (A) and between two adjacent benchmarks (B). Data Fuhrmann et al. [2014]. Labeling: A: Vorwald Fault Zone, B: Wehratal Shear Zone, C: Eggberg Fault Zone

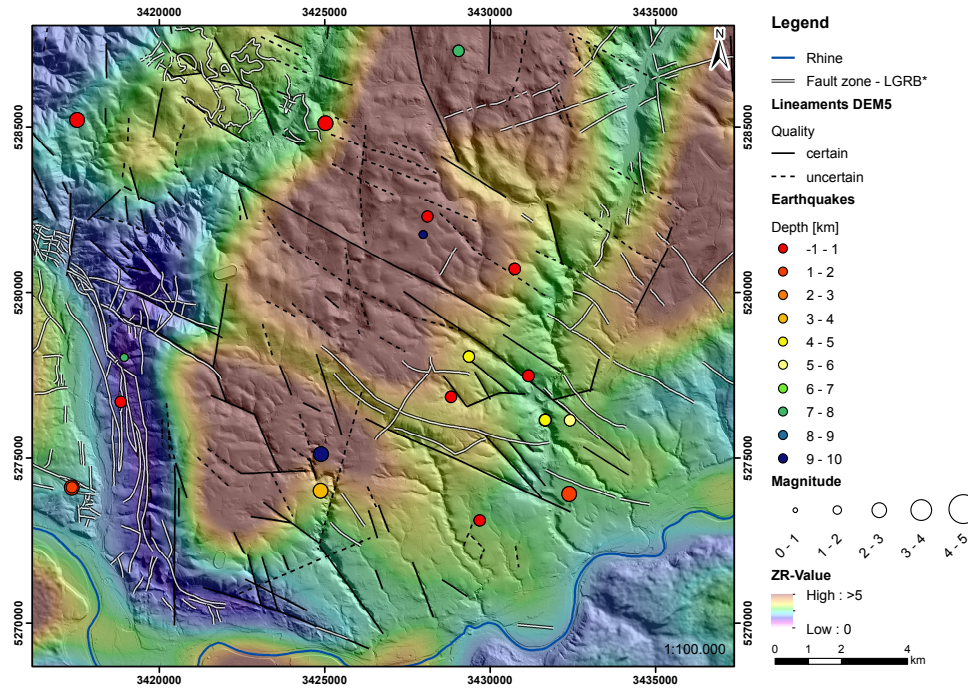


Figure 7.9: Morphotectonic analysis of the Vorwald block in the SE Schwarzwald. The ZR-value distribution (color code) reveal the topographic relief of the crystalline basement; warm colors indicate a moderate, cold colors indicate a large surface roughness. Seismic activity of individual fault zones (line elements) can not be verified due the lack in information regarding the fault geometry but earthquake distribution still point at a general neotectonic activity of NNW and NW structures.

These WNW-ESE and NNE-SSW striking faults may accommodate differential uplift motion within the basement. Earthquake focal plane solutions show that strike-slip faulting with secondary normal faulting are the dominant faulting regimes (Fig. 7.9; Plenefisch and Bonjer [1997]; Bonjer [1997]; Kastrup et al. [2004]).

CONCLUDING DISCUSSION

8.1 IMPLICATIONS FOR EGS RESERVOIRS IN THE UPPER RHINE GRABEN

Generally, determination of structural geological and geomechanical reservoir properties is limited to time and cost-consuming drillings that finally reflect only a small portion of the whole reservoir. Complementary studies in reservoir analogues have often been shown, e.g. for oil and gas production, that they can fill this lack in information. However, reliability of the knowledge transfer from the analogue into the reservoir must always be proved.

In this thesis structural geological, geomechanical, and geomorphological studies have been conducted for the crystalline basement of the southern Schwarzwald (Section 6 and 7), which is assumed to be a fairly good analogue for the EGS relevant, petrothermal reservoir rocks in the URG. Lineament mappings reveal existence of predominant fault strike directions in the basement with a distinct maximum to NNE-SSW in the FRANZKE data set and to (W)NW-(E)SE in the ASTER-DEM and LIDAR-DEM5 data sets (Section 6.4.2). Slip- and Dilation Tendency analyses point at increased shear reactivation potentials of subvertical structures that strike approximately W(NW) or (E)SE. When assuming that the statistical distribution of the described fault pattern in the Schwarzwald analogue was representative, then the proposed geomechanical anisotropy should be also observable in the crystalline basement within the graben center.

Verification of this structural pattern in the URG is challenging since only few information on fault distributions in the basement are available. The former Basel geothermal site provides a perfect access to an enhanced EGS reservoir in a distance to the outcropping analogue rocks of only 10 km. Previous analysis of the hydraulic stimulation and the seismic risk allows to compare the occurrence of critically stressed fractures/faults in a natural and engineered environment.

8.1.1 *The 2006 stimulation of the Basel EGS*

In 2006 approximately 11'500 m³ of water were injected into the 5 km-deep well in Basel. The granite in the open hole section below 4629 m depth was hydraulically stimulated with a maximum wellhead pressure of 30 MPa and a maximum flow rate of 50 l s⁻¹ [Häring et al., 2008]. During the hydraulic stimulation, more than 13'500 earthquakes were induced close to

the injection point [Dyer et al., 2010]. Most of the seismicity occurred during the water injection with event magnitudes of up to M_L 2.6. Although flow rate was first reduced and later stopped, a M_L 3.4 event occurred five hours after shut in. Figure 8.1 gives a brief overview of the structural geological information that have been inferred from analyses of the induced seismicity.

The hypocenters of the more than 3500 locatable events are restricted to a NNW–SSE oriented lens-shaped cloud, about 1.2 km in diameter and 200 m wide, with a single offsetting branch to the ESE [Baer et al., 2007; Deichmann et al., 2008]. The overall alignment of the microseismicity is hence consistent with the estimated direction of maximum horizontal stress of $N_{144}^{\circ}E \pm 14^{\circ}$ [Valley and Evans, 2009], which is furthermore in excellent agreement with the stress field derived from the natural seismicity observed in the wider Basel region [Plenefisch and Bonjer, 1997; Kastrup et al., 2004]. Fault plane solutions for the 28 strongest events, with M_L between 1.7 and 3.4 that occurred between 3.12.2006 and 6.5.2007, indicated movements on approximately E-W and N-S striking fracture planes (Fig. 8.1d; Deichmann and Ernst [2009]; Deichmann and Giardini [2009]). Processing of individual multiplets, representing groups of events that can be interpreted as having similar focal mechanisms and rupture plane orientations, clearly point at reactivation of distinct fracture/fault planes in the reservoir. They generally vary in azimuth and dip but indicate preferential stick-slip movements along steeply dipping and NNW and ESE striking structures (Fig. 8.1e; Dyer et al. [2010]; Kraft and Deichmann [2014]). This observation of rather NNW-SSE trending crustal discontinuities, as inferred from the multiplets processing, and rather N-S and E-W striking nodal planes of the 28 largest events, as derived from the single event analysis, clearly point at different rupture plane orientations for large and small magnitude events. Whereas the interpreted rupture planes from the multiplets show rather small angles to S_H , the fault plane solutions of the large magnitude events point at shear angles of approximately 45° . The reason for this discrepancy is still in the focus of scientific studies, which often suggest that uncertainties in the data account for it [e.g. Kraft and Deichmann, 2014]. However, slip- and dilation tendency analyses may explain these findings.

Dyer et al. [2010] have shown, that frictional failure started close to the casing shoe at the start of the stimulation. Many of these early microseismic events represent a NNE trending multiplet, indicating reactivation of a NNE trending rupture plane in close vicinity of the well. Häring et al. [2008] have shown that the predominant natural fracture set in the reservoir contains (N)NW-(S)SE striking features with steep dip angles $>60^{\circ}$ to W-SW. Two major cataclastic fractures zones of unknown geometry are repeatedly assumed to intersect the open hole section. Analysis of logging data by Ziegler et al. [2015] furthermore indicates that fractures of this dominant structural trend a) are spatially clustered into 10-100 m wide zones of high fracture frequency, b) show considerable argillic alteration, and c) are partially open. These zones are unfavorably oriented for shear reactivation in the ambient stress field (Fig. 8.1e, f). They are characterized by small slip tendencies and very large dilation tendencies, i.e. when they have high dip angles. I suggest that continuous pressurization caused dilatant opening of these fractures, probably without exceeding the minimum principal stress. In this case, pure shear motions along these structures play only a subordinate role albeit they were observed as repeated stick-slip events. Repeating

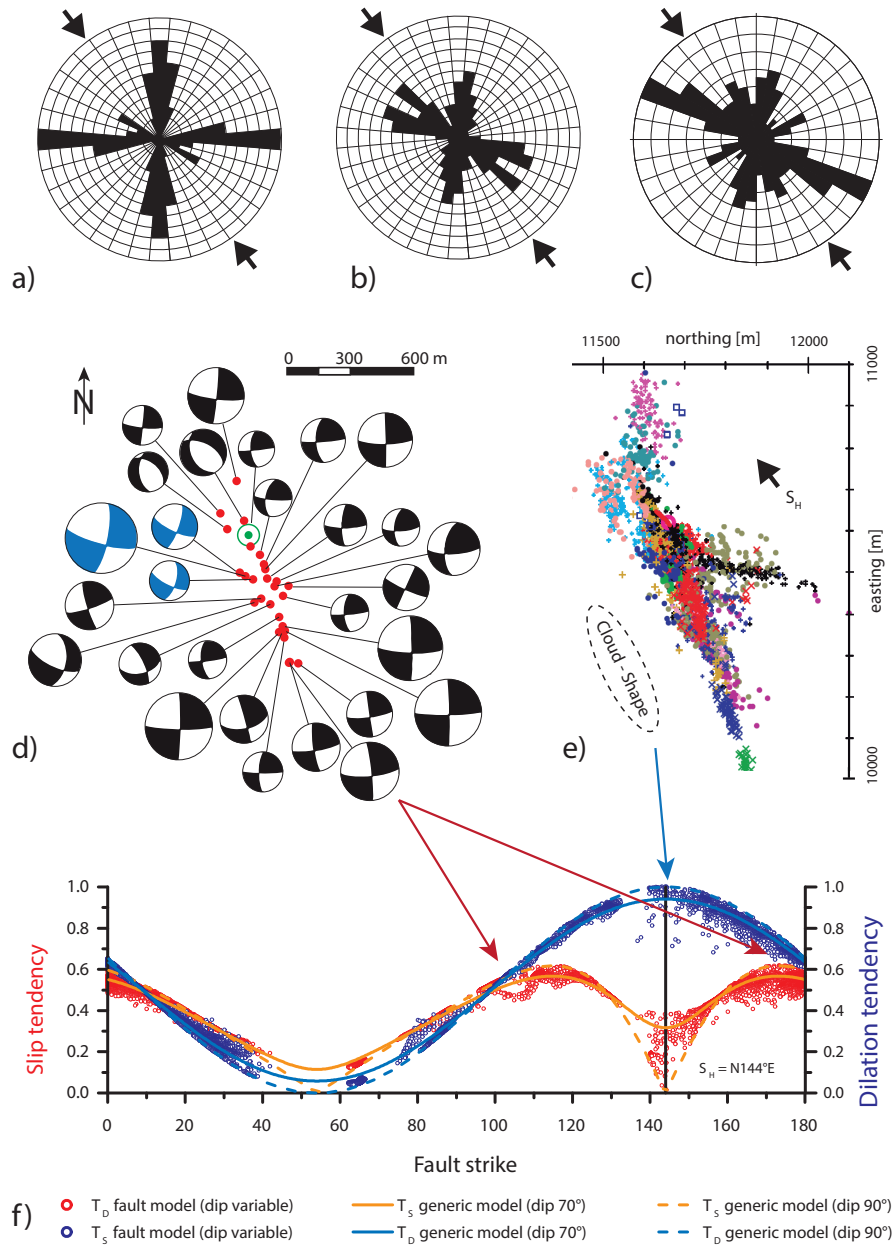


Figure 8.1: Analysis of the seismicity induced during the Basel EGS stimulation in 2006. Rose diagrams show the strike of the focal mechanism nodal planes for the largest 28 induced events (a), 30 naturally occurring earthquakes (b) [both after [Deichmann and Giardini, 2009](#)], and for the LIDAR-DEM5 lineament mapping in the southern Schwarzwald (c; see section 6). (d) Epicenter map with the focal mechanisms for the 28 largest events [after [Deichmann and Ernst, 2009](#)]. The size of each stereograph is proportional to magnitude ($1.7 \leq M_L \leq 3.4$). The location of the Basel geothermal well is indicated by the green circle. The blue focal mechanisms are part of the mainshock family. (e) Horizontal sections through the multiplets, indicating groups of events that can be interpreted as having similar focal mechanisms and fracture orientations [after [Dyer et al., 2010](#)]. (f) Slip- and dilation tendency analysis of major fault zones in the Basel-Riehen area (see Fig. 5.12).

earthquakes along a single fault patches (asperities) have been described also for the induced sequences in the Soultz EGS by [Bourouis and Bernard \[2007\]](#). They propose that repeated events occur as response to increased fault weakening due to rising pore pressure. The observation of repeated slip of the early stimulated fracture zones in Basel, which are characterized by distinct argillic alteration, may also be interpreted as repeated failure of asperities on small creeping faults.

I assume for the early phase of the Basel stimulation that a) the increase in pore pressure caused dilatant opening of fractures that are unfavorably oriented for shearing (large T_D & small T_S values), b) multiplets point at repeated shear reactivation of individual fault patches (asperities), and c) the weakening effect of rising pore pressure probably is caused by aseismic fault creep in their surrounding that in turn increases the loading on the asperities as postulated by [Bourouis and Bernard \[2007\]](#). Such fault behavior would imply rather similar failure processes in the Basel and Soultz EGS during pressurization of the reservoir. The combination of primarily dilatant opening (large T_D values), secondarily shear reactivation (small T_S values), and aseismic fault creep of NNW striking fractures may partly explain the occurrence of small magnitude events subparallel to S_H and thus explains the observed NNW alignment of the multiplets. The overall shape of the NNE oriented lens-shaped seismic cloud seems to be controlled by dilatant failure of pre-existing fracture zones in the direction of the maximum dilation tendency.

The large magnitude events are related to N-S and E-W striking nodal planes. Faults of these orientations are optimally oriented for shear reactivation in the ambient state of stress, when assuming a friction coefficient of $\mu = 1$ and optimal shear angles of $\pm 45^\circ$ to S_H . These faults show maximum slip tendencies and moderate dilation tendencies (Fig. 8.1d, f). During continuous pressurization, these structures are prone for pure shear reactivation as sinistral and dextral strike-slip faults. The steady increase of pore pressure during and after injection may have triggered large areas of these pre-existing and critically stressed faults. Regional activity of this structural trend is clearly indicated by both the naturally occurring earthquakes that show similar focal mechanisms [[Plenefisch and Bonjer, 1997](#); [Kastrup et al., 2004](#)] and the morphotectonic analysis of the southern Schwarzwald as described in section 6 and 7.

The application of the slip tendency and dilation tendency theory for description of the evolution of induced seismicity in Basel is in good agreement with the observations during the reservoir stimulation. This analysis still has to be treated as first order approach since coupled processes in the fractured reservoir have not been addressed in this study. Magnitudes of the slip- and dilation tendency values of a stimulated fracture plane increase linearly with increasing flow rates and pore pressures, disregarding the poroelastic behavior of the porous rock matrix. According to the theory of poroelasticity [[Biot, 1941](#); [Wang, 2000](#)], the pore fluid pressure and the stress field are coupled. An increase or decrease in the fluid content in a continuous porous rock matrix will increase or decrease the pore fluid pressure, but also tends to expand the volume of the rock matrix, including the pore space. This coupled process induces additional stresses and pressures, which are distributed over time by diffusion, depending on the permeability and the poroelastic properties of the porous matrix. Thus, an increase of the injection rate often is observed to be followed by a small increase of

pressure due to the elastic opening of the fractures and the additionally created permeability. An analogous coupling exists between the temperature and the stress field [Zimmerman, R. W., 2000], it is described by the theory of thermoelasticity [Nowacki, 1986]. In the course of injection of cold water in a high-temperature reservoir, temperature changes result in expansion or contraction of the rock and the fluid, causing additional thermal stresses. A massive perturbation of pore fluid pressure and temperature thus can result in rock failure through a lowering of the effective stresses. Both coupled processes and their impact on the in situ state of stress and hence on the rock failure conditions are not incorporated in the slip- and dilation tendency analysis. However, the structural geological interpretation of the induced seismicity of the Basel EGS stimulation, as well as the proposed geomechanical processes for the fault reactivation, are in good agreement with the following results I have obtained for the southern Schwarzwald.

- The conducted ASTER-DEM and LIDAR-DEM₅ lineament mappings in the southern Schwarzwald point at complex fault patterns with a predominant strike direction N110°E to N130°E (Section 6.4.1). The lineament mapping of Franzke et al. [2003] implies that most of the faults strike approximately between N170°E and N10°E. Despite a minor counterclockwise rotation of 20°, both fault trends are in good agreement with the orientations of the focal mechanism nodal planes for the largest 28 induced events in Basel and the focal mechanisms that have been derived from naturally occurring earthquakes (Fig. 8.1a,b,c). Due to the fact that N-S striking structures are less often observed as lineaments on the high resolution DEMs, I consider the (W)NW-(E)SE striking structures being the predominant fault trend in the crystalline basement of the Schwarzwald. The statistical fault distribution in the reservoir analogue hence may be considered to be representative for the crystalline basement in the graben center, at least for the southern segment of the URG. The identification of similar structural patterns in the Basel reservoir and in the Schwarzwald confirms that the use of remote sensing techniques in outcropping reservoir analogues can add reliable structural information to often uncertain reservoir models.
- The morphotectonic analysis of the southern Schwarzwald basement and the precise leveling data clearly point at neotectonic activity of predominantly (W)NW-(E)SE striking faults. Faults of this orientation, e.g. the Vorwald Fault Zone, can be followed along their fault traces on the surface by often clearly developed topographic expressions (Section 7.4.3). Precise levelings across such faults indicate displacement rates of $>1 \text{ mm a}^{-1}$. These faults probably are critically stressed for shear reactivation in the ambient state of stress and thus may be preferred candidates for induced large magnitude events during hydraulic treatments of EGS reservoirs in the southern URG. Assuming that such critically stressed faults in the basement do not extend into the overlying sediments, they probably will not be recognized by seismic surveys. Such hidden faults may be capable of hosting significant induced seismicity, as experienced for the Basel EGS stimulation, i.e. when they are intersecting or are in close vicinity to the injection well.

8.2 IMPLICATIONS FOR HYDROTHERMAL RESERVOIRS IN THE UPPER RHINE GRABEN

In the Basel EGS, NNE-SSW and WNW-ESE trending fault zones are assumed to be critically stressed. In the southern URG, the (WN)W-(ES)E trend is associated with faults of Variscan age or Permo-Carboniferous troughs [e.g. [Ustaszewski, 2004](#)]. Such critically stressed structures probably control both the fluid flow and reactivation potential [[Barton et al., 1995](#); [Sibson, 1996](#); [Ito and Zoback, 2000](#)]. They may represent primary targets for petrothermal systems in the URG, showing increased fracture permeabilities and good stimulation potentials. Similar conclusions can be drawn for non-stimulated, hydrothermal reservoirs in the URG, which often occur in deep sediments along the (N)NE - (S)SW striking main boundary faults. NW to NNW trending faults, as inferred in Bruchsal and Riehen, probably dissect graben-parallel faults, which are the most frequently observed structures close to the main boundary faults. A distinct fault-bounded compartmentalization of hydrothermal reservoirs has to be expected for Bruchsal and Riehen. In both reservoirs NW to NNW striking faults are interpreted to (partly) control subsurface fluid flow since conducted tracer tests between the NNE-SSW aligned doublet wells have not shown expected breakthrough curves during continuous circulation. Reconstruction of the tectonic and structural geological evolution of a fault-bounded compartmentalization in Bruchsal and Riehen is challenging. Polyphase rift evolution of the URG caused by repeatedly changes of the ambient stress field formed a complex pattern of faults of different strike directions. Formation of rifting-related synsedimentary Cenozoic faults and reactivation of pre-rift crustal discontinuities result in structural settings that can hardly be reconstructed on the basis of 2D seismic sections. In Bruchsal, NW to NNW striking faults are interpreted as high angle transfer faults that strike orthogonal to the eastern main boundary fault, which is composed of a set of NNE-SSW striking en echelon normal faults. A steeply dipping transfer fault, as a structural stepover delimiting intrabasinal fault blocks, may explain both the vertical displacements that are observed on the 2D seismic sections from N to S and the existence of synthetic and antithetic normal fault. Similar structural configurations at basin scale has been described for the northern URG by [Derer et al. \[2005\]](#). One should be aware that also accommodation zones locally can lead to lateral changes in subsidence rates along the rift axis of an extending terranes [e.g. [Faulds and Varga, 1998](#)]. In this case, relay ramps or faulted relay ramps that connect the hanging wall of one fault to the footwall of another fault probably transfer the strain between the en echelon synthetic normal faults. A south facing relay ramp could also explain the southward increasing displacement rates. In contrast to a transfer fault, such a relay ramp should be expressed by a distinct southward dipping of the formations sub-parallel to the main boundary fault, which could not be deduced from the E-W aligned 2D seismic sections. Verification of the structural settings of both reservoirs seems impossible, since no high-resolution 3D seismic surveys are available. However, sub-vertical structures that strike NW-SE are aligned parallel to S_H and thus show highest tendency for dilatant opening (maximum dilation tendencies). These zones are not prone for shear reactivation in the southern URG. Due to the regional strike-slip faulting regime, maximum reactivation potentials (maximum slip tendencies) should be observed for faults that strike approximately $\pm 30-45^\circ$ to S_H . In

the central and northern segments of the URG, where a transitional normal to strike-slip faulting regime prevails, shear reactivation of these NW-SE trending faults as oblique normal faults seems possible. Fault zones of this orientation are characterized by large slip tendencies and large dilation tendencies. In both segments of the URG the most critically stressed faults may be identified along this strike direction. Recalling that in Riehen and Bruchsal no immediate connection between the production and the injection wells during tracer experiment was observed [Schill and Klingler, 2011], I suppose that these steeply dipping faults may act as highly conductive hydraulic boundaries. Similar to deep EGS reservoirs, they probably act as preferential fluid-pathways and thus most likely represent dominant structural controls in hydrothermal reservoirs. This may account for both, pre-existing Variscan faults, as proposed for Riehen, and Cenozoic rift-related transfer zones, as proposed for Bruchsal. The existence of geomechanical anisotropies in sedimentary rocks may not only affect the geothermal projects but also hydrocarbon or CO₂ sequestration projects.

8.3 IMPLICATIONS FOR STRESS FIELD CHARACTERIZATIONS

Estimates on the frictional failure of rock require both definition of the fault or fracture geometry and the in-situ state of stress. Especially the latter is poorly constrained in the URG. I could show, exemplary for the geothermal site of Bruchsal, how stress measurements in deep seated sediments can be evaluated to still infer indirectly the local stress condition (Section 4). In Bruchsal extrapolation of measurements from sedimentary cover rocks to greater depths is hampered by the following reasons: a) magnitudes and orientations of the principal stresses are biased by geological unconformities and lithological variations, b) potential stress decoupling processes within specific clay-, salt-, and anhydrite-bearing units probably cause significant stress field perturbations, and c) estimates of maximum horizontal stress magnitudes are missing, as is frequently the case. In such conditions, the critical stress concept may constrain the S_H magnitude [Zoback et al., 2003]. According to frictional equilibrium, one can assume that the ratio between maximum and minimum effective stresses cannot exceed the one required to cause slip on pre-existing faults that are optimally oriented to the principal stress field [Jaeger et al., 2007; Moos and Zoback, 1990]. Thus I suggest, that the effective differential stresses in Bruchsal are also bounded by a critical ratio. The revised stress field model for the Bruchsal area predicts a transitional normal to strike-slip faulting regime. On the one hand, this prognosis is slightly different to existing stress field model of that region that consistently point at a pure normal-faulting regime. On the other hand, it is in good accordance with the well constrained stress models at Soultz, which is located in the same segment of the URG. However, the robust stress characterization for the Soultz reservoir down to 5 km depth allows to test our proposed stress model for plausibility, i.e. the assumed limitation of the differential stress. Figure 8.2 shows a compilation of stress-depth relations of the principal stresses in Soultz, which have been obtained by Valley [2007]; Valley and Evans [2007]; Cornet et al. [2007] for the crystalline basement.

The stress-depth ratios for P_p , S_H , and S_v show only slight variations in the magnitudes and thus seem to be well constrained. On the contrary, previous studies do not impose very tight constraints on the magnitude

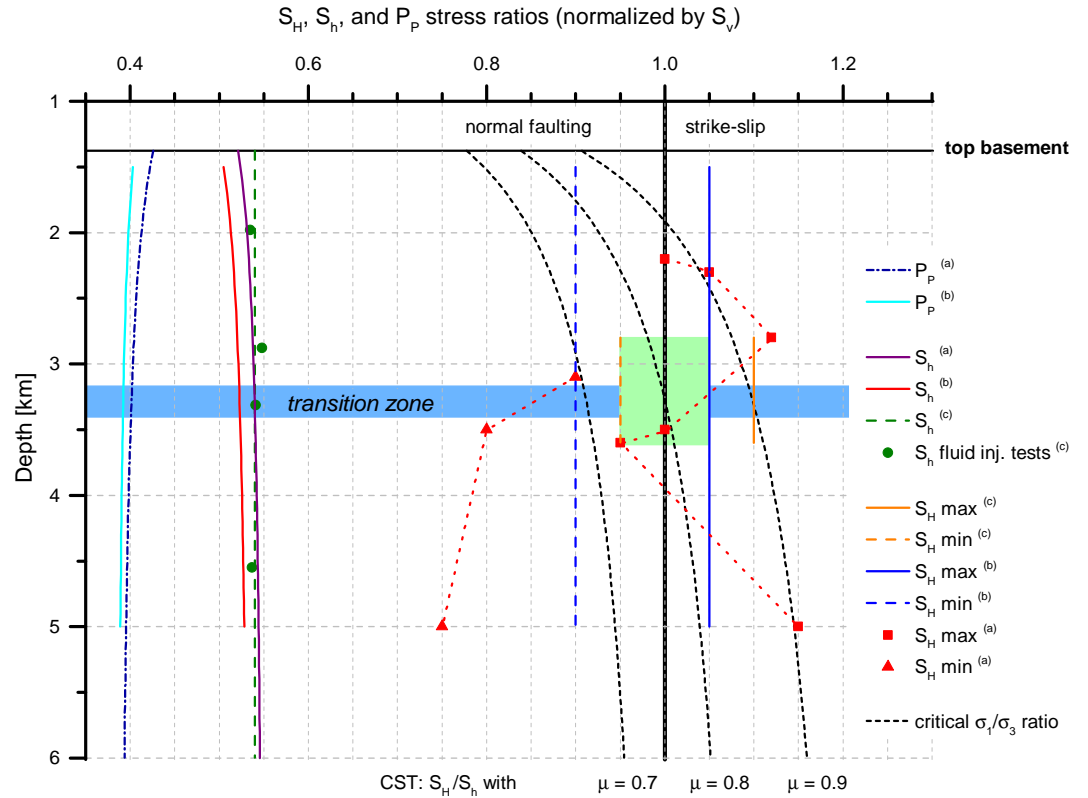


Figure 8.2: Stress characterization at Soultz-sous-Forêts showing measured and constrained stress-depth profiles for the pore pressure (P_p), the minimum (S_h), and the maximum (S_H) horizontal stresses (each normalized by S_v). Stress magnitudes have been obtained by Valley [2007] (a), Valley and Evans [2007] (b), and Cornet et al. [2007] (c) by integrating the weight of the overburden (S_v), maximum pressures attained during massive fluid injections and well test (S_h), and the analysis of the presence or absence of compressive and tensile failure of the wellbore and induced seismicity (S_H). The best fit of the S_H -gradient is highlighted by the green square. The black dashed lines show S_H -gradients that were calculated on the basis of the critical stress concept (CST) for different friction coefficients (μ).

of S_H . Generally, almost identical magnitudes are observed for S_H and S_v . The best fit estimate of the S_H magnitude is marked as green square in Figure 8.2. Interestingly, the best fit constraint of the S_H magnitude in Soultz can be reproduced by application of the critical stress theory. Calculation of the maximum allowed differential stress requires only reliable estimates for P_p , S_h , and S_v , which is always the case in Soultz (see Eq. 2.39). The black dashed lines in Figure 8.2 indicate stress-depth ratios for S_H that were obtained for friction coefficients of 0.7, 0.8, and 0.9. The one for $\mu = 0.8$ is in very good agreement with the previously obtained best fit estimate of the S_H magnitude. The widely accepted sub-equality between the vertical and the maximum horizontal principal stress is also indicated by the critical stress concept. This concept of limited differential stresses on the basis of a 0.8 friction coefficient surprisingly leads to

S_H magnitudes that exceed those of the vertical stress in the depth of about 3.4 km, predicting a switch in maximum stress orientation from vertical to horizontal. This gradual transition from a normal faulting regime in upper part of the reservoir to a strike slip faulting regime in the deeper part has been previously concluded by Cuenot et al. [2006] from analyses of focal mechanisms. The required friction coefficients of 0.8 is furthermore in perfect agreement to what is suggested for frictional failure processes in Soultz by Cornet [2007] and to various deep well stress measurements in different tectonic regimes [Zoback and Healy, 1992; Brudy et al., 1997]. Hence, I conclude that the application of the critical stress concept leads to reliable stress-depth ratios in the URG, although the resulting linear stress profiles are considered to be a first rough estimate of the in-situ state of stress. Nevertheless I believe that the observations in Soultz support the plausibility of a) the stress field models that we described for Bruchsal, Riehen, and the southern Schwarzwald, and b) the calculations of the slip- and dilation tendencies, due to the fact that both concepts base on the same fundamental predictions of the classical Coulomb friction law.

The enhanced geothermal systems (EGS) concept seems to be the most promising way to access the huge resources of heat in low enthalpy regions such as the Upper Rhine Graben. The EGS technology is considered to play an important role for the future energy production but exploitation of the geothermal resource is still hampered by larger investment costs for the realization of projects and the level of uncertainty in the exploratory phase of new projects. The observations of insufficient enhancements of existing permeable structures and the occurrence of felt earthquakes during a hydraulic stimulation highlights the urgent need for further research of the associated geomechanical processes. I hope that the described implications for the EGS and hydrothermal reservoirs, as well as for future stress field characterizations, help to improve the understanding of the hydro mechanically coupled processes under stimulation conditions and lead to better prognoses of favorably structural settings and fault patterns in the Upper Rhine Graben. Both will be needed to increase the magnitude of economically recoverable geothermal resources in SW Germany.

BIBLIOGRAPHY

- Ahorner, L. (1975). Present-day stress field and seismotectonic block movements along major fault zones in central europe. *Tectonophysics*, 29(1-4):233–249.
- Anderson, E. M. (1951). *The dynamics of faulting and dyke formation with applications to Britain*. Oliver and Boyd.
- Anderson, R. A., Ingram, D. S., and Zanier, A. M. (1973). Determining fracture pressure gradients from well logs. *JPT, Journal of Petroleum Technology*, 25:1259–1268.
- Angelier, J., Bergerat, F., Dauteuil, O., and Villemin, T. (1997). Effective tension-shear relationships in extensional fissure swarms, axial rift zone of northeastern iceland. *Journal of Structural Geology*, 19(5):673–685.
- Arlegui, L. E. and Soriano, M. A. (1998). Characterizing lineaments from satellite images and field studies in the central ebro basin (ne spain). *International Journal of Remote Sensing*, 19(16):3169–3185.
- Bächler, D., Kohl, T., and Rybach, L. (2003). Impact of graben-parallel faults on hydrothermal convection – rhine graben case study. *Physics and Chemistry of the Earth, Parts A/B/C*, 28(9-11):431–441.
- Baer, M., Deichmann, N., Braunmiller, J., Clinton, J., Husen, S., Fäh, D., Giardini, D., Kästli, P., Kradofer, U., and Wiemer, S. (2007). Earthquakes in switzerland and surrounding regions during 2006. *Swiss Journal of Geosciences*, 100(3):517–528.
- Baillieux, P., Schill, E., and Dezayes, C. (2011). 3-d structural regional model of the egs soultz site (northern upper rhine graben, france): insights and perspectives. *Proceeding of 36th Workshop on Geothermal Reservoir Engineering*, SGP-TR-191<hal-00582900>.
- Baillieux, P., Schill, E., Edel, J.-B., and Mauri, G. (2013). Localization of temperature anomalies in the upper rhine graben: insights from geophysics and neotectonic activity. *International Geology Review*, 55(14):1744–1762.
- Barton, C. A., Zoback, M. D., and Moos, D. (1995). Fluid-flow along potentially active faults in crystalline rock. *Geology*, 23(8):683–686.
- Bartz, J. (1974). Die mächtigkei des quartärs im oberrheingraben. In Illies, J. H. and Fuchs, K., editors, *Approaches to taphrogenesis*, volume no. 8 of *Scientific report - Inter-Union Commission on Geodynamics*, pages 78–87. Schweizerbart (Nägele u. Obermiller), Stuttgart.
- Baumann, H. (1981). Regional stress field and rifting in western europe. *Tectonophysics*, 73(1-3):105–111.
- Behrmann, J. H., Hermann, O., Horstmann, M., Tanner, D. C., and Bertrand, G. (2003). Anatomy and kinematics of oblique continental rifting revealed: A three-dimensional case study of the southeast upper rhine graben (germany). *AAPG Bulletin*, 87(7):1105–1121.

- Bellani, S., Brogi, A., Lazzarotto, A., Liotta, D., and Ranalli, G. (2004). Heat flow, deep temperatures and extensional structures in the larderello geothermal field (Italy): constraints on geothermal fluid flow. *Journal of Volcanology and Geothermal Research*, 132(1):15–29.
- Bertleff, B., Hammer, W., Joachim, H., Koziorowski, G., Stober, I., Strayle, G., Villinger, E., and Werner, J. (1987). Hydrogeothermiebohrungen in Baden-Württemberg: Eine Übersicht. *Zeitschrift der Deutschen Geologischen Gesellschaft*, 138:411–423.
- Bertrand, G., Elsass, P., Wirsing, G., and Luz, A. (2006). Quaternary faulting in the upper Rhine Graben revealed by high-resolution multi-channel reflection seismic. *Comptes Rendus Geoscience*, 338(8):574–580.
- Biot, M. (1941). General theory of three-dimensional consolidation. *Journal of Applied Physics*, 12:155.
- Boigk, H. and Schoeneich (1970). Die tiefenlage der Permbasis im nördlichen Teil des Oberrheingrabens. In *Graben Problems*, pages 45–55. Illies, J.H., Mueller, S.
- Bonjer, K.-P. (1997). Seismicity pattern and style of seismic faulting at the eastern border fault of the southern Rhine Graben. *Tectonophysics*, 275(1–3):41–69.
- Bonjer, K. P., Gelbke, C., Gilg, B., Rouland, D., Mayer-Rosa, D., and Massinon, B. (1984). Seismicity and dynamics of the upper Rhine Graben (earthquakes). *Journal of Geophysics - Zeitschrift für Geophysik*, 55(1):1–12.
- Bönnemann, C., Schmidt, B., Ritter, J., Gestermann, N., Plenefisch, T., Wegler, U., Schulz, R., Heidbach, O., Erbas, K., Baisch, S., Rothert, E., Hauffe, P., Baumgärtner, J., Hettkamp, T., Rogulic, B., Teza, D., Baria, R., Fritschen, R., Pettitt, W., and Andrews, J. (2010). Das seismische Ereignis bei Landau vom 15. August 2009.
- Bonnet, E., Bour, O., Odling, N. E., Davy, P., Main, I., Cowie, P., and Berkowitz, B. (2001). Scaling of fracture systems in geological media. *Reviews of Geophysics*, 39(3):347–383.
- Bons, P. D., Fusswinkel, T., Gomez-Rivas, E., Markl, G., Wagner, T., and Walter, B. (2014). Fluid mixing from below in unconformity-related hydrothermal ore deposits. *Geology*, 42(12):1035–1038.
- Bourouis, S. and Bernard, P. (2007). Evidence for coupled seismic and aseismic fault slip during water injection in the geothermal site of Soultz (France), and implications for seismogenic transients. *Geophysical Journal International*, 169(2):723–732.
- Brace, W. F. and Kohlstedt, D. L. (1980). Limits on lithospheric stress imposed by laboratory experiments. *Journal of Geophysical Research*, 85(B11):6248.
- Brown, K., Kopf, A., Underwood, M., and Weinberger, J. (2003). Compositional and fluid pressure controls on the state of stress on the Nankai subduction thrust: A weak plate boundary. *Earth and Planetary Science Letters*, 214(3):589–603.

- Brudy, M., Zoback, M. D., Fuchs, K., Rummel, F., and Baumgärtner, J. (1997). Estimation of the complete stress tensor to 8 km depth in the ktb scientific drill holes: Implications for crustal strength. *Journal of Geophysical Research*, 102(B8):18453.
- Bull, W. B. (2007). *Tectonic geomorphology of mountains: a new approach to paleoseismology*. Blackwell Publishing Ltd, Oxford.
- Burbank, D. W. and Anderson, R. S. (2012). *Tectonic geomorphology*. Blackwell Publishing Ltd, Oxford, 2nd edition.
- Byerlee, J. (1978). Friction of rocks. *Pure and Applied Geophysics*, 116(4-5):615–626.
- Carey-Gailhardis, E. and Mercier, J. L. (1992). Regional state of stress, fault kinematics and adjustments of blocks in a fractured body of rock: application to the microseismicity of the rhine graben. *Journal of Structural Geology*, 14(8-9):1007–1017.
- Castaing, C., Halawani, M. A., Gervais, F., Chilès, J. P., Genter, A., Bourguine, B., Ouillon, G., Brosse, J. M., Martin, P., Genna, A., and Janjou, D. (1996). Scaling relationships in intraplate fracture systems related to red sea rifting. *Tectonophysics*, 261(4):291–314.
- Clauser, C. and Villinger, H. (1990). Analysis of conductive and convective heat transfer in a sedimentary basin, demonstrated for the rheingraben. *Geophysical Journal International*, 100(3):393–414.
- Collettini, C., Niemeijer, A., Viti, C., and Marone, C. (2009). Fault zone fabric and fault weakness. *Nature*, 462(7275):907–910.
- Collettini, C. and Trippetta, F. (2007). A slip tendency analysis to test mechanical and structural control on aftershock rupture planes. *Earth and Planetary Science Letters*, 255(3-4):402–413.
- Cornet, F. H. (2007). Introduction to the special section on induced seismicity. *International Journal of Rock Mechanics and Mining Sciences*, 44(8):1077–1078.
- Cornet, F. H. (2015). *Elements of crustal geomechanics*. Cambridge University Press, Cambridge.
- Cornet, F. H., Berard, T., and Bourouis, S. (2007). How close to failure is a granite rock mass at a 5 km depth? *International Journal of Rock Mechanics and Mining Sciences*, 44(1):47–66.
- Cornet, F. H. and Burlet, D. (1992). Stress-field determinations in france by hydraulic tests in boreholes. *Journal of Geophysical Research*, 97(B8):11829–11849.
- Cornet, F. H. and Röckel, T. (2012). Vertical stress profiles and the significance of "stress decoupling". *Tectonophysics*, 581:193–205.
- Coulomb (1773). Application des règles de maxima et minima à quelques problèmes de statique relatifs à l'architecture. *Mémoires de Mathématiques et de Physiques présentés à l'Académie Royale des Sciences*, 7:343–382.

- Cuenot, N., Charley, J., Dorbath, L., and Haessler, H. (2006). Faulting mechanisms and stress regime at the european HDR site of Soultz-sous-Forêts, France. *Geothermics*, 35(5-6):561–575.
- Curewitz, D. and Karson, J. A. (1997). Structural settings of hydrothermal outflow: Fracture permeability maintained by fault propagation and interaction. *Journal of Volcanology and Geothermal Research*, 79(3):149–168.
- Deichmann, N., Baer, M., Clinton, J., Husen, S., Fäh, D., Giardini, D., Kästli, P., Kradolfer, U., and Wiemer, S. (2008). Earthquakes in Switzerland and surrounding regions during 2007. *Swiss Journal of Geosciences*, 101(3):659–667.
- Deichmann, N. and Ernst, J. (2009). Earthquake focal mechanisms of the induced seismicity in 2006 and 2007 below Basel (Switzerland). *Swiss Journal of Geosciences*, 102(3):457–466.
- Deichmann, N. and Giardini, D. (2009). Earthquakes induced by the stimulation of an enhanced geothermal system below Basel (Switzerland). *Seismological Research Letters*, 80(5):784–798.
- Delouis, B., Haessler, H., Cisternas, A., and Rivera, L. (1993). Stress tensor determination in France and neighboring regions. *Tectonophysics*, 221(3-4):413–438.
- Demoulin, A., Launoy, T., and Zippelt, K. (1998). Recent crustal movements in the southern Black Forest (Western Germany). *Geologische Rundschau*, 87(1):43–52.
- Derer, C. E., Schumacher, M. E., and Schafer, A. (2005). The northern upper Rhine Graben: basin geometry and early syn-rift tectono-sedimentary evolution. *International Journal of Earth Sciences*, 94(4):640–656.
- Derry, L., Evans, M., Darling, R., and France-Lanord, C. (2009). Hydrothermal heat flow near the main central thrust, central Nepal Himalaya. *Earth and Planetary Science Letters*, 286(1):101–109.
- Dershowitz, W. S. and Einstein, H. H. (1988). Characterizing rock joint geometry with joint system models. *Rock Mechanics and Rock Engineering*, 21(1):21–51.
- Dezes, P., Schmid, S. M., and Ziegler, P. A. (2004). Evolution of the European Cenozoic rift system: interaction of the Alpine and Pyrenean orogens with their foreland lithosphere. *Tectonophysics*, 389(1-2):1–33.
- Doebli, F., Olbrecht, W., Illies, J. H., and Fuchs, K. (1974). An isobath map of the Tertiary base in the Rhine Graben. *Approaches to Taphrogenesis., Inter-Union Commission on Geodynamics, Scientific report No. 8., Schweizerbart, Stuttgart, Germany, pp. 71–72.*
- Dorbath, L., Cuenot, N., Genter, A., and Frogneux, M. (2009). Seismic response of the fractured and faulted granite of Soultz-sous-Forêts (France) to 5 km deep massive water injections. *Geophysical Journal International*, 177(2):653–675.

- Dresmann, H., Keulen, N., Timar-Geng, Z., Fugenschuh, B., Wetzels, A., and Stunitz, H. (2010). The south-western black forest and the upper rhine graben main border fault: thermal history and hydrothermal fluid flow. *International Journal of Earth Sciences*, 99(2):285–297.
- Dyer, B. C., Schanz, U., Spillmann, T., Ladner, F., and Häring, M. O. (2010). Application of microseismic multiplet analysis to the basel geothermal reservoir stimulation events. *Geophysical Prospecting*, 58(5):791–807.
- Echtler, H. P. and Chauvet, A. (1991). Carboniferous convergence and subsequent crustal extension in the southern schwarzwald (sw germany). *Geodynamica Acta*, 5(1-2):37–49.
- Edel, J. B. and Fluck, P. (1989). The upper rhenish shield basement (vosges, upper rhinegraben and schwarzwald): Main structural features deduced from magnetic, gravimetric and geological data. *Tectonophysics*, 169(4):303–316.
- Edel, J. B., Schulmann, K., and Rotstein, Y. (2007). The variscan tectonic inheritance of the upper rhine graben: evidence of reactivations in the lias, late eocene-oligocene up to the recent. *International Journal of Earth Sciences*, 96(2):305–325.
- Edel, J. B. and Weber, K. (1995). Cadomian terranes, wrench faulting and thrusting in the central-europe variscides - geophysical and geological evidence. *Geologische Rundschau*, 84(2):412–432.
- Einsele, G. and Ricken, W. (1995). The wutach gorge in sw germany – late würmian (periglacial) downcutting versus holocene processes. In Hagedorn, J., editor, *Late Quaternary and present-day fluvial processes in Central Europe*, volume 100, pages 65–87. Schweizerbart Science Publishers, Stuttgart, Germany.
- Eisbacher, G. H., Becker, A., and Clauß, B. (1989a). Geothermisches projekt bruchsal, phase 5 und 6: Tektonische untersuchungen: Report unpublished.
- Eisbacher, G. H. and Fielitz, W. (2008). Eine spätvariszische (325 ma) w-fallende abschiebung als lithosphärische schwächezone unter dem oberrhein-graben: 12th symposium "tektonik, struktur- und kristallingeologie". *Geotectonic Research*, 95(01):39–40.
- Eisbacher, G. H., Lüschen, E., and Wickert, F. (1989b). Crustal-scale thrusting and extension in the hercynian schwarzwald and vosges, central europe. *Tectonics*, 8(1):1–21.
- Emmermann, R. (1967). *Die Differentiation des Albtalgranites (Süd-schwarzwald), dargestellt an den Leitelementen Zr, Ti, Ca, Sr, Ba, K, Rb und Si*. PhD thesis, Universität Karlsruhe, Karlsruhe.
- Emmermann, R. and Lauterjung, J. (1997). The german continental deep drilling program ktb: Overview and major results. *Journal of Geophysical Research: Solid Earth* (1978–2012), 102(B8):18179–18201.
- Engelder, T. and Leftwich, J. T. (1997). A pore-pressure limit in overpressured south texas oil and gas fields: Seals, traps and the petroleum system. *AAPG Memoir*, 67:255–267.

- England, P. and Molnar, P. (1990). Surface uplift, uplift of rocks, and exhumation of rocks. *Geology*, 18(12):1173–1177.
- Faulds, J. E., Coolbaugh, M. F., Bouchot, V., Moek, I., and Oguz, K. (2010). Characterizing structural controls of geothermal reservoirs in the great basin, usa, and western turkey: Developing successful exploration strategies in extended terranes. *International Geothermal Association. World Geothermal Congress 2010, Apr 2010, France. 11 p.*
- Faulds, J. E., Hinz, N. H., Coolbaugh, M. F., Cashman, P. H., Kratt, C., Dering, G., Edwards, J., Mayhew, B., and McLachlan, H. (2011a). Assessment of favorable structural settings of geothermal systems in the great basin, western usa. *Geothermal Resources Council Transactions*, 35:777–783.
- Faulds, J. E., Hinz, N. H., Coolbaugh, M. F., Steininger, R., and Pennell, B. (2011b). Structural investigations of great basin geothermal fields: Applications and implications. *Great Basin Evolution and Metallogeny, Vols I and II*, pages 361–372.
- Faulds, J. E. and Varga, R. J. (1998). The role of accommodation zones and transfer zones in the regional segmentation of extended terranes. In Faulds, J. E., editor, *Accommodation zones and transfer zones*, volume 323 of *Special paper / The Geological Society of America*, pages 1–45. Geological Soc. of America, Boulder, Colo.
- Ferrill, D. A., Winterle, J., Wittmeyer, G., Sims, D., Colton, S., Armstrong, A., and Morris, A. P. (1999). Stressed rock strains groundwater at yucca mountain, nevada. *GSA Today*, 9(5):1–8.
- Fischer, H., Hauber, L., and Wittmann, O. (1971). *Geologischen atlas der schweiz: Blatt 1047 - basel mit erläuterungen: 1:25000.*
- Fjaer, E., Holt, R. M., Horsrud, P., Raaen, A. M., and Risnes, R. (2008). *Petroleum Related Rock Mechanics*. Elsevier, 2nd edition edition.
- Flöttmann, T. and Oncken, O. (1992). Constraints on the evolution of the mid german crystalline rise - a study of outcrops west of the river rhine. *Geol. Rundsch. (Geologische Rundschau)*, 81:515–543.
- Formento-Trigilio, M. L. and Pazzaglia, F. J. (1998). Tectonic geomorphology of the sierra nacimiento: traditional and new techniques in assessing long-term landscape evolution in the southern rocky mountains. *Journal of Geology*, 106(4):433–453.
- Forster, C. and Smith, L. (1989). The influence of groundwater flow on thermal regimes in mountainous terrain: a model study. *Journal of Geophysical Research*, 94(B7):9439–9451.
- Franzke, H. J., Werner, W., and Wetzel, H.-U. (2003). Die anwendung von satellitenbilddaten zur tektonischen analyse des schwarzwalds und des angrenzenden oberrheingrabens. *Jh. Landesamt für Geologie, Rohstoffe und Bergbau Baden-Württemberg LGRB*, 39:25–54.
- Fuhrmann, T., Heck, B., Knöpfler, A., Masson, F., Mayer, M., Ulrich, P., Westerhaus, M., and Zippelt, K. (2013). Recent surface displacements in the upper rhine graben — preliminary results from geodetic networks. *Tectonophysics*, pages 300–315.

- Fuhrmann, T., Westerhaus, M., Zippelt, K., and Heck, B. (2014). Vertical displacement rates in the upper rhine graben area derived from precise leveling. *Journal of Geodesy*, 88(8):773–787.
- Fuhrmann, T. and Zippelt, K. (2013). Berechnung und beurteilung rezenter vertikaler oberflächenbewegungen abgeleitet aus wiederholten präzisionsnivellements in den regionen nordschweiz und südwestdeutschland rezenter vertikaler oberflächenbewegungen abgeleitet aus wiederholten präzisionsnivellements in den regionen nordschweiz und südwestdeutschland: Nab 12-33.
- Gaucher, E., Schoenball, M., Heidbach, O., Zang, A., Fokker, P. A., Van Wees, J. D., and Kohl, T. (2015). Induced seismicity in geothermal reservoirs: A review of forecasting approaches. *Renewable and Sustainable Energy Reviews*, 52:1473–1490.
- Genter, A., Evans, K., Cuenot, N., Fritsch, D., and Sanjuan, B. (2010). Contribution of the exploration of deep crystalline fractured reservoir of soultz to the knowledge of enhanced geothermal systems (egs). *Comptes Rendus Geoscience*, 342(7–8):502–516.
- Gephart, J. W. and Forsyth, D. W. (1984). An improved method for determining the regional stress tensor using earthquake focal mechanism data: application to the san fernando earthquake sequence. *Journal of Geophysical Research*, 89(B11):9305–9320.
- Geyer, O. F. and Gwinner, M. P. (2011). *Geologie von Baden-Württemberg*. Schweizerbart'sche Verlagsbuchhandlung (Nägele u. Obermiller), Stuttgart, 5th editio edition.
- Gischig, V. S. and Preisig, G. (2015). Hydro-fracturing versus hydro-shearing: A critical assessment of two distinct reservoir stimulation mechanisms. *Proceeding of the 13th International Congress of Rock Mechanics, ISRM 2015,, 10-13 May, 2015, Montreal, Canada*.
- Greiner, G. (1975). In situ stress measurements in southwest germany. *Tectonophysics*, 29(1-4):265–274.
- Greiner, G. (1978). *Spannungen in der Erdkruste: Bestimmung und Interpretation am Beispiel von In-situ-Messungen im Süddeutschen Raum*. PhD thesis, Karlsruhe University.
- Grimmer, J. C., Ritter, J., Eisbacher, G. H., and Fielitz, W. (2016). The late variscan control on location and asymmetry of the upper rhine graben. *International Journal of Earth Sciences*, accepted.
- Grohmann, C. H., Smith, M. J., and Riccomini, C. (2011). Multiscale analysis of topographic surface roughness in the midland valley, scotland. *IEEE Transactions on Geoscience and Remote Sensing*, 49(4):1200–1213.
- Guglielmetti, L., Comina, C., Abdelfettah, Y., Schill, E., and Mandrone, G. (2013). Integration of 3d geological modeling and gravity surveys for geothermal prospection in an alpine region. *Tectonophysics*, 608:1025–1036.
- Gürler, B., Hauber, L., and Schwander, M. (1987). Die geologie der umgebung von basel mit hinweisen über die nutzungsmöglichkeiten von erdwärme. *beitr. geol. karte der schweiz, n.f., lfg. 160, bern. Beitr. geol. Karte Schweiz, Liefg. 160*.

- Haldimann, P., Naef, H., and Schmassmann, H. (1984). Fluviale erosions- und akkumulationsformen als indizien jurigpleistozäner und fluviale erosions- und akkumulationsformen als indizien jurigpleistozäner und holozäner bewegungen in der nordschweiz und angrenzenden gebieten: Ntb 84-16.
- Häring, M. O., Schanz, U., Ladner, F., and Dyer, B. C. (2008). Characterisation of the basel 1 enhanced geothermal system. *Geothermics*, 37(5):469–495.
- Hauber, L. (1993). Der südliche rheingraben und seine geothermische situation. *Bull. Ver. schweiz. Petroleum-Geol. u. -Ing.*, 60(137):53–69.
- Hauser-Fuhlberg, M., Rahn, W., Rothengatter, P., Bechler, K., and Mainka, U. (2012). Pumpspeicherwerk forbach - geotechnisches und hydrogeologisches gutachten.
- Heidbach, O., Tingay, M., Barth, A., Reinecker, J., Kurfes, D., and Müller, B. (2008). The world stress map database release 2008, doi:10.1594/gfz.wsm.rel2008.
- Heidbach, O., Tingay, M., Barth, A., Reinecker, J., Kurfess, D., and Muller, B. (2010). Global crustal stress pattern based on the world stress map database release 2008. *Tectonophysics*, 482(1-4):3–15.
- Henk, A. (1993). Late orogenic basin evolution in the variscan internides: the saar-nahe basin, southwest germany. *Tectonophysics*, 223(3):273–290.
- Henk, A. (1997). Gravitational orogenic collapse vs plate-boundary stresses: a numerical modelling approach to the permo-carboniferous evolution of central europe. *Geologische Rundschau*, 86(1):39–55.
- Hergert, T. and Heidbach, O. (2011). Geomechanical model of the marmara sea region-ii. 3-d contemporary background stress field. *Geophysical Journal International*, 185(3):1090–1102.
- Hess, J., Lippolt, H., and Kober, B. (1995). The age of the kagenfels granite (northern vosges) and its bearing on the intrusion scheme of late variscan granitoids. *Geologische Rundschau*, 84(3):568–577.
- Hinsken, S., Ustaszewski, K., and Wetzell, A. (2007). Graben width controlling syn-rift sedimentation: the palaeogene southern upper rhine graben as an example. *International Journal of Earth Sciences*, 96(6):979–1002.
- Huber, M. and Huber-Aleffi, A. (1984). Das kristallin des südschwarzwaldes: Ntb 84-30.
- Huber, M. and Huber-Aleffi, A. (1990). Zur tektonik des südschwarzwaldes: Ntb 90-03.
- Hudson, J. and Priest, S. (1983). Discontinuity frequency in rock masses. *International Journal of Rock Mechanics and Mining Sciences & Geomechanics Abstracts*, 20(2):73–89.
- Huenges, E. and Zimmermann, G. (1999). Rock permeability and fluid pressure at the ktb: Implications from laboratory-and drill hole-measurements. *Revue de l'Institut Francais du Petrole*, 54(6):689–694.

- IEA (2011). Technology roadmap: Geothermal heat and power.
- Illies, J. H. (1962). Oberrheinisches grundgebirge und rheingraben. *Geologische Rundschau*, 52(1):317–332.
- Illies, J. H. (1975). Recent and paleo-intraplate tectonics in stable europe and the rhinegraben rift system. *Tectonophysics*, 29(1-4):251–264.
- Illies, J. H. and Greiner, G. (1979). Holocene movements and state of stress in the rhinegraben rift system. *Tectonophysics*, 52(1-4):349–359.
- Illies, J. H., Prodehl, C., Schmincke, H. U., and Semmel, A. (1979). The quaternary uplift of the rhenish shield in germany. *Tectonophysics*, 61(1-3):197–225.
- Ingebritsen, S. E., Sherrod, D. R., and Mariner, R. H. (1989). Heat flow and hydrothermal circulation in the cascade range, north-central oregon. *Science*, 243(4897):1458–1462.
- Ito, T. and Zoback, M. D. (2000). Fracture permeability and in situ stress to 7 km depth in the ktb scientific drillhole. *Geophysical Research Letters*, 27(7):1045–1048.
- Jaeger, J. C., Cook, N G W, and Zimmermann, R. W. (2007). *Fundamentals of Rock Mechanics*. Blackwell Publishing, Malden MA, USA, 4th edition edition.
- Jordan, G., Meijninger, B. M. L., Hinsbergen, D. J. J. v., Meulenkamp, J. E., and Dijk, P. M. v. (2005). Extraction of morphotectonic features from dems: Development and applications for study areas in hungary and nw greece. *International Journal of Applied Earth Observation and Geoinformation*, 7(3):163–182.
- Kalt, A., Altherr, R., and Hanel, M. (1995). Contrasting p-t conditions recorded in ultramafic high-pressure rocks from the variscan schwarzwald (f.r.g.). *Contributions to Mineralogy and Petrology*, 121(1):45–60.
- Kalt, A., Altherr, R., and Hanel, M. (2000). The variscan basement of the schwarzwald. *European Journal of Mineralogy*, 12(2):1–43.
- Kastrup, U., Zoback, M. L., Deichmann, N., Evans, K. F., Giardini, D., and Michael, A. J. (2004). Stress field variations in the swiss alps and the northern alpine foreland derived from inversion of fault plane solutions. *Journal of Geophysical Research*, 109(B1).
- King Hubbert, M. and Rubey, W. (1959). Role of fluid pressure in mechanics of overthrust faulting: Part i. mechanics of fluid-filled porous solids and it's application to overthrust faulting. *Geological Society of America Bulletin*, 70(2):115–166.
- Klee, G. and Rummel, F. (1999). Stress regime in the rhinegraben basement and in the surrounding tectonic units. *Bulletin d'Hydrogeologie*, 17, Special Issue:135–142.
- Kohl, T., Andenmatten, N., and Rybach, L. (2003). Geothermal resource mapping - example from northern switzerland. *Geothermics*, 32(4):721–732.

- Korsch, R. J. and Schäfer, A. (1995). The permo-carboniferous saar-nahe basin, south-west germany and north-east france: basin formation and deformation in a strike-slip regime. *Geologische Rundschau*, 84(2):293–318.
- Korvin, G. (1989). Fractured but not fractal: Fragmentation of the gulf of sues basement. *Pure and Applied Geophysics PAGEOPH*, 131(1-2):289–305.
- Kraft, T. and Deichmann, N. (2014). High-precision relocation and focal mechanism of the injection-induced seismicity at the basel egs. *Geothermics*, 52:59–73.
- Krantz, R. W. (1991). Measurements of friction coefficients and cohesion for faulting and fault reactivation in laboratory models using sand and sand mixtures. *Tectonophysics*, 188(1-2):203–207.
- Krecher, M. and Behrmann, J. H. (2007). Tectonics of the vosges (ne france) and the schwarzwald (sw germany): evidence from devonian-carboniferous active margin basins and their deformation. *Geotectonic Research*, 95(1):61–86.
- Krohe, A. and Eisbacher, G. H. (1988). Oblique crustal detachment in the variscan schwarzwald, southwestern germany. *Geologische Rundschau*, 77(1):25–43.
- Larroque, J. M., Etchecopar, A., and Philip, H. (1987). Evidence for the permutation of stresses s_1 and s_2 in the alpine foreland - the example of the rhine graben. *Tectonophysics*, 144(4):315–322.
- Larroque, J. M. and Laurent, P. (1988). Evolution of the stress field pattern in the south of the rhine graben from the eocene to the present. *Tectonophysics*, 148(1-2):41–58.
- Laubscher, H. (2001). Plate interactions at the southern end of the rhine graben. *Tectonophysics*, 343(1-2):1–19.
- Link, K. (2009). *Die thermo-tektonische Entwicklung des Oberrheingraben-Gebietes seit der Kreide*. PhD thesis, Albert-Ludwigs-Universität, Freiburg i.Br.
- Lisle, R. J. and Srivastava, D. C. (2004). Test of the frictional reactivation theory for faults and validity of fault-slip analysis. *Geology*, 32(7):569.
- Lockner, D. A., Morrow, C., Moore, D., and Hickman, S. (2011). Low strength of deep san andreas fault gouge from safod core. *Nature*, 472(7341):82–86.
- Mälzer, A., Rösch, H., Misselwitz, I., Ebert, M., and Moosmann, D. (1988). Höhenänderungen höhenänderungen in der nordschweiz und im süd-schwarzwald bis zum bodensee: Ntb 84-30.
- Marschall, H. R., Kalt, A., and Hanel, M. (2003). P-t evolution of a variscan lower-crustal segment: A study of granulites from the schwarzwald, germany. *Journal of Petrology*, 44(2):227–253.
- McClure, M. W. and Horne, R. N. (2014). An investigation of stimulation mechanisms in enhanced geothermal systems. *International Journal of Rock Mechanics and Mining Sciences*, 72:242–260.

- Mégel, T. and Rybach, L. (2000). Production capacity and sustainability of geothermal doublets. *Proceedings World Geothermal Congress 2000*, Kyushu - Tohoku, Japan, May 28 - June 10:849–854.
- Meixner, J., Schill, E., Gaucher, E., and Kohl, T. (2014). Inferring the in situ stress regime in deep sediments: an example from the bruchsal geothermal site. *Geothermal Energy*, 2(7).
- Meixner, J., Schill, E., Grimmer, J. C., Gaucher, E., Kohl, T., and Klingler, P. (2016). Structural control of geothermal reservoirs in extensional tectonic settings: an example from the upper rhine graben. *J Struct Geol*, 82.
- Michael, A. J. (1984). Determination of stress from slip data: faults and folds. *Journal of Geophysical Research*, 89(B13):11517–11526.
- Michon, L., Balen, R. T. V., Merle, O., and Pagnier, H. (2003). The cenozoic evolution of the roer valley rift system integrated at a european scale. *Tectonophysics*, 367(1–2):101 – 126.
- Moeck, I., Schandelmeier, H., and Holl, H. G. (2009). The stress regime in a rotliegend reservoir of the northeast german basin. *International Journal of Earth Sciences*, 98(7):1643–1654.
- Moeck, I. S. (2014). Catalog of geothermal play types based on geologic controls. *Renewable and Sustainable Energy Reviews*, pages 867–882.
- Mohr, C. O. (1914). *Abhandlungen aus dem Gebiete der Technischen Mechanik*. Ernst und Sohn, Berlin, 2nd edition edition.
- Moore, D. E. and Lockner, D. A. (2007). Friction of the smectite clay montmorillonite: A review and interpretation of data. In Dixon, T. H. and Moore, J. C., editors, *The Seismogenic zone of subduction thrust faults*, pages 317–345. Columbia University Press, New York.
- Moos, D. and Zoback, M. D. (1990). Utilization of observations of well bore failure to constrain the orientation and magnitude of crustal stresses: Application to continental, deep-sea drilling project, and ocean drilling program boreholes. *Journal of Geophysical Research*, 95(B6):9305–9325.
- Morris, A., Ferrill, D. A., and Henderson, D. B. (1996). Slip-tendency analysis and fault reactivation. *Geology*, 24(3):275–278.
- Morrow, C., Radney, B., and Byerlee, J. (1992). Frictional strength and the effective pressure law of montmorillonite and Illite clays. In Evans, B. and Wong, T.-f., editors, *Fault mechanics and transport properties of rocks*, pages 69–88. Academic press Ltd., San Diego, CA, US.
- Müller, B., Zoback, M. L., Fuchs, K., Mastin, L., Gregersen, S., Pavoni, N., Stephansson, O., and Ljunggren, C. (1992). Regional patterns of tectonic stress in europe. *Journal of Geophysical Research*, 97(B8):11783.
- Müller, M., Niederding, F., and Wanninger, A. (1988). Tectonic style and pressure distribution at the northern margin of the alps between lake constance and the river inn. *Geologische Rundschau*, 77(3):787–796.
- Müller, W. H., Naef, H., and Graf, H. R. (2002). Geologische entwicklung der nordwestschweiz, neotektonik und langzeitzzenarien zürcher weinland: Ntb 99-08.

- Naef, H., Diebold, P., and Schlanke, S. (1985). Sedimentation und tektonik im tertiär der nordschweiz: Ntb 85-14.
- Nash, G. D. and Johnson, G. W. (2003). Conceptualization and implementation of a tectonic geomorphology study for geothermal exploration in the great basin, u.s.a. *Transactions - Geothermal Resources Council*, 27:663–667.
- Nowacki, W. (1986). *Thermoelasticity*. Elsevier Science, Burlington, 2nd ed. edition.
- Odling, N., Gillespie, P., Bourguin, B., Castaing, C., Chilés, J. P., Christensen, N. P., Fillion, E., Genter, A., Olsen, C., Thrane, L., Trice, R., Aarseth, E., Walsh, J. J., and Watterson, J. (1999). Variations in fracture system geometry and their implications for fluid flow in fractured hydrocarbon reservoirs. *Petroleum Geoscience*, 5(4):373–384.
- O’leary, D. W., Friedman, J. D., and Pohn, H. A. (1976). Lineament, linear, lineation: Some proposed new standards for old terms. *Bulletin of the Geological Society of America*, 87(10):1463–1469.
- Paschen, R., Oertel, D., and Grünwald, R. (2003). Möglichkeiten geothermischer stromerzeugung in deutschland: Sachstandsbericht.
- Peters, G. and van Balen, R. (2007). Pleistocene tectonics inferred from fluvial terraces of the northern upper rhine graben, germany. *Tectonophysics*, 430(1-4):41–65.
- Peters, G. and van Balen, R T (2007). Tectonic geomorphology of the northern upper rhine graben, germany. *Global and Planetary Change*, 58(1-4):310–334.
- Pflug, R. (1982). *Bau und Entwicklung des Oberrheingrabens*. *Erträge der Forschung*, 184: 145 S.,. Wissenschaftliche Buchgesellschaft, Darmstadt.
- Plaumann, S., Roth, J. P., and Sauer, K. (1967). Rock density in the upper rhine valley. *The Rhinegraben Progress Report 1967. Mem. Ser. Cart. Geol. Alsace Lorraine*, 26: 114-115.
- Plenefisch, T. and Bonjer, K. P. (1997). The stress field in the rhine graben area inferred from earthquake focal mechanisms and estimation of frictional parameters. *Tectonophysics*, 275(1-3):71–97.
- Pribnow, D. and Schellschmidt, R. (2000). Thermal tracking of upper crustal fluid flow in the rhine graben. *Geophysical Research Letters*, 27(13):1957–1960.
- Regenauer-Lieb, K. and Petit, J. P. (1997). Cutting of the european continental lithosphere: Plasticity theory applied to the present alpine collision. *Journal of Geophysical Research B: Solid Earth*, 102(B4):7731–7746.
- Reiter, W., Elfert, S., Glotzbach, C., and Spiegel, C. (2015). Plio-pleistocene evolution of the north alpine drainage system: new constraints from detrital thermochronology of foreland deposits. *International Journal of Earth Sciences*, 104(3):891–907.

- Ritter, J., Wagner, M., Bonjer, K. P., and Schmidt, B. (2009). The 2005 heidelberg and speyer earthquakes and their relationship to active tectonics in the central upper rhine graben. *International Journal of Earth Sciences*, 98(3):697–705.
- Roeloffs, E. A. (1988). Fault stability changes induced beneath a reservoir with cyclic variations in water level. *Journal of Geophysical Research*, 93(B3):2107–2124.
- Roller, J., Schill, E., Stober, I., Schneider, J., Neumann, T., and Kohl, T. (2015). Hydrochemical characterisation of a major central european heat flux anomaly: the bürchau geothermal spring system, southern black forest, germany. *Geothermal Energy*, 3(1).
- Roll, A. (1979). Versuch einer volumenbilanz des oberrheintalgrabens und seiner schultern. *Geologisches Jahrbuch*, A52:3–82.
- Rotstein, Y., Edel, J. B., Gabriel, G., Boulanger, D., Schaming, M., and Munsch, M. (2006). Insight into the structure of the upper rhine graben and its basement from a new compilation of bouguer gravity. *Tectonophysics*, 425(1-4):55–70.
- Rotstein, Y. and Schaming, M. (2011). The upper rhine graben (urg) revisited: Miocene transtension and transpression account for the observed first-order structures. *Tectonics*, 30.
- Rotstein, Y., Schaming, M., and Rouse, S. (2005). Tertiary tectonics of the dannemarie basin, upper rhine graben, and regional implications. *International Journal of Earth Sciences*, 94(4):669–679.
- Rowland, J. V. and Sibson, R. H. (2004). Structural controls on hydrothermal flow in a segmented rift system, taupo volcanic zone, new zealand. *Geofluids*, 4(4):259–283.
- Rummel, F. and Baumgärtner, J. (1987). Hydrofrac spannungsmessungen in den geothermischen erkundungsbohrungen des kontinentalen tiefbohrprogramms im schwarzwald und in der oberpfalz (report).
- Sahara, D., Schoenball, M., Kohl, T., and Müller, B. (2014). Impact of fracture networks on borehole breakout heterogeneities in crystalline rock. *International Journal of Rock Mechanics and Mining Sciences*, pages 301–309.
- Sanjuan, B., Millot, R., Dezayes, C., and Brach, M. (2010). Main characteristics of the deep geothermal brine (5km) at soultz-sous-forêts (france) determined using geochemical and tracer test data. *Comptes Rendus Geoscience*, 342(7-8):546–559.
- Sauer, K., Nägele, R., Tietze, R., and Kreutzkamp, H. (1981). *Geothermische Synthese des Oberrheingrabens zwischen Karlsruhe und Mannheim: Bestandsaufnahme*. Veröff. des geologischen Landesamtes Baden-Württemberg, Freiburg i.Br.
- Sawatzki, G., Hann, H. P., Groschopf, R., and Villinger, E. (2003). Geologische karte von baden-württemberg / badenweiler-lenzkirch-zone (süd-schwarzwald): Erläuterungen mit hinweisen für exkursionen.

- Schaltegger, U. (2000). U–pb geochronology of the southern black forest batholith (central variscan belt): timing of exhumation and granite emplacement. *International Journal of Earth Sciences*, 88(4):814–828.
- Scheiber, T., Fredin, O., Viola, G., Jarna, A., Gasser, D., and Łapińska-Viola, R. (2015). Manual extraction of bedrock lineaments from high-resolution lidar data: methodological bias and human perception. *GFF*.
- Schill, E., Cuenot, N., Genter, A., and Kohl, T. (2015). Review of the hydraulic development in the multi-reservoir / multi-well egs project of soultz-sous-forêts. *Proceedings World Geothermal Congress,, 19-25 April 2015, Melbourne, Australia*.
- Schill, E. and Klingler, P. (2011). Increase of productivity in the riehen geothermal system (switzerland): Tracer test and reservoir. *Mitteilungen der Geotechnik Schweiz*, 161:35–40.
- Schindler, M., Baumgärtner, J., Gandy, T., Hauffe, P., Hettkamp, T., Menzel, H., Penzkofer, P., Teza, D., Tischner, T., and Wahl, G. (2010). Successful hydraulic stimulation techniques for electric power production in the upper rhine graben, central europe. *Proceedings World Geothermal Congress,, 25-29 April 2010, Bali, Indonesia*.
- Schleicher, H. and Fritsche, R. (1978). Zur petrologie des triberger granites (mittlerer schwarzwald). *Jh. Landesamt für Geologie, Rohstoffe und Bergbau Baden-Württemberg LGRB*, 20:15–41.
- Scholz, C. H. (2010). *The Mechanics of Earthquakes and Faulting*. Cambridge University Press, Cambridge, 2 edition.
- Schumacher, M. E. (2002). Upper rhine graben: Role of preexisting structures during rift evolution. *Tectonics*, 21(1)(1):1006.
- Schwarz, M. (2005). *Evolution und Struktur des Oberrheingrabens – quantitative Einblicke mit Hilfe dreidimensionaler thermomechanischer Modellrechnungen*. PhD thesis, Universität Freiburg, Freiburg i.Br.
- Schwarz, M. and Henk, A. (2005). Evolution and structure of the upper rhine graben: insights from three-dimensional thermomechanical modelling. *International Journal of Earth Sciences*, 94(4):732–750.
- Sibson, R. H. (1977). Fault rocks and fault mechanisms. *Journal of the Geological Society*, 133(3):191–213.
- Sibson, R. H. (1996). Structural permeability of fluid-driven fault-fracture meshes. *Journal of Structural Geology*, 18(8):1031–1042.
- Sikaneta, S. and Evans, K. F. (2012). Stress heterogeneity and natural fractures in the basel egs granite reservoir inferred from an acoustic televiewer log of the basel-1 well. *Proceeding of 37th Workshop on Geothermal Reservoir Engineering, SGP-TR-194*.
- Simpson, D. W., Leith, W. S., and Scholz, C. H. (1988). Two types of reservoir-induced seismicity. *Bulletin - Seismological Society of America*, 78(6):2025–2040.

- Sissingh, W. (1998). Comparative tertiary stratigraphy of the rhine graben, bresse graben and molasse basin: correlation of alpine foreland events. *Tectonophysics*, 300(1-4):249–284.
- Sittler, C. (1969). The sedimentary trough of the rhine graben. *Tectonophysics*, 8(4):543–560.
- Stein, R. S., Barka, A. A., and Dieterich, J. H. (1997). Progressive failure on the north anatolian fault since 1939 by earthquake stress triggering. *Geophysical Journal International*, 128(3):594–604.
- Stein, R. S., King, G. C., and Lin, J. (1992). Change in failure stress on the southern san andreas fault system caused by the 1992 magnitude = 7.4 landers earthquake. *Science*, 258(5086):1328–1332.
- Streit, J. E. and Hillis, R. R. (2004). Estimating fault stability and sustainable fluid pressures for underground storage of co2 in porous rock. *Energy*, 29(9):1445–1456.
- Tembe, S., Lockner, D. A., Solum, J. G., Morrow, C. A., Wong, T. F., and Moore, D. E. (2006). Frictional strength of cuttings and core from safod drillhole phases 1 and 2. *Geophysical Research Letters*, 33(23).
- Tembe, S., Lockner, D. A., and Wong, T. F. (2010). Effect of clay content and mineralogy on frictional sliding behavior of simulated gouges: Binary and ternary mixtures of quartz, illite, and montmorillonite. *Journal of Geophysical Research: Solid Earth*, 115(3).
- Terzaghi, K. (1936). The shearing resistance of saturated soils and the angle between planes of shear. In: *Proceedings of the First International Conference on Soil Mechanics and Foundation Engineering*, pages 54–56, Harvard University Press, Cambridge, Massachusetts.
- Timar-Geng, Z., Fuegenschuh, B., Wetzel, A., and Dresmann, H. (2006a). Low-temperature thermochronology of the flanks of the southern upper rhine graben. *International Journal of Earth Sciences*, 95(4):685–702.
- Timar-Geng, Z., Fügenschuh, B., Wetzel, A., and Dresmann, H. (2006b). The low-temperature thermal history of northern switzerland as revealed by fission track analysis and inverse thermal modelling. *Eclogae Geologicae Helvetiae*, 99(2):255–270.
- Townend, J. (2003). *Mechanical constraints on the strength of the lithosphere and plate-bounding faults*. PhD thesis, Stanford University, Stanford, CA, US.
- Townend, J. and Zoback, M. D. (2000). How faulting keeps the crust strong. *Geology*, 28(5):399–402.
- Twiss, R. J. and Moore, E. M. (2007). *Structural Geology*. Susan Finnemore Brennan, New York, second edi edition.
- Ustaszewski, K. (2004). Reactivation of pre-existing crustal discontinuities: the southern upper rhine graben and the northern jura mountains - a natural laboratory. *Faculty of Science*, PhD Thesis.
- Valley, B. and Evans, K. F. (2007). Stress state at soultz-sous-forêts to 5 km depth from wellbore failure and hydraulic observations. *Proceeding of 32nd Workshop on Geothermal Reservoir Engineering*, pages 329–338.

- Valley, B. and Evans, K. F. (2009). Stress orientation to 5 km depth in the basement below basel (switzerland) from borehole failure analysis. *Swiss Journal of Geosciences*, 102(3):467–480.
- Valley, B. C. (2007). The relation between natural fracturing and stress heterogeneities in deep-seated crystalline rocks at soultz-sous-forêts (france). *ETH Repozentrale Hönggerberg, HIL C45, Zürich (2007)*. <http://dx.doi.org/10.3929/ethz-a-005562794>, page 260.
- Villemin, T., Alvarez, F., and Angelier, J. (1986). The rhinegraben - extension, subsidence and shoulder uplift. *Tectonophysics*, 128(1-2):47–59.
- Villinger, E. (1998). Zur flußgeschichte von rhein und donau in südwestdeutschland. *Jahresberichte und Mitteilungen des Oberrheinischen Geologischen Vereins*, 80:361–398.
- Wang, H. (2000). *Theory of Linear Poroelasticity with Application to Geomechanics and Hydrogeology*. Princeton University Press.
- Wellmann, J. F., Horowitz, F. G., Schill, E., and Regenauer-Lieb, K. (2010). Towards incorporating uncertainty of structural data in 3d geological inversion. *Tectonophysics*, 490(3-4):141–151.
- Wickert, F., Altherr, R., and Deutsch, M. (1990). Polyphase variscan tectonics and metamorphism along a segment of the saxothuringian-moldanubian boundary: The baden-baden zone, northern schwarzwald (f.r.g.). *Geologische Rundschau*, 79(3):627–647.
- Wileveau, Y., Cornet, F. H., Desroches, J., and Blumling, P. (2007). Complete in situ stress determination in an argillite sedimentary formation. *Physics and Chemistry of the Earth*, 32(8-14):866–878.
- Wirth, E. (1962). Die erdöllagerstätten badens. *Abh. geol. Landesamtes Baden-Württemberg, Freiburg i.Br*, 4(4):63–80.
- Wolter, K. E. (1987). *Untersuchung der in situ-Spannung, Residualspannung und der Mikroriss-Systeme in Graniten Süddeutschlands*. PhD thesis, Karlsruhe University.
- Worum, G., Michon, L., van Balen, R T, van Wees, J D, Cloetingh, S., and Pagnier, H. (2005). Pre-neogene controls on present-day fault activity in the west netherlands basin and roer valley rift system (southern netherlands): role of variations in fault orientation in a uniform low-stress regime. *Quaternary Science Reviews*, 24(3-4):473–488.
- Worum, G., van Wees, J D, Bada, G., van Balen, R T, Cloetingh, S., and Pagnier, H. (2004). Slip tendency analysis as a tool to constrain fault reactivation: A numerical approach applied to three-dimensional fault models in the roer valley rift system (southeast netherlands). *Journal of Geophysical Research*, 109(B2).
- Zang, A. and Stephansson, O. (2010). *Stress Fields of the Earth's Crust*. Springer, Berlin, first edition edition.
- Ziegler, M., Valley, B., and Evans, K. F. (2015). Characterisation of natural fractures and fracture zones of the basel egs reservoir inferred from geophysical logging of the basel-1 well. *Proceedings World Geothermal Congress,, 19-25 April, Melbourne, Australia*.

- Ziegler, P. and Dèzes, P. (2007). Cenozoic uplift of variscan massifs in the alpine foreland: Timing and controlling mechanisms. *Global and Planetary Change*, 58(1):237–269.
- Ziegler, P. A. (1990a). Collision related intra-plate compression deformations in western and central europe. *Journal of Geodynamics*, 11(4):357–388.
- Ziegler, P. A. (1990b). *Geological atlas of Western and Central Europe*. Shell Internationale Petroleum Maatschappij, Geol. Soc. Publ. House, Bath, UK, 2 edition.
- Ziegler, P. A. (1992). European cenozoic rift system. *Tectonophysics*, 208(1-3):91–111.
- Ziegler, P. A. and Dezes, P. (2005). Evolution of the lithosphere in the area of the rhine rift system. *International Journal of Earth Sciences*, 94(4):594–614.
- Ziegler, P. A. and Fraefel, M. (2009). Response of drainage systems to neogene evolution of the jura fold-thrust belt and upper rhine graben. *Swiss Journal of Geosciences*, 102(1):57–75.
- Ziegler, P. A., Schumacher, M. E., Dezes, P., van Wees, J.-D., and Cloetingh, S. (2006). Post-variscan evolution of the lithosphere in the area of the european cenozoic rift system. *Geological Society, London, Memoirs*, 32(1):97–112.
- Zimmerman, R. W. (2000). Coupling in poroelasticity and thermoelasticity. *International Journal of Rock Mechanics and Mining Sciences*, 37(1-2):79–87.
- Zoback, M. D. (2010). *Reservoir Geomechanics*. Cambridge University Press.
- Zoback, M. D., Barton, C. A., Brudy, M., Castillo, D. A., Finkbeiner, T., Grolimund, B. R., Moos, D. B., Peska, P., Ward, C. D., and Wiprut, D. J. (2003). Determination of stress orientation and magnitude in deep wells. *International Journal of Rock Mechanics and Mining Sciences*, 40(7-8):1049–1076.
- Zoback, M. D. and Healy, J. H. (1992). In situ stress measurements to 3.5 km depth in the cajon pass scientific research borehole: implications for the mechanics of crustal faulting. *Journal of Geophysical Research*, 97(B4):5039–5057.

DECLARATION OF AUTHORSHIP

Inferring the in-situ stress regime in deep sediments: an example from the Bruchsal geothermal site (Section 4)

Citation:

Meixner, J.; Schill, E.; Gaucher, E.; Kohl, T. (2014). Inferring the in situ stress regime in deep sediments: an example from the Bruchsal geothermal site, *Geothermal Energy*, (2), 7, doi:10.1186/s40517-014-0007-z.

This study was conducted under the framework of the LOGRO project to characterize the state of stress in deep seated sediments of the URG. I constructed the 3D structural geological model in PETREL and GOCAD on the basis of existing seismic sections, which I had reinterpreted. I analyzed the well log data and constructed the stratigraphic and lithological well profiles. E. Gaucher helped to evaluate existing stress models and supported determination of the proposed in-situ state of stress. E. Schill and T. Kohl improved the manuscript and assessed the chain of argumentation for plausibility. I wrote the manuscript and accompanied it through the review process.

Structural control of geothermal reservoirs in extensional tectonic settings: An example from the Upper Rhine Graben (Section 5)

Citation:

Meixner, J.; Grimmer, J.C.; Schill, E.; Gaucher, E.; Kohl, T.; Klingler, P. (2016). Structural control of geothermal reservoirs in extensional tectonic settings: An example from the Upper Rhine Graben. *Journal of Structural Geology*, (82), p. 1-15, doi: 82, 10.1016/j.jsg.2015.11.003.

This study aimed to investigate the role of geomechanical anisotropies in orthogonal fault patterns for subsurface fluid flow in the geothermal reservoirs of Bruchsal and Riehen. P. Klingler kindly provided the structural data for Riehen and reviewed the results. I constructed the structural geological 3D models for both sites in PETREL and GOCAD. J.C. Grimmer improved the discussion of the obtained fault patterns towards to a more regional point of view. I reviewed the existing stress data, developed a stress field model, and performed the slip- and dilation tendency analyses. E. Gaucher checked all for plausibility. E. Schill and T. Kohl significantly im-

proved the manuscript. I wrote the manuscript and accompanied it through the review process.

Lineament analysis for identification of fault zones in crystalline basement of the southern Schwarzwald (Germany) (Section 6)

Citation:

Meixner, J.; Grimmer, J.C.; Schill, E.; Becker, A.; Kohl, T. (submission in 2016). This section is prepared for submission in *Journal of Structural Geology* but will be supplemented by the major finding and conclusion from the Basel EGS stimulation (Section 8).

This study addresses the application of remote sensing techniques for identification of geothermal relevant faults in the crystalline basement of the Upper Rhine Graben. Kindly introduced in the topic by A. Becker, I conducted the morphotectonic and hydrographic analyses for the study area and compiled the result in a GIS database. Structural geological interpretation of the obtain fault pattern was supported by J.C. Grimmer. As always, E. Schill helped to reveal the important geomechanical implications for deep EGS systems in the URG, which arise from our findings. Together with T. Kohl, and with no mercy, she checked the results for consistency, which finally will improve the quality of the manuscript. I wrote the manuscript and I'm going to handle the review process.

ACKNOWLEDGMENTS

Ich muss vielen Leuten dankbar sein für ihre Unterstützung in der Zeit der Ausarbeitung dieser Arbeit.

Mein erster Dank gilt meinem Referenten Thomas Kohl, der mich all die Jahre betreut und unterstützt hat. Du hast es mir ermöglicht, an diesem spannenden Thema zu arbeiten und hast immer neue Impulse für neue Ideen und Konzepte geliefert. Mehr als einmal hat dein unerschütterlicher Glaube an meine fachlichen Fähigkeiten mir Mut und Zuversicht mit auf den Weg gegeben. Dafür danke ich dir ganz persönlich. Es ist für mich ein Privileg, mit dir zusammenzuarbeiten.

Christoph Hilgers danke ich für seine kurzfristige Zusage, meine Arbeit als Korreferent zu begleiten. Unter Nachbarn hilft man sich halt.

Drei Personen möchte ich einen besonderen Dank aussprechen.

Zuallererst ist da Eva Schill. Du warst die richtige Person, zur richtigen Zeit, am richtigen Ort. Du hast mich am Anfang meiner Arbeit aus einer Phase völliger Orientierungslosigkeit herausgeholt. Du hast mir beigebracht, wissenschaftlich zu denken und wissenschaftlich zu arbeiten. Wissenschaftlich zu schreiben gehörte leider nicht dazu. Deine kritischen Analysen und Reviews, aber auch dein Talent immer die richtigen Fragen zu stellen, haben aber letztendlich die Qualität meiner Arbeit unglaublich verbessert. Ohne Dich wäre die Arbeit so nie fertig geworden. Ich bin froh, dass ich dich hab. Danke für alles.

Als nächstes möchte ich Emmanuel Gaucher danken. Du warst immer für mich da, wenn ich Fragen oder Probleme hatte. Dein Wissen und dein gutes Gemüt machen dich nicht ohne Grund zum Anlaufpunkt Nr.1 bei uns. Die Freundschaft zu dir in den letzten Jahren war wunderbar. Danke für viele lehrreiche Diskussionen und Ratschläge.

Als letztes möchte ich Martin Schoenball hervorheben. Du hast mir beigebracht, wie wissenschaftliches Arbeiten in Perfektion aussehen kann. Dein analytischer Verstand hat mehrmals Unklarheiten und Ungereimtheiten in meinen Ergebnissen entdeckt. Ich hoffe, du liest

diese Arbeit nicht.

Weiterhin möchte ich allen Kollegen am Institut dafür danken, dass sie ein so harmonisches Arbeitsklima ermöglichen. Danke an Caro, Pia, Sebastian, Robin, Roman, Fabian und alle anderen für die tollen Stunden bei den ATMs.

Ich danke Jens Grimmer für die tollen Diskussionen zur Geologie und Tektonik. Du hast mich gelehrt, bei all meinen lokalen Studien nie das Große und Ganze aus den Augen zu verlieren.

Ein Dank geht an Frank Schilling, Birgit Müller, Philipp Blum und Inga Moeck, die immer für Fragen und inspirierende Diskussionen offen waren. Inga, ich hoffe ich sehe dich mal wieder auf einer Konferenz.

Ein großer Dank geht noch an Silke und Regina. Ihr seid das Öl, das all die kleinen Zahnräder in unserer Abteilung am Laufen hält.

Christian Scheffzük sei gedankt für die spannenden Abschweifungen in die Chemie und Teilchenphysik während der Mittagspausen. Es ist toll, dass du mein Hobby zu deinem Beruf gemacht hast.

Zu guter Letzt danke ich meiner Familie, Fritzi, Valerie und Erik. Es gibt keinen schöneren Grund, die Arbeit zu verlassen als Euch. In Zukunft werde ich wieder mehr Zeit für euch haben. Ich liebe Euch.

Danke!